The Dissertation Committee for Iván Ramírez
certifies that this is the approved version of the following dissertation:

Spectroscopic Properties of Granulation in K-type Dwarf Stars

Committee:

Carlos Allende Prieto, Supervisor

David L. Lambert, Supervisor

Christopher Sneden

John Scalo

Martin Asplund

Spectroscopic Properties of Granulation in K-type Dwarf Stars

by

Iván Ramírez, M.A.

DISSERTATION

Presented to the Faculty of the Graduate School of
The University of Texas at Austin
in Partial Fulfillment
of the Requirements
for the Degree of

DOCTOR OF PHILOSOPHY

THE UNIVERSITY OF TEXAS AT AUSTIN
May 2008

To my parents Rufino and Catalina,

and brothers Carlos, Sergio, and Henry

Acknowledgments

I am extremely grateful to my advisors, Carlos Allende Prieto and David L. Lambert for making this work possible. I was lucky enough to have the opportunity to work with Carlos, whose enthusiasm for finding better ways of doing things is contagious, and learn from him the basics as well as the intricate machinery involved in the field of stellar spectroscopy. Our efforts were always masterfully complemented by David's expertise and helpful advice. I thank them both for teaching me how to produce good science.

This thesis was motivated by the possibility of comparing our observations to theoretical calculations based on 3D model atmospheres. I thank Martin Asplund for providing such models and Lars Koesterke for helping with his 3D spectrum synthesis code. I also thank them for their comments on the original manuscript. The comments, suggestions, and constructive criticism of the members of my research committees, John Scalo, Peter Höflich, Chris Sneden, and J. Craig Wheeler, were very useful and I thank them for their involvement in my progress as a graduate student. I am also grateful to Jorge Meléndez for helping me get into graduate school and for his collaboration with several other projects.

This work required very high-quality data and I am therefore indebted to the McDonald Observatory support staff, in particular D. Doss, for making my several visits to Mt. Locke very productive. I also thank the HET observers, in particular S. Rostopchin and M. Shetrone, for their patience in handling my requests to observe naked-eye objects with a 9.2 m telescope!

Throughout the course of my graduate studies I have had the chance to meet personally and interact by correspondence with several astronomers that have contributed to the development of this thesis and other projects I have been involved with. My sincere thanks go to B. E. Reddy, S. Redfield, T. Bensby, M. Endl, I. Hubeny, B. Cochran, P. E. Nissen, M. Gerbaldi, F. Pont, and J. Borrero. I am also grateful for the help and friendship of many of the UT astronomy students (some of which are already PhDs!), in particular J. Sobeck, R. Wittenmyer, I. Roederer, D. Yong, and J. Simmerer. I would like to give a special thank you to my soul mate Andrea Urban for her friendship, unconditional support, and patience, as well as for proofreading the original manuscript and attempting to improve my spoken English.

Finally, I thank C. Burns of the UT visualization group for helping me produce nice 3D plots and the internet community at IRAF.NET for their IRAF support. This research has made use of the SIMBAD database, operated at CDS, Strasbourg, France. The solar granulation image from the Swedish Vacuum Solar Telescope shown in Fig. 1.1 was downloaded from the Institute for Solar Physics website (`http://www.solarphysics.kva.se`). The Swedish Vacuum Solar Telescope was operated on the island of La Palma by the Royal Swedish Academy of Sciences in the Spanish Observatorio del Roque de los Muchachos of the Instituto de Astrofísica de Canarias.

Spectroscopic Properties of Granulation in K-type Dwarf Stars

Publication No. ________________

Iván Ramírez, Ph.D.
The University of Texas at Austin, 2008

Supervisors: Carlos Allende Prieto
David L. Lambert

The presence of surface convection in K-type dwarfs is revealed in very high quality spectra ($R \simeq 180,000$, $S/N \gtrsim 300$) of nine bright stars. Relative radial velocities between pairs of spectra of the same object are determined with a mean accuracy of 12 m s^{-1}, which is necessary for achieving high S/N without distorting the spectral line shapes by coadding individual frames. The observed asymmetries and wavelength shifts of the Fe I absorption line profiles are mainly due to granulation. The bisectors of the strongest Fe I lines have a span of about 100 m s^{-1} and the central wavelengths of the weakest Fe I lines are shifted by up to -200 m s^{-1}. The blueshifts decrease for stronger Fe I lines, but they become independent of line strength for equivalent widths larger than about 100 mÅ. The detection of this "plateau" in the velocity shifts of the strongest Fe I lines is necessary to remove the uncertainty introduced by granulation, which is of the order of hundreds of meters per second, in the determination of absolute radial velocities. Line profiles computed using a 3D model atmosphere accurately reproduce the observations. Statistical tests show that the theoretical line asymmetries and wavelength shifts correspond to the observed ones at a 90–95% confidence level, thus validating the 3D model for spectroscopic studies of abundances and fundamental parameters of K-dwarfs. We find that 3D effects reduce the difference in the iron abundance determined separately from Fe II and Fe I lines, which is about 0.15 dex for 1D models, by two thirds, thus alleviating significantly the iron ionization imbalance problem in K-dwarfs. However, the 3D iron abundances from Fe I lines show a small dependence with excitation potential, similar to the 1D case, possibly due to non-LTE effects that have not been taken into account. We also find that the 3D correction to the effective temperatures of solar metallicity K-dwarfs derived with the infrared flux method is about +30 K. Finally, we show that the 3D spectrum synthesis of molecular bands greatly improves the agreement with the observational data compared to the 1D analysis, which overestimates the abundances derived from molecular features by a factor of 2.

Table of Contents

Chapter 1

Introduction

1.1 Solar and stellar granulation

Dedicated observations of the Sun's disk allowed William Herschel to recognize that, in addition to spots, "corrugations" extended over its surface in a continuously evolving pattern (Herschel 1801a,b). Subsequent observers confirmed the findings of Herschel and, after a short debate as to whether the structures resembled willow leaves, rice grains, or oat grains (Dawes 1864, Nasmyth 1865), the term *granulation* was finally adopted for this phenomenon. The term proved to be accurate at the turn of the century, when the first good photographs of the solar disk became available (Janssen 1896).

High quality granulation images, similar to that shown in Fig. 1.1, have been obtained from the ground at a number of facilities, for example Pic du Midi Observatory (e.g., Roudier & Muller 1987, Dialetis et al. 1988), the Swedish Vacuum Solar Telescope (e.g., Scharmer et al. 1985, Hirzberger et al. 1997, Getling & Brandt 2002), the Dutch Open Telescope (Rutten et al. 2004), among many others. Spatially resolved spectrograms of solar granulation have also been acquired (e.g., Roudier et al. 1991, Nesis et al. 1992), allowing a better characterization of its dynamical properties, in recent years

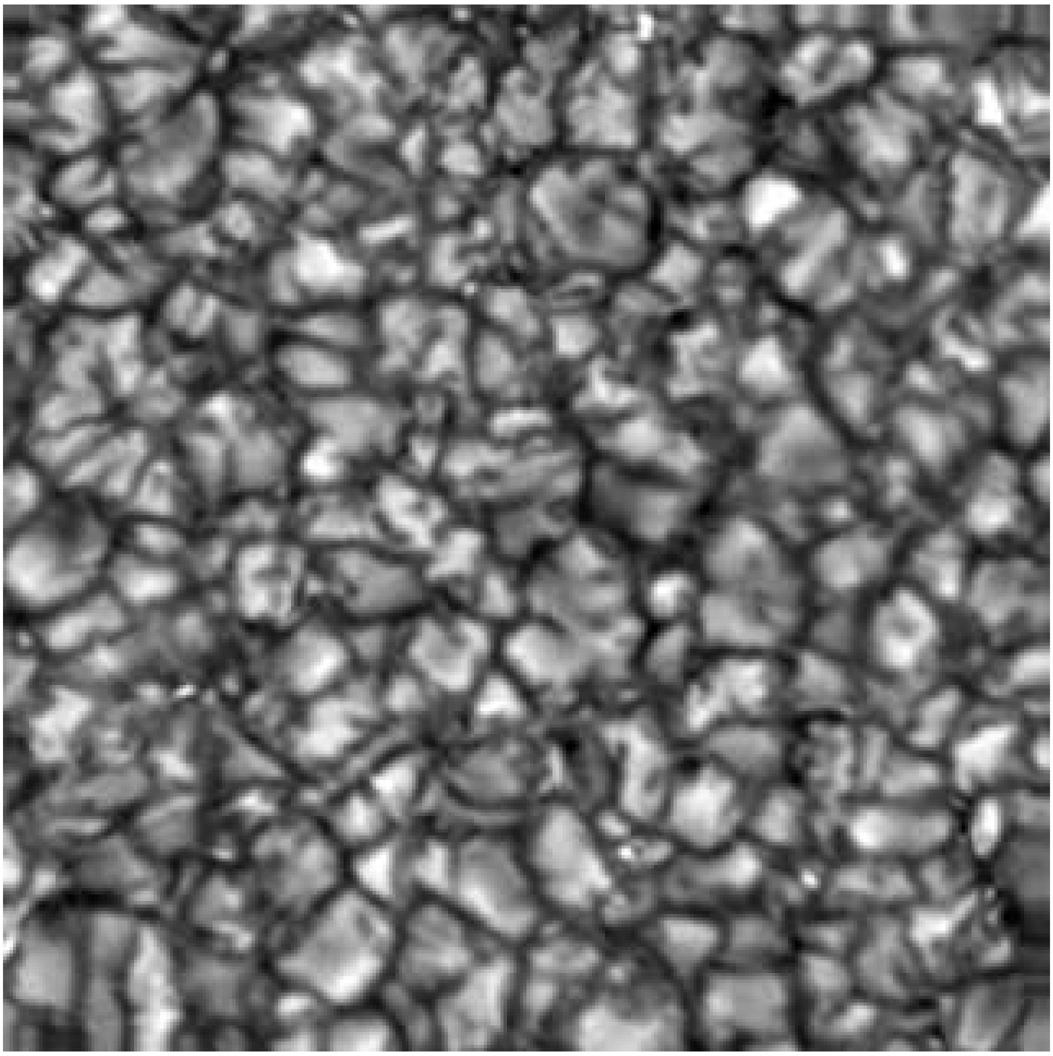

Figure 1.1: This G-band (430.5 nm) image of a $\sim 30'' \times 30''$ field shows the granulation pattern near the solar disk center observed with the 50 cm Swedish Vacuum Solar Telescope.

particularly using the Michelson Doppler Imager (MDI) aboard the SOHO satellite (e.g., Lawrence et al. 1999, Hathaway et al. 2000). Currently, the best available images and spectrograms of solar granulation are being obtained with the Swedish 1-m Solar Telescope (Scharmer et al. 2003), which uses adaptive optics to reach diffraction limited spatial resolution (about 0.1 arcseconds, $0.1''$, or approximately 70 km on the solar surface). The basic observational properties of solar granulation have been reviewed by Bray et al. (1984) and Muller (1999), and are summarized below.

Solar granulation consists of bright and hot upflows (granules of roughly polygonal shape) surrounded by dark and cold downflows (intergranular lanes). Most granules have sizes between $1''$ and $2''$, with an average separation of a few tenths of an arcsecond, which corresponds to the width of the intergranular lanes. Area histograms, however, show that the number of granules increases very rapidly for small sizes, thus making the concept of mean granule size, from an observational point of view, ill-defined.

Time series observations show that most of the large granules experience fragmentation. After growing to sizes between about $2''$ and $5''$, these granules “explode” from their central regions, where intergranular lanes appear, generating about three to four smaller granules. Some granules also appear to emerge from the intergranular areas, while shrinking granules disappear into them. Although it is also ill-defined (it is not clear when a granule is born or ceases to exist), the mean lifetime of a recognizable granule is about 10 minutes (see Chapter 2 in Bray et al. 1984 for more details).

Doppler spectrograms demonstrate that there is a strong correlation between the granulation intensity and velocity fields, with a small dependence of the degree of correlation on photospheric height. The observed root mean square (RMS) vertical velocity is of the order of 1 km s^{-1} (although it depends on height, reaching a maximum of about 4 km s^{-1} near the visible surface) while the RMS intensity contrast[1] is about 15 % in the visible spectral range.

The observed properties of solar granulation suggest a convective origin and it is now well established that this phenomenon is the visible manifestation of sub-surface convective motions. Solar interior models predict that the temperature gradient of the gas in last third of the solar radius is larger than the adiabatic temperature gradient, making it unstable to convection. When the rising gas from this convective envelope reaches the photosphere, it cools down rapidly by radiation losses. Since the opacity decreases steeply with gas temperature, the temperature of the photosphere decreases abruptly as hydrogen recombines and the gas becomes suddenly transparent. As a result, horizontal pressure gradients are no longer supported by the central upflow, which then decelerates as the granule expands until it either becomes a downflow, explodes into smaller granules separated by thin downflows, or merges with another upflow. The cool downflows become filamentary due to mass conservation; their higher densities force them to fall rapidly into deeper layers to compensate for the mass transported by the rising low density upflows.

---

[1] The intensity contrast is defined as $2 \times (I_{\max} - I_{\min})/(I_{\max} + I_{\min})$, where $I_{\max}$ is the intensity of the bright granules and $I_{\min}$ that of the dark intergranular lanes (e.g., Bray et al. 1984, p. 45).

Hydrodynamic simulations including the effect of the radiation field are necessary to better understand solar granulation. Two-dimensional, as well as three-dimensional radiative-hydrodynamic models have been computed from basic fluid dynamics principles (e.g., Nordlund 1982, Steffen & Freytag 1991, Stein & Nordlund 1998, Robinson et al. 2003, Vögler 2004). Even though, due to computational limitations, these models describe only a small, hopefully representative, piece of the solar envelope and have a limited spatial resolution, they have been remarkably successful at reproducing the observed properties of solar granulation.

Signatures of solar granulation are also present in the Sun's absorption line spectrum. In the spatially unresolved solar spectrum, the high degree of correlation between the intensity and velocity fields produce characteristic line shapes and central wavelength shifts that constitute excellent probes for solar granulation, given the non-local nature of spectral line formation (details are given in Sect. 1.4). Hydrodynamic simulations of solar granulation have also been successful at reproducing these absorption line signatures (e.g., Dravins et al. 1981, Steffen & Freytag 1991, Asplund et al. 2000b).

Since, according to the theory of stellar interiors, non-negligible convective envelopes are present in cool stars (spectral type F and later on the main sequence, G and later for supergiants; see, e.g., Hansen & Kawaler 1994), it is expected that they also experience granulation on their surfaces. With a few notable exceptions, stellar disks are completely unresolved and, therefore, there are no near-future prospects for direct observations of stellar granulation.

Furthermore, even if it were possible, in some of these stars the granulation pattern is expected to be hidden beneath the visible surface (Sect. 3.1.1). However, as in the solar case, we expect the granulation effects to be also present in stellar spectra. Very careful observations are required to detect the signatures of granulation in this manner (Dravins 1987a). High quality data have been used by several authors to show that stars with convective envelopes experience granulation with different degrees of intensity and velocity contrasts (e.g., Dravins 1987b, Allende Prieto et al. 2002, Gray 1982, 2005; see also our Appendix A). Gray & Nagel (1989) have even defined a granulation boundary on the HR diagram based on observations of spectral line asymmetries in hot and cool stars. They suggest that, contrary to cooler stars, the shape and magnitude of the line asymmetries in hot stars (A-type and hotter on the main sequence, F-type and hotter for the supergiants) cannot be related to deep envelope convection.

As in the solar case, hydrodynamic models of inhomogeneous stellar atmospheres (e.g., Nordlund & Dravins 1990, Trampedach 2007) satisfactorily reproduce the spectroscopic signatures of granulation (e.g., Dravins & Nordlund 1990b, Allende Prieto et al. 2002). These theory vs. observation comparisons, however, are scarce; they have been performed for only a few stars and often using a limited set of spectral features. There is an urgent need for quantitative testing of the fundamental predictions of these hydrodynamic simulations in order to better understand stellar granulation and its impact on the observed spectra.

1.2 The chemical compositions of stars

High resolution spectroscopy is currently the best approach to the determination of chemical compositions of stars. By measuring an absorption line strength, we can quantify the abundance of the element responsible for the absorption at that particular wavelength, as long as we are able to construct realistic models for line absorption in stellar photospheres, including a reasonable knowledge of the physics involved in the absorption process and the physical conditions (temperature, density, pressure, etc.) of every point on the stellar photosphere. Granulation plays an important role for the latter but we will defer the details to Sect. 1.2.3. This section provides an overview of the standard techniques of stellar abundance determination, a very short summary of some of the abundance studies relevant to this work, and how granulation, an effect that has been largely ignored, has had a significant impact on them.

Throughout this thesis, we will use the standard definitions and notation adopted in the stellar abundance field. For example, the abundance of an element X, with number density N_{X}, with respect to hydrogen, is given by

$$A(\mathrm{X}) = A_{\mathrm{X}} = \log(N_{\mathrm{X}}/N_{\mathrm{H}}) + 12 \ , \tag{1.1}$$

while the abundance of X with respect to the Sun ($A_{\mathrm{X}}^{\odot}$ being the abundance of X in the solar photosphere) is

$$[\mathrm{X}/\mathrm{H}] = A_{\mathrm{X}} - A_{\mathrm{X}}^{\odot} \ . \tag{1.2}$$

As it is customary, we will often use the iron abundance [Fe/H] as a proxy for the overall stellar *metallicity*. The ratio of abundances of the elements X and Y, with respect to the solar value, is therefore given by

$$[\mathrm{X/Y}] = [\mathrm{X/H}] - [\mathrm{Y/H}] \ . \tag{1.3}$$

1.2.1 Classical model atmospheres and spectroscopic analyses

The goal of stellar atmosphere modeling is to determine the physical properties of the regions from where radiation escapes. We refer to as “classical” models those that are calculated adopting the following conventional set of assumptions:

- Plane parallel geometry.- A gas cube extending to the deepest layers of the photosphere is assumed to be representative of any photospheric region (in stars with extended atmospheres, this geometry is replaced by a spherically symmetric envelope).
- Hydrostatic equilibrium.- The pressure gradient equals the gravitational force at large scales everywhere (radiation pressure is included in the calculations, which is particularly important for hot stars).
- Energy flux conservation.- The total energy flux (radiative and convective; the latter often obtained from a parameterized model of convection transport) is conserved throughout the stellar atmosphere.
- Local Thermodynamic Equilibrium (LTE).- The atomic level populations and ionization fractions are assumed to be those given by the Boltzmann and Saha equations for the local kinetic temperature.

- One-dimensionality.- The gas is static and homogeneous; only one variable (namely depth in the plane parallel geometry or radius in spherically symmetric models) is required to describe the full range of physical quantities across the photosphere.

In addition to these basic assumptions, it is also customary to ignore the effects of magnetic fields, rotation, and chromospheric activity. Furthermore, the chemical composition is assumed to be the same everywhere.

All these simplifications are reasonably justified but must not be ignored when the results that are obtained from the models are used for theoretical interpretations, in particular when those results are internally inconsistent or do not fit into well established theories.

Classical model atmospheres have been computed by several groups. The most commonly used models are those computed with the codes ATLAS (Kurucz 1979, 1993a) and MARCS (Gustafsson et al. 1975). Non-LTE models for hot stars and white dwarfs have been computed by Hubeny & Lanz (1995) and Lanz & Hubeny (1995), respectively. For very cool dwarfs, the Phoenix model atmospheres (e.g., Hauschildt et al. 1999) are becoming quite popular, while Sudarsky et al. (2003) and Burrows et al. (2006) have also recently computed models for giant planets and brown dwarfs, respectively. In practice, grids of model atmospheres in the $T_{\mathrm{eff}}, \log g, [\mathrm{Fe/H}]$ space are made available by these groups while users, to save computing time, interpolate to the fundamental parameters of their problem stars. Interpolation errors are often assumed to be small so they are neglected.

Spectrum synthesis uses the model atmosphere pertinent to the problem star and a line-list to calculate spectral lines. Accurate atomic data (transition probabilities, energy of the levels, collisional broadening constants, etc.) are necessary for the analysis. For the purposes of this work, we will assume that these atomic data are very well known. The careful line selection that we adopted guarantees that this is a realistic assumption.

The equation of radiative transfer is solved along rays in the model photosphere for a given set of frequencies (or wavelengths or velocities). The continuum and line opacities are calculated using the temperature and pressure information from the models. After adding the thermal, collisional, and rotational broadening effects, the result is a theoretical spectral line. With the input data and model set, one can modify the input abundances of all elements until the predicted spectral lines match the observations.

By comparing the spectral lines computed in this way with the observations, it is clear that additional line broadening is necessary, in particular to explain why the predicted equivalent widths of strong saturated lines are significantly smaller than the observed ones. In classical stellar abundance work, this missing broadening is accounted for with the concepts of macroturbulence and microturbulence (Struve & Elvey 1934). In this formulation (see, e.g., Gray 1978, 1992 for more details), the microturbulence is related to motions on a scale smaller than the photon mean free path and is taken into account in the spectral line calculation by convolving the absorption coefficient with a microturbulence profile $\eta(\Delta v)$; i.e.,

$$\alpha = \alpha' * \eta(\Delta v) \ , \tag{1.4}$$

where α' is the absorption coefficient without microturbulence, before solving the radiative transfer problem.[2] Following Struve & Elvey (1934), the microturbulence profile is generally assumed to have a Gaussian shape; i.e.,

$$\eta(\Delta v) = (\pi v_t^2)^{-1/2} e^{-(\Delta v/v_t)^2} \ , \tag{1.5}$$

where v_t is the microturbulent velocity or, as it is more often referred to as, *the* microturbulence.

On the other hand, motions that extend beyond the photon mean free path and therefore do not enter the radiative transfer problem, are referred to as macroturbulence, and affect the intensity spectrum I_ν^0 by means of a macroturbulence profile $\Theta(\Delta v)$ such that

$$I_\nu = I_\nu^0 * \Theta(\Delta v) \ . \tag{1.6}$$

Several different forms of the macroturbulence profile have been formulated (e.g., the isotropic and radial-tangential models described in Gray 1975), in which one or two macrotubulent velocity parameters are introduced. In general, however, only one macrotubulent velocity $v_{\rm mac}$, or simply *the* macroturbulence, is adopted (i.e., analyses often use one-parameter models or use the same value for the two parameters).

---

[2] The $*$ symbol denotes convolution, i.e., $(f*g)(x) = \int f(x')g(x-x')dx'$ is the convolution of f and g, which are functions of the independent variable x.

The term “turbulence” is misleading in this context, given that these motions are not turbulent, as defined in standard fluid dynamics theory (e.g., Landau & Lifshitz 1987). Instead, these motions are related to the granulation velocity field (Dravins & Nordlund 1990a, their Sect. 7.4; Asplund et al. 2000b). As such, the concepts of macro and microturbulence do not take into account the correlations between temperature, density, pressure, intensity, and velocity fields that are characteristic of the granulation phenomenon. Therefore, even though they have proven useful, the macro and microturbulence parameterization constitutes a poor representation of the physics involved in this important component of the spectral line broadening.

In practice, several spectral features are available from a high resolution spectrum. The abundances of several elements can be determined from a single spectrum using an appropriate model atmosphere and an accurate line list. Computer codes to synthesize spectral lines from model atmospheres and line lists, such as SYNTHE (Kurucz 1993b),[3] MOOG (Sneden 1973),[4] SYNSPEC (Hubeny 1988, Hubeny & Lanz 1995),[5] SPECTRUM (Gray & Corbally 1994),[6] and others, are readily available and have evolved to work with almost any flavor of model atmosphere. Thus, the determination of chemical compositions of stars using classical methods has become a routine exercise and it is, therefore, crucial to be critical about every basic assumption involved.

---

[3] `http://kurucz.harvard.edu/programs/SYNTHECD`

[4] `http://verdi.as.utexas.edu/moog.html`

[5] `http://nova.astro.umd.edu/Synspec43/synspec.html`

[6] `http://www.phys.appstate.edu/spectrum/spectrum.html`

1.2.2 A quick survey of classical abundance studies

Thanks to the availability of atomic databases, grids of model atmospheres, and spectrum synthesis codes, a large number of studies concerning the determination of chemical compositions of stars have been published in the last few decades. We will not attempt to describe all of them, or even a representative group (for complete reviews see Cayrel & Strobel 1966, Wheeler et al. 1989, and McWilliam 1997). Instead, we will concentrate on those that are relevant for this thesis and will cite only relatively recent papers. In that sense, the following is not a historical summary but a motivational background for the present study.

– *The Sun*

In a seminal paper, Anders & Grevesse (1989) showed that, with few exceptions, the abundances of elements in the solar photosphere, as determined using the classical spectroscopic methods described in Sect. 1.2.1, agree with those measured in a particular class of meteorites, the CI carbonaceous chondrites, at the level of about 10 to 20%, depending on the set of elements used for comparison (Fig. 1.2).[7] These small differences are well within the observational and measurement errors. The meteoritic abundances are expected to reflect those of the solar photosphere because meteorites were formed with material from the solar nebula and some have never experienced physicochemical

---

[7] Note that these meteoritic abundances are not on an absolute scale but have been renormalized to agree, on average, with the solar abundances of a sample of elements (Si, Mg, Fe, Ca, among others).

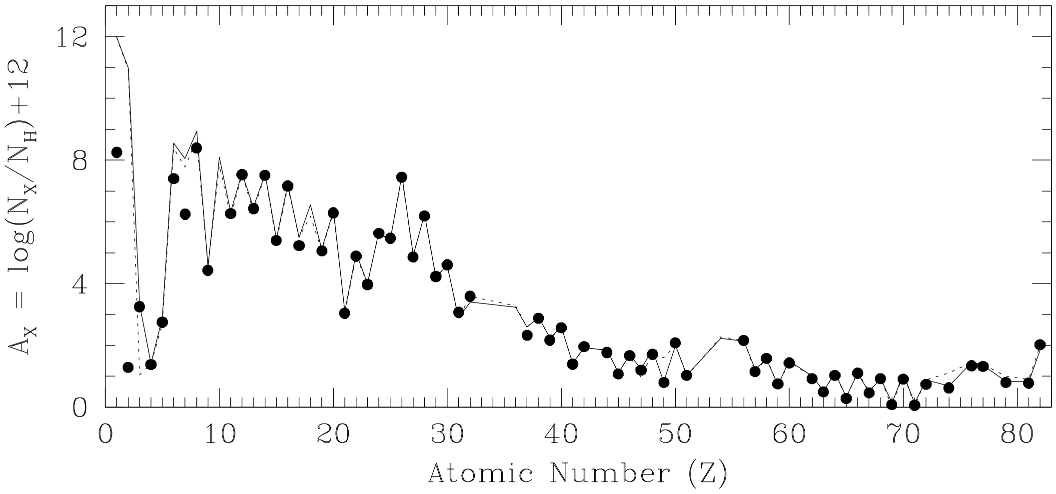

Figure 1.2: The solar chemical composition. The photospheric abundances by Anders & Grevesse (1989) are show with the solid line; the dotted lines correspond to the revised abundances by Asplund et al. (2005b). Filled circles represent the abundances in CI chondrites, which are obtained as fractional abundances relative to Si (instead of H as in the case of the photospheric abundances) but have been re-scaled to allow a direct comparison with the photospheric values (e.g., Palme & Jones 2005).

processes. Among the different types of meteorites, the chemical composition of CI chondrites is the best match to the photospheric abundances (e.g., Palme & Jones 2005). The good agreement between photospheric and meteoritic abundances has been confirmed by several authors thereafter and many of the original discrepancies have been resolved by adopting more accurate transition probabilities for the spectral lines used to determine the photospheric abundances. Thus, these results have been used to support the classical method of stellar abundance determination.

CI chondrites have not retained volatile elements such as carbon, nitrogen, and oxygen, among others. The photospheric CNO abundances, however, can be constrained from helioseismology and models of the solar interior. The observed frequencies of solar oscillations depend on the depth of the convection zone (e.g., Basu & Antia 1997), which, in turn, depends on the heavy element content, which is dominated by CNO (e.g., Bahcall et al. 2004). The CNO abundances given by Anders & Grevesse (1989; $A_{\rm C} = 8.56, A_{\rm N} = 8.05, A_0 = 8.93$) agree reasonably well with those obtained using this independent method. In recent years, however, this agreement has been compromised, giving rise to one of the most fundamental problems of contemporary stellar astrophysics (Sect. 1.2.3). When very accurate atomic physics is used (including better laboratory transition probabilities, proper identification of line-blends, and non-LTE effects), classical abundance determinations fail to provide consistent results for carbon and oxygen in the Sun; i.e., different spectral features result in abundance differences that are larger than the expected observational errors. The solution to these problems (Sect. 1.2.3) has resulted in a significant downward revision of the solar C and O abundances (see the reviews by Asplund 2005 and Allende Prieto 2007).

– ***Nearby stars***

Nearby stars are prime targets for stellar abundance work due to their brightness, which makes it possible to obtain high resolution, high signal-to-noise spectra of them and because their fundamental parameters can be accurately determined; their trigonometric parallaxes can be measured with high precision and the effects of interstellar reddening are negligible, for example. Most nearby stars belong to the so called thin disk of the Galaxy; locally only about 10% of them are thick disk members. Halo stars are even more rare in the solar vicinity. Studies of nearby stars have shown that chemical evolution has occurred in the Galaxy (e.g., Edvardsson et al. 1993). This is a remarkable observational result that has been qualitatively and quantitatively explained by theoretical models (e.g., Timmes et al. 1995, Chiappini et al. 1997, Kobayashi et al. 2006). Systematic differences in the abundance patterns of thin and thick disk stars (e.g., Bensby et al. 2005, Reddy et al. 2006, Ramírez et al. 2007), as well as halo members (e.g., Nissen & Schuster 1997, Fulbright 2000), have provided strong constraints to theories of Galaxy formation.

There is no doubt that spectroscopic studies of nearby stars have provided a wealth of useful information for general astrophysics and cosmology. It is, therefore, very important to check that the abundances determined using classical methods are self-consistent. Interestingly, the iron abundance determinations in FGK stars are not; currently, there is no general agreement as to whether iron line formation in FGK stars is well modeled. Some have suggested that when correct atmospheric parameters and atomic data are employed, it is impossible to make the iron abundance determined from neutral iron (Fe I) lines agree with that given by the singly ionized iron (Fe II) lines (e.g. Allende Prieto et al. 2004, Yong et al. 2004, Schuler et al. 2006b, Ramírez et al. 2007; Fig. 1.3). On the other hand, by systematically altering the atmospheric parameters $T_{\rm eff}$ and $\log g$, others claim that the ionization balance of

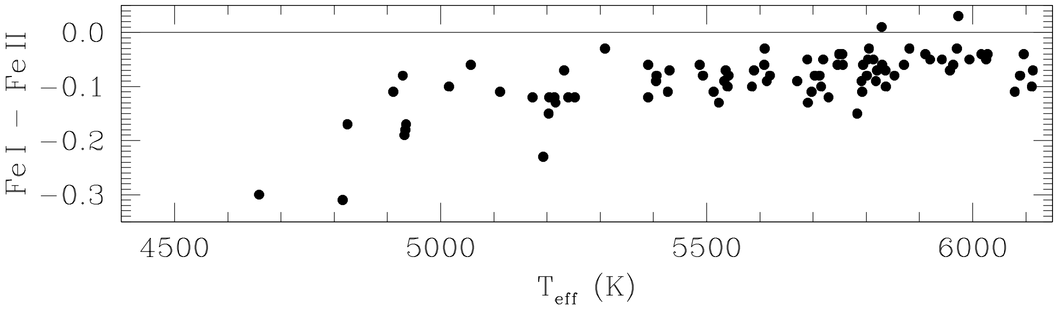

Figure 1.3: Difference between the mean iron abundance derived from Fe I and Fe II lines according to Ramírez et al. (2007) for stars in the solar neighborhood ($d < 100$ pc) with $\log g > 4.2$, [Fe/H] > -0.2, as a function of $T_{\rm eff}$. Above 5500 K, an almost constant difference of 0.07 dex is present. At lower temperatures, the discrepancy worsens, reaching a maximum difference of about 0.30 dex at $T_{\rm eff} \lesssim 4800$ K.

iron lines can be satisfied. This tuning of the parameters, however, can lead to erroneous results, in particular for nearby stars for which the fundamental properties are well determined.

The lack of internal consistency in the iron abundance determination is alarming, since [Fe/H] is used as a proxy for the overall metallicity of stars and even entire stellar populations, including galaxies. The ionization problem is present in both metal rich and metal poor stars but it becomes severe for very cool dwarfs, which are the most numerous stars in the Galaxy. Other elements showing similar line-to-line discrepancies are calcium (Allende Prieto et al. 2004) and chromium (Sobeck et al. 2007). In these studies, the atomic data are very accurate and the stellar parameters are well known, which leads us to conclude that some more fundamental ingredient of the classical method of abundance determination needs to be revised.

It has been suggested that non-LTE effects are responsible for the ionization imbalance problems mentioned above. Unfortunately, non-LTE calculations are quite complicated and, in many cases, limited by the accuracy of the relevant collisional and radiative rates or the computer power available. Nevertheless, several important efforts have been made (e.g., Shchukina & Trujillo Bueno 2001, Korn et al. 2003, Mashonkina et al. 2007).

Another important discrepancy has been reported for the oxygen abundance in K-dwarfs (e.g., Morel & Micela 2004, Schuler et al. 2006a). Morel & Micela (2004) showed that the oxygen abundance determined from the 630 nm [O I] line is well behaved in a sample of RS CVn binaries, field subgiants and disk dwarfs, as well as in stars in the Pleiades and Hyades clusters; i.e., it is roughly solar ($[\mathrm{O/H}] \simeq 0$) and independent of T_{eff}. However, the abundances obtained from the 777 nm O I triplet diverge at low temperatures, reaching values as high as $[\mathrm{O/Fe}] \simeq 2$ dex for $T_{\mathrm{eff}} \simeq 4500$ K (Fig. 1.4). Since the coolest stars of their sample are also the ones with the largest chromospheric activity, they suggested that a stellar activity related effect could be responsible for the discrepancies and that the temperature correlation could be consequential. However, Schuler et al. (2006a) have found no correlation between activity indicators and the 777 nm oxygen abundance. In any case, by comparing Figs. 1.3 and 1.4, it seems that the iron ionization and the oxygen abundance problems in K-dwarfs are related.

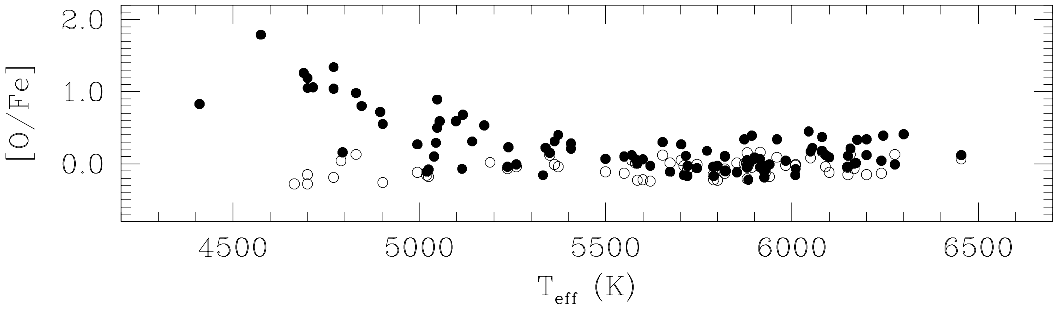

Figure 1.4: Oxygen abundances of the Morel & Micela (2004) sample stars obtained from the 630 nm [O I] line (open circles) and the 777 nm O I triplet (filled circles) as a function of stellar effective temperature. Note that the discrepancies start at $T_{\rm eff} \simeq 5500$ K and worsen at lower temperatures, resembling the behavior of the abundances in the iron ionization problem (Fig. 1.3) and thus suggesting a common origin.

– *Metal-poor stars*

The study of metal deficient stars has broadened the impact of the stellar abundance field since it can be linked not only to the early stages of galaxy formation but also to the study of the first stars and Big Bang nucleosynthesis (see, for example, the review by Beers & Christlieb 2005). Particularly interesting topics within this field include those related to the lithium and oxygen abundances.

Spite & Spite (1982) discovered that the lithium abundance in unevolved metal-poor warm stars is roughly independent of metallicity, thus suggesting a pre-stellar origin. A significant difference between the primordial lithium abundance in metal poor stars and that predicted by Big Bang nucleosynthesis models remains to be explained (e.g., Lambert 2004), probably by a revision of the fundamental parameters of metal-poor turn-off stars (Meléndez & Ramírez 2004), diffusion and mixing in stellar evolution models (Korn et al. 2006), or non-standard Big Bang nucleosynthesis models (e.g., Steigman 2006). However, it is also possibly related to fundamental limitations of classical abundance analyses.

Oxygen abundances can be determined in metal-poor stars, both dwarfs and giants, using a number of spectral features. Classical spectroscopic abundance determination techniques, however, have provided inconsistent results over the years. One illustrative example is that of the so called "oxygen abundance problem," in which the exact form of the oxygen abundance trend, [O/Fe] vs. [Fe/H], at low metallicities has been the subject of intense debate (see the introduction in Meléndez et al. 2006 for a short summary and references). While some authors have suggested that the [O/Fe] ratios remain constant at a level of about 0.5 dex as the lowest stellar metallicities are reached, others claim that the [O/Fe] ratios increase with lower [Fe/H] values, reaching values as high as 1 dex at [Fe/H] $= -3$.

Admittedly, the observation of some of the oxygen features is difficult (e.g., the molecular bands in the IR need accurate corrections for fringing and the forbidden line at 630 nm requires very high S/N ratios when it becomes very weak) while others are subject to large systematic errors such as strong non-LTE effects (e.g., the 777 nm O I triplet). However, even when these effects are taken into account, to the extent that it is currently possible, some discrepancies remain.

Another interesting topic in the metal-poor star field is that of the carbon enhanced metal poor (CEMP) stars. It has been shown that a significant fraction of metal-poor stars ([Fe/H] < -2) have [C/Fe] ratios larger than 1 dex. Although the actual percentage of CEMP stars is uncertain (between 7 and 20%; e.g., Lucatello et al. 2005, Cohen et al. 2005), their very existence remains a puzzle. Possible explanations include massive carbon production in the first stars, enhanced internal production of carbon in stars with very low iron abundances, and contamination of photospheric abundances by a companion of intermediate mass during its AGB phase (see Beers & Christlieb 2005). As for the oxygen abundances, the carbon features in stellar spectra are also subject to a series of observational and modeling uncertainties. For example, the carbon abundances are often determined from molecular features (e.g., CN, CH, C_2), which are very sensitive to the temperature structure of the line-forming regions; a relatively small change in the temperature of the relevant photospheric layers can significantly alter the rate of molecule formation and therefore the predicted band strength, thus leading to incorrect abundances in spectroscopic analyses.

As has been shown by the examples given above, stellar abundances have wide implications for several other fields, in particular chemical evolution, but we are at the risk of drawing incorrect conclusions on the light of several problems and uncertainties. In this context, any improvement to the modeling of stellar spectra, whether it is simple or complex to implement, will be greatly beneficial to our understanding of cosmochemistry.

1.2.3 The impact of granulation

Compared to the spectral lines computed with classical, static models, granulation simulations predict different line strengths due to the presence of temperature and density inhomogeneities as well as a different atmospheric structure.

The abundances of carbon and oxygen, for example, have been recently determined in the Sun using a variety of spectral features, including both atomic and molecular transitions, by Asplund et al. (2004, 2005a). A comparison of the abundances determined using the semi-empirical Holweger & Muller (1974) 1D model with those obtained using their 3D hydrodynamic simulation shows that the 3D results are internally more consistent. While the 1D models result in line-to-line abundance differences of about 0.2 dex, the 3D abundances are consistent at the level of a few hundreds of a dex (see Table 1 in Asplund 2005). Note, however, that not only the use of the 3D model is responsible for this good internal agreement; recent improvements in the non-LTE treatment of certain features and the recognition of line blends in others have also contributed to this important result.

In the Sun, the mean temperature structure is not significantly different from that predicted by 1D models and it is mainly because of the inhomogeneities that the abundance results are more consistent in the 3D than in the 1D model. For example, at the depths of molecule formation, there are regions that are cooler than the mean 1D prediction. In these regions, the molecular formation rate increases, leading to an overall stronger absorption. In the hotter regions, less molecules are formed but since the rate of molecule formation does not vary linearly with temperature, this decrease does not compensate the increase of the number of molecules in the cool regions. Overall, the temperature inhomogeneities result in larger number densities of molecules compared to the homogeneous (1D) case, which make the predicted lines stronger and therefore require smaller abundances to match the observations. Indeed, the 3D abundances determined from molecular features are smaller than those obtained with 1D models.

The CO abundances of the Sun are now well determined, as the line-to-line discrepancies have been solved with the use of more realistic models. However, the recent revision of these abundances has resulted in an decrease of the solar overall metal abundance by about 30%, which has led to a severe disagreement with the abundances that are inferred from helioseismology observations interpreted with stellar interior models (Bahcall et al. 2004, 2005; Delahaye & Pinsonneault 2006, Basu & Antia 2008). Introducing granulation in the solar abundance determination has therefore solved one problem at the expense of revealing a new and probably more fundamental one. Regardless of whether its solution lies in a revision of the 3D abundances or the ingredients of stellar interior modeling (e.g., opacities), it will be beneficial for both fields and for our understanding of our primary reference star and others alike.

Perhaps the most extreme revisions to stellar abundances due to the inclusion of granulation effects on line formation occur at low metallicities. In static one-dimensional radiative equilibrium models, the collective effect of bound-bound transitions increases the temperature of the deep layers (often referred to as *line-blanketing*) and decreases those of the upper layers compared to the line-free case (e.g., Carbon 1979). The first effect is due to the fact that absorption lines decrease the energy flux at certain wavelengths but, since the total radiative energy flux must be conserved, the continuum level has to increase, which is achieved by increasing the temperature. On the other hand, the lines become optically thin as one approaches the external layers due to the lower densities, and let the radiative energy flow; the temperature must then decrease in these layers so that flux redistribution produces constant energy flux across the outer layers. Thus, in 1D radiative equilibrium models spectral lines produce “surface cooling” and we expect this effect to be less important in metal-poor stars. The situation in 3D hydrodynamic simulations is different owing to the proper treatment of convective energy transport. Ascending gas in the upper layers cools adiabatically due to its expansion and the spectral lines now act primarily as energy absorbers, converting radiative into thermal energy, thus *heating* these photospheric layers. Interestingly, at low metallicities, the balance between the dominating process of adiabatic cooling and its counterpart, surface heating by spectral lines, occurs at lower temperatures compared to 1D radiative equilibrium models (Asplund et al. 1999).

The difference between the 1D and 3D predictions for the mean temperature of the outer layers of metal-poor stars, due mainly to the mechanism described above, are of the order of 1000 K (e.g., Asplund 1999, Asplund & García Pérez 2001, Collet et al. 2006, 2007). This large temperature correction is extremely important for line formation calculations of features that are temperature sensitive, such as high excitation potential transitions and, in particular, molecular bands. For example, Asplund & García Pérez (2001) reported 3D abundance corrections of up to 0.7 dex to the [O/Fe] ratios determined from the UV OH lines in warm ($T_{\rm eff}$ = 6200 K) metal-poor ([Fe/H] = −3) turn-off stars. For cooler and slightly more metal-rich stars, the corrections are smaller but still significant.

The temperature and metallicity dependence of the 3D corrections to the [O/Fe] ratios in metal-poor stars is probably at the root of the oxygen abundance problem mentioned in Sect. 1.2.2, where some studies, in particular those that used UV OH lines to determine the oxygen abundances, suggested increasingly [O/Fe] values with lower metallicities, while others suggested a flat [O/Fe] vs. [Fe/H] trend. The 3D corrections make the slope in the [O/Fe] vs. [Fe/H] trend shallower, thus solving, at least partially, the oxygen abundance problem in metal-poor stars (Asplund & García Pérez 2001, Meléndez et al. 2006).

We note here that we are not suggesting that 3D corrections alone are the solution to all problems in standard stellar abundance work; there are other sources of significant error. For example, in metal-poor stars, the steeper temperature gradient of the line-forming regions in the 3D models compared to 1D predictions can strengthen non-LTE effects (Asplund 2005). Asplund et al. (1999) predicted 3D-LTE corrections to the 1D-LTE lithium abundances, derived from the 670.8 nm Li I line, of the order of 0.2–0.3 dex, but already noticed that a proper treatment of 3D non-LTE effects could reduce the size of the corrections. Indeed, Asplund et al. (2003) showed that, with respect to the lithium abundances, the full 3D-NLTE calculations differ from the 1D-LTE ones by only about 0.05 dex. This balancing of 1D-3D and LTE-NLTE effects obtained for the 670.8 nm Li I line is not expected to be the rule but a particularly remarkable coincidence. For example, the 3D and non-LTE corrections to the oxygen abundances determined from O I lines have the same sign (Asplund et al. 2004, Asplund 2005).

We conclude this section by adding that the impact of granulation on the abundance of elements determined from molecular species can be also very important for the interpretation of data from massive spectroscopic surveys such as GAIA (e.g., Perryman 2005), RAVE (e.g., Steinmetz et al. 2006), APOGEE (Majewski et al. 2007), and SDSS/SEGUE (e.g., Re Fiorentin et al. 2007). There, molecular features (e.g., the CH, NH, OH, CN, etc.) can be used as constraints to search for particular types of stars or derive CNO abundances, for example.

1.3 The importance of studying K-dwarfs

K-dwarfs are by far more numerous than solar-type stars in the Galaxy. Even though the Sun is a very well-studied star that serves at a starting point for studies of late-type stars, understanding the properties of cooler stars requires further investigation. Besides improving our knowledge of K-dwarfs, understanding the physics at these lower temperatures may also serve to grasp the realm of the even cooler, and more numerous, M-type stars in the Galaxy.

The main-sequence lifetime of a star, in years, can be estimated from $t_{\rm ms} = 10^{10}(M/M_\odot)^{-2.5}$ (e.g., Hansen & Kawaler 1994). A typical early K-dwarf star has a mass of about $0.8M_\odot$, which implies a lifetime of about 1.7×10^{10} years, or 17 Gyr. Our current best estimate for the age of the Universe comes from the *Wilkinson Microwave Anisotropy Probe* (WMAP) and it corresponds to 13.73 ± 0.12 Gyr (Hinshaw et al. 2008). No K-dwarf (and, evidently, no other cooler dwarf star) has therefore evolved off the main sequence yet, much less died.

Since the lifetimes of K-dwarfs are larger than the age of the Galaxy, as opposed to F and early G main-sequence stars, samples of K-dwarfs are free from biases in chemical evolution studies due to stellar death. Although M-dwarf and cooler star samples are also free from these biases, the analysis of their spectra is complicated by the abundance of molecules and condensates (dust, clouds), which make the model atmosphere computation difficult (uncertain opacities, molecular equilibrium) and the spectroscopic analysis arduous (ill-defined continuum, atomic lines blended with molecular bands). In addition, they are very faint and therefore difficult to observe at high resolution and S/N (e.g., Woolf & Wallerstein 2005, Bean et al. 2006).

The classical example of the advantage of using samples of long-lived stars is the one related to the so-called G-dwarf problem; in the solar neighborhood, closed box chemical evolution models predict many more metal deficient ([Fe/H] $\simeq -1$) stars than observed (e.g., Pagel & Patchett 1975, Tinsley 1980).

Since some of the early G-dwarfs may have already left the main sequence or even died, the metallicity distribution of G-dwarfs should be corrected to account for the rate of stellar death before comparing it to the theoretical predictions. If a sample of K, instead of G-dwarfs is used to characterize the metallicity distribution of the solar neighborhood, these evolutionary corrections are not needed anymore, and their associated uncertainties are removed from the analysis. Interestingly, K-dwarfs samples also show the same pattern of lack of metal deficient stars, thus leading to an equivalent K-dwarf problem (e.g., Flynn & Morell 1997, Rocha Pinto & Maciel 1998b, Kotoneva et al. 2002, Casuso & Beckman 2004).

Several possible solutions to the G and K-dwarf problems have been proposed (e.g., Rana 1991); in particular, the addition of infalling gas into the models (e.g., Matteucci & François 1989, Chiappini et al. 1997, Colavitti et al. 2008) has been a successful improvement, even though Haywood (2006) has recently suggested that the inclusion of the thick disk population results in an observed metallicity distribution compatible with the closed box model predictions. As noted by Haywood, in the light of other evidence, the chemical evolution of the solar neighborhood is likely to be more complex than that assumed in closed box or infall models.

In the context of the K-dwarf metallicity distribution being used as a fundamental constraint for chemical evolution models, we stress the fact that there is a severe problem in the classical spectroscopic determination of iron abundances (Sect. 1.2.2), which are the proxy for metallicity and are used to calibrate the photometric abundance scales (e.g., Schuster & Nissen 1989) that are the basis of those chemical evolution studies. As we saw in Sect. 1.2.2, the iron ionization problem may be associated with that of the oxygen abundances in K-dwarfs, which could be related to stellar activity or other factors not considered in the modeling of K-dwarf spectra. Thus, perhaps the solution to the K-dwarf problem lies in the stellar abundances and not in the chemical evolution models.

From a more practical point of view, K-dwarf spectra are also useful for radial velocity determinations due to the large number of spectral lines present, which allow us to determine very accurate radial velocities using the cross-correlation method (e.g., Tonry & Davis 1979). Currently, radial velocity uncertainties of a fraction of 1 km s^{-1} are considered reasonable for studies of kinematics and stellar abundances. Even with the highest S/N and highest resolving power spectra, these uncertainties cannot be reduced, in an absolute sense, below a level of a few hundreds of meters per second due to two systematic errors which are independent of the quality of the data and the technique of radial velocity determination. The first of these is the relativistic gravitational redshift, which can be, however, reasonably well estimated from stellar mass (M) and radius (R) determinations:

$$\frac{\Delta\lambda}{\lambda} = \frac{GM}{c^2R} , \tag{1.7}$$

where c is the speed of light and G the gravitational constant (the exact form of the gravitational redshift is slightly different but this approximation is valid for typical values of $M/R << c^2/G$). Using the measured solar mass and radius, we find that the gravitational redshift of the solar spectral lines is 636 m s^{-1}. Due to the Earth's gravitational field, however, the expected observed value from the ground is 633 m s^{-1} instead (e.g., Dravins et al. 1999). The second uncertainty is due to granulation effects; the fact that spectral lines are asymmetric and shifted compared to their laboratory wavelengths (Sect. 1.4). Typically, this will introduce uncertainties of the order of several hundreds of meters per second. If both of these effects are properly taken into account, the uncertainty in the *absolute* radial velocity of the standard stars, some of which are K-dwarfs (e.g., Stefanik et al. 1999), could be reduced to only a few tens of meters per second (Sect. 4.4). Standard stars with very accurate absolute radial velocities can be crucial for massive kinematic (and abundance) surveys such as GAIA. In particular, constant radial velocity objects can replace comparison lamps as wavelength calibrators, provided their absolute radial velocities are accurately known.

1.4 Granulation signatures on stellar spectra and their detection

Spectrum synthesis in classical, hydrostatic model atmospheres predict (almost) perfectly symmetric lines whose central wavelengths correspond exactly to the input laboratory wavelengths given that all sources of line broadening (natural, thermal, collisional, and "turbulent") are symmetric and do not introduce overall Doppler shifts. Note that, even though collisional broadening introduces asymmetries and “pressure shifts,” they are negligible compared to the observed ones (Allende Prieto et al. 1997). A static and homogeneous model atmosphere does not produce asymmetries or net wavelength shifts either given that all spatially resolved profiles are in principle equal. However, the behavior of spectral lines that form in real stellar atmospheres, which are non-static and inhomogeneous, is fundamentally different.

The simplest way to understand the basic signatures of granulation in the solar and stellar spectra is by looking at the correlation between the emergent intensity (or temperature) and vertical velocity fields in a spatially resolved situation (i.e., looking at line profiles coming from different parts of the photosphere). Line profiles coming from bright, hot granules are blueshifted because the material is rising and therefore approaching the observer. On the other hand, line profiles coming from the dark, cool intergranular lanes are redshifted because the gas in these regions is flowing towards the base of the photosphere. The continuum level of the upflow line-profile is higher than that of the line-profile associated with the cool downflow. Thus, if the granulation pattern is unresolved, the observed line profile will be an integrated profile dominated by the blueshifted component. The profile is then asymmetric and its central wavelength is blueshifted.

A toy model for the granulation signatures in a line profile is shown in Fig. 1.5 (cf. Dravins et al. 1981). It is assumed that three quarters (75%) of the photosphere is covered by hot, bright granules with a continuum intensity that is 10 % larger than the average photospheric intensity. The other quarter

(25%) of the photosphere is covered by cool, dark intergranular lanes whose continuum intensities are 0.7 times the average photospheric intensity. An intrinsic line broadening of 2.5 $\mathrm{km\,s^{-1}}$ has been added to the spatially resolved profiles. The upward velocity of the granules is set to 1.2 $\mathrm{km\,s^{-1}}$ and the downward velocity of the intergranular lanes is 3.6 $\mathrm{km\,s^{-1}}$. Integration of the spatially averaged profiles over the stellar disk results in an asymmetric line profile (see solid line in the lower panel of Fig. 1.5); the major contribution to its flux comes from the blueshifted elements and the presence of the redshifted elements produces the asymmetry. Note also that the wavelength of the line center is blueshifted.

An important concept for studies of granulation is that of the **line bisector**, which is shown in Fig. 1.5 with the thick solid line in the lower panel. The line bisector quantifies the asymmetry and is defined as the location of the midpoints of the horizontal segments between the wings of the spectral line. The bisector of a symmetric profile is a vertical line (see dotted lines in the lower panel of Fig. 1.5). Another important definition is that of the net central wavelength shift of the spectral line. As explained above, granulation induces a net blueshift in the observed spatially unresolved line profiles, which is often referred to as the **convective blueshift**.

For illustration purposes, the relative intensities and velocities adopted in the simple model shown in Fig. 1.5 are larger than those representative of solar granulation (Sect. 1.1). Compared to the predictions of static models (the dotted lines in Fig. 1.5), the granulation effects, as shown in Fig. 1.5, are

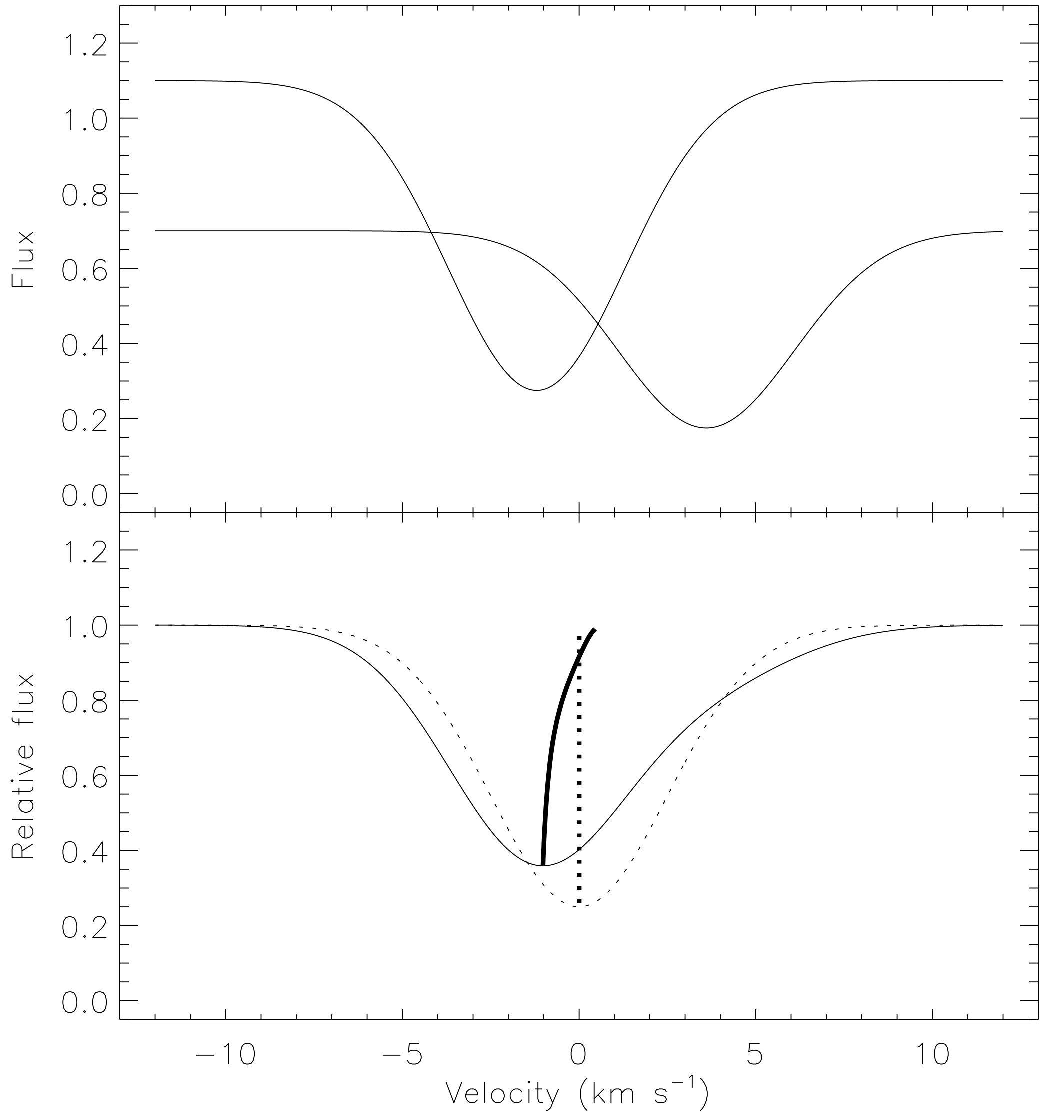

Figure 1.5: Toy model for the line asymmetry and central wavelength shift due to granulation. Top panel: spatially resolved profiles of a bright granule (blueshifted) and a dark intergranular lane (redshifted). The abscissa corresponds to the absolute flux in units of the average continuum intensity. Bottom panel: normalized spatially averaged profile (thin solid line) and its *bisector* (thick solid line). The dotted lines correspond to the line profile and bisector obtained in a static model (adapted from Dravins et al. 1981, their Fig. 1).

of the order of 1 $\mathrm{km\,s^{-1}}$. In the Sun, a more typical number is about 0.5 $\mathrm{km\,s^{-1}}$. Independent of the absolute values, bisectors shaped by granulation have, in general, the characteristic C-shape shown in Fig. 1.5. In fact, the *inverted* C-shape bisectors in hot stars observed by Gray & Nagel (1985) suggest a different origin and have allowed them to draw a granulation boundary on the HR diagram.

Following Dravins (1987a), at least 5 independent points across the spectral line are required to reasonably define a line bisector. Thus, for typical strong lines with a full width of about 10 $\mathrm{km\,s^{-1}}$, we need at least 2 $\mathrm{km\,s^{-1}}$ resolution, or $R = \lambda/\Delta\lambda = 150,000$. Weaker lines, of course, will require a higher resolving power.

In practice, the feasibility of measuring line bisectors also depends on the magnitude of the granulation effects. In K-dwarfs, which are the subject of this thesis, these effects are very small, of the order of tens to a few hundreds of meters per second. Fig. 1.6 shows a numerical experiment of a spectral line bisector calculated using a three-dimensional K-dwarf model atmosphere (Sect. 3.1.1). The synthetic spectral line was convolved with instrumental profiles corresponding to $R = 60,000$; 120,000; and 200,000 spectrographs, while random noise corresponding to $S/N = 100$, 300, and 1000 was also added. Each panel in Fig. 1.6 corresponds to a different combination of R and S/N values.

Fig. 1.6 shows that only at the highest resolving power ($R = 200,000$) and signal-to-noise ratio ($S/N = 1000$) is the line bisector well defined. To

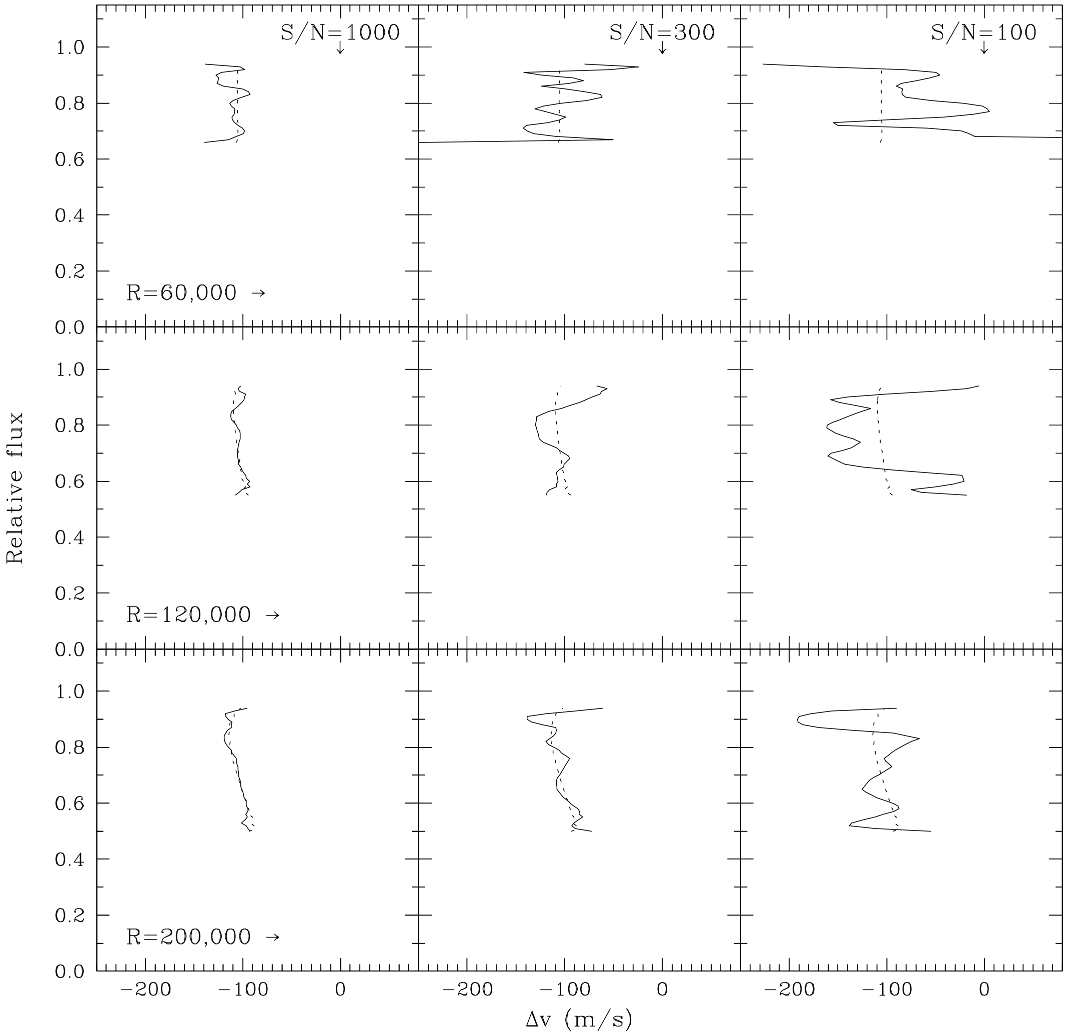

Figure 1.6: Bisector of a spectral line calculated with our 3D K-dwarf model atmosphere. Each panel corresponds to a combination of R (spectral resolution) and S/N (signal-to-noise) ratio for the synthetic line profile. The dotted line in each panel corresponds to the bisector obtained with infinite S/N.

reach this high S/N value, however, the very long exposure times required for typical K-dwarfs (even the brightest nearest ones) make the observations impractical for mid-sized telescopes. At $S/N = 300$, the line bisector is noisy, but the overall C-shape is still detectable. For a lower resolving power, $R = 120,000$, only at the highest S/N ratios are the granulation signatures still convincingly detectable, even though the departure from a straight line is not very significant. Other combinations of R and S/N clearly do not provide a fair measure of the granulation effects.

Note that Fig. 1.6 does not consider the effects of line blends, which are particularly important in K-dwarfs due to the large number of metallic lines in the spectrum. Even the smallest blends that can be visibly recognized will severely distort the shapes of the line bisectors. Thus, the situation presented in Fig. 1.6 corresponds to an ideal case. In real K-dwarf spectra, the detection of the granulation signatures is much more difficult.

One way to overcome the effect of unseen blends and limited signal-to-noise ratios is to group bisectors of lines of the same species and similar strength, given that they form in roughly the same photospheric layers and are, therefore, expected to see similar granulation temperature and velocity fluctuations. In this context, wide spectral coverage observations are ideal in order to select a significant number of clean lines from the spectra. The larger the number of lines, the better the average line bisectors will be since we expect line blends to add roughly random noise to the ensemble of line bisectors.

The 2dcoudé spectrograph on the 2.7 m Telescope at McDonald Observatory is capable of delivering $R \sim 200,000$ spectra (Sect. 2.2). Signal-to-noise ratios of about 300 for nearby K-dwarfs require reasonable exposure times. An important feature of the data that can be obtained at this facility is the wide spectral coverage, which, as explained above, is of great advantage, in particular for the K-dwarf case. Thus, in principle, we posses the technical capabilities to detect the signatures of granulation in K-dwarfs. In Chapter 2, we describe the details of the observations that we made with this goal in mind. In Chapter 3, these observations are compared to the predictions of a 3D model atmosphere. Then, in Chapter 4, we use the 3D model to quantify the effects of granulation on the determination of K-dwarf abundances and fundamental parameters.

Chapter 2

Observations

Theoretical models predict that the granulation effects on spectral line shapes and central wavelengths in K-dwarfs are on the order of tens to a few hundreds of meters per second (Sect. 3.1). High resolution spectra ($R \gtrsim 200,000$) with very high signal-to-noise ratios ($S/N > 300$) are thus required to reliably detect them (Sect. 1.4). Previous observational studies of granulation in K-dwarfs (e.g., Dravins 1987b, Gray 1982, 2005) have used very high quality data but with an otherwise limited spectral coverage, sometimes involving the analysis of only one spectral feature. Although the quality of our observations is similar or just slightly superior to that of these pioneering studies, our wavelength coverage surpasses, by far, all of them. As it was argued in Sect. 1.4 and will be shown in Sect. 3.2, a wide spectral coverage has important advantages. In this chapter, the target selection, acquisition, and processing of the observations are described.

2.1 Target selection

In principle, the goal is to observe one early K-type dwarf star of near solar metallicity to compare its spectrum with the predictions of a 3D model atmosphere, computed using parameters corresponding to such a star (Sect. 3.1.1). In practice, however, it is better to observe a small sample of stars with parameters close to that of the 3D model in order to take into account possible systematic errors in the stellar parameters and explore the effects of different rotational velocities and possibly activity levels on the shapes of spectral lines.

A typical early K-dwarf has an absolute visual magnitude of $M_V \sim 6.5$. Considering the high spectral resolution under consideration (see next section), the aperture of the telescope and the efficiency of the spectrograph–detector system used in this work limit our observations to stars brighter than $V \sim 6.5$. To reach a $S/N \sim 300$ for a $V \sim 6.5$ star, about 3 hours of observation are required. A star with $V \sim 7.0$ would require more than 7 hours of observation to reach the same S/N (in fact, we observed one star with $V = 7.2$ but could only reach $S/N \sim 100$). Therefore, we selected only stars brighter than $V \sim 6.5$, which implies distances closer than or at about 10 pc.

The Spectroscopic Survey of Stars in the Solar Neighborhood ($\mathrm{S^4N}$, Allende Prieto et al. 2004) includes all early K-dwarfs (K2 and earlier) within 15 pc. We used this catalog to select our targets by constraining their published effective temperatures to the range $4600\,\mathrm{K} < T_{\mathrm{eff}} < 5200\,\mathrm{K}$ and metallicities to $-0.25 < [\mathrm{Fe/H}] < +0.25$, in addition to their observability from McDonald Observatory. Nine K-type dwarf stars were selected in this way and are listed in Table 2.1.

In addition to the K-dwarfs, we also obtained spectra of Procyon and

HIP	V	d	SpT	M_V	$T_{\rm eff}$	[Fe/H]	Notes
	mag	pc		mag	K	dex	
37279	0.3	3.50	F5	2.7	6677	+0.08	Procyon
···	···	···	G2	4.8	5777	+0.00	Sun (skylight)
96100	4.7	5.77	K0	5.9	5218	−0.22	
26779	6.2	12.24	K1	5.8	5150	+0.11	
16537	3.7	3.22	K2	6.2	5052	−0.08	ϵ Eri
88601	4.0	5.09	K0	5.5	5050	−0.04	
64797	6.5	11.23	K2	6.0	4915	−0.15	
37349	7.2	14.20	K2	6.4	4889	+0.00	
86400	6.5	10.71	K3	6.4	4833	−0.05	Ref.
114622	5.6	6.53	K3	6.5	4743	+0.09	
23311	6.2	8.81	K3	6.5	4641	+0.26	

Table 2.1: Sample observed in this work. Basic data (V, SpT) was obtained from SIMBAD. Distances and absolute magnitudes are based on *Hipparcos* parallaxes. The atmospheric parameters $T_{\rm eff}$ and [Fe/H] are those determined by Allende Prieto et al. (2004). HIP 86400 is our reference star for the model comparison, given that it has parameters virtually identical to those of the 3D model (Sect. 3.1.1).

the day skylight, the latter as a proxy for the solar spectrum, to check the accuracy of our data reduction procedures, given that these stars have very high quality spectra available from previous studies (e.g., Griffin & Griffin 1996, Kurucz et al. 1984). Note, however, that the skylight spectrum obtained in this manner may be slightly different than the real solar spectrum given that the sky fills the spectrograph slit completely, therefore making the data reduction different from that of a point source, and it is known that aerosol and Rayleigh-Brillouin scattering affects slightly the observed line strengths (Gray et al. 2000).

2.2 Observations and data reduction

Spectra for our sample stars were obtained with the 2dcoudé spectrograph (Tull et al. 1995) on the 2.7 m Harlan J. Smith Telescope at McDonald Observatory using the cs21 mode (grating e2, focus f1), which delivers a spectral resolution of $R \sim 180,000$ (but see Sect. 2.5). The detector (TK3), placed at the focal station f1, is a 2048×2048 Tektronix CCD ($24\,\mu$m pixels) with a very low read-out noise and almost no dark current. The e2 grating is a 52.67 grooves mm^{-1} R2 echelle from Milton Roy Co. and the slit dimensions are $L(\text{length}) = 3.47\,\text{mm}$, $W(\text{width}) = 145\,\mu\text{m}$. The field scale is 2.35 arcsec mm^{-1} and therefore the width of the slit corresponds to 0.34 arcsec.

In the cs21 mode, a single exposure results in an echelle spectrum of about 20 orders (apertures), each of them covering approximately 20 Å. By tilting the spectrograph grating to 7 different positions (setups), full coverage from 5580 to 7900 Å was achieved (see Fig. 2.1 and Table 2.2 for details). K-dwarf absorption line spectra are very crowded in the blue spectral range due to the large ratio of line to continuum opacities. To avoid the uncertainties associated with strong line blending, no observations of this wavelength region were made.

A typical single exposure of 20 minutes for a $V \sim 6$ star resulted in a $S/N \sim 100$ under good observing conditions. The exposures were limited to 20 minutes to avoid significant cosmic ray contamination and blurring of the spectral line profiles due to the Earth's orbital motion. The impact of the latter depends on the location of the star in the sky and the epoch of

	Instrumental Setup						
Aperture	P1	P2	P3	P4	P5	P6	P7
1	5487 – 5508	5506 – 5527	5524 – 5545	5542 – 5564	5561 – 5582	5579 – 5600	5598 – 5619
2	5577 – 5599	5596 – 5617	5615 – 5636	5633 – 5655	5652 – 5673	5671 – 5692	5689 – 5711
3	5670 – 5692	5689 – 5711	5708 – 5730	5727 – 5749	5746 – 5768	5765 – 5787	5784 – 5806
4	5766 – 5788	5786 – 5808	5805 – 5827	5824 – 5846	5844 – 5866	5863 – 5885	5882 – 5904
5	5865 – 5888	5885 – 5908	5905 – 5928	5925 – 5947	5944 – 5967	5964 – 5987	5984 – 6006
6	5968 – 5991	5989 – 6011	6009 – 6032	6029 – 6052	6049 – 6072	6069 – 6092	6089 – 6112
7	6075 – 6098	6096 – 6119	6116 – 6139	6136 – 6160	6157 – 6180	6177 – 6200	6197 – 6221
8	6185 – 6209	6206 – 6230	6227 – 6251	6248 – 6272	6269 – 6292	6289 – 6313	6310 – 6334
9	6300 – 6324	6321 – 6345	6342 – 6367	6364 – 6388	6385 – 6409	6406 – 6430	6427 – 6451
10	6419 – 6444	6441 – 6465	6462 – 6487	6484 – 6508	6505 – 6530	6527 – 6551	6548 – 6573
11	6542 – 6568	6564 – 6590	6586 – 6611	6608 – 6633	6630 – 6655	6652 – 6677	6674 – 6699
12	6671 – 6696	6693 – 6719	6715 – 6741	6738 – 6763	6760 – 6786	6783 – 6808	6805 – 6831
13	6804 – 6830	6827 – 6853	6850 – 6876	6873 – 6899	6895 – 6922	6918 – 6944	6941 – 6967
14	6943 – 6970	6966 – 6993	6990 – 7016	7013 – 7040	7036 – 7063	7059 – 7086	7083 – 7109
15	7088 – 7114	7111 – 7139	7135 – 7162	7159 – 7186	7183 – 7210	7207 – 7234	7230 – 7258
16	7238 – 7266	7263 – 7290	7287 – 7315	7311 – 7339	7336 – 7363	7360 – 7388	7384 – 7412
17	7396 – 7424	7421 – 7449	7445 – 7474	7470 – 7499	7495 – 7523	7520 – 7548	7545 – 7573
18	7560 – 7589	7586 – 7615	7611 – 7640	7636 – 7665	7662 – 7691	7687 – 7716	7712 – 7741
19	7732 – 7762	7758 – 7788	7784 – 7814	7810 – 7840	7836 – 7865	7862 – 7891	7888 – 7917
20	7912 – 7942	7938 – 7968	7965 – 7995	7991 – 8022	8018 – 8048	8045 – 8075	8071 – 8101

Table 2.2: Approximate wavelength coverage of each aperture for each of the instrumental setups used for our observations.

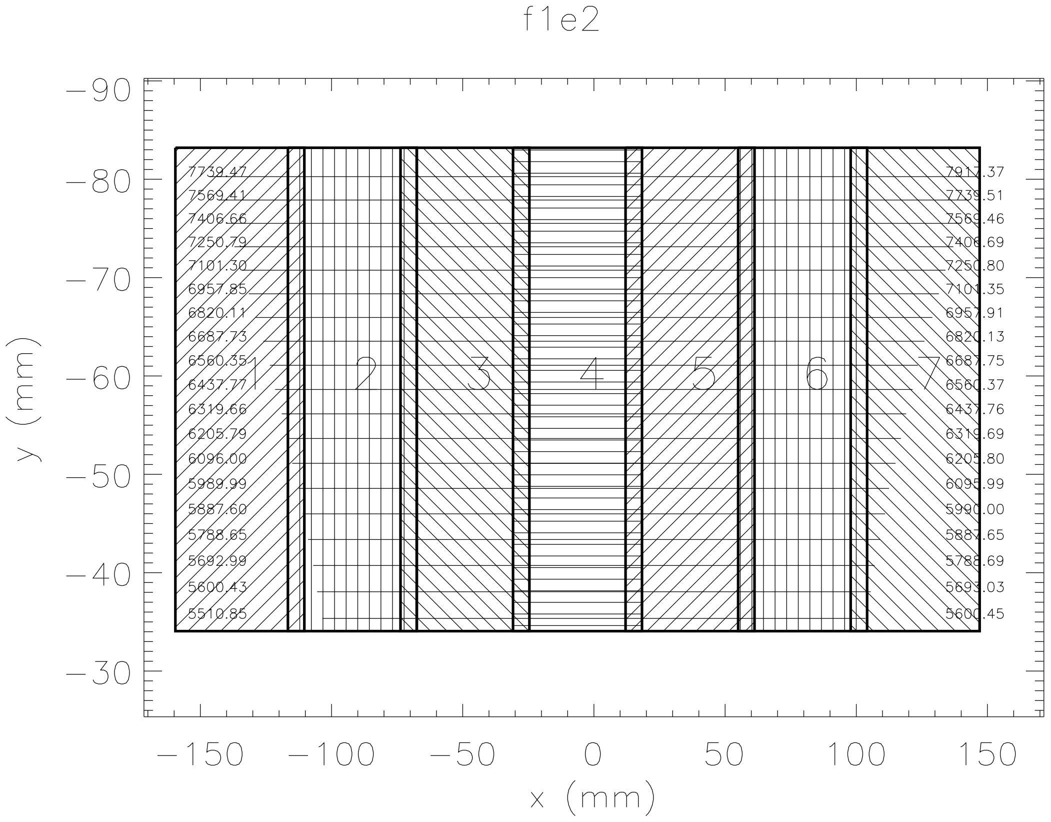

Figure 2.1: Schematic view of the configurations used at the 2dcoudé spectrograph (cs21 mode) to achieve complete spectral coverage from 5580 to 7800 Å. The long horizontal lines represent the actual spectral orders (minimum and maximum wavelengths are shown on each side). Each of the numbered areas marked with short horizontal, vertical, and diagonal lines has the dimensions of the TK3 detector and therefore correspond to one instrumental setup. Note that contiguous settings have an overlap of about 2 Å. This figure was generated with the IDL codes by C. Allende Prieto (`http://hebe.as.utexas.edu/2dcoude/`).

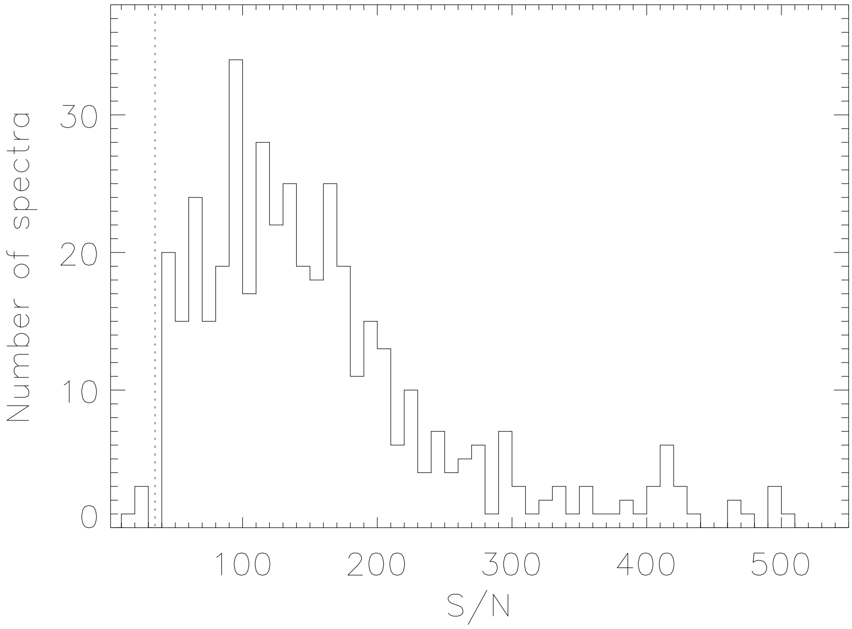

Figure 2.2: Distribution of S/N per pixel for our cs21 observations. The dotted line marks the minimum S/N of the spectra used in this work.

observation but its maximum value is of the order of a few tens of meters per second for one hour exposures. Fig. 2.2 shows the distribution of S/N values for our observations. They were obtained from the mean number of counts N in the continuum of each order, assuming that the noise is dominated by Poisson statistics, i.e. $S/N \simeq \sqrt{N}$. Only four spectra with $S/N < 35$ were discarded due to their negligible flux contribution. To reach our required signal-to-noise ratio ($S/N \gtrsim 300$), several single exposures of the same setup were co-added before merging them into a single spectrum. The following two sections explain the details of the co-adding and merging procedures. The log of observations is provided in Table 2.3.

Table 2.3: Log of observations. For each object and observing run, the number of exposures (y) per instrumental setup (x) are given as Px - y.

Object	Observing run				
	25–28 Feb 06	19–24 Apr 06	03–08 Aug 06	23–27 Nov 06	08–14 May 07
Procyon				P1 - 2	
				P2 - 3	
				P3 - 2	
				P4 - 1	
	P5 - 2			P5 - 1	
	P6 - 1			P6 - 2	
				P7 - 3	
Skylight		P1 - 2			
		P2 - 2			
		P3 - 2			
		P4 - 2			
		P5 - 2			
		P6 - 2			
		P7 - 3			
HIP 96100				P1 - 3	
				P2 - 2	
				P3 - 3	
					P4 - 5
				P5 - 3	
				P6 - 3	
				P7 - 12	
HIP 26779					P1 - 14
				P2 - 4	
					P3 - 6
				P4 - 5	
				P5 - 6	
				P6 - 5	
				P7 - 14	

Table 2.3 – continued from previous page

Object	Observing run				
	25–28 Feb 06	19–24 Apr 06	03–08 Aug 06	23–27 Nov 06	08–14 May 07
ϵ Eri				P1 - 3	
	P2 - 2				
	P3 - 2				
	P4 - 7				
	P5 - 3			P5 - 1	
	P6 - 4				
	P7 - 6			P7 - 2	
HIP 88601		P1 - 2	P1 - 2		
			P2 - 5		
	P3 - 2				
	P4 - 4				
	P5 - 4		P5 - 2		
	P6 - 4				P6 - 2
					P7 - 4
HIP 64797		P1 - 8			
	P2 - 7	P2 - 11			
	P3 - 8	P4 - 2			
	P4 - 21	P4 - 1			
	P5 - 9	P5 - 4			
	P6 - 14	P6 - 1		P6 - 1	
	P7 - 16	P7 - 4			
HIP 37349		P1 - 4			
		P2 - 7			
	P3 - 4				
	P4 - 4				
	P5 - 5	P5 - 2			
	P6 - 4				
	P7 - 6	P7 - 1			

Table 2.3 – continued from previous page

Object	Observing run				
	25–28	19–24	03–08	23–27	08–14
	Feb 06	Apr 06	Aug 06	Nov 06	May 07
HIP 86400		P1 - 4	P1 - 4		
			P2 - 6		
		P3 - 7			
		P4 - 8			P4 - 2
			P5 - 3		P5 - 10
			P6 - 4	P6 - 1	P6 - 7
					P7 - 16
HIP 114622				P1 - 5	
			P2 - 4		
				P3 - 2	
			P4 - 3		
			P5 - 4	P5 - 1	
			P6 - 3		
			P7 - 4	P7 - 4	
HIP 23311				P1 - 9	
				P3 - 4	
				P4 - 4	
				P5 - 5	
				P6 - 4	
				P7 - 10	

Data reduction was performed using the standard IRAF[1] `echelle` package. Bad pixels were first removed and the overscan correction was then performed. Very high S/N flat fields were applied to the object spectra to correct for pixel-to-pixel sensitivity differences. Scattered light was removed using high order polynomial fits to the counts between spectral orders. Compari-

---

[1] IRAF is distributed by the National Optical Astronomy Observatories, which are operated by the Association of Universities for Research in Astronomy, Inc., under cooperative agreement with the National Science Foundation – `http://iraf.noao.edu`

son lamp (ThAr) spectra were obtained approximately every hour to ensure a very accurate wavelength calibration. Two ThAr spectra, one taken before and the other one after two exposures of a given target, were used to determine the wavelength solution of each object spectrum. The solution was found by two-dimensional fitting of the ThAr line positions, using high order ($\sim 5-6$) polynomials, with an RMS scatter of 5×10^{-4} Å. Instead of linearizing the wavelength solutions (by resampling each order to a wavelength scale of constant step), the actual pixel-to-wavelength relations were preserved to minimize interpolation errors in the observed counts. Fig. 2.3 shows an example of a reduced spectrum. The first and last apertures are often only partially within the detector and are thus excluded from further study.

In addition to the 2dcoudé data, we obtained spectra of our sample stars using the High Resolution Spectrograph (HRS; Tull 1998, Hill et al. 2006) on the 9.2 m Hobby-Eberly Telescope (HET) for wavelength calibration purposes (details are given in Sect. 2.4). This instrument is capable of delivering $R \sim 120,000$ spectra with complete wavelength coverage from 6000 to 7900 Å (red chip) and from 4100 to 5900 Å (blue chip) in one single exposure. The data reduction was similar to that applied to the 2dcoudé data. For these spectra, the accuracy of the polynomial fits to the ThAr line positions for the wavelength calibration was about 10^{-3} Å for the red chip and 5×10^{-4} Å for the blue chip. Exposure times were set to reach $S/N \sim 750$ at the center of the red chip and were split into several single exposures to avoid saturation. The procedures described in the next section were also applied to these data.

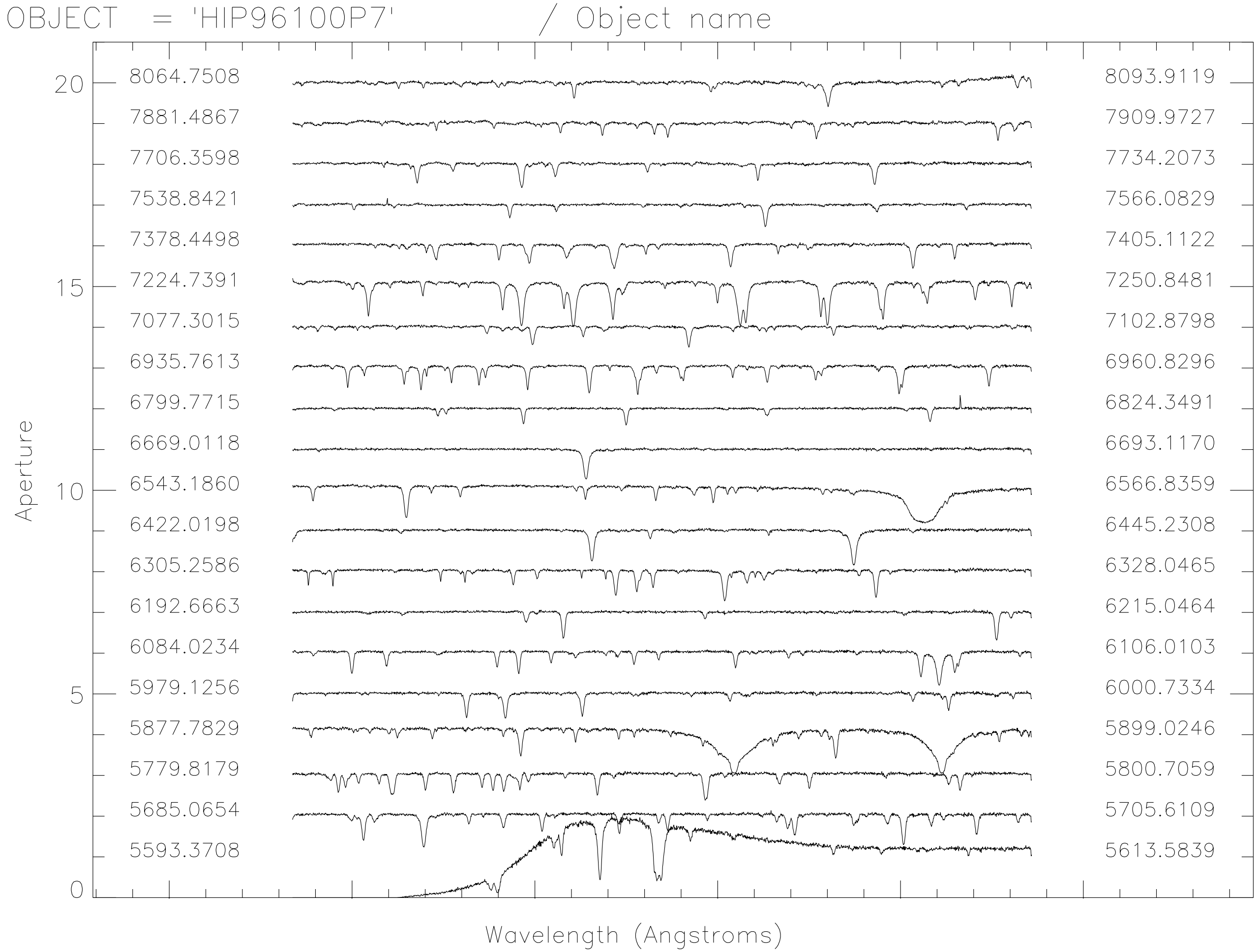

Figure 2.3: Sample spectrum from our 2dcoudé–cs21 observations.

2.3 Shifting and co-adding: increasing the S/N ratios

As explained above, several individual exposures of each setup were required to reach high signal-to-noise ratios. Co-adding them is not trivial because even after correcting for the Earth's motion, wavelength shifts due to the intrinsic radial velocity of the star (e.g., due to binarity, variability, and presence of planets) or instrumental and environmental effects (the 2dcoudé spectrograph is not inside a vacuum chamber) are present between exposures. These shifts are on the order of tens to hundreds of meters per second and, therefore, of the same magnitude as the effects we are trying to resolve. Consequently, these shifts must be taken into account before co-adding in order to keep the spectra useful for granulation studies.

We determined radial velocity shifts between pairs of spectra of the same object by cross-correlation in the Fourier space, after rebinning the original spectra to have a constant step in $\log \lambda$. Orders severely affected by telluric lines (more than 50% of the λ range) were removed from this calculation (see Table 2.4).

The peak of the cross-correlation function (CCF) was defined by the 21 points nearest to the peak and the maximum was found by fitting the CCF peak to a Gaussian profile. We tested several other cases, for example cross-correlation in pixel space, parabolic and cubic fits to the peak of the CCF, as well as different number of points defining the CCF peak. However, we found the Fourier-Gaussian combination with 21 peak points to be the most reliable and efficient one. For example, parabolic and cubic fits are only robust when

Interval (Å)	Prominent telluric features
6275 – 6330	O_2, H_2O
6470 – 6575	H_2O
6868 – 7406	O_2, H_2O
7594 – 7710	O_2
7860 – 8030	H_2O
8090 – 8200	H_2O

Table 2.4: Wavelength intervals severely affected by telluric lines in our 2dcoudé-cs21 spectral range. Any spectral order containing more than 50% of any part of these intervals was discarded for the relative radial velocity determinations.

few points (~ 5) are used, thus making the peak determination less accurate than the Gaussian case, where a broad range of larger numbers of CCF peak points ($\sim 10-30$) can be used. Also, the cross-correlation computation is faster in the Fourier space, where essentially $n_p \log n_p$ basic operations are required (n_p is the number of pixels), than in pixel space, which requires n_p^2 basic operations instead.

It is important to mention that our cross-correlation calculations were not made using the widely popular IRAF `fxcor` task but the IDL `xc` code of Allende Prieto (2007). As mentioned in Sect. 2.2, we preserved the pixel to wavelength relations in our spectra instead of resampling them to a wavelength solution of constant step ("linearization"). Because of the way it is written, IRAF's task `fxcor` requires the input spectra to be linearized. In any cross-correlation involving a radial velocity determination, the spectra have to be interpolated to a common $\log \lambda$ (or velocity) scale. Therefore, two sets of interpolations are being performed when using the `fxcor` task (linearization and $\log \lambda$). Our algorithm, based on `xc`, avoids one interpolation, because it uses the original, not linearized, spectra. This is likely to be the main reason why `xc` is superior to `fxcor`; tests on three pairs of spectra showed that `xc` provided results that were about 30% more consistent than those given by `fxcor`. The consistency level was assessed using the radial velocities determined from several different spectral orders for a given pair of spectra.

Determining the uncertainty of the cross-correlation (XC) procedure described above is a difficult task. Monte Carlo simulations using both synthetic spectra and an observed high S/N spectrum predicted errors of only about 4 m s^{-1} for $R = 200,000$ and $S/N = 100$. The procedure involved creating a large number of simulated spectra from the original one by adding random noise, and performing many XC operations to determine the radial velocity shifts between them, which in principle should be zero (if they are not artificially shifted). The standard deviation from the mean value was adopted as the predicted uncertainty. In practice, however, this is a very optimistic error, given that it does not take into account other effects such as pixel shifts that are non-linear in velocity and order-to-order scatter due to instrumental distortions, the fact that spectral lines are not symmetric or at their rest wavelengths due to granulation effects, incompleteness or uncertainties in the atomic data used for the calculation of the synthetic spectra, telluric lines, etc. Thus, we estimated the error from the order-to-order scatter only. Using this method, we find that our relative radial velocities have a mean error of about 14 m s^{-1} (Fig. 2.4).

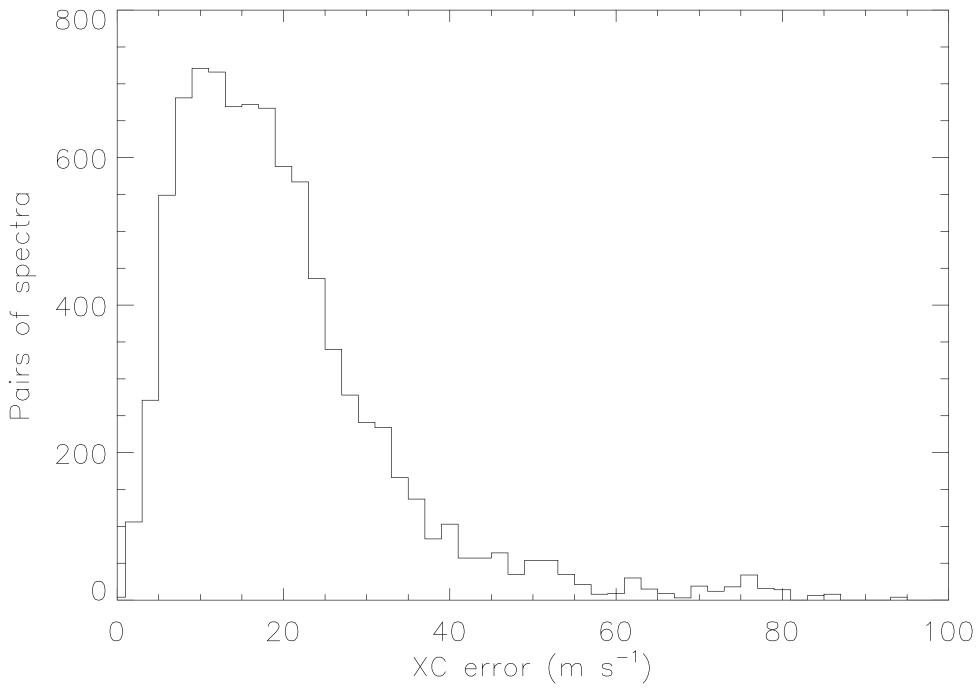

Figure 2.4: Distribution of the order-to-order scatter of the radial velocities determined using the XC method applied to pairs of 2dcoudé-cs21 spectra. An imaginary line at approximately 14 m s^{-1} divides the histogram into two equal areas and is adopted as our mean error for the relative radial velocity determination. As a comparison, the mean value is 20.5 m s^{-1} and the median 18.0 m s^{-1}

The standard approach to the determination of radial velocity shifts between spectra is to cross-correlate them with a reference spectrum of known radial velocity. In our case, we do not have access to a reference spectrum of higher quality than the data (e.g., high resolution synthetic spectra including line asymmetries over the whole spectral range of our observations). In this work, the number of spectra co-added for a single faint object in a given setup was typically between 5 and 10. Instead of cross-correlating each of them with a single reference spectrum, we cross-correlated all of them with each other. We then used all the measurements to refine the shifts of all spectra with respect to the first one of the list using the "self-improvement" prescription by Allende Prieto (2007). In this method, the relative velocity of a given pair of spectra is obtained not only from their cross-correlation but also using information from the cross-correlation of them with other spectra, if available. For example, if v_{12} is the relative velocity of the 1-2 pair, the self-improved value of v_{12}, if there is a third spectrum from which v_{13} and v_{23} can be measured, is

$$v'_{12} = \frac{2v_{12} + v_{13} - v_{23}}{3} \; . \tag{2.1}$$

This expression, of course, can be generalized to the case where any number of spectra are available.

Using this procedure, the mean error in the relative radial velocities was reduced by about 15%, a value determined via Monte Carlo simulations. One spectrum of very high S/N was used to generate 5 other spectra of different S/N values by adding random noise (a second case was calculated generating 10 spectra). We then applied the XC procedure to these 10 spectra and found their relative radial velocities. The standard deviation of these values was adopted as the mean XC error. We then applied the self-improvement technique to the simulated data and re-determined the standard deviation of the relative radial velocities. We call the ratio of the pre to post self-improvement standard deviations the "improvement factor." One hundred tests were performed for each run of noise level. Fig. 2.5 shows the result of this exercise.

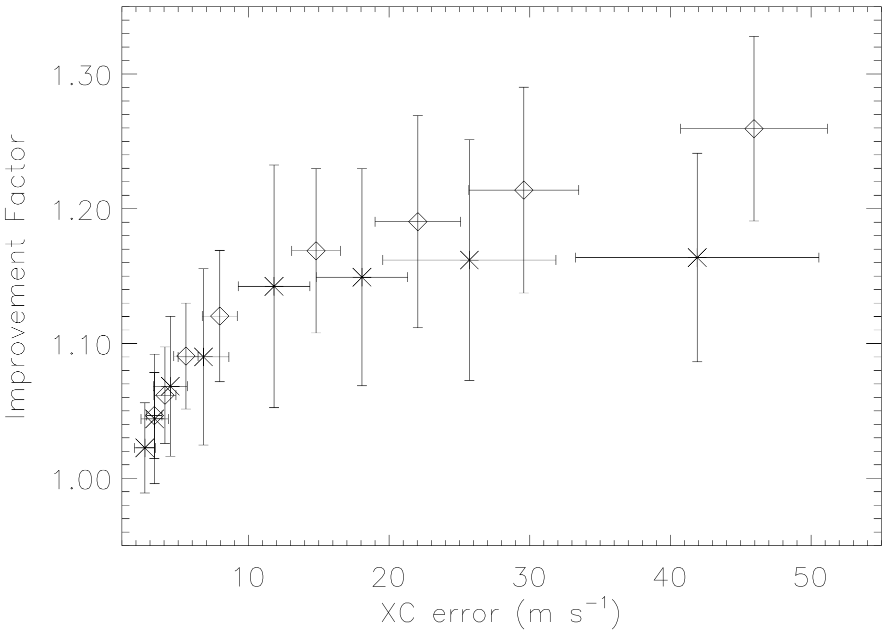

Figure 2.5: The improvement factor of the self-improvement technique is shown here as a function of XC error. The error bars correspond to the 1σ extent of the 100 Monte Carlo tests (see text for details). Crosses correspond to the case with 5 spectra and diamonds to the case of 10 spectra entering this simulated self-improvement calculations.

As expected, the improvement ratio is larger when the XC error is larger, i.e., when the S/N is low, and when the number of spectra involved in the calculation is larger. Note also that not much improvement is made by adding more spectra if the data is already of high quality. The average improvement factor for our observations, 1.15, was obtained by interpolation in this figure, using the mean XC error value of 14 m s^{-1} determined above.

Thus, on average, the self-improvement technique reduced the uncertainty in our relative radial velocity values only marginally, from 14 m s^{-1}

to approximately 12 m s^{-1}. As explained by Allende Prieto (2007), this improvement does not correspond to a $\sqrt{n}$ factor (n being the number of spectra involved in the calculation), given that the errors in the relative velocities are not uncorrelated. For example, there is a contribution from the noise of spectrum number 1 to the the uncertainties of both v_{12} and v_{13} in Eq. 2.1.

After correcting for the radial velocity shifts, the spectra were coadded using an algorithm that minimizes interpolation errors in the observed fluxes. When coadding, each original pixel has to be interpolated to some common wavelength scale. One may be tempted to use the wavelength solution of one of the spectra and interpolate the rest to that dispersion at the risk of introducing large interpolation errors. Instead, we determined, for each set of spectra to be coadded, a wavelength solution such that the flux interpolation distances are minimized.

The pixel-to-wavelength relation of the first spectrum was used as a starting reference. The mean difference between adjacent pixels, $\delta\lambda$, was then determined. For each pixel in the reference spectrum, we defined a box extending to $\pm\delta\lambda/2$ around its wavelength. Next, we looked at the rest of the spectra and found all pixels with wavelengths within that box. The average wavelength of all those pixels was then adopted for that particular position. The procedure is illustrated in Fig. 2.6. In this way, the mean interpolation distance was reduced by a factor of 2, compared to the case in which the spectra are interpolated to the dispersion of the first (or any other reference) spectrum. The interpolation distance for the linear case (i.e., rebinning the spectra to a common constant step dispersion) is substantially larger (a typical factor of 5 to 10) but, as explained above, we avoided this type of interpolation.

Following the rebinning procedure described above, the exposures were coadded using simple sums of counts. Cosmic rays were already efficiently removed in the standard echelle spectra reduction procedure (Sect. 2.2) and so no extra filters were applied in this step. The average percentage of pixels lost due to the slightly different wavelength coverage of the exposures was about 1%. In only a few cases, in particular when exposures of the same setup for the same star were obtained in different observing runs (therefore making it difficult to reproduce exactly the same instrumental setting), this number increased to about 5–10%.

2.4 Normalization and "merging"

As explained in Sect. 2.1, all of our sample stars are included in the S^4N survey of Allende Prieto et al. (2004). This study provides atlases of spectra covering the wavelength range from 362 to 921 nm, obtained mainly with the 2dcoudé spectrograph operating in the cs23 mode, which delivers a spectral resolution $R \simeq 60,000$. The continuum normalization of these data is superb; not only were the blaze shapes removed by fitting high order polynomials to the upper envelopes of the observed fluxes in each order, but also the smooth variation of the blaze shapes in the direction perpendicular to the dispersion was taken into account, thus removing the instrumental response with a very careful two-dimensional modeling, as described in Barklem et al. (2002). This

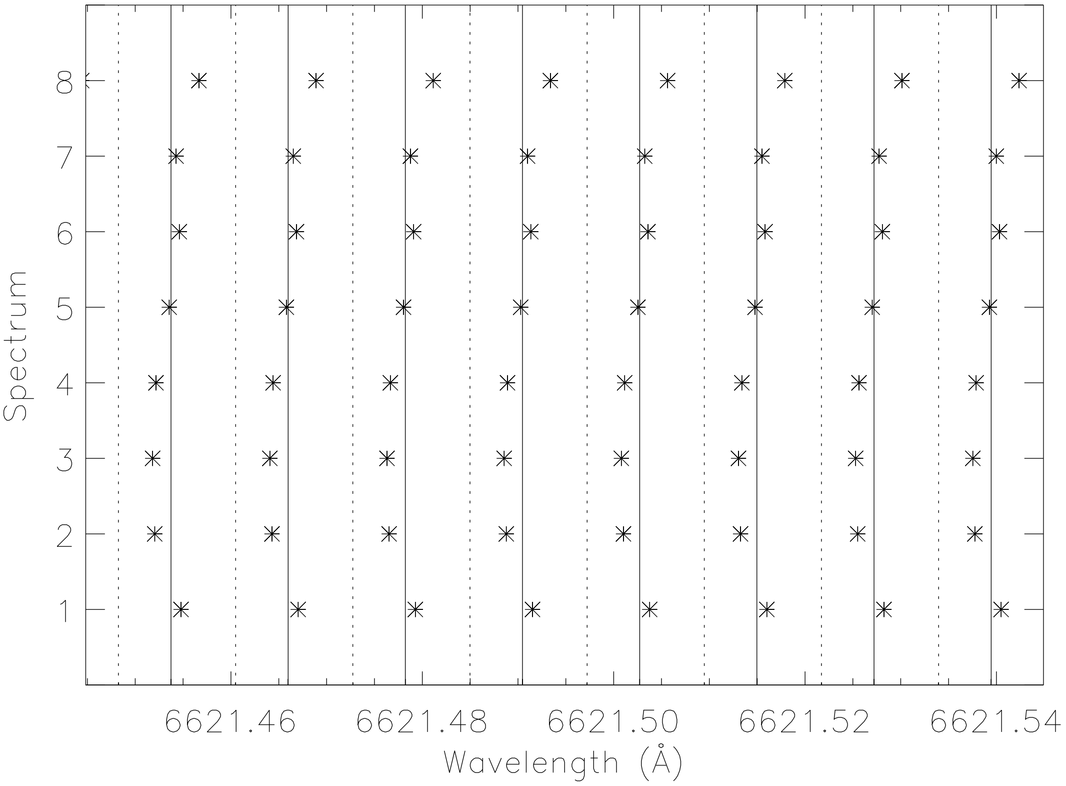

Figure 2.6: Rebinning of the individual exposures before coadding. Each asterisk corresponds to the wavelength of a pixel in each of the eight spectra shown here (a very small section has been selected for clarity). The dotted lines enclose intervals of length $\delta\lambda$ centered on the wavelengths of spectrum 1 (see text). The solid lines are the averages of all the asterisks in each $\delta\lambda$ box. Before coadding, all spectra are rebinned to the wavelengths marked here with the solid lines, thus minimizing the total interpolation distance for the flux calculations.

normalization was essentially “passed on” to our already coadded spectra using the procedure described below.

Each order of our coadded cs21 spectra (one instrumental setup only) was divided by its corresponding cs23 piece from the S^4N data set, after lowering the resolution of the cs21 data to match that of the cs23 data, correcting for radial velocity shifts, and rebinning to a common wavelength scale. In principle, the result should be a smooth line corresponding to the shape of the continuum (the upper “envelope”) of the cs21 observations. However, due to the finite S/N values and temporal variations of the strengths of some lines (in particular the telluric ones), this envelope had to be smoothed out using a median filter of width equal to 100 pixels (about 2 Å). The cs21 data were then divided by this envelope in each order, for each instrumental setup. An example of the application of this procedure is given in Fig. 2.7.

The coadded and normalized cs21 data (7 setups for each object) were finally merged using an HET spectrum of the same object as a radial velocity template. Note that the spectra for each setup can have a different radial velocity, since we only removed relative, and not absolute, Doppler shifts (Sect. 2.3). Cross-correlation with synthetic spectra or a radial velocity standard do not take into account the effects of line asymmetries and wavelength shifts due to granulation with the precision that we require. Synthetic spectra are computed using static models (no high resolution synthetic spectrum covering the spectral range of our observations and computed with 3D simulations has been published yet) while the magnitude of the granulation effects are dependent

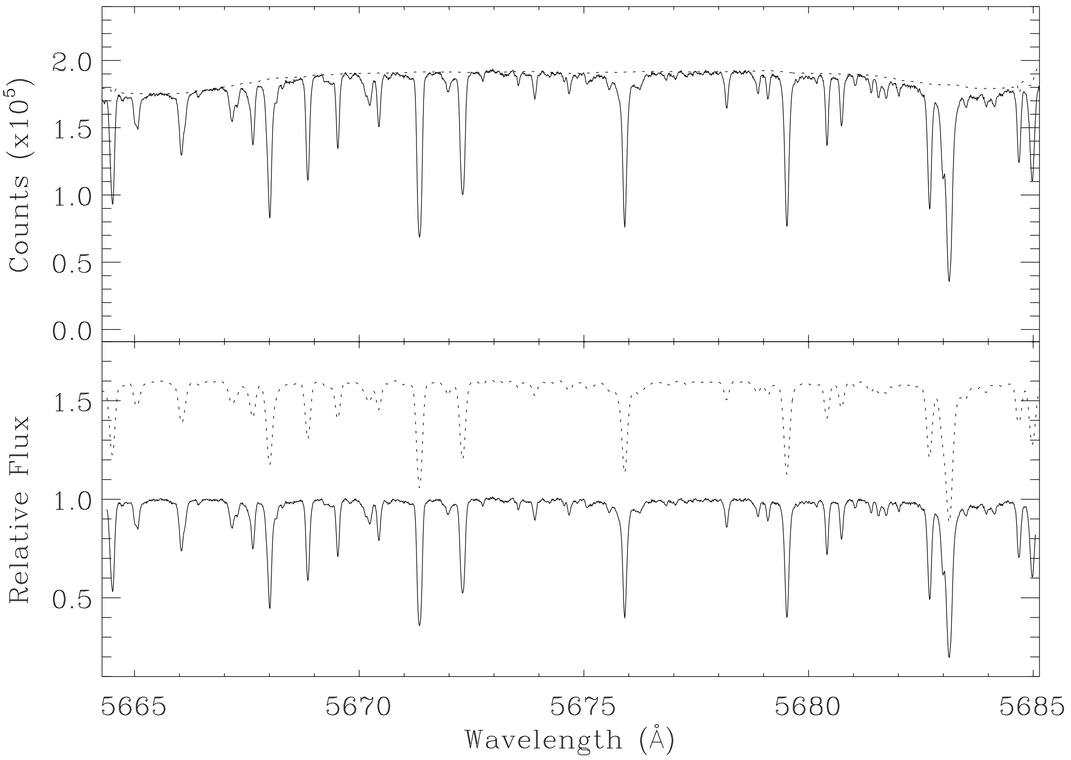

Figure 2.7: Lower panel: normalized cs21 spectrum (solid lines) and S^{4}N spectrum (dotted lines). Top panel: total number of counts (after co-adding) in a spectral order of a given instrumental setup. The dotted line corresponds to the smoothed ratio of these data (lowered in resolution to approximately 60,000) and its corresponding piece in the S^{4}N spectrum (the dotted line in the lower panel). As it is clearly seen, this ratio resembles very well the shape of the continuum in our observations.

on stellar parameters and, most likely, the radial velocity standard will have parameters different from those of the target star (finding “twin” stars is a difficult task, especially when limited by distance, as evidenced by the search for solar twins; e.g., Meléndez & Ramírez 2007). Therefore, we adopted the ideal case of using the same star as the radial velocity standard.

Each order of a cs21 setup was cross-correlated with its corresponding piece in the HET-HRS spectrum, after lowering the resolution of the former to match the $R \sim 120,000$ of the HRS, to determine the radial velocity needed to align the cs21 spectrum with the HET-HRS spectrum wavelength solution. The robust (iterated and weighted) average shift of all orders for each setup was adopted to correct the cs21 data, thus removing inaccurate shifts from orders affected by telluric lines and/or instrumental defects. In the regions of overlap, a weighted mean for the fluxes was calculated after adopting a common robust rebinning (see previous section). Fig. 2.8 illustrates this step of the data processing.

On average, the order-to-order scatter of the radial velocities used for the merging of setups was 70 m s^{-1}. This error is significantly larger than the 12 m s^{-1} error quoted in Sect. 2.3 for the order-to-order scatter of the cs21 data alone, in part due to the lower resolving power of HRS, but also probably because of distortions in the wavelength-to-pixel mapping of HRS. Note that the regions of overlap of the different cs21 setups are small compared to the wavelength coverage of each order. Only within the regions of overlap, spectral line shapes are affected by this large merging error of 70 m s^{-1}. The majority

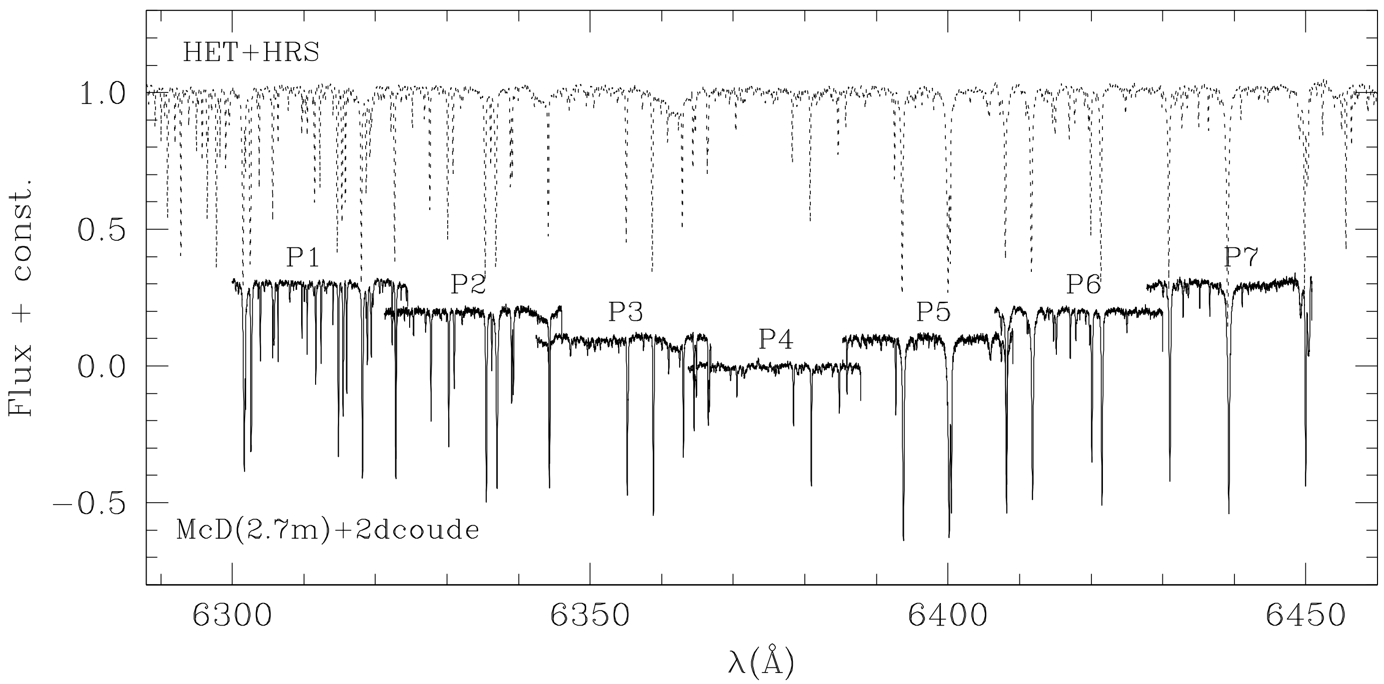

Figure 2.8: Merging of spectra from different instrumental setups (P1-7). Only one order per setup is shown here; note that each setup has about 20 orders in different wavelength regions (Table 2.2). The fluxes have been shifted arbitrarily in the vertical direction for clarity. The cs21 pieces (P1-7) have been aligned with the HET+HRS spectrum by means of cross-correlation.

of spectral lines, however, are not in the regions of overlap and the wavelength mapping within a spectral line (in fact within a spectral order of about 20 Å) is still accurate at the 12 m s^{-1} level. On the other hand, in the final merged spectrum, the absolute wavelength scale of all setups and orders combined is uncertain to about 70 m s^{-1}. This 70 m s^{-1} uncertainty will have an effect only in our measurements of wavelength shifts (Sect. 3.2.2) but not in the line profiles or their bisectors.

In summary, the careful continuum normalization of the S^4N spectra was passed on to each setup of our cs21 spectra and all these pieces were put together using a high quality HET spectrum as a radial velocity template. The final result is a one-dimensional continuum normalized spectrum with the fluxes from all orders and setups merged into a single array of data.

2.5 The resolving power of 2dcoudé-cs21

Before moving on to the next chapter on the validation of a 3D model using the data described in this chapter, it is necessary to determine accurately the resolving power of the spectrograph used (2dcoudé-cs21), since it affects the shapes of the observed spectral line profiles. It is also important to check whether the quality of the spectra has been preserved over the time span of our multiple observing runs.

To calculate the resolving power of 2dcoudé-cs21, we used the ThAr exposures. The FWHM of the peak of the autocorrelation function of a ThAr spectrum is equal to $\sqrt{2}$ times the FWHM of the ThAr lines, which we will refer to as FWHM_X. Note that the Th lines are sharper than the Ar lines due to their different atomic weights, which makes thermal broadening more important for the latter (see below). Since there are more Th lines than Ar lines, the FWHM of the autocorrelation function is dominated by the Th lines. The actual resolving power, however, is slightly different than the one given by λ/FWHM_X due to the contribution from thermal broadening to the observed widths of the Th lines (this is discussed in more detail below). However, we can study the λ/FWHM_X values to track for time variations in the resolving power of the spectrograph given that the contribution of thermal broadening to the width of the Th lines is relatively small. In principle, it is best to measure the FWHM of Th and Ar lines separately but only a few strong lines with reliable identification are available in each setup and therefore the autocorrelation method works best in these cases (we did measure Th and Ar lines separately in the *merged* ThAr spectra discussed below).

The time variation of the λ/FWHM_X values is show in Fig. 2.9. Values for all the ThAr exposures taken during our observing runs are shown there as a function of time. The λ/FWHM_X values vary significantly with time, even within a given run of a few days. From one run to another (months apart), the change in the mean λ/FWHM_X values is significant. Temperature broadening effects alone cannot explain the diversity of values seen in Fig. 2.9. Less than 10% of the broadening of Th lines is thermal (see below). Considering changes of 10% in the temperature of the ThAr lamp (which was actually well controlled), the total broadening would be affected by only $0.1 \times \sqrt{0.1} = 3\%$

or less, yet in Fig. 2.9 we see variations of up to 25%.

This degradation of the image quality (2dcoudé-cs21 was intended to deliver $R \gtrsim 200,000$ at all times) was due to a large difference in temperature between the slit room and the spectrograph room, which resulted in a large tube seeing in the collimator primary mirror tube. This problem has been documented by P. MacQueen (2007, private communication) and temporarily solved by insulating the collimator and minimizing the temperature difference between the slit and spectrograph rooms. Our data, however, suffer from this effect and we therefore need to estimate an "effective" resolving power for each of our objects, depending on when they were observed.

To assess an effective resolving power to our merged cs21 spectra (the ones that we will use in the next chapters), we first combined all the ThAr exposures used to determine the wavelength solutions of each object exposure using methods similar to those described in Sect. 2.3. Then the merged ThAr atlases (one for each sample star) were used to measure the FWHM of individual Th and Ar lines using the line identifications of Murphy et al. (2007). In this way, we could determine FWHM values of Th lines (f_{Th}) and Ar lines (f_{Ar}) separately. Note that this procedure is valid only when the exposure times of all the ThAr frames are equal, as in our case.

The thermal broadening (σ) is inversely proportional to the square root of the atomic weight W; thus

$$\frac{\sigma_{\mathrm{Th}}}{\sigma_{\mathrm{Ar}}} = \left(\frac{W_{\mathrm{Ar}}}{W_{\mathrm{Th}}}\right)^{1/2} = 0.415. \tag{2.2}$$

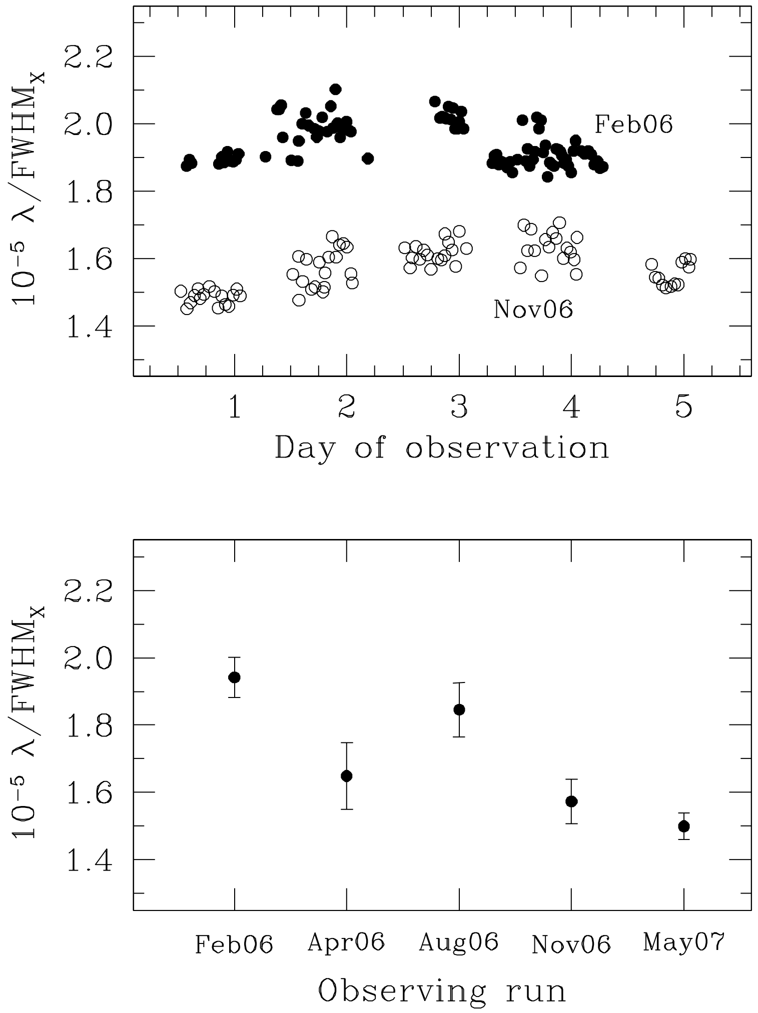

Figure 2.9: Time variation of the λ/FWHM_X values obtained from the autocorrelation of single ThAr exposures. The top panel shows the results for two observing runs while the bottom panel shows the average λ/FWHM_X for each of the observing runs (the error bars correspond to the standard deviations from the mean value).

If the instrumental FWHM is f, we can approximate (although the ThAr line profiles were slightly asymmetric, Gaussian fits made reasonably good first-order approximations):

$$f^2 + \sigma_{\mathrm{Th}}^2 = f_{\mathrm{Th}}^2 \tag{2.3}$$

$$f^2 + \sigma_{\mathrm{Ar}}^2 = f_{\mathrm{Ar}}^2 \tag{2.4}$$

from which we obtain an expression for the instrumental FWHM that is independent of temperature:

$$f^2 = \frac{f_{\mathrm{Th}}^2 - 0.17 f_{\mathrm{Ar}}^2}{0.83} \ . \tag{2.5}$$

The resolving power is then λ/f.

In practice, we measured the FWHM of several Th and Ar lines at different wavelengths and fitted the FWHM vs. λ relations using smooth functions. Then we applied Eq. 2.5 to determine the effective resolving power (as a function of λ) for each of our targets. Fig. 2.10 shows an example of this procedure.

Examining the effective resolving power of all our sample stars, we find that the minimum and maximum values are 160,000 and 210,000, respectively. As we show later in Chapter 3, these differences affect only marginally the observed line bisectors and wavelength shifts.

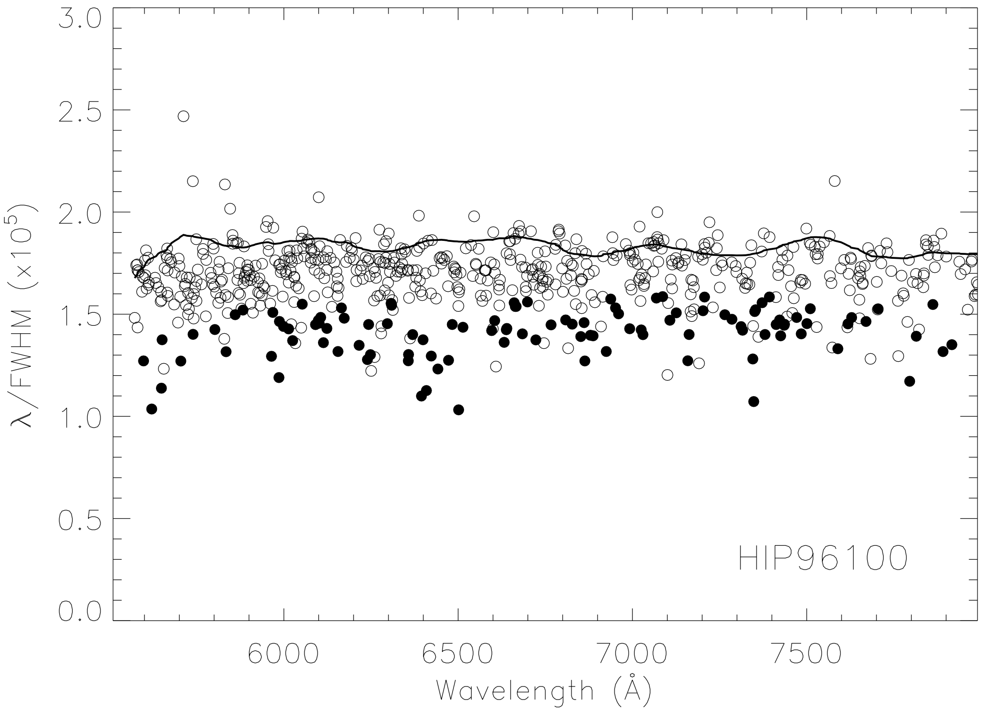

Figure 2.10: The effective resolving power of the merged spectrum of HIP 96100 is shown with the solid line. The open circles correspond to measurements of Th lines and the filled circles correspond to Ar lines. The effective resolving power is larger than the Th measurements because the thermal broadening was removed (see text for details).

Chapter 3

Validating a 3D Model

The physics of the granulation problem, namely radiatively driven convection, is very complex; it is three-dimensional, time-dependent, non-local, and non-linear. Parameterized models of granulation may require a large number of free parameters whose physical interpretation is obscure. Furthermore, they do not guarantee a unique solution. On the other hand, the continuous growth of computer power is allowing us to solve this problem numerically using only the basic physical laws of hydrodynamics, including radiative transfer in the energy equation. A better understanding of solar and stellar granulation is thus possible using numerical simulations.

The goal of this thesis is to understand the surface inhomogeneities (granulation) present in K-dwarf stars and explore their impact on the determination of fundamental parameters and chemical compositions derived from a star's spectral energy distribution. A theoretical granulation model has been calculated for this purpose but we should not use it before it has been carefully tested for its most fundamental predictions. In this chapter, the 3D model atmosphere used in this dissertation is described, as well as the tests performed to validate it.

3.1 Line formation in 3D model atmospheres of K-dwarfs

3.1.1 Hydrodynamic simulations

A three-dimensional radiative-hydrodynamic LTE model atmosphere was computed for this work by M. Asplund using the methods described in Stein & Nordlund (1998). A plane parallel box of the stellar envelope was modeled by solving the fluid dynamics equations of mass continuity,

$$\frac{\partial\rho}{\partial t} + \nabla\cdot(\rho\mathbf{v}) = 0 \ , \tag{3.1}$$

momentum conservation,

$$\rho\frac{\partial\mathbf{v}}{\partial t} + \rho(\mathbf{v}\cdot\nabla)\mathbf{v} = \rho\mathbf{g} - \nabla P + \rho\nabla\cdot\overline{\sigma} \ , \tag{3.2}$$

and energy conservation,

$$\rho\frac{\partial e}{\partial t} = -\rho\mathbf{v}\cdot\nabla e - P\nabla\cdot\mathbf{v} + Q_{\mathrm{rad}} + Q_{\mathrm{visc}} \ . \tag{3.3}$$

In these equations, ρ, $\mathbf{v}$, and $\mathbf{g}$ are the density, velocity, and gravitational field, respectively; P and e represent the gas pressure and internal energy; $\overline{\sigma}$ is the viscous stress tensor; and Q_{rad} and Q_{visc} are the radiative heating and viscous dissipation. All these quantities depend on the position (x, y, z) within the simulation box and time (t).

The temperature T is linked to these equations through the equation of state and by the radiative heating rate

$$Q_{\mathrm{rad}} = \int\oint \kappa_\nu(I_\nu - S_\nu)\, d\Omega\, d\nu \ , \tag{3.4}$$

which is determined by solving the radiative transfer equation along several rays. The variables of integration ν and Ω in Eq. 3.4 are the frequency of radiation and solid angle, respectively. The temperature determines the values of the absorption coefficient, κ_ν, and the source function, S_ν, and it depends primarily on the total energy flux that goes through the photosphere.

In the calculation of the 3D model, the equation of state (as given by Mihalas et al. 1988), continuum opacities, and source functions were obtained by interpolation in the tables included in the updated MARCS stellar atmosphere package (e.g., Gustafsson et al. 1975). The adopted line opacities were those by Kurucz (1993a,b).

The model consists of $150 \times 150 \times 82$ grid points representing a rectangular box of the following geometrical dimensions: $4.7 \times 4.7 \times 3.2$ Mm ($1\,\mathrm{Mm} = 10^6\,\mathrm{m}$). The simulation box has periodic horizontal boundaries, gas is allowed to escape at the top, while the density and energy of the incoming gas at the bottom boundary are adjusted to conserve the entropy. Other top and bottom boundary conditions can be applied but, in general, they have a small impact on the final result (see Stein & Nordlund 1998 for details). After relaxation, the simulation was run for about one hour of stellar time. The time step adopted in the calculations was about 0.2 seconds but only 180 snapshots were saved, of which the last 101 were used in this work. The geometrical extent and time span of the simulation are representative of the K-dwarf photospheric granulation given that it shows the complete evolution of several well defined granules.

Surface gravity, chemical composition, and entropy of the gas entering the simulation box are the fundamental parameters for the 3D model calculation. The effective temperature is a result of the simulation and it varies slightly between snapshots. The effective temperature that results from the calculation of our 3D model is about 4820 K. The other input parameters were $\log g = 4.5$ and $[\mathrm{Fe/H}] = 0.0$. The solar abundances adopted are those given by Grevesse & Sauval (1998).

Fig. 3.1 shows the temperature structure of the 3D K-dwarf model atmosphere in the upper 1 Mm layers (this is the portion of the model that was used for the spectral line calculations, as explained in Sect. 3.1.2). The rapid decrease of temperature with atmospheric height just below the visible surface (depth = 0),[1] attributed to the feedback between radiation losses and decreasing opacity, is the most prominent feature. There, across a layer of only about 100 km, the gas temperature drops about 4000 K. In the regions of line formation (depth < 0), the temperature fluctuations have extremes that differ by almost 1000 K (the RMS value, however, is smaller, as explained below).

Also shown in Fig. 3.1 are one-dimensional models computed with the ATLAS (Kurucz 1979, 1993a) and MARCS (Gustafsson et al. 1975, 2003) codes.[2] It is clear that, in the regions of line-formation, the 1D and 3D models

---

[1] The "depth" variable corresponds to the geometrical depth, increasing inward, and it is zero at the plane where the spatially-averaged Rosseland optical depth is equal to one.

[2] The references given here correspond to those that describe the basic properties of the models. Several improvements have been made since their publication. The models presented in Fig. 3.1 are those available at: `http://kurucz.harvard.edu/grids.html` (the "odfnew" version) and `http://marcs.astro.uu.se/`.

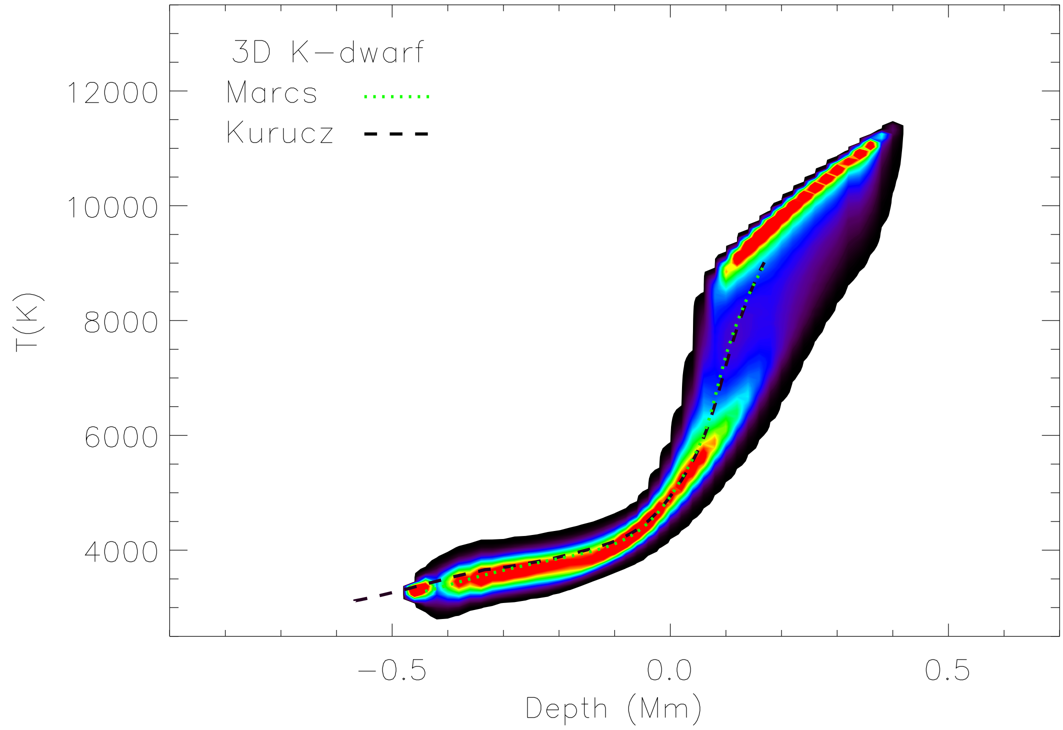

Figure 3.1: Temperature structure of the 3D K-dwarf model atmosphere near the visible surface (the full simulation extends much deeper than shown here). The color code represents the number of grid points at a given temperature and depth, with red being the largest and dark blue the smallest number. The dotted green line and dashed black line correspond to temperature structures of 1D model atmospheres (see legend on the top left). The depth scale is set to zero at the geometrical plane where the mean Rosseland optical depth is equal to 1; i.e., at the "visible" surface.

show very similar temperature structures if, for the latter, the average value of the temperature is obtained at each depth. We must warn, however, that it is because of the temperature fluctuations that the 3D model is more realistic and that the similarity quoted above with 1D models should not be used as an excuse to claim that 1D and 3D models of K-dwarf photospheres are equivalent. The reason why the average 3D and 1D temperature structures are similar is because 3D models are nearly in radiative equilibrium at solar metallicity.

A snapshot of the temperature structure of our 3D model is shown in Fig. 3.2. Clearly, the largest temperature fluctuations, which resemble the granulation pattern, occur well below the visible surface. Thus, in this model, the largest granulation intensity contrasts are “hidden,” using the term coined by Dravins & Nordlund (1990a) in their study of a granulation model for α Cen B (spectral type K1V).

The temperature and velocity fields near the geometrical surface of zero depth are shown in Fig. 3.3 for a given snapshot of the simulation. The basic properties of granulation are satisfactorily reproduced by the 3D model. Hot granules have the largest upward velocities and appear to be expanding from their center. The horizontal velocity field converges toward intergranular lanes, which are cooler and have the largest downward velocities. This correlation between the vertical velocity and temperature fields is illustrated also in Fig. 3.4. A similar, albeit weaker correlation, is predicted for the density and vertical velocity fields (Fig. 3.5). In this case, the downdrafts (positive vertical velocity) contain higher density gas. The correlation does not look

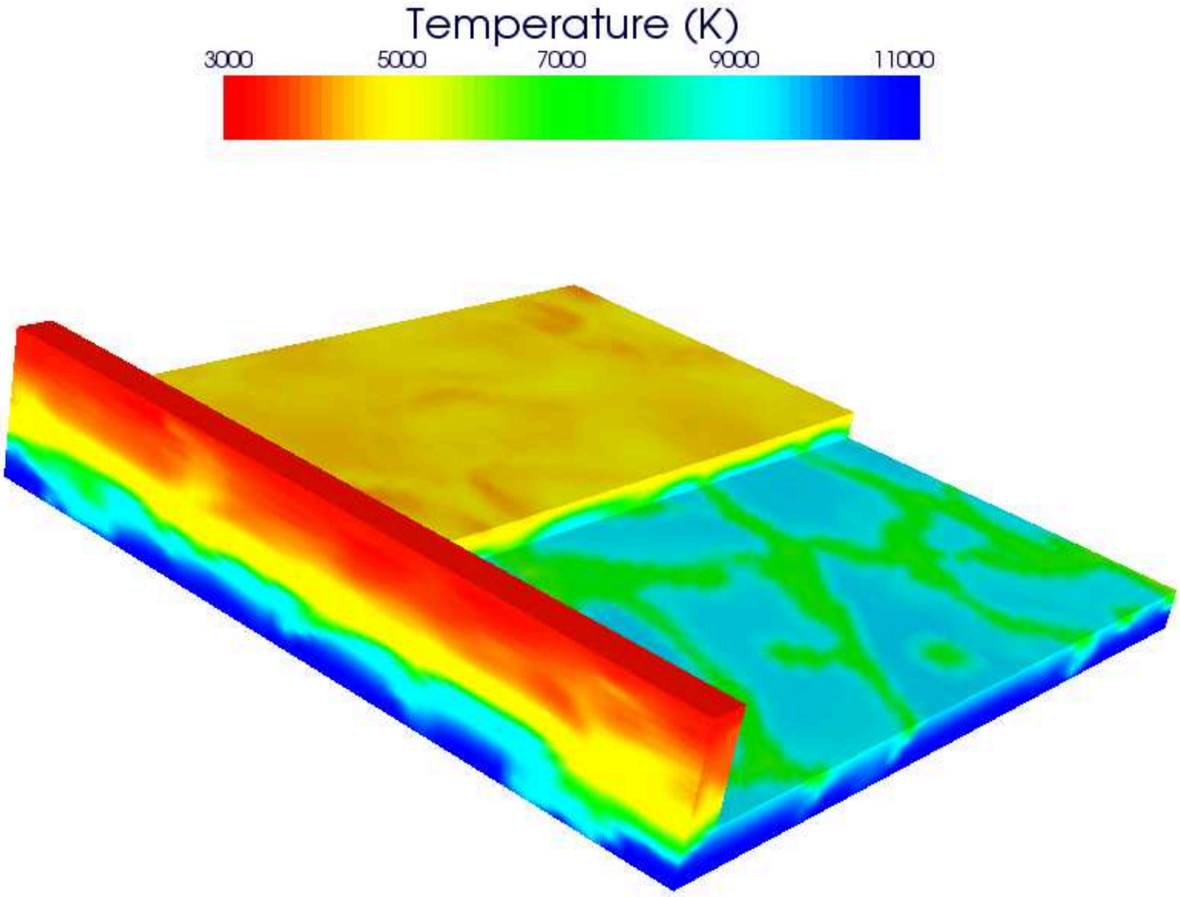

Figure 3.2: Temperature structure of a snapshot of our 3D K-dwarf model atmosphere. Two horizontal cuts are shown; one 150 km below the visible surface (depth = -0.15 Mm; predominant colors are green and blue) and another one at the visible surface (depth = 0; predominant color is yellow). The granulation pattern is clearly seen at depth = -0.15 Mm. At the visible surface, the inhomogeneities persist but to a lesser extent and the granulation pattern is a very weak one.

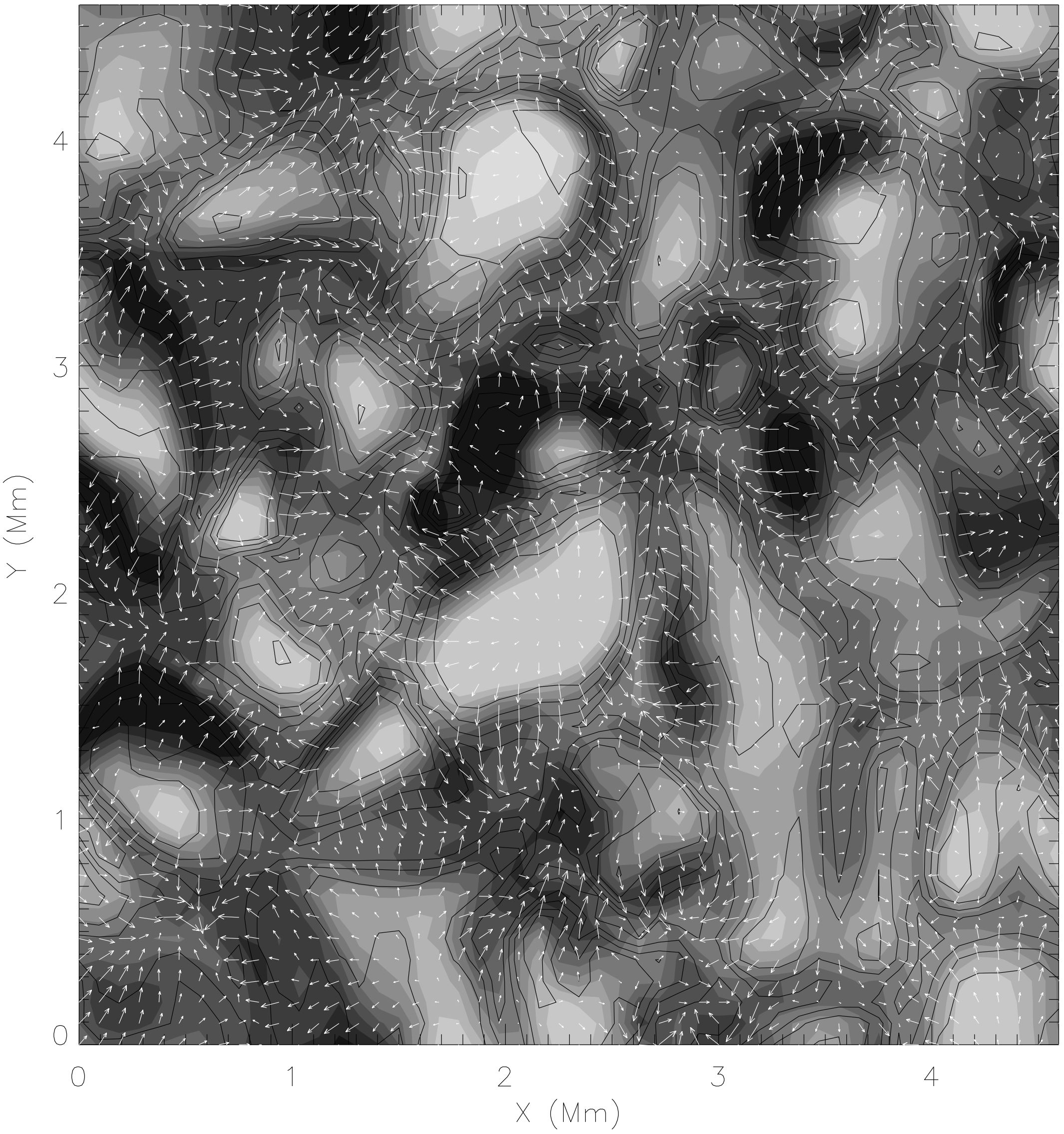

Figure 3.3: Temperature and velocity fields of a snapshot of the 3D K-dwarf model atmosphere at the geometrical depth corresponding to a mean Rosseland optical depth $\tau \sim 1$ (i.e., the “visible” surface). The velocity field is superimposed on the temperature field and is represented with solid lines (vertical component) and arrows (horizontal component). In this snapshot, the temperature extremes differ by about 1600 K (cf. Fig. 3.1) while the vertical velocities range from about -4 to $+4$ $\mathrm{km\,s^{-1}}$.

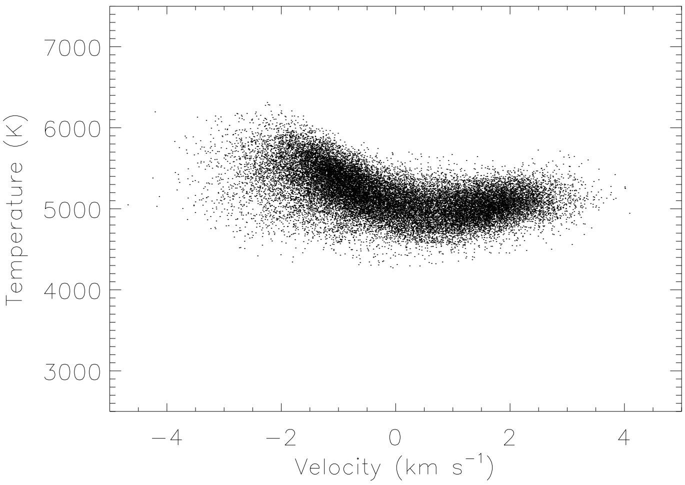

Figure 3.4: Correlation between temperature and vertical velocity for the first 10 snapshots of the 3D K-dwarf model atmosphere at the geometrical depth corresponding to $\tau \sim 1$.

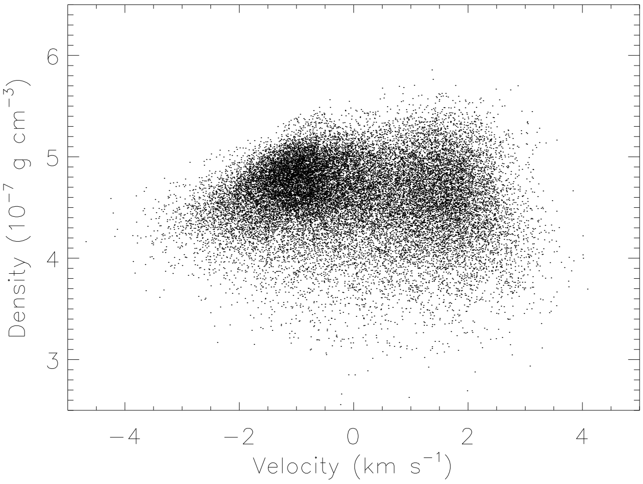

Figure 3.5: Correlation between density and vertical velocity for the first 10 snapshots of the 3D K-dwarf model atmosphere at the geometrical depth corresponding to $\tau \sim 1$.

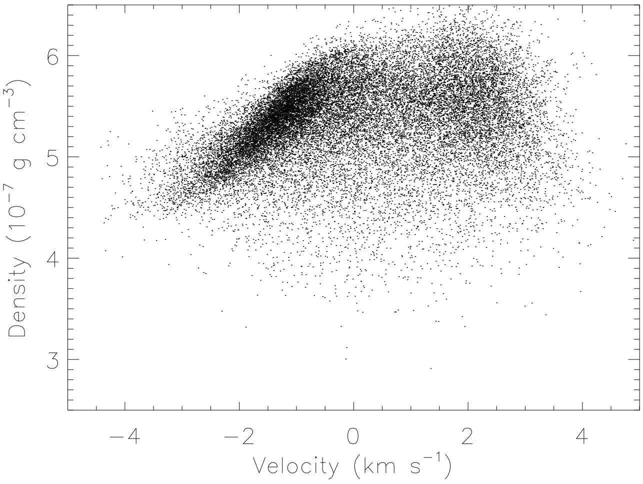

Figure 3.6: As in Fig. 3.5 but at the geometrical depth corresponding to about 50 km below the $\tau \sim 1$ plane.

very strong at this depth but it becomes pronounced only a few layers below, as it can be seen by comparing Figs. 3.5 and 3.6.

Although it is not shown here, the predicted granulation pattern also evolves in time as expected; large granules explode producing two or more smaller granules as intergranular lanes develop between them (see, e.g., Stein & Nordlund 1998 for the solar case). A visual inspection of the simulation shows that the mean lifetime of recognizable granules is between 5 and 10 minutes.

The fluctuations of the temperature, velocity, and density fields in the 3D simulation as a function of depth are quantified by their root mean square (RMS) values. The maximum RMS of all these parameters occur at a depth of about +0.1 Mm (Fig 3.7). In this layer, the RMS values are about 1200 K,

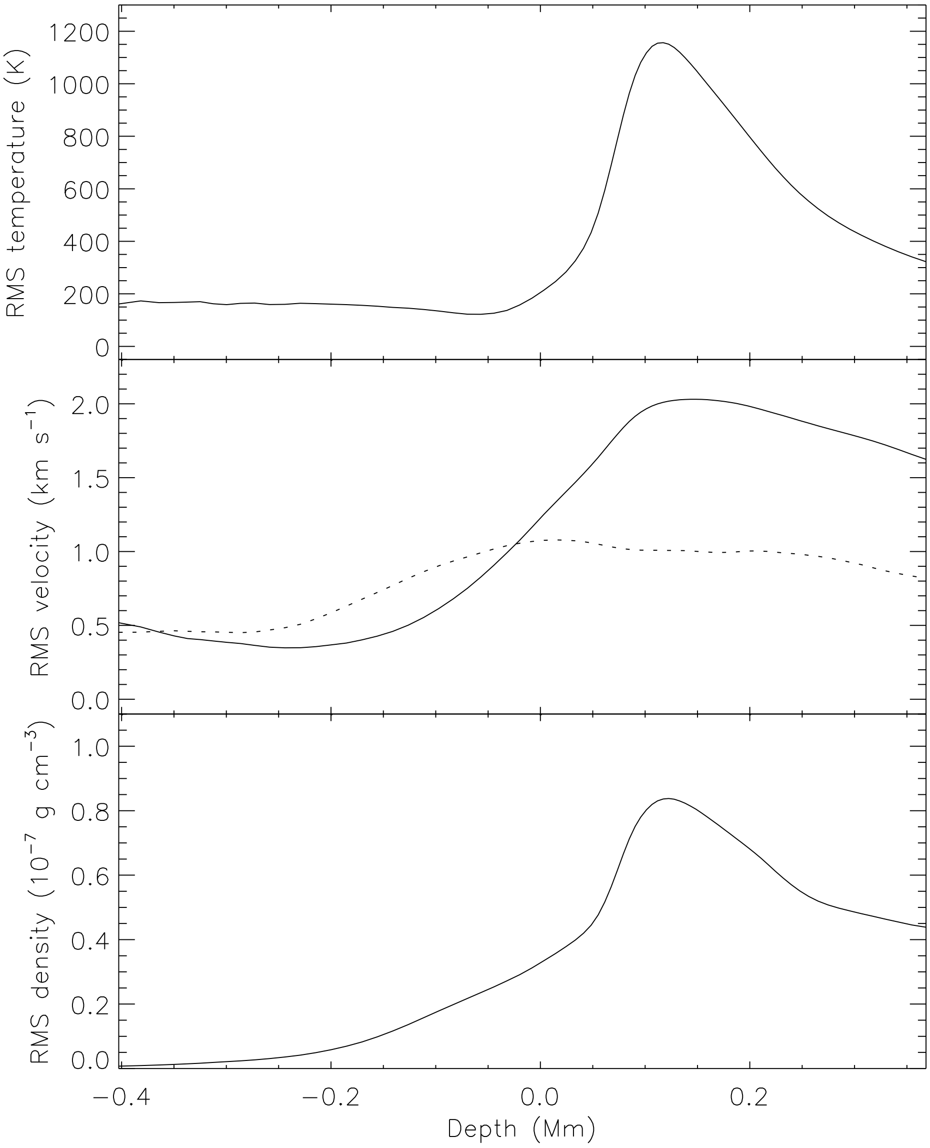

Figure 3.7: Root mean square values of the temperature, velocity, and density fields according to our 3D model atmosphere (all snapshots included). In the middle panel, the solid line corresponds to the vertical component of the velocity while the dotted line corresponds to the horizontal component.

2 $\mathrm{km\,s^{-1}}$ (vertical component only), and 0.8×10^{-7} $\mathrm{g\,cm^{-3}}$. In the regions of line formation (depth < 0), the RMS temperature is roughly constant at about 200 K while the RMS vertical velocity decreases with height, from about 1.3 $\mathrm{km\,s^{-1}}$ at the visible surface to only about 0.5 $\mathrm{km\,s^{-1}}$ at the top of the simulation box.

Similar 3D simulations for the Sun (Stein & Nordlund 1998, Asplund et al. 2000b; $T_{\mathrm{eff}} = 5777\,\mathrm{K}$, $\log g = 4.44$, $[\mathrm{Fe/H}] = 0$) and Procyon (Allende Prieto et al. 2002; $T_{\mathrm{eff}} = 6500\,\mathrm{K}$, $\log g = 4.0$, $[\mathrm{Fe/H}] = -0.05$) are available for comparison. The temperature and velocity fluctuations are larger in the Procyon than in the solar model. At the visible surface, for example, the RMS temperature of Procyon is about 8% compared to 4.5% of the solar case. In the K-dwarf model, the corresponding value is even lower, about 4.0%. Obviously, in the absolute values, the differences are larger. The peak RMS velocities of the Procyon, Sun, and K-dwarf model are 5, 4, and 2 $\mathrm{km\,s^{-1}}$, respectively. Thus, there is clearly an effective temperature dependence such that hotter stars experience larger temperature and velocity fluctuations than cooler stars.

The dependence of the strength of the granulation effects, as quantified by the RMS temperature and velocity fields, on the stellar effective temperature has been explained by Nordlund & Dravins (1990). The convective flux scales with the total flux so that cooler stars transport less convective energy than hotter stars. In addition, cooler stars are denser and therefore small velocities are enough to transport the convective flux.

As it has been stated several times, the granulation pattern results from the sharp decline in the gas temperature due to radiation losses and the subsequent lowering of the continuous opacity, which is extremely temperature dependent. In the Procyon model, this occurs very close to the visible surface but it occurs a few tens to hundreds of km below it in the cooler models (about 100 km in our K-dwarf case; see Fig. 3.1). Thus, in addition to having larger temperature and velocity contrasts, hotter 3D models have their granulation pattern visible on their surfaces, a phenomenon labeled “naked granulation” by Nordlund & Dravins (1990) for the case of Procyon.

Although in the cooler models, such as our K-dwarf simulation, the largest temperature contrasts are hidden (see Fig. 3.2), the velocity fields associated with them reach larger heights, in particular the regions of line formation. For example, Fig. 3.7 clearly shows that, even though the RMS temperature ceases to decline shortly after reaching the visible surface, the RMS velocity continues to decay for another 200 km. We therefore expect to see the granulation effects on absorption lines in K-dwarf spectra.

The spectra of K-dwarfs, in particular those with near solar and super-solar metallicities, are very rich in absorption lines. For spectroscopic studies of granulation, iron is an ideal element; it has a large mass, which implies low thermal broadening and therefore a high sensitivity to non-thermal fields, one isotope is much more abundant than the others, thus reducing the impact of asymmetries due to fine structure, it is abundant, and its atomic structure is very complex, allowing a very large number of transitions. Furthermore, contrary to most other heavy elements, very reliable laboratory data are available for iron. In this chapter, we deal with the detection of the granulation signatures using Fe lines exclusively.

3.1.2 Spectrum synthesis in 3D

Single spectral lines were computed with the 3D synthesis code "`lte-H`" (e.g. Asplund et al. 2000b). The equation of transfer was solved along several rays throughout the upper 0.8 Mm of the simulation box. The contribution from deeper layers to the emergent flux is negligible, thus justifying the use of only the upper layers in the line calculations. To improve the vertical sampling, which is necessary due to the rapid change of the local physical parameters in this region and the sensitivity of the line opacities to these quantities, the upper 0.8 Mm of the simulation box was interpolated to a grid of 82 depth points. In the horizontal direction, of the original 150×150 grid, a coarser 50×50 grid was adopted by eliminating two of every three grid points along the x and y axes, thus keeping the same geometrical dimensions. This has the advantage of significantly reducing computing time while keeping the results essentially unchanged (Asplund et al. 2000a). The model used for the line calculation is therefore a $50 \times 50 \times 82$ grid (i.e., 205,000 mesh points).

The time interval between snapshots of the 3D simulation used for the spectral line calculations is about 40 seconds. For the line calculations we used only every other snapshot, thus reducing the computing time by a factor of 2 compared to the case where all snapshots are used. Tests showed that using every other simulation snapshot instead of all of them produced essentially the same results. The maximum difference in flux from this experiment was from less than 0.01% for weak lines to about 0.04% for the strongest lines. Tests using one every four and one every eight snapshots showed that this maximum flux difference increased by factors of only two (i.e., about 0.08%) and three (0.12%), respectively. Note that the use of several snapshots not only takes into account the time-dependence of the granulation phenomenon but it can also be interpreted as the equivalent of increased spatial coverage.

Along each ray, the equation of radiative transfer was solved using 8 axial ($\mu = \cos\theta$ in the standard stellar atmosphere theory notation) and 8 azimuthal (ϕ) angles. The number of frequencies adopted in each case was 71, with a spacing corresponding to 0.4 $\mathrm{km\,s^{-1}}$. For strong lines, this frequency sampling was not enough to reach the full extent of the wings and we therefore repeated the calculation using 71 frequencies with a spacing of 1.5 $\mathrm{km\,s^{-1}}$. We did this instead of calculating the whole wide spectral range with fine spacing to save computing time. The two results were then merged into a single spectral line with 142 frequencies.

As for the model atmosphere computation, LTE level populations and ionization fractions were adopted in the line calculations. Look-up tables for the equation of state and opacity for the wavelength region in which the problem spectral line is located were calculated before solving the radiative transfer. Interpolation from these tables during the spectral line synthesis instead of on-the-fly calculations minimize computing time.

Each line was computed for 3 different values of the oscillator strength (or $\log gf$). In addition to calculating the line with its measured $\log gf$ value, lines corresponding to $\log gf \pm 0.5$ were also computed. Note that this is equivalent to computing each spectral line for three different abundances, namely A_{X} and $A_{\mathrm{X}} \pm 0.5$ dex.

We calculated line profiles for the 119 Fe I and 13 Fe II lines used by Ramírez et al. (2007), which are representative of the line-lists adopted in many FGK stellar abundance studies. The sources of the atomic data are reliable; transition probabilities have been accurately measured in the laboratory, often by more than one group and averaged, while the collisional broadening parameters (van der Waals damping constants) have been obtained from recent theoretical calculations (see Sect. 4.2 in Ramírez et al. 2007 for details and references).

The Doppler shifts introduced by the velocity field of the simulation were properly taken into account in the synthesis of the absorption line profiles, as well as the thermal and collisional broadening. The microturbulence and macroturbulence parameters are not necessary in 3D spectrum synthesis (Sects. 3.2 and 4.1) and were therefore not used. Note that no external sources of line broadening have been taken into account at this point. The next section deals with the effects of rotational and instrumental broadening on our predicted spectral line profiles.

3.1.3 Disk-averaged line profiles

Since our goal is to compare spectral lines calculated with the 3D model with observations of distant stars, we need to calculate disk-averaged profiles taking into account external sources of line broadening. The calculation of flux from intensities is straightforward and very accurate, provided enough rays (μ and ϕ angles) are included in the calculation. The rotationally broadened intensity is given by

$$I(\Delta v, \mu, \phi, V \sin i) = \frac{1}{2\pi} \int_0^{2\pi} I(\Delta v - V \sin i \sin\theta \cos\phi', \mu, \phi)\, d\phi' \ , \tag{3.5}$$

where $V \sin i$ is the projected rotational velocity of the star, and ϕ' the latitude angle on the stellar disk. The frequency dependence of the intensity has been replaced here with a velocity variable $\Delta v = c\Delta\nu/\nu$. The disk averaged line profile is then given by

$$F(\Delta v, V \sin i) = \int_0^{2\pi} \int_0^1 I(\Delta v, \mu, \phi, V \sin i)\, \mu\, d\mu\, d\phi \ . \tag{3.6}$$

To explore the effect of the projected rotational velocity on line profiles affected by granulation, we computed line profiles with different $V \sin i$ values and determined their line bisectors (Fig. 3.8). At first sight, we can conclude that between $V \sin i = 0$ and 1 $\mathrm{km\,s^{-1}}$, the shape of the line bisector is only slightly affected by stellar rotation and it therefore retains most of the granulation signatures. On the other hand, for projected rotational velocities larger than 1 $\mathrm{km\,s^{-1}}$, the effects of stellar rotation must be taken into account to properly characterize the granulation effects.

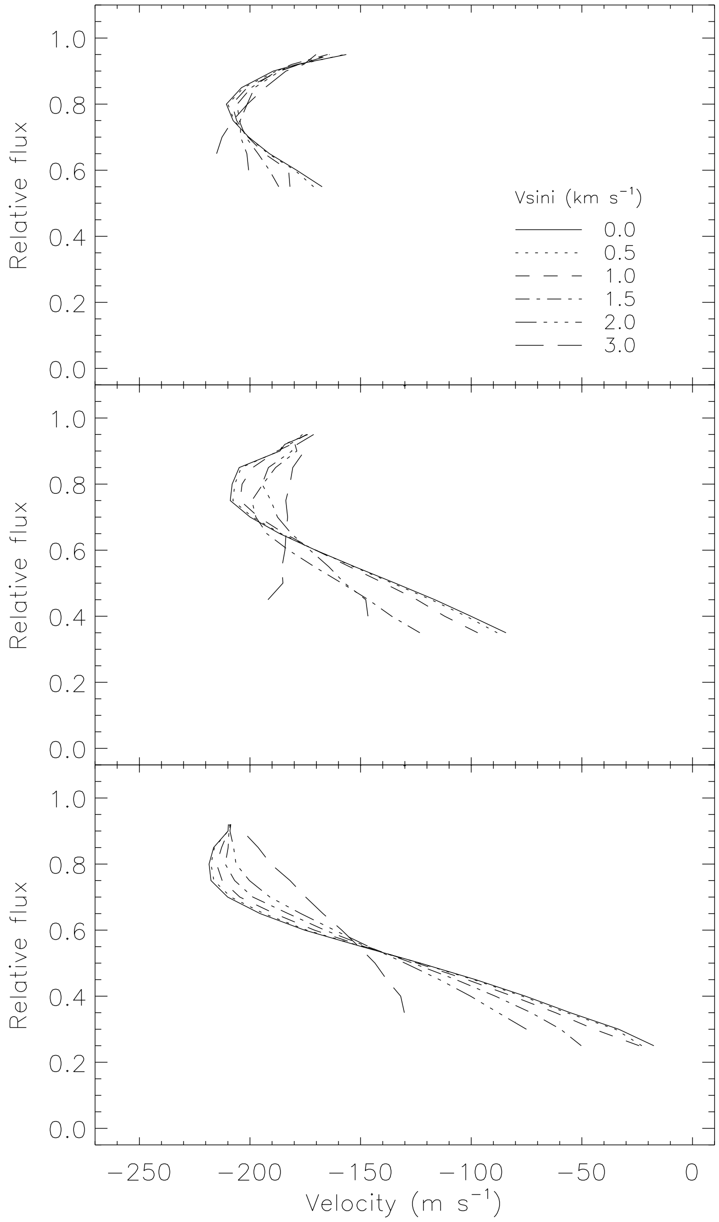

Figure 3.8: Bisectors of the theoretical 5228.4 Fe I line computed for three different values of $\log gf$ (from top to bottom panels, see text in Sect. 3.1.2) and several values of the projected rotational velocity $V \sin i$ (see legend in the top panel). The predicted convective blueshift has been taken into account.

The effect of the rotational velocity on the convective blueshifts is also illustrated in Fig. 3.8. Interestingly, although the line profiles become more symmetric for larger $V \sin i$ values, the absolute value of the convective blueshift is increased. This is probably related to the "rotation effect" discussed by Gray & Toner (1985) and Gray (1986) on the basis of their numerical experiments using two component granulation models. We stress here, however, that this increase in the convective blueshift is an external effect that is not associated with the strength of the granulation inhomogeneities. Rotation is not taken into account in the computation of the model atmosphere, only in the calculation of disk-averaged line profiles from the emergent intensities.

Our sample stars have $V \sin i$ values between about 0.5 and 3.0 km s^{-1} (Table 3.3). For practical purposes, all line profiles were calculated with only two values of the projected rotational velocity; $V \sin i = 0$ and $V \sin i = 1.5\ \mathrm{km\,s^{-1}}$. For other rotational velocities, instead of recalculating the flux from the spatially resolved intensities for every spectral line, we used the $V \sin i = 0$ flux profiles and convolved them with rotational profiles (e.g., Gray 1992) of FWHM determined by the $V \sin i$ values, assuming the following limb-darkening law:

$$I/I_0 = 1 - \epsilon + \epsilon \cos\theta \ , \tag{3.7}$$

where I_0 is the intensity at the disk center. This rotational convolution was performed using I. Hubeny's ROTIN3[3] code, which uses $\epsilon = 0.6$ by default.

---

[3] `http://nova.astro.umd.edu/Synspec43/synspec-frames-rotin.html`

According to Claret (1998; see also Claret & Giménez 1990), the limb darkening coefficient ϵ in K-dwarfs varies between about 0.55 in the I band and 0.70 in the V band, where the spectral lines of interest for this work are. We show below that the results from these calculations are remarkably accurate for the line bisectors compared to those obtained from spatially resolved profiles, but they fail at reproducing the rotationally affected convective blueshifts.

In Fig. 3.9 we show a spectral line computed with two different values of $V \sin i$, zero and 1.5 $\mathrm{km\,s^{-1}}$, both have been obtained from spatially resolved intensity profiles that resulted in the full 3D spectrum synthesis. We also show there a third profile that was calculated from the $V \sin i = 0$ flux profile after convolving it with a Gaussian rotation profile corresponding to $V \sin i = 1.5$ $\mathrm{km\,s^{-1}}$, as described in the previous paragraph. The line bisectors associated with these profiles are also shown in Fig. 3.9. It is clear that, regarding only the shape of the line bisector, the full calculation (obtained from the spatially resolved intensities) for the $V \sin i = 1.5$ $\mathrm{km\,s^{-1}}$ case agrees very well with the artificially broadened profile. Note, however, that the rotationally broadened profile is more noisy than the profile computed from the actual intensities; most likely due to interpolation errors in the ROTIN3 code, which are propagated to the measurement of the bisector (I. Hubeny, private communication). Nevertheless, we expect these errors to cancel out when averaging line bisectors of several broadened flux profiles, as we will in fact have to do later. Therefore, rotational broadening can be reasonably added to the $V \sin i = 0$ flux profiles, as described above, to explore the effect of $V \sin i$ on

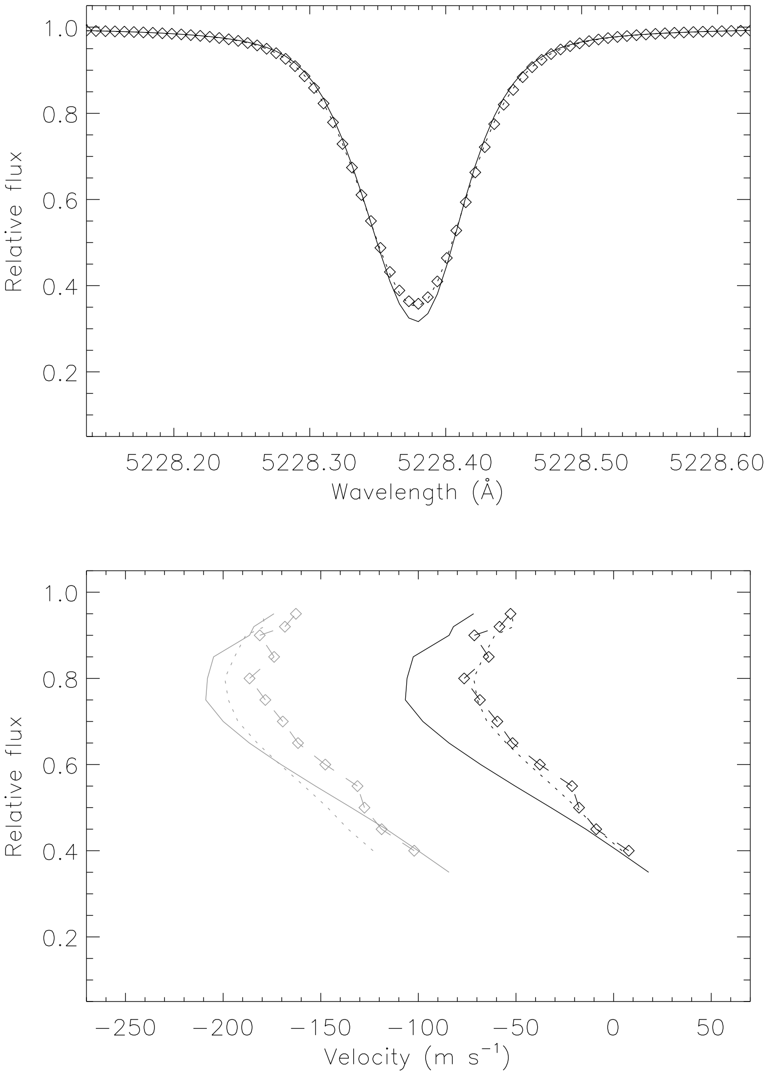

Figure 3.9: Top panel: the 3D line profile calculated with $V \sin i = 0$ (solid line) is shown along with the 3D profile computed with $V \sin i = 1.5$ km s^{-1} (dotted line) and the $V \sin i = 0$ profile convolved with a Gaussian rotation profile of $V \sin i = 1.5$ km s^{-1} (diamonds). Bottom panel: Line bisectors corresponding to the profiles shown in the top panel. The gray bisectors include the effect of the convective blueshift. The black bisectors are measured with respect to the central wavelength of the lines (i.e., ignoring the convective blueshift).

the line bisectors, which saves computing time and disk space. The situation is different for the convective blueshifts. The artificially broadened flux profile does not account for the extra shift added by the full $V \sin i \neq 0$ calculations. For the moderately strong line case shown in Fig. 3.9, the rotationally affected convective blueshift is underestimated by about 30 m s^{-1}.

The observed spectral line profiles have an additional external broadening due to the finite value of the spectral resolution of our observations, which, as we saw in Sect. 2.5, was not constant due to instrumental imperfections, but was found to vary between 160,000 and 210,000 among our spectra. To explore the effects of the spectral resolution on the theoretical line profiles, we performed tests convolving the rotationally broadened lines with Gaussian instrumental profiles of FWHM = λ/R, where R is the resolving power. One result of such experiment is shown in Fig. 3.10. As it is clear from this figure, the effects of a variable resolving power (between 160,000 and 210,000) on measurements of line asymmetries are relatively small, provided the profiles have already been rotationally broadened using typical $V \sin i$ values for K-dwarfs. Lower resolution makes the lines more symmetric but, in our range of resolving power and typical values of projected rotational velocity, the asymmetry is reduced, on average, by only a few meters per second.

The line bisector is an excellent probe of line formation in stellar granulation given that, roughly, at each flux depth its value is sensitive to the inhomogeneities of a certain range of photospheric layers. We thus expect the shapes of bisectors of lines of a given strength to be similar. There will be,

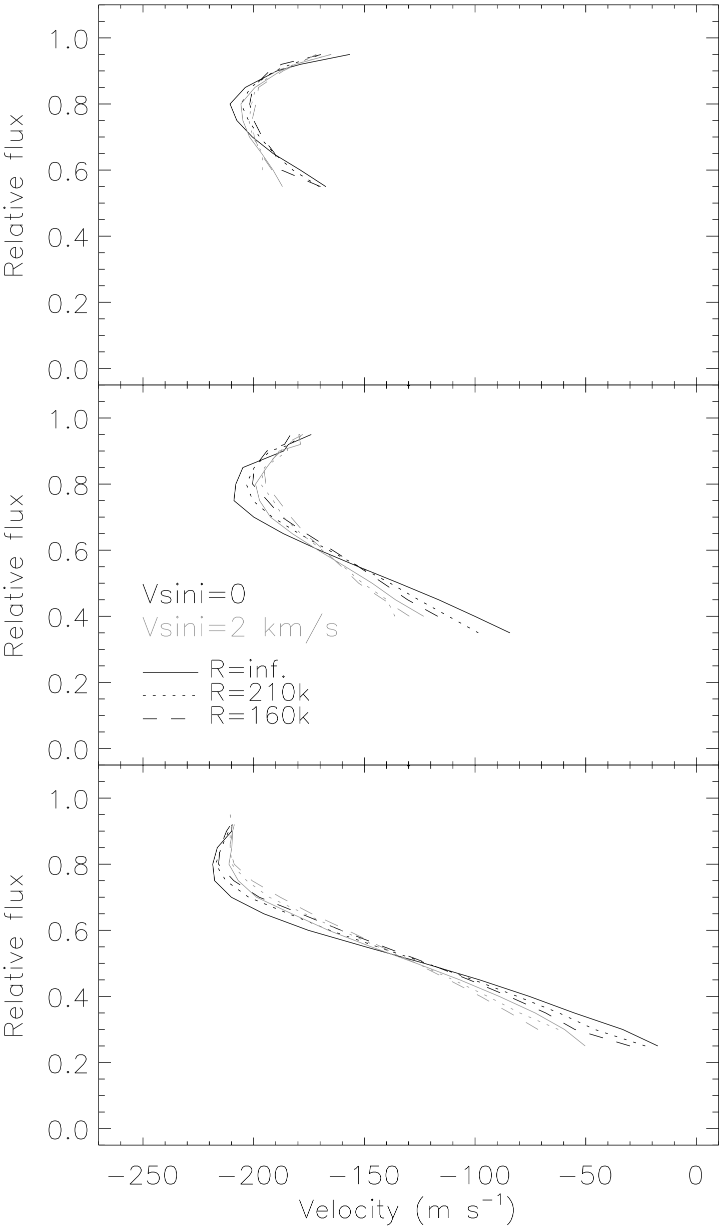

Figure 3.10: Bisectors of the theoretical 5228.4 Fe I line computed for three different values of $\log gf$ (from top to bottom panels, see text in Sect. 3.1.2), $V \sin i = 0$ (black lines) and 2 km s^{-1} (gray lines), and three values of the resolving power: infinite (solid lines), $R = 210,000$ (dotted lines), and $R = 160,000$ (dashed lines).

of course, differences due to dissimilar transition properties such as oscillator strength, excitation potential, collisional broadening, etc. Nonetheless, grouping lines of similar strength to obtain mean theoretical line bisectors will be necessary in the context of this thesis (specifically to compare with average, robust measurements; Sect. 3.2).

The mean theoretical line bisectors for Fe I lines with depth around 0.30, 0.45, and 0.65 are given in Table 3.1 and are shown in Fig. 3.11. These bisectors were obtained from the individual line bisectors but for values of the spectral resolution and projected rotational velocity typical of our study ($R = 180,000$ and $V \sin i = 1.5$ km s^{-1}). The error bars shown in Fig. 3.11 correspond to the 1-σ standard deviation from the mean, which is the *intrinsic* dispersion that we would expect from comparison with observed lines. For clarity, Fig. 3.11 shows the line bisectors measured with respect to the line center, i.e., ignoring the convective blueshifts. Fig. 3.12 shows these bisectors including the effect of the convective blueshift.

According to the 3D model, the strong Fe I lines (line-depth of about 0.3) in K-dwarf spectra have bisectors with a backslash (\) shape. The positions of their cores are only slightly different from their laboratory wavelengths (a few tens of m s^{-1}) and the uppermost parts of the bisector do not return to zero velocity but reach a value of about -100 m s^{-1}. Intermediate strength (line depth of about 0.5) Fe I lines have the characteristic C-shape discussed in Sect. 1.4; their central wavelengths are shifted by about -100 m s^{-1} with respect to their rest frame values and the velocity shift of the top of their line

	$0.25 < y_{min} < 0.45$			$0.45 < y_{min} < 0.60$			$0.60 < y_{min} < 0.90$		
y	Δv	$\sigma(\Delta v)$	n	Δv	$\sigma(\Delta v)$	n	Δv	$\sigma(\Delta v)$	n
0.30	8.3	14.5	7						
0.35	6.5	14.6	23						
0.40	1.5	10.3	36						
0.45	−6.1	8.6	38	10.9	20.3	8			
0.50	−15.1	9.4	38	2.1	17.7	27			
0.55	−24.7	11.4	38	3.3	13.2	46			
0.60	−34.7	14.3	38	−3.6	8.6	57			
0.65	−44.7	17.4	38	−10.0	10.8	57	2.5	14.4	9
0.70	−55.0	21.2	38	−16.3	13.3	57	3.0	7.5	14
0.75	−65.7	25.1	38	−24.0	16.4	57	−0.2	5.9	14
0.80	−75.9	30.3	38	−30.9	20.6	57	−4.2	6.6	15
0.85	−83.6	34.5	38	−36.8	25.9	57	−3.4	9.7	15
0.90	−86.3	37.6	38	−38.9	30.1	57	−3.9	13.3	18
0.92	−86.3	39.3	38	−36.8	34.3	57	0.4	13.9	18
0.95	−83.4	43.3	38	−33.2	40.3	57	11.9	18.0	18

Table 3.1: Mean line bisectors according to the K-dwarf 3D model atmosphere. The velocities are given in m s^{-1}, σ corresponds to the standard deviation with respect to the mean value, and n is the number of individual bisectors used to calculate the mean. These mean bisectors are also shown in Fig. 3.11. For this calculation, it was assumed that $V \sin i = 1.5$ km s^{-1} and $R = 180,000$.

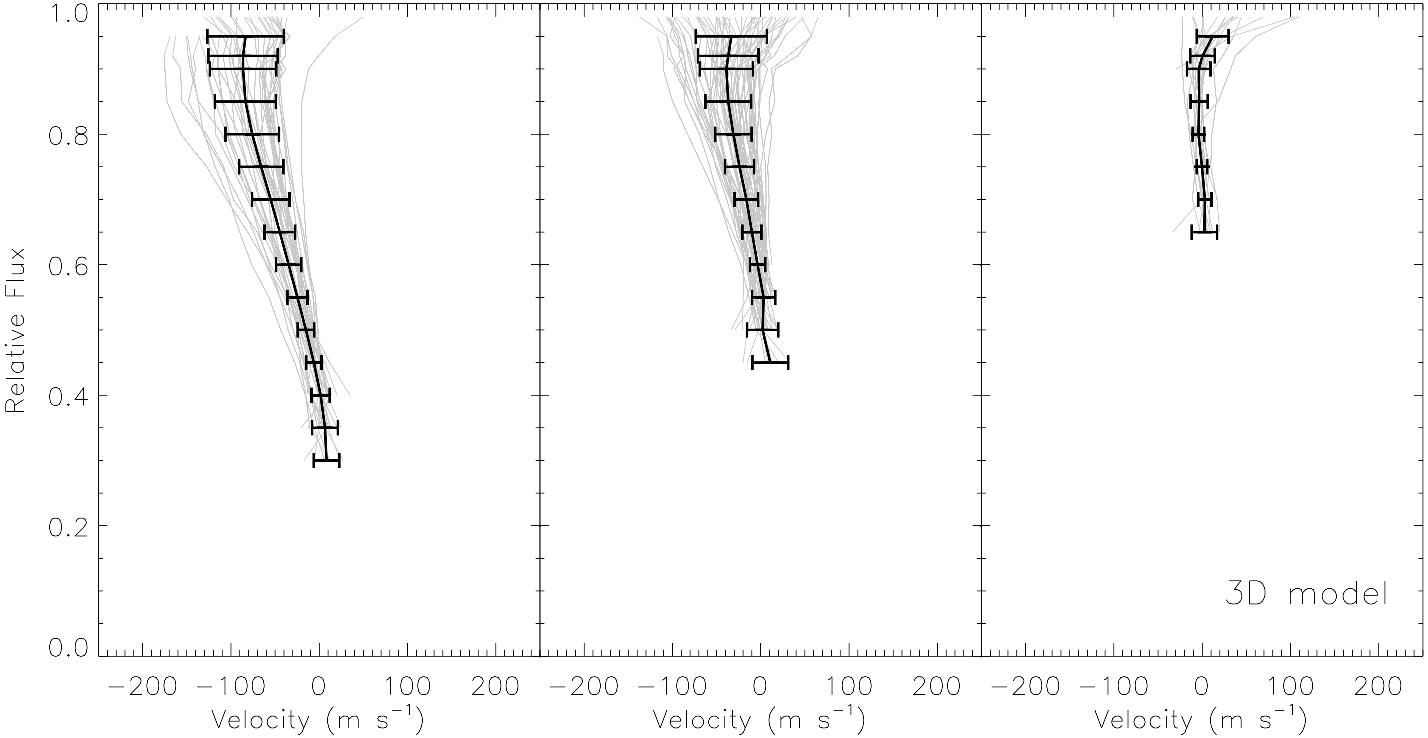

Figure 3.11: Mean bisectors for the 3D model (black solid lines with error bars) obtained from individual line bisectors (gray lines). The error bars correspond to a 1σ scatter. The mean bisectors are tabulated in Table 3.1. For this calculation, it was assumed that $V \sin i = 1.5$ km s^{-1} and $R = 180,000$.

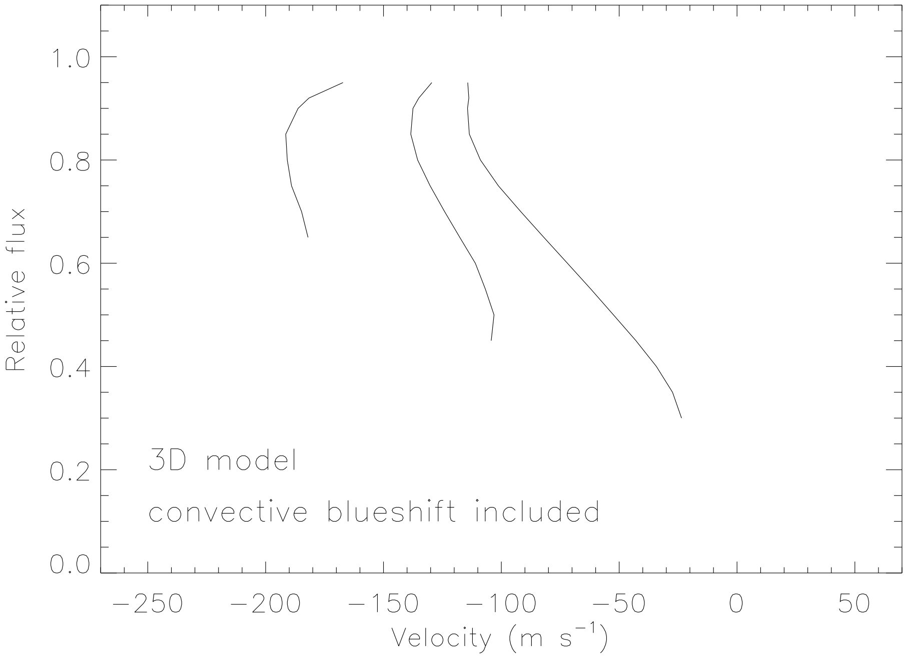

Figure 3.12: Theoretical mean line bisectors (cf. Table 3.1 and Fig. 3.11) including the effects of the convective blueshift.

bisectors is about −20 m s^{-1} more towards the blue. The weaker Fe I lines experience large convective blueshifts; their central wavelengths are shifted by about −180 m s^{-1}. As opposed to stronger lines, in this case the top of the line bisector has a wavelength shift that is about +10 to +20 m s^{-1} larger (i.e., towards the red) than the core.

The effects of the projected rotational velocity and finite spectral resolution on the mean line bisectors are illustrated in Figs. 3.13 and 3.14. From them we draw the same conclusions that we arrived at when we discussed individual lines (Figs. 3.9 and 3.10). It is clear that, given the properties of

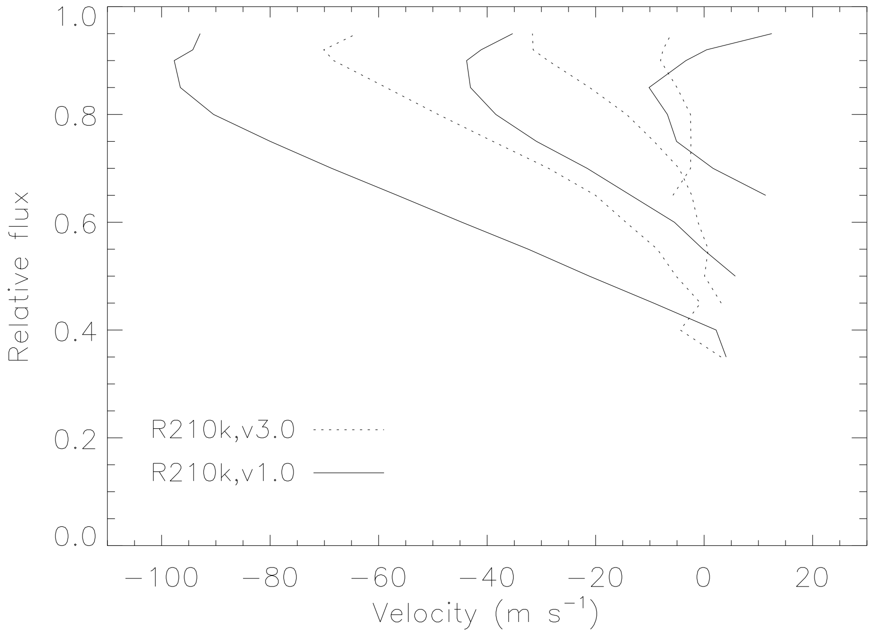

Figure 3.13: Effect of the projected rotational velocity ($V \sin i$) on the mean theoretical line bisectors. Calculations adopting a spectral resolution of 210,000 (R210K) with two values of $V \sin i$: 3.0 km s^{-1} (v3.0, dotted lines) and 1.0 km s^{-1} (v1.0, solid lines), are show. The line bisectors are shown here with respect to their central wavelength (i.e., ignoring their convective blueshifts).

our observations and our sample of stars, rotation has a larger impact than spectral resolution on the line bisectors and wavelength shifts.

The central wavelength shifts (i.e., the convective blueshifts) predicted by our 3D calculations are shown in Fig. 3.15 for the two values adopted for the projected rotational velocity and after convolving the line profiles with Gaussian instrumental profiles of spectral resolution $R = 180,000$. The effects of the spectral resolution on this relation are discussed later. We calculated

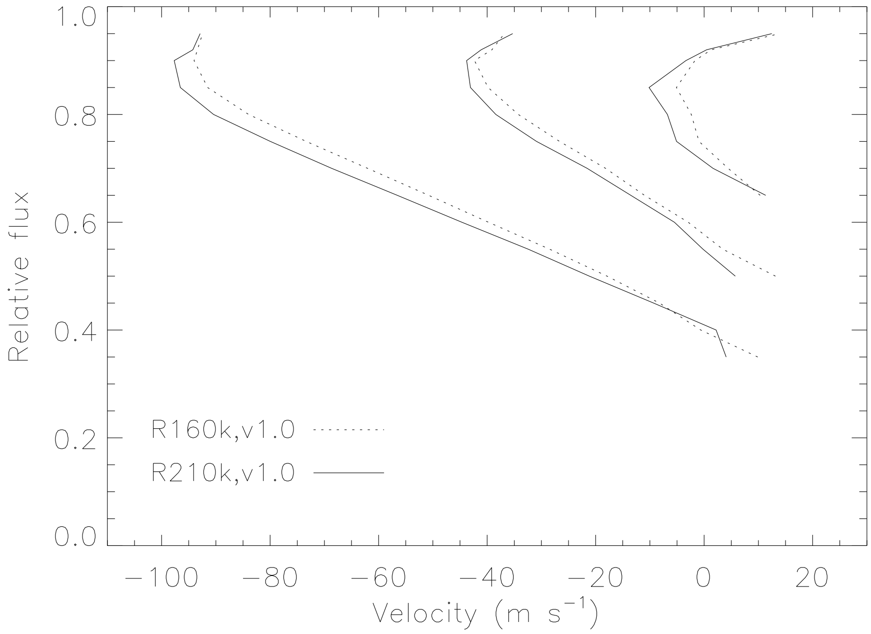

Figure 3.14: Effect of the spectral resolution ($R = \lambda/\Delta\lambda$) on the mean theoretical line bisectors. Calculations adopting two values of the spectral resolution: 160,000 (R160k, dotted lines) and 210,000 (R210K, solid lines), and $V \sin i = 1$ km s^{-1} (v1.0) are shown. The line bisectors are shown here with respect to their central wavelength (i.e., ignoring their convective blueshifts).

theoretical line shifts for the 119 Fe I and 13 Fe II lines for which we computed line bisectors above. To improve the statistics, the three theoretical lines computed per spectral feature (one for the measured $\log gf$ and the other two for $\log gf \pm 0.5$) are shown in Fig. 3.15. In addition, we added 6 very strong Fe I lines to study this relation at large equivalent widths. The atomic data adopted for these strong lines are given in Table 3.2.

As expected, Fig. 3.15 shows the characteristic signature of granulation.

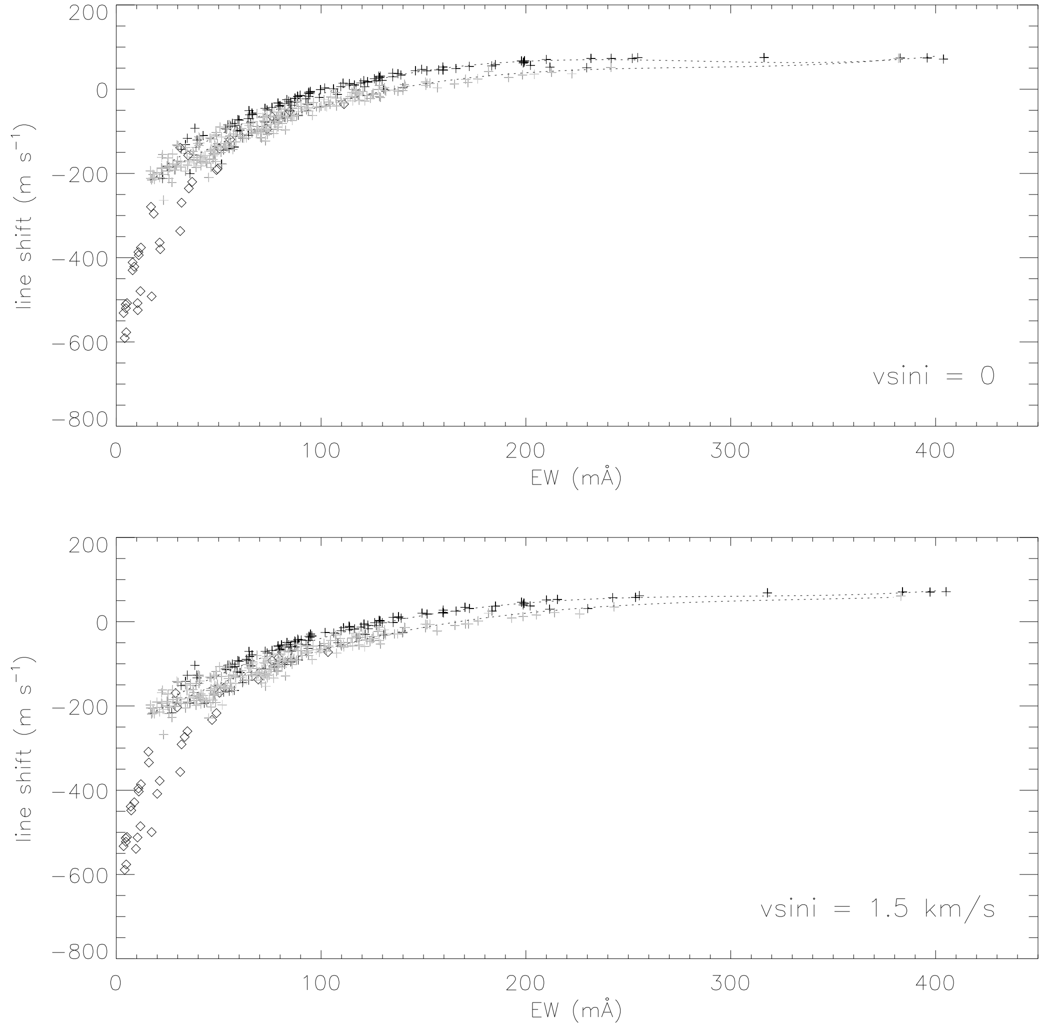

Figure 3.15: Central wavelength shifts predicted by our K-dwarf 3D model atmosphere calculations for two values of $V \sin i$. Crosses correspond to Fe I lines and diamonds to Fe II lines. The Fe I lines have been grouped into low excitation potential (EP < 3.5 eV, black symbols) and high excitation potential (EP > 3.5 eV, gray symbols) lines. The dotted lines are cubic fits to the predicted line shifts of the two EP groups.

Wavelength (Å)	$\log gf$	EP (eV)	σ (a.u.)	α
5741.85	-1.67	4.26	725	0.232
6252.56	-1.77	2.40	326	0.245
6335.32	-2.18	2.20	275	0.261
6411.65	-0.72	3.65	820	0.247
6430.85	-1.95	2.18	272	0.257
6677.99	-1.42	2.69	313	0.268

Table 3.2: Strong Fe I lines added to the line list of Ramírez et al. (2007) for the calculation of theoretical line bisectors and wavelength shifts. The last two columns are the van der Waals damping constants obtained by Barklem et al. (2000); σ is the broadening cross section for an atom-perturber relative velocity $v_0 = 10^6$ cm s^{-1}, given in atomic units (1 a.u. $= 2.8 \times 10^{-17}$ cm^2), and α the velocity parameter, which is related to the temperature dependence of the cross-section ($\sigma \propto T^{(1-\alpha)/2}$). Transition probabilities are from the accurate laboratory measurements of the Oxford group (e.g., Blackwell et al. 1976).

The weakest lines, those that are formed in deep photospheric layers that experience the largest granulation effects, have the largest (in absolute value) wavelength shifts. As the lines get stronger, and therefore the line formation depth decreases reaching higher photospheric layers with weaker granulation contrasts, the shifts get smaller. The difference between the maximum and minimum convective blueshifts for the Fe I lines is about 250 m s^{-1}.

The Fe II lines seem to follow a slightly different trend in the line shift vs. equivalent width (EW) relation, although they also experience larger shifts for weaker lines. For EW values between 15 and 40 mÅ, the convective blueshifts of Fe II lines are, on average, about 100 m s^{-1} larger (i.e., bluer or more negative) than those of Fe I lines, owing, most likely, to their deeper formation depths (the Fe II number density increases with depth as larger temperatures are required to ionize the neutral iron atom). At these deeper layers, the intensity and velocity fields are strongly correlated. Furthermore, the weakest Fe II lines (EW < 10 mÅ) show convective blueshifts as large as 800 m s^{-1}. Although it would be ideal to look for the granulation signatures using Fe II lines, in K-dwarfs they are very weak and only a small number of them are available for accurate line profile measurements.

The spread in the line shift vs. equivalent width relations shown in Fig. 3.15 is due to smaller correlations between line shift and the other spectral line properties (Fig. 3.16). There are very weak correlations between line shift and wavelength and transition probability but a very significant one with excitation potential; between EP $\simeq 2.5$ and 4.5 eV, the average lineshift decreases by about 50 m s^{-1}. Due to this correlation, there appear to be two branches in the line shift vs. EW relations shown in Fig. 3.15, which are, however, due to the fact that our line selection was such that fewer lines of intermediate EP were included; most of our Fe I lines have either EP $\simeq 2.5$ eV or EP $\simeq 4.5$ eV. If our line selection would have resulted in a more uniform EP distribution, the two branches would be merged and, therefore, the fits to the two branches shown in Fig. 3.15 (and also Fig. 3.17 and Figs. 3.33 to 3.43) roughly represent the upper and lower limits of the theoretical line shift vs. EW relation.

The effect of the projected rotational velocity on the line shift vs. EW relation is shown in Fig. 3.17. As we showed in Figs. 3.8 and 3.9, the convective blueshift is strengthened for larger $V \sin i$ values (the "rotation effect") but the

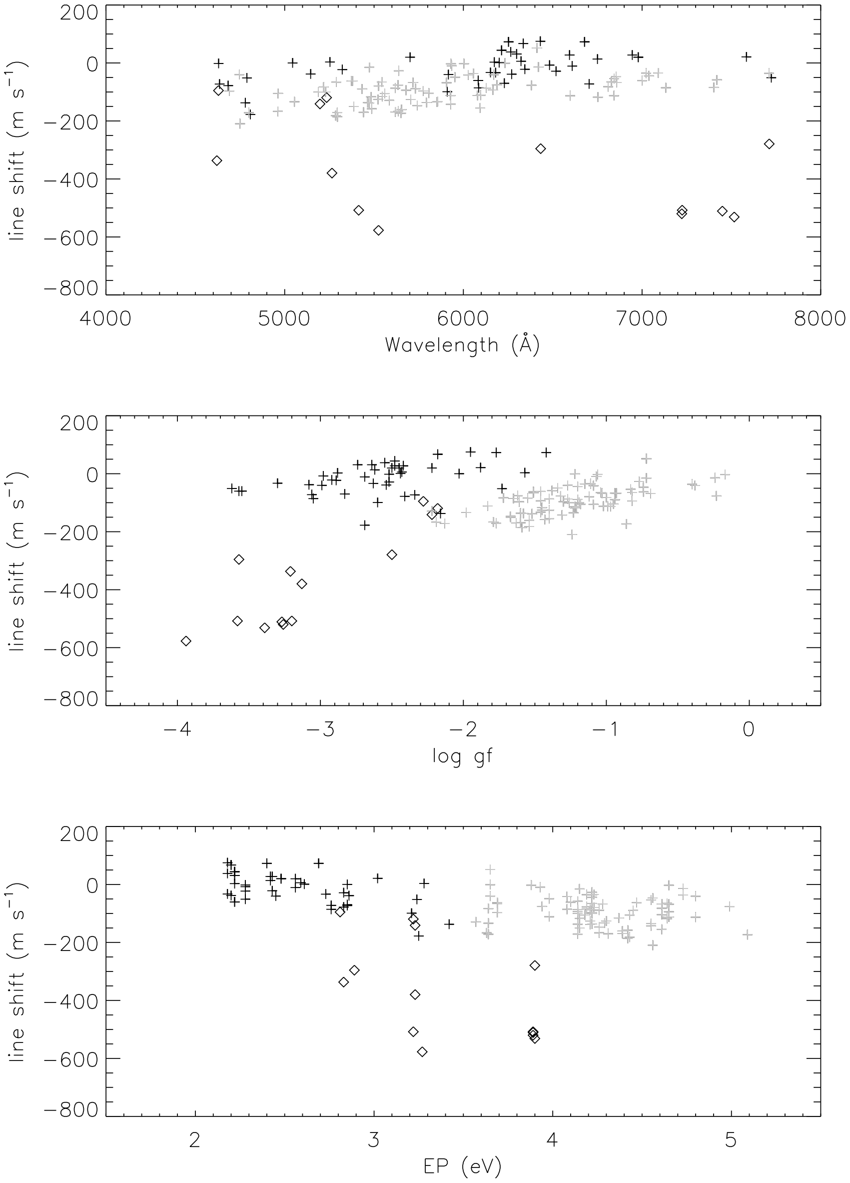

Figure 3.16: Relation between the theoretical line shifts shown in Fig. 3.15 and the spectral line properties: wavelength, $\log gf$ (transition probability), and EP (excitation potential of the lower level of the transition). Symbols are the same as in Fig. 3.15. The line shifts are those derived for $V \sin i = 0$ and only lines computed for one of the $\log gf$ values (the laboratory one) are shown.

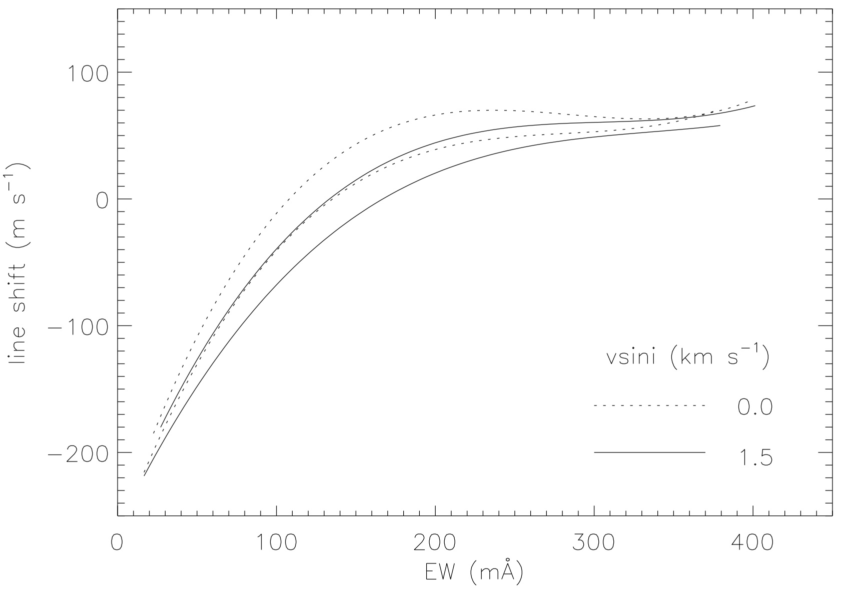

Figure 3.17: Comparison of the theoretical mean line shift vs. equivalent width relations shown in Fig. 3.15. The two relations shown for each $V \sin i$ value correspond to the two EP groups of Fig. 3.16.

slope in the line shift vs. EW relation remains nearly unchanged, in particular for EW $<$ 200 mÅ.

Interestingly, for the strongest lines, the model predicts a convective *redshift* of about 70 m s^{-1}, which suggests a reversal of the granulation pattern; i.e., at the highest atmospheric layers, the contribution to the light from cool downflows dominate. This result, however, is somewhat counterintuitive. The correlation between velocity and intensity fields decreases as one reaches higher atmospheric layers and, therefore, one would expect the net central wavelength shift of the strongest lines to be nearly zero. Even if the granulation pattern is reversed in some photospheric layer, we would expect the redshift to decrease shortly after, provided we continue probing higher layers with stronger absorption lines. A hint of this effect is shown in Figs. 3.15 and 3.17 for the non-rotation ($V \sin i = 0$) model, where at EW $\simeq$ 200 mÅ the line shift, which is already a redshift, seems to start decreasing for larger EW values. However, the line shifts do not return to zero but, instead, define a plateau at about 70 m s^{-1} and even seem to continue increasing for the largest EW values. Similar convective redshifts were predicted for the solar case but they are not supported by the observations, which suggests that this is an artifact of the limited numerical resolution or it is due to deficiencies in the modeling of the outer boundary (Asplund et al. 2000b). In addition, the effects of an active chromosphere and non-LTE, which are not taken into account in our 3D model, may become very important in these outer layers.

We estimated the depth of formation for all the spectral lines used to determine the theoretical line shifts and bisectors using the response function $\mathcal{R}$, which is defined as:

$$\mathcal{R}(\log \tau) = \frac{|\mathrm{EW}^{(1)} - \mathrm{EW}|}{\mathrm{EW}} \ , \tag{3.8}$$

where τ is the Rosseland optical depth, EW the equivalent width computed from an unperturbed model atmosphere and $\mathrm{EW}^{(1)}$ the equivalent width of the same line computed with a model atmosphere that has been modified at the optical depth τ with a temperature perturbation of 5 K. The average depth of formation ($< \log \tau >$) and its extent ($\Delta \log \tau$) are then obtained from:

$$< \log \tau >= \frac{\int \log \tau \mathcal{R} \ d \log \tau}{\int \mathcal{R} \ d \log \tau} \ , \tag{3.9}$$

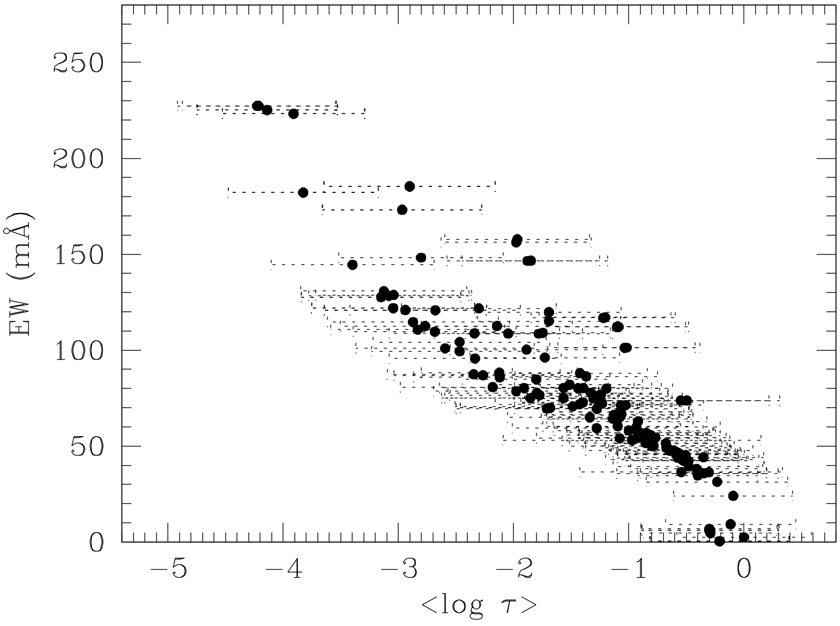

Figure 3.18: Average depth of absorption line formation as a function of equivalent width for the iron lines used in this work.

$$(\Delta \log \tau)^2 = \frac{\int (\log \tau - < \log \tau >)^2 \mathcal{R} \; d \log \tau}{\int \mathcal{R} \; d \log \tau} \; . \tag{3.10}$$

Although it has been claimed that a proper calculation of absorption line formation depths should be done using contribution functions (e.g., Magain 1986, Achmad et al. 1991), our approach provides good first order approximations. In any case, the line formation depth is ill defined, given that lines form over a wide range of photospheric layers (Sanchez Almeida et al. 1996). For practical reasons, we used a Kurucz 1D model atmosphere for these calculations. The layers affected by the uncertainties that produce the apparently incorrect convective redshifts are those for which $\log \tau < -3$, which roughly correspond to lines of EW > 150 mÅ (Fig. 3.18).

3.2 Measurement of the granulation signatures

Since spectral line profiles are affected by extrinsic broadening sources whose effects are not negligible for the purposes of this thesis, namely finite resolving power of the spectrograph and stellar rotation, which affect the accurate measurements of line bisectors and wavelength shifts (Sect. 3.1.3); it is important to first quantify the magnitude of this external broadening in our data. We dealt with the spectral resolution issue in Sect. 2.5. The measurements of stellar rotation are summarized below.

Most of our sample stars have one or more entries in The Catalog of Stellar Projected Rotational Velocities (Glebocki et al. 2000), which is a compilation of $V \sin i$ values available in the literature and, therefore, determined using a number of different techniques such as Fourier transform of line-profile (FTPL), cross-correlation (C-C), calibrated line-width at half maximum (FWHM), and convolution with calculated rotational broadening (Conv). Table 3.3 lists the values given in this catalog for our sample of K-dwarfs (the original references are also provided). Entries giving only upper or lower limits as well as very old and uncertain values have been excluded.

Using our observations, we determined $V \sin i$ values using the FWHM method adopted by Fekel (1997). Note that, strictly speaking, this method requires a set of calibrating stars, which we do not have due to the low number of stars in our sample, and therefore we adopted Fekel's calibrated relation between measured FWHM and total broadening (given in his Sect. 3). To determine the rotational FWHM in our spectra we first measured the FWHM

Object	$V \sin i$ (km s^{-1})	Technique	Reference
HIP 96100	0.6 ± 0.8	FWHM	Fekel (1997)
	0.8 ± 0.4	FTLP	Gray (1984)
	1.1 ± 0.6	FWHM	TW
HIP 26779	4.0 ± 0.6	C-C	Gaidos et al. (2000)
	3.0 ± 0.6	FWHM	TW
ϵ Eri	1.5 ± 2.0	C-C	Benz & Mayor (1984)
	2.0 ± 0.8	FWHM	Fekel (1997)
	2.2 ± 0.4	FTLP	Gray (1984)
	1.7 ± 0.3	Conv	Saar & Osten (1997)
	1.4 ± 1.0	Conv	Saar & Osten (1997)
	1.0 ± 0.5	FTLP	Smith (1983)
	2.5 ± 1.3	C-C	Tokovinin (1992)
	2.5 ± 0.7	FWHM	TW
HIP 88601	3.1 ± 0.8	FWHM	Fekel (1997)
	3.3 ± 1.0	FTLP	Smith (1978)
	1.6 ± 0.4	FTLP	Gray (1984)
	2.5 ± 0.6	FWHM	TW
HIP 64797	3.9 ± 0.8	FWHM	Fekel (1997)
	2.8 ± 0.6	Conv	Hale (1994)
	2.5 ± 0.7	FWHM	TW
HIP 37349	2.2 ± 0.7	FWHM	TW
HIP 86400	2.6 ± 2.0	C-C	Benz & Mayor (1984)
	1.7 ± 0.7	FWHM	TW
	1.6 ± 0.2	Conv*	TW
HIP 114622	2.1 ± 0.8	FWHM	Fekel (1997)
	1.8 ± 0.6	FWHM	TW
HIP 23311	0.8 ± 0.8	Conv	Saar & Osten (1997)
	1.4 ± 1.8	C-C	Tokovinin (1992)
	2.1 ± 0.8	FWHM	TW

Table 3.3: $V \sin i$ values reported in the literature for our K-dwarf sample stars. Values determined in this work (TW) are also given, in particular that for HIP 86400 (*), which was determined using our 3D model (Table 3.4 and Fig. 3.19). See text for details.

values of all lines in the Ramírez et al. (2007) Fe I line list with $\lambda > 5600$ Å, and determined the mean total FWHM. Then we subtracted in quadrature the instrumental profile, as measured by the local resolving power (Sect. 2.5), and a macroturbulent velocity of 2.5 km s^{-1} typical of K-dwarfs (the same value was adopted by Fekel 1997). The results of this calculation are also shown in Table 3.3.

By convolving the line profiles predicted by the 3D model with projected rotational velocity profiles, as described in Sect. 3.1.3, we determined a more accurate $V \sin i$ value for HIP 86400. We did not perform similar calculations for the other sample stars because the strength and FWHM of the line profiles are very sensitive to the stellar parameters, in particular effective temperature, and only HIP 86400 has parameters identical (within observational errors) to those of the 3D model atmosphere.

We selected 14 of the "cleanest" iron lines available in the HIP 86400 spectrum and computed the difference between observed and predicted profile around ±0.15 Å of the line center using only two free parameters, namely the $\log gf$ value (or, equivalently, iron abundance) and $V \sin i$. By minimizing the difference between observed and predicted profiles, using a χ^2-like scheme, we determined the $V \sin i$ value of HIP 86400. No additional broadening, in particular microturbulence or macroturbulence, was necessary to accurately fit the observed line profiles. The results of this calculation are given in Table 3.4 and two of the best fits to the data are illustrated in Fig. 3.19. The average of the $V \sin i$ values listed in Table 3.4, weighted by the quality of each fit

λ (Å)	$V \sin i$ (km s^{-1})	A(Fe)	ξ^2
5560.21	1.0	7.45	0.0053227
5638.26	1.8	7.50	0.0083912
5793.92	1.1	7.45	0.0047272
5856.09	1.8	7.45	0.0057782
6082.71	1.1	7.35	0.0069980
6096.67	1.6	7.55	0.0038083
6151.62	1.6	7.40	0.0056212
6173.34	2.0	7.50	0.0125232
6187.99	1.7	7.55	0.0032741
6200.31	1.7	7.55	0.0058648
6270.23	1.6	7.40	0.0015095
6703.57	1.6	7.55	0.0071746
6750.15	1.6	7.45	0.0123300
6945.21	2.0	7.35	0.0170028
Average	1.57 ± 0.20	7.44 ± 0.06	$\cdots$

Table 3.4: Projected rotational velocity ($V \sin i$) of HIP 86400 determined from fits to observed line profiles with rotationally broadened 3D model predictions. The last column gives the total difference between predicted (th) and observed (obs) profiles, $\xi^2 = \sum (f_{\rm th} - f_{\rm obs})^2$ in the inner ± 0.15 Å from the line center.

(as quantified by the ξ^2 parameter given in Table 3.4), is $V \sin i = 1.57 \pm 0.20$ km s^{-1}.

3.2.1 Line bisectors

Using the processed spectra of our sample stars (Chapter 2), we measured the bisectors of a large number of spectral lines listed in the Nave et al. (1994) multiplet table for Fe I. In our available spectral range ($5580 < \lambda < 7800$ Å), Nave et al. list about 900 lines, most of which are weak or blended. For each spectrum, we examined the neighboring ± 1 Å of all ~ 900

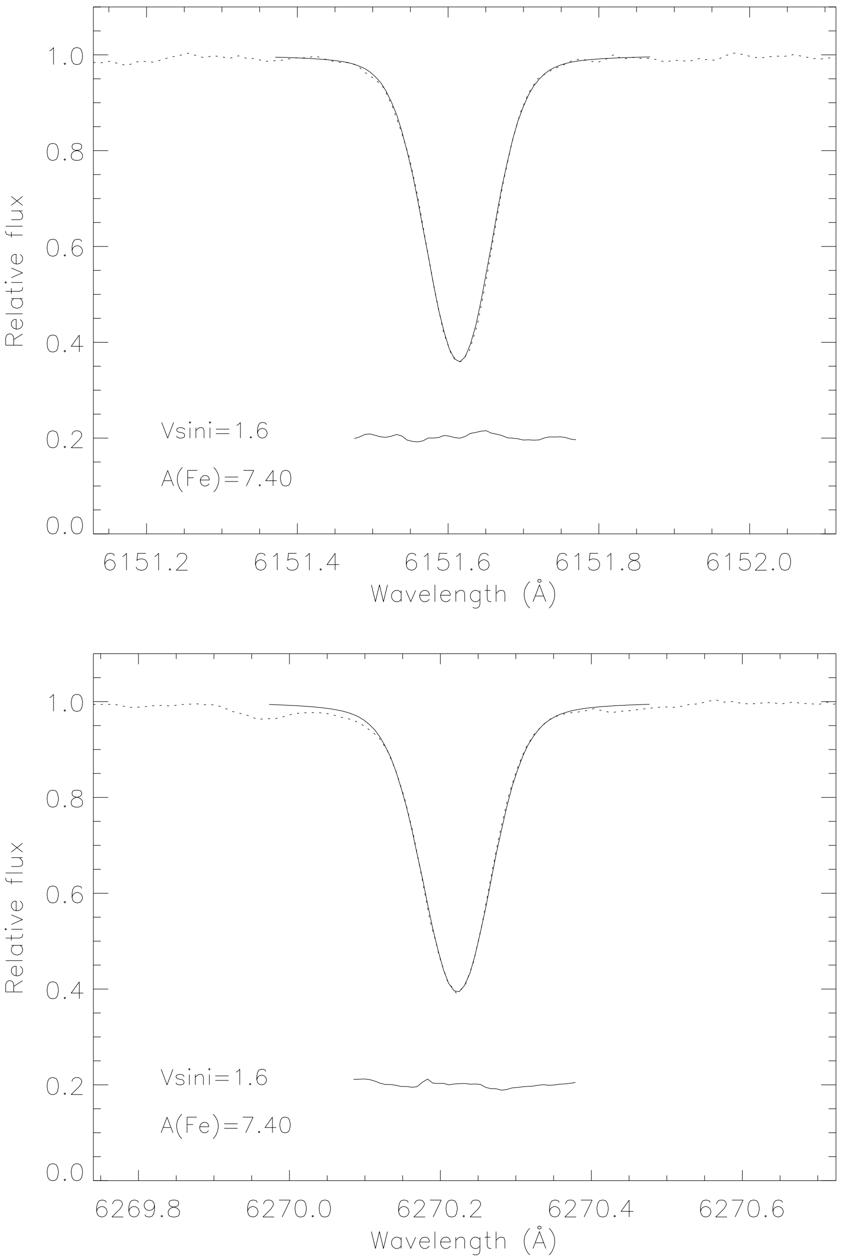

Figure 3.19: Minimum χ^2 model fits (solid lines) to the observed line profiles (dotted lines) in our HIP 86400 spectrum. Residuals around ±0.15 Å of the line center are shown at 0.2 relative flux.

Fe I lines mentioned above and attempted to measure their line bisectors. Very weak lines with minimum normalized flux values above 0.98 were immediately discarded because, for the purposes of this thesis, they are severely affected by blends and noise, even in the spectra with the largest S/N ratios. Spectral lines in regions where the local S/N was below 200 (as estimated from the total number of counts in the local continuum) were also discarded, except for HIP 37349, which has $S/N \sim 100$ everywhere.

The line bisectors were measured by determining, via interpolation, isoflux wavelength (or velocity) points on each wing of the line, after resampling the original profiles to a constant wavelength step of 0.005 Å using cubic spline interpolations. The error bars were obtained by propagating the observational errors of our spectra, as quantified by the local continuum signal-to-noise ratio. Hereafter, the line bisectors are measured with respect to the central wavelength of the line, i.e., the base of the bisectors will always be at zero velocity. The measurement of convective blueshifts is discussed separately in Sect. 3.2.2.

The large number of metallic lines observed in K-dwarfs suggests that many of the Fe I lines given in the Nave et al. catalog are blended in the observed stellar spectra. In many cases the blends will be clearly distinguishable by visual inspection and a line selection could be made in this manner. However, even weak line blends can significantly distort the shape of the line bisectors, and, given that the line asymmetries are very small in K-dwarfs, these blends should be avoided using a different approach. One may be tempted to look at the bisectors as they are being calculated for each line, and keep only those that have the "correct" shape. Of course, the problem with this approach is that we do not know a priori what this correct shape is. Although we expect the bisectors to have a characteristic C-shape, choosing from lines whose bisectors have that particular property may hide some other important effects that could also introduce asymmetry, or perhaps attenuate it.

Thus, instead of selecting subjectively spectral lines based on visual inspection of the line itself or its bisector, we adopted an automated scheme in which the *smoothness* of the line-bisector was used as evidence that the line is not blended. For each bisector measured, we computed the slope $d(\Delta v)/df$, with Δv being the abscissa values of the line bisector and f their corresponding normalized fluxes. Bisectors for which $d(\Delta v)/df > 200$ m s^{-1} per 0.02 normalized flux units were discarded. We stress here the fact that this procedure does not select bisectors based on their shape but discards those that are affected by an "external" component that could be a line blend, residual cosmic rays, or even unusually large noise at a given wavelength. Furthermore, the selection is symmetric; i.e., distortions to the bisectors originating from both sides of the spectral line are taken into account. Also, if distortions remain after the cleaning phase, they are expected to be symmetric; if very small blends, those for which $d(\Delta v)/df < 200$ m s^{-1} per 0.02 normalized flux units, remain, they will typically be on both sides of the spectral lines.

Even after this selection of smooth bisectors, the level of noise was relatively high, as expected for the typical signal-to-noise ratios of our observations, which are about 300 (Fig. 1.6). As was mentioned before in Sect. 3.1.3, the shape of the line bisector depends primarily on the line strength. The line-depth is a rough estimate of where in the stellar photosphere the spectral line is being formed and, therefore, features of similar line-depth are expected to have similar line bisectors. Thus, the noise in the bisectors can be reduced by averaging bisectors of spectral lines of similar strength. This is shown in Fig. 3.20 for the case of the star HIP 96100. Similar mean line bisectors were computed for all the stars in our sample and are shown in Figs. 3.21 to 3.31.

Typically between 50 and 100 lines were included in the calculation of the strongest mean line bisectors (depth between 0.2 and 0.4), between 100 and 150 lines for lines with depth between 0.4 and 0.6, and from about 100 to 200 for the weak mean line bisector (depth between 0.6 and 0.9). Thus, about 40% of the lines listed by Nave et al. survived our objective selection criteria. In the calculation of the mean line bisectors, we took into account the uncertainties associated with each individual bisector. Therefore, even though there are significantly discrepant line bisectors in Fig. 3.20, for example, their uncertainties are probably large and do not contribute significantly to the mean line bisector.

The line-to-line standard deviation from the mean line bisectors is about 50 m s^{-1} at mid flux values; it is very small at the minimum flux values and it increases as one approaches the continuum level, which is expected due to the impact of small blends and continuum noise. At the base, the mean bisectors have standard deviations of only about 10 m s^{-1}, while

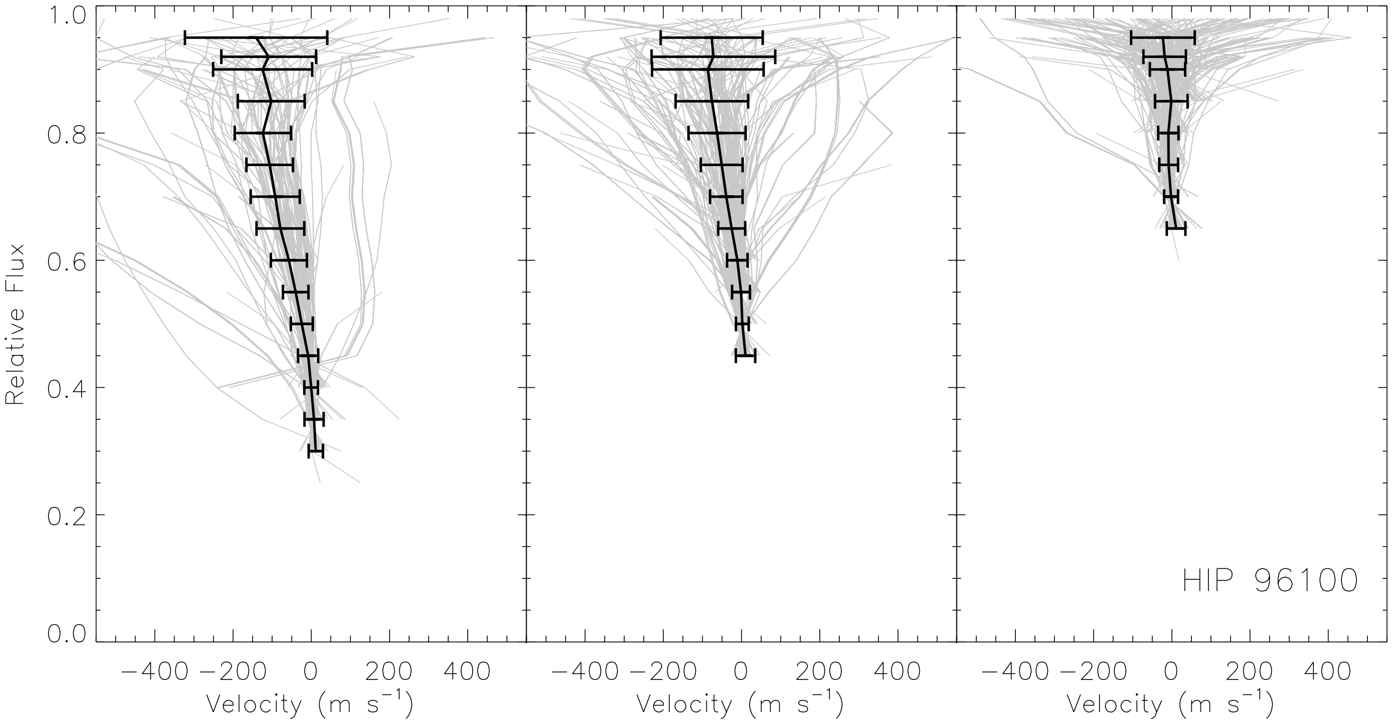

Figure 3.20: Mean bisectors for HIP 96100 (black solid lines with error bars) obtained from individual line bisectors (gray lines). The error bars correspond to a 1σ scatter.

near the continuum the scatter can be as large as 100–200 m s^{-1}. It is reasonable, although not strictly correct, to assume that the line bisectors of lines of similar strength are identical. In that case, the standard deviation (σ) is simply a measure of the noise and the actual measurement error of the mean line bisectors should be given as the standard error ($\sigma/\sqrt{n}$) of the n line bisectors used in each group. This is the reason why the error bars shown in Figs. 3.21 to 3.31 correspond to the standard error.

The mean theoretical line-bisectors, as computed with our 3D model (cf. Fig. 3.11), are also shown in Figs. 3.21 to 3.31 in gray. Note that these theoretical line bisectors include the effect of a projected rotational velocity of 1.5 km s^{-1} and an instrumental Gaussian profile corresponding to a spectral resolution $R = 180,000$, which are representative of the sample.

The basic observed shape of the bisectors, namely a C-shape for the weak line and a \(backslash)-shape for the strongest one, is well reproduced by the model. Quantitatively, however, there are measurable differences.

For example, the mean line bisectors for HIP 96100 (Fig. 3.21) are clearly larger than those predicted by the 3D model. There are three reasons that can possibly explain this. First, the star is almost 400 K hotter than the 3D model, second, its metallicity is lower than solar ([Fe/H] $= -0.22$), and, finally, its projected rotational velocity is the lowest among our sample stars ($V \sin i \simeq 0.9$ km s^{-1}). Note that the granulation effects, and in fact the absolute magnitude of the inhomogeneities, are predicted to increase with effective temperature (Sect. 3.1.1) and also with decreasing metallicity, although prob-

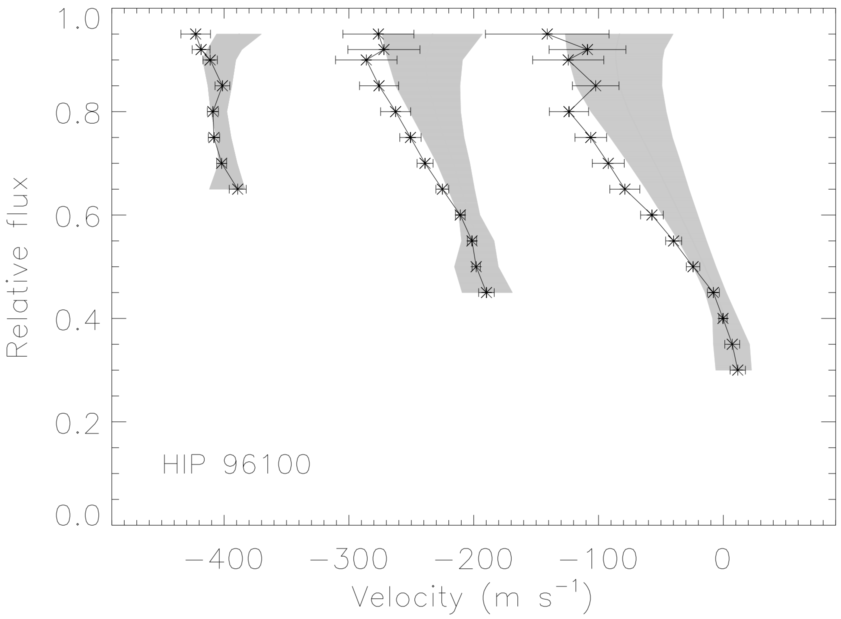

Figure 3.21: Mean line bisectors for HIP 96100. The shaded areas represent the 1σ extent of the 3D theoretical predictions for lines with similar strength (we adopted $V \sin i = 1.5$ km s^{-1} and $R = 180,000$ for their calculation). All line bisectors were measured with respect to their central wavelengths; shifts of -200 and -400 m s^{-1} have been applied here to the weaker lines for clarity. The error bars correspond to the standard error of the line-to-line scatter, i.e., $\sigma/\sqrt{n}$, where σ is the standard deviation and n the number of lines.

ably the latter effect is significantly smaller (e.g., Allende Prieto et al. 1999), while low projected rotational velocities ($V \sin i < 1$ km s^{-1}) were shown not to affect the shape of the line bisectors significantly (Fig. 3.8).

In this context, it is interesting to see the case of the next few hotter stars, HIP 26779, ϵ Eri, HIP 88601, HIP 64797, and HIP 37349, which are about 50–300 K warmer than the 3D model and yet do not show bisectors larger than the 3D model predictions (Figs. 3.29 to 3.24). In fact, in some

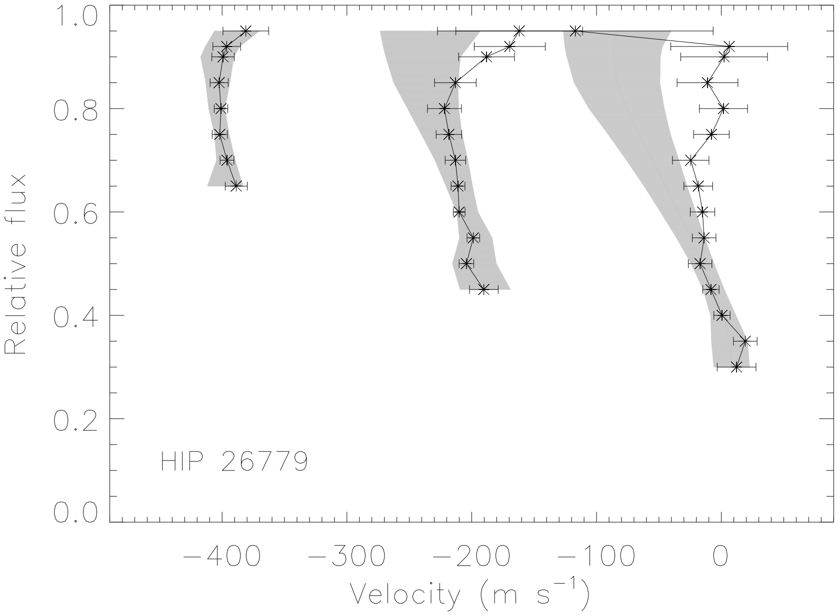

Figure 3.22: As in Fig. 3.21 for HIP 26779.

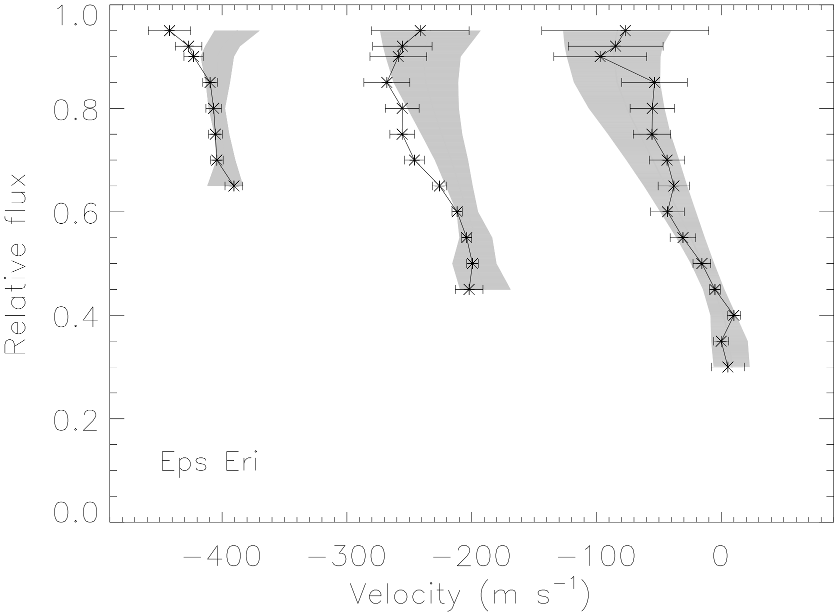

Figure 3.23: As in Fig. 3.21 for ϵ Eri.

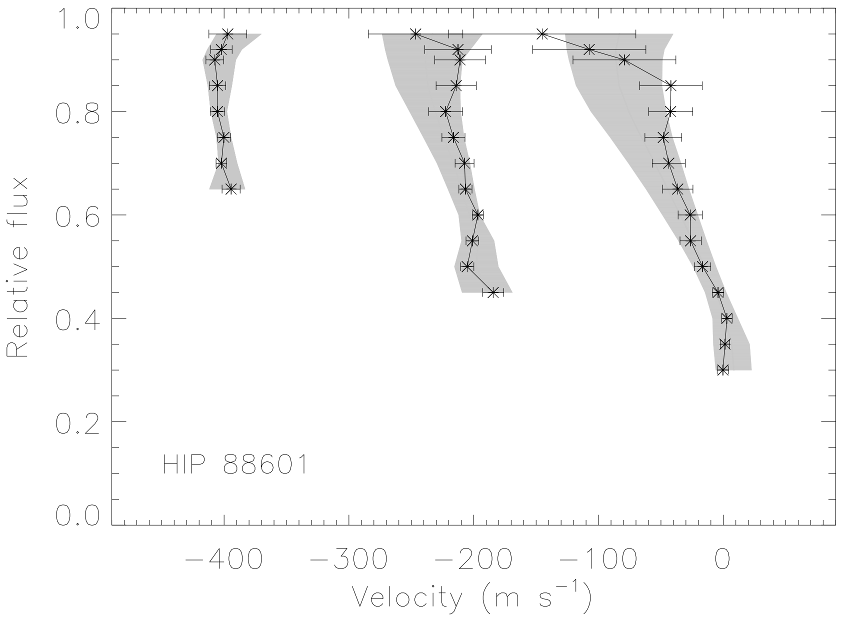

Figure 3.24: As in Fig. 3.21 for HIP 88601.

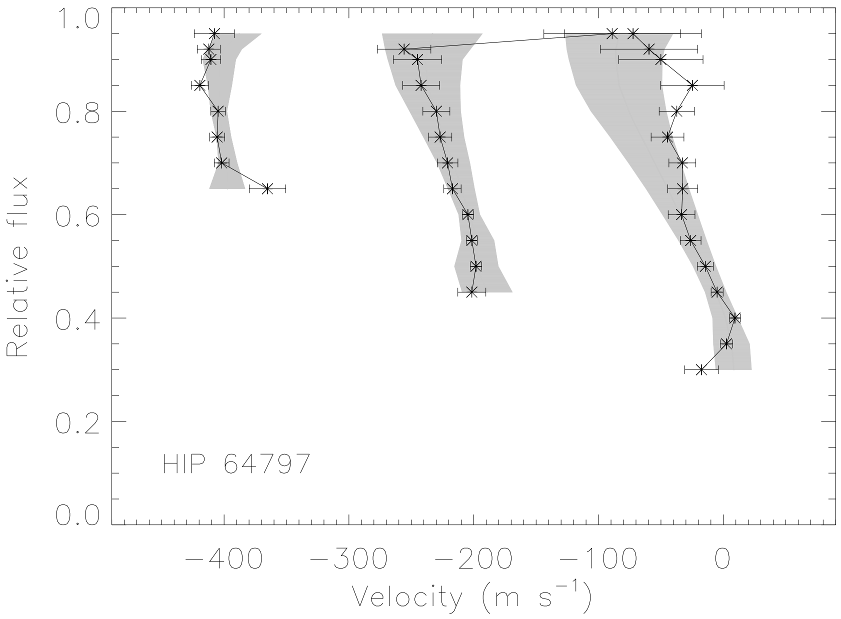

Figure 3.25: As in Fig. 3.21 for HIP 64797.

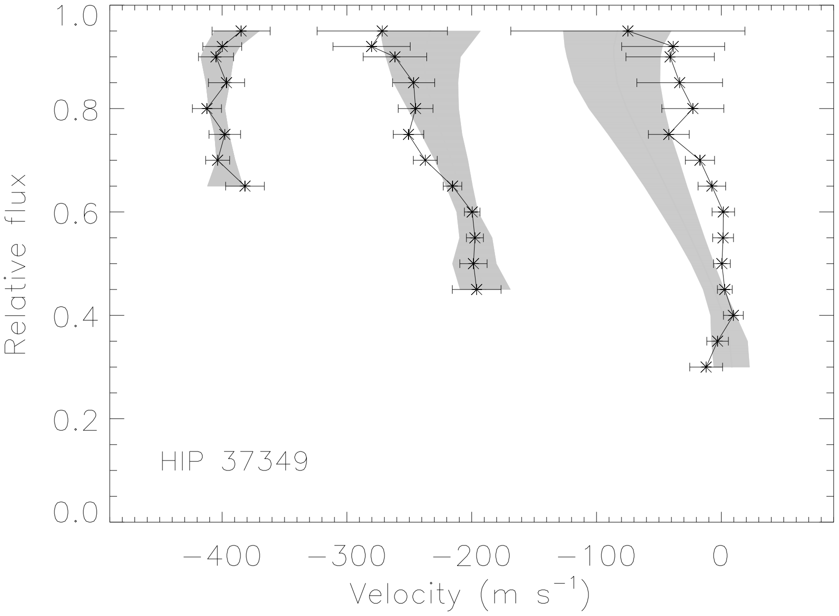

Figure 3.26: As in Fig. 3.21 for HIP 37349.

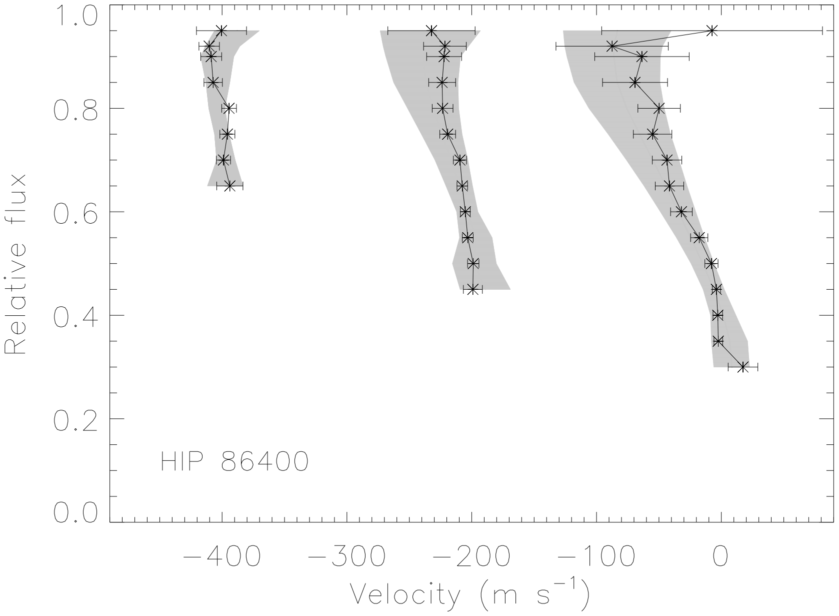

Figure 3.27: As in Fig. 3.21 for HIP 86400.

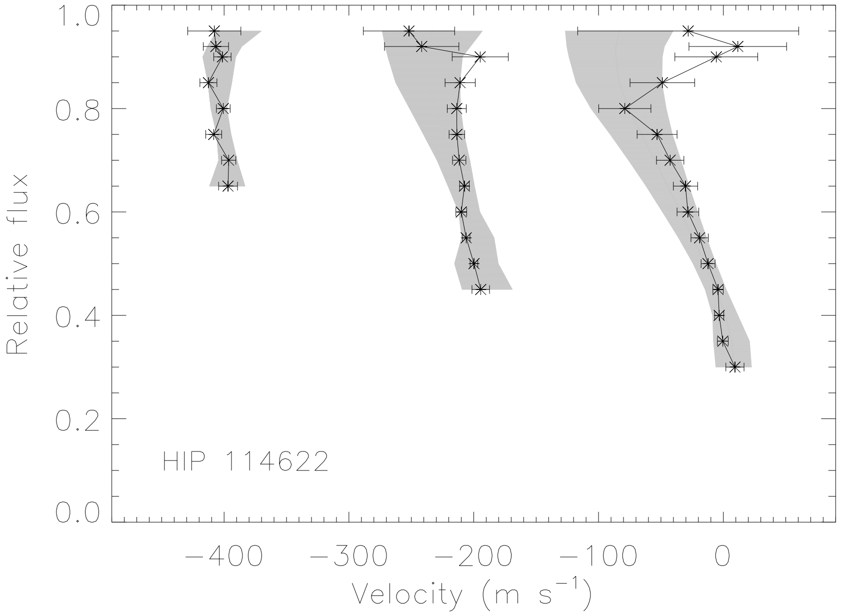

Figure 3.28: As in Fig. 3.21 for HIP 114622.

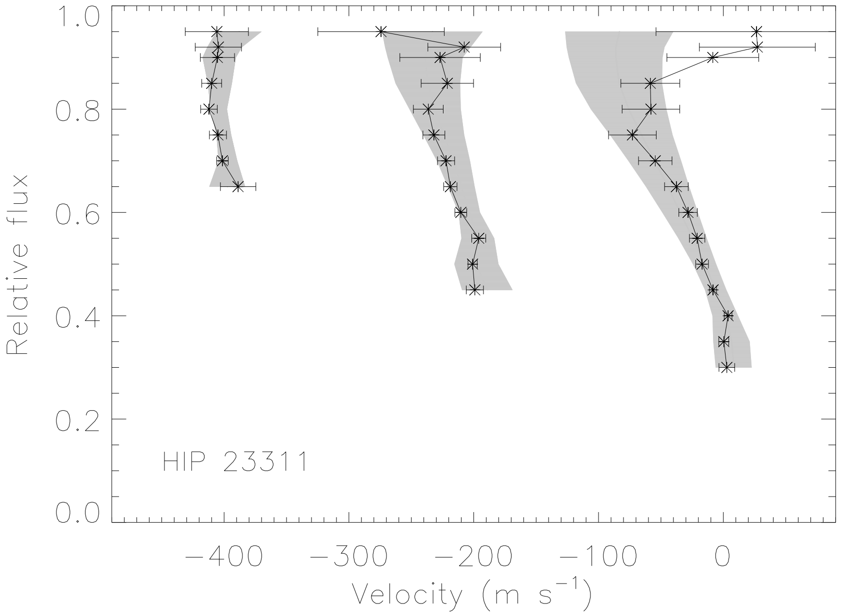

Figure 3.29: As in Fig. 3.21 for HIP 23311.

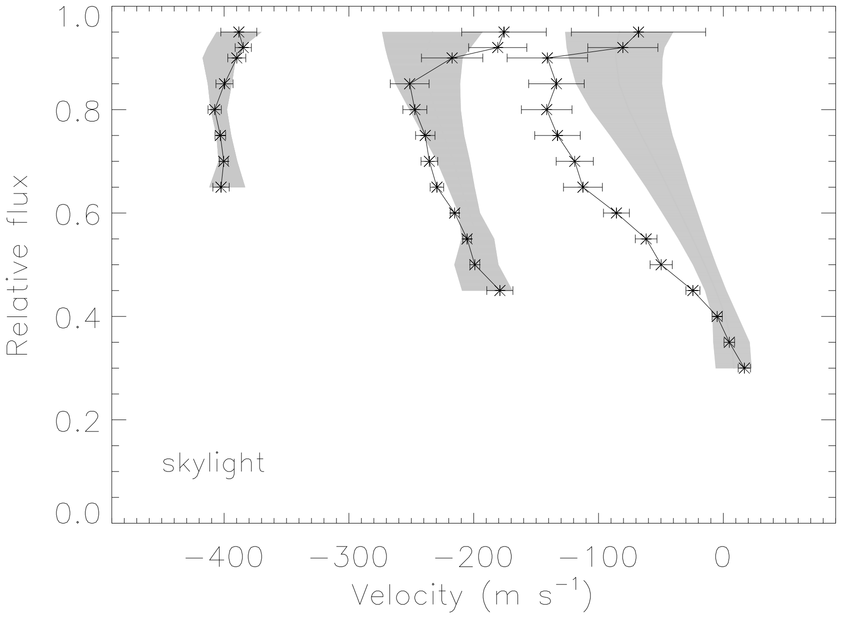

Figure 3.30: As in Fig. 3.21 for the skylight.

cases they are smaller. The reason for this is probably the large $V \sin i$ values of these stars (approximately between 2 and 3 km s^{-1}, see Table 3.3), which, as seen in Figs. 3.8 and 3.13, can reduce the extent of the line bisectors by up to 40%. We note here that the data for HIP 64797 and HIP 37349 are more noisy than the average. Most of the observations for HIP 64797 were made under poor weather conditions while the relative faintness of HIP 37349 only allowed us to reach $S/N \sim 100$.

In addition to the stellar rotation effect in the 5 stars mentioned above, it is also interesting to see that they show high levels of chromospheric activity (with the possible exception of HIP 88601), as evidenced by their Ca II H and K line profiles (Fig. 3.32). The H and K line observations shown in Fig. 3.32 have

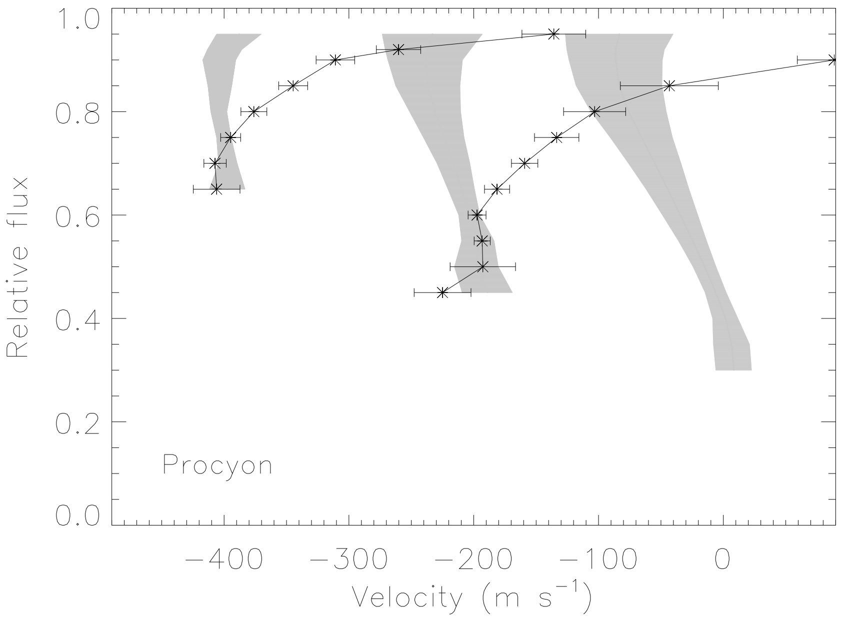

Figure 3.31: As in Fig. 3.21 for Procyon. Very strong lines were not available in the spectral range of our Procyon observations and therefore no observed mean line bisector of depth around 0.3 is shown.

been acquired from the spectroscopic survey of Allende Prieto et al. (2004), reducing the resolution of their spectra to about $R = 8,000$ for clarity in the illustration.

Chromospheric effects on spectral line formation have not been studied in enough detail yet as to quantitatively determine their impact on our line bisector measurements. Nevertheless, the fact that the signatures of granulation seem to be slightly modified in the most active stars in our sample suggests a casual correlation. An active chromosphere may have an impact on the line shapes and intensities in several ways. Emission may fill the cores of some lines, as it is obvious in the H and K lines, but it may be also present to a

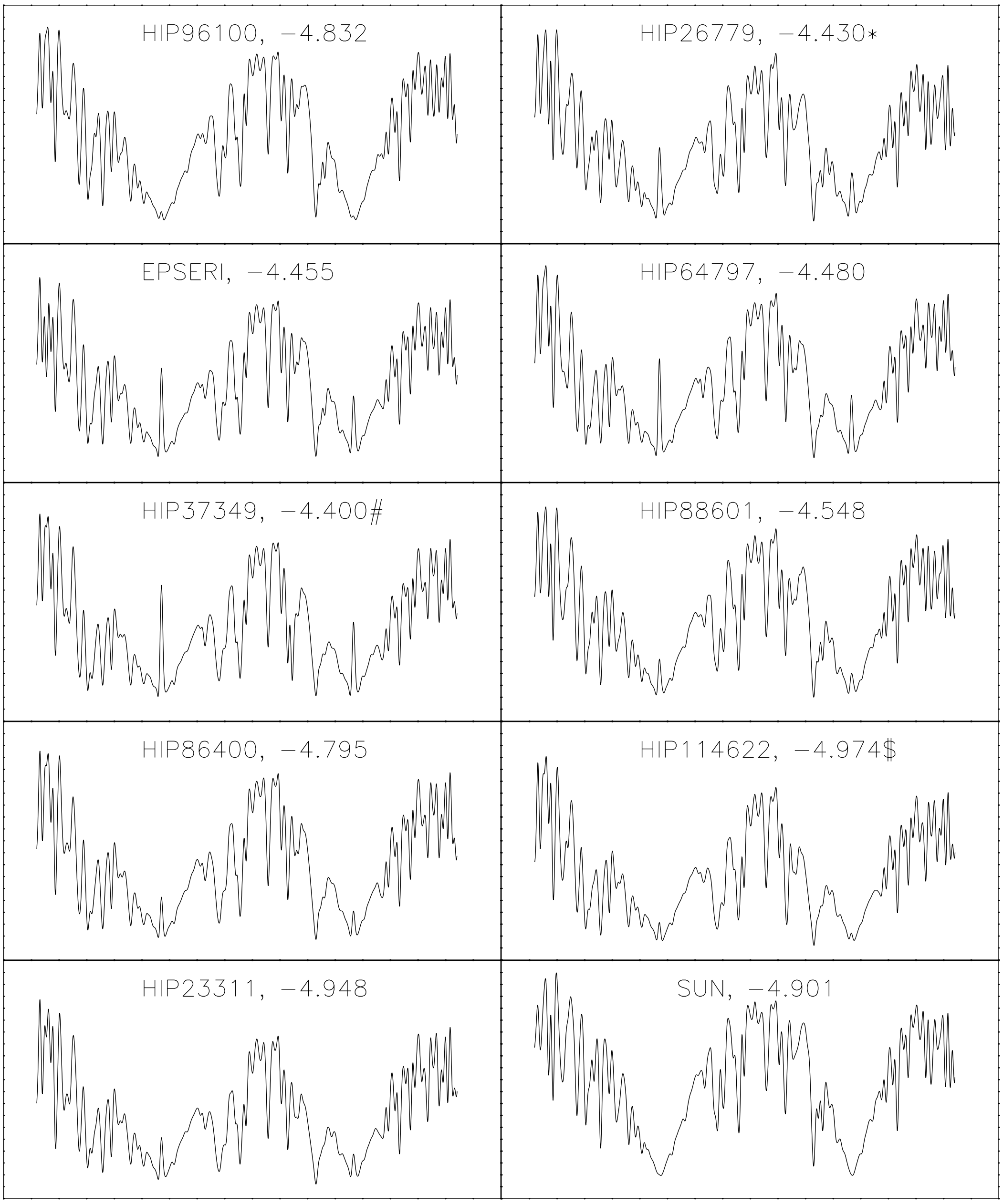

Figure 3.32: Medium resolution spectra of our K-dwarfs and the Sun in the region around the Ca II H and K lines ($3900\,\text{Å} < \lambda < 4000$ Å). The activity index $R'_{\rm HK}$ is shown in each panel, as given by Saar & Brandenburg (1999), except for the cases marked with the following symbols: [*] = Rocha Pinto & Maciel (1998a), [#] = King et al. (2003), [$] = Saar & Donahue (1997).

lesser extent in weaker lines. Zeeman splitting could be measurable due to the presence of strong magnetic fields (e.g., Gray 1984a, Borrero 2008), while magnetic pressure may have an impact on the photospheric structure. It is, therefore, tempting to conclude that the line bisectors (and therefore the line asymmetries) are weakened by the presence of strong magnetic fields and/or stellar activity.

HIP 86400 is our reference star because it has parameters very close to those adopted in the calculation of the 3D model atmosphere. A visual inspection of Fig. 3.27 shows already that the agreement between the observed and predicted mean line bisectors is remarkable. As we will see below (Table 3.5), the likelihood that the 3D model is reproducing the observations of HIP 86400 is about 95% if we use $V \sin i = 1.5$ km s^{-1}, which is approximately the correct projected rotational velocity of this star (Table 3.4). However, this number increases slightly for the $V \sin i = 2.0$ km s^{-1} calculations, which suggest that the line asymmetry is being weakened or that the 3D model is not predicting the correct magnitude of the granulation contrasts.

The coolest stars in our sample, HIP 114622 and HIP 23311, have both relatively low $V \sin i$ values ($\lesssim 2$ km s^{-1}, Table 3.3) and are only about 100 and 200 K cooler than our 3D model. Their spectra is richer in spectral lines compared to those of our other sample stars and this is perhaps the reason why their mean bisectors show large deviations from the theoretical expectation near the continuum (Figs. 3.28 and 3.29). In fact, the mean bisectors approach zero velocity there, which points to the influence of numerous blends randomly distributed on both sides of the spectral lines. Nonetheless, far from the continuum, the 3D model predictions agree quite well with the observations of these two cooler stars. Therefore, it is likely that the granulation contrast does not change significantly in dwarf stars of effective temperature between 4600 and 4800 K.

To make sure that our measurements of line asymmetries are not affected by observational or data processing artifacts, we obtained mean line bisectors in our skylight (Fig. 3.30) and Procyon (Fig. 3.31) spectra. The mean bisectors of the skylight have magnitudes larger than those predicted by the K-dwarf 3D model (expect perhaps for the weakest line). Note, however, that the skylight observations were significantly different than the stellar ones. Skylight enters the slit from a solar port located on the roof of the spectrograph room and the light fills the slit completely, thus occupying (each spectral order) several rows of the CCD detector. In principle, the orders should be aligned so that a vertical cut across it results in iso-wavelength pixels. In practice, the alignment is not perfect and blurring of the spectral line profiles may happen. Another source of error in these measurements can be attributed to scattering of light in the Earth's atmosphere (Gray 2000). In fact, solar line bisectors have been determined using the actual solar spectrum (e.g, Kurucz et al. 1984) by several authors (e.g., Dravins et al. 1981, Asplund et al. 2000b, Allende Prieto et al. 2002), who show that their amplitudes are about twice as large as those shown in Fig. 3.30. Note, however, that the Kurucz et al. atlas has a resolving power of 500,000.

The mean bisectors measured in the Procyon spectrum, however, are in excellent agreement with those measured elsewhere (e.g., Dravins 1987b, Allende Prieto et al. 2002). Note that the metallic lines in the spectrum of this hotter star are, in general, weaker than those observed in K-dwarfs and, in our spectral range, very few strong lines are available. This is the reason why Fig. 3.31 does not show the strongest mean line bisector.

To quantitatively asses the quality of the 3D model fits to the observed line bisectors, we used χ^2 statistics. For each star we determined

$$\chi^2 = \sum_{i=1}^{n_{\mathrm{bp}}} \frac{[(\Delta v)_{i,\mathrm{obs}} - (\Delta v)_{i,\mathrm{th}}]^2}{\sigma^2_{\mathrm{i,th}} + \sigma^2_{\mathrm{i,obs}}} \ , \tag{3.11}$$

where the Δv are the bisector abscissa values, observed (obs) and theoretical (th), whose uncertainties are given by the σ values, and n_{bp} is the number of bisector flux points. The probability that a given observed mean line bisector (of average line depth f) is equivalent to the theoretical bisector was then obtained from

$$p_f = 1 - \mathrm{PDF}(\chi^2, n_{\mathrm{bp}} - 1) \ , \tag{3.12}$$

where PDF is the probability distribution function of the χ^2 distribution (e.g., Abramowitz & Stegun 1972). Table 3.5 shows the results of this statistical test for three different values of $V \sin i$ adopted for the 3D model predictions. Procyon is not included there because it has zero probabilities in all cases.

The probability that the model corresponds to HIP 96100 is below 30% for the two larger $V \sin i$ values adopted but about 75% for $V \sin i =$ 1 km s^{-1}, thus strengthening our arguments given above that this star is too

	$V \sin i = 1.0$ km s^{-1}				
Object	$p_{0.30}$	$p_{0.45}$	$p_{0.65}$	$< p >$	Δp
HIP 96100	87	54	84	75	18
HIP 26779	0	25	86	37	44
ϵ Eri	92	35	33	53	33
HIP 88601	42	63	98	68	28
HIP 64797	6	30	96	44	46
HIP 37349	0	88	92	60	52
HIP 86400	59	77	66	67	8
HIP 114622	16	54	94	55	39
HIP 23311	13	79	99	64	45
skylight	0	46	57	34	30

	$V \sin i = 1.5$ km s^{-1}				
Object	$p_{0.30}$	$p_{0.45}$	$p_{0.65}$	$< p >$	Δp
HIP 96100	28	23	34	28	5
HIP 26779	0	35	96	43	48
ϵ Eri	99	29	3	44	49
HIP 88601	85	81	99	88	9
HIP 64797	20	50	9	26	21
HIP 37349	0	82	74	52	45
HIP 86400	93	99	70	87	15
HIP 114622	47	84	91	74	23
HIP 23311	32	97	90	73	35
skylight	0	23	62	28	31

	$V \sin i = 2.0$ km s^{-1}				
Object	$p_{0.30}$	$p_{0.45}$	$p_{0.65}$	$< p >$	Δp
HIP 96100	1	11	13	8	6
HIP 26779	8	55	93	52	42
ϵ Eri	99	13	0	37	53
HIP 88601	94	98	98	97	2
HIP 64797	30	40	1	24	20
HIP 37349	2	62	62	42	34
HIP 86400	96	99	77	91	12
HIP 114622	78	96	73	82	12
HIP 23311	54	94	61	69	21
skylight	0	16	64	27	33

Table 3.5: Probability (%) that the observed mean bisectors are equivalent to those predicted by the 3D model. Values for three average line depths are given, as well as their mean and standard deviation. The boxed entries correspond to our reference star, HIP 86400.

hot compared to the model and its projected rotational velocity is relatively small. For HIP 26779 and ϵ Eri, the probabilities are inconsistent between the three line depths given. For the latter, for example, the strongest line seems to fit very well the model predictions, in particular for large $V \sin i$ values, yet the other two make very poor matches to the theoretical expectation. On average these two stars have probabilities below or about 50%.

HIP 88601 is a very interesting case. For all three values of $V \sin i$, it shows probabilities above 50%, which are reasonably consistent between lines of different strength. Furthermore, the probability increases for larger $V \sin i$, as expected due to the relatively large projected rotational velocity of the star. In fact, considering its measured $V \sin i \simeq 2$ km s^{-1}, the likelihood that this star corresponds to the 3D model is about 97%. Note, however, that HIP 88601 is about 200 K hotter than the 3D model and so we would expect the magnitude of the line bisectors to be larger. Therefore, if we assume that the 3D model is realistic, some other effect has to be compensating for the difference.

The two stars with low quality observations, HIP 64797 and HIP 37349, show very low probabilities in Table 3.5. Until better data is acquired for these objects, it would be unwise to draw quantitative conclusions from this analysis.

Our reference star, HIP 86400, matches the 3D model predictions remarkably well, in particular for the higher $V \sin i$ values. Discarding the weakest line, which seems to be affected by noise and blends (the bisector looks almost vertical), the probability of this star being well represented by the

3D model is about 70%, 96%, and 98% for the $V \sin i = 1.0$, 1.5, and 2.0 cases, respectively (including the weak line reduces these numbers by about 8% each). Since the measured projected rotational velocity of this star is $V \sin i = 1.57 \pm 0.20$ km s^{-1} (Table 3.3) and the best fit to the measured line bisectors occurs at higher projected rotational velocities, it is possible that there are effects beyond granulation that make the line profile more symmetric or that the 3D model predicts too small granulation intensity and velocity contrasts.

For the two coolest K-dwarfs of our sample, HIP 114622 and HIP 23311, the probabilities are generally above 50%. This may confirm our hypothesis that the granulation effects on line profiles do not change significantly between effective temperatures of 4600 and 4800 K.

Finally, the agreement between the 3D K-dwarf model predictions and the observations of the skylight spectrum is very poor, as expected, with a probability of about 30% or lower. In fact, the corresponding probability for the strongest line is 0.

3.2.2 Wavelength shifts

The second fundamental test of granulation signatures in stellar spectra involves measuring central wavelength shifts (Sect. 1.4). A large convective blueshift is expected to occur for the weakest lines, which are formed in deep layers and see strong granulation contrasts, while the cores of strong lines are expected to be nearly unshifted given that they form in the highest photospheric layers, where the correlation between intensity and velocity fields is weak. We should therefore look at the relation between line shift and line strength (quantified by the line equivalent width) to determine the magnitude of the granulation effects and compare them to the model predictions.

Unfortunately, there are large uncertainties in the determination of the line shifts from our observed spectra, some of which are independent of the quality of the data. For example, very accurate laboratory wavelengths for large numbers of spectral features are necessary. The catalog by Nave et al. (1994) is perhaps one of the most accurate and complete line lists currently available for this purpose. Nevertheless, the central wavelengths measured by them, in the best cases, have uncertainties of about 75 m s^{-1}.

A second uncertainty is that related to the gravitational redshift, which depends on the stellar mass to radius ratio (Sect. 1.3, Eq. 1.7). However, this is a systematic uncertainty and will only affect the absolute values of the line shifts but not the relative ones. Therefore, if we relax the constraint on the absolute line shifts and concentrate only on the relative differences, this uncertainty can be avoided. This is a particularly useful assumption given that the absolute radial velocities of our sample stars are not known with enough accuracy to take this effect into account (see, however, Sect. 4.4).

We measured the central wavelengths of as many Fe I lines as possible included in the Nave et al. (1994) catalog. We restricted our measurements to only those lines that wavelengths measured with uncertainties below 75 m s^{-1}. The central wavelengths were obtained by fitting fourth order polynomials to the 11 points closest to the flux minimum. Tests were made with third order polynomials and 7 to 15 points but the results were not significantly different.

Since the wavelength shifts in the solar spectrum have been measured with great accuracy (e.g., Allende Prieto & García López 1998) and the convective blueshift vs. equivalent width relation is well defined there, we used our results for the skylight spectrum to perform a line selection. Only those lines for which the convective blueshifts were between 2σ of the mean line shift vs. equivalent width trend were used. Statistically, this selection reduces the impact of line blends and misidentifications.

As stated above, our measured line shifts could be systematically displaced with respect to their absolute values due to the gravitational redshift and the uncertainty in the absolute stellar radial velocity. Thus, we adopted an arbitrary zero point using the central wavelength shifts of the strongest lines. Basically, the mean line shift of the strongest lines was set to zero. A more detailed description will be given below.

The line shift vs. equivalent width relations for our sample stars are shown in Figs. 3.33 to 3.43, along with the model predictions, for which we adopted $R = 180,000$ and $V \sin i = 1.5$ km s^{-1}. In each panel, we show the individual line shifts as well as averaged values in bins of equivalent width (the filled circles with error bars in Figs. 3.33 to 3.43) to allow a better visualization given the large scatter observed. The bins have a width of 10 mÅ below EW $= 100\,$mÅ and 35 mÅ above it. When the number of data points per bin is lower than 3, the bin-averaged values are not shown.

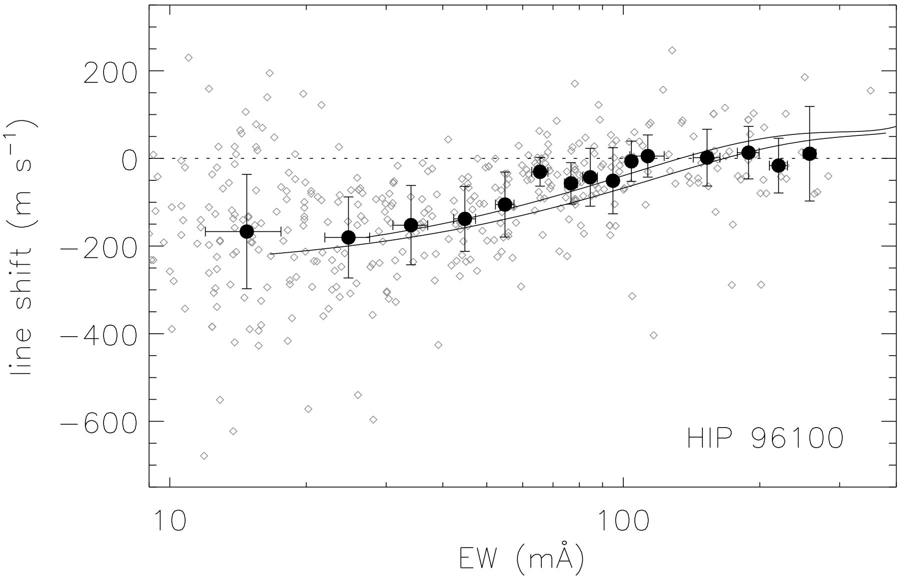

Figure 3.33: Central wavelength shifts measured in the HIP 96100 spectrum as a function of line equivalent width (small diamonds). The filled circles with error bars represent average values in bins of equivalent width. The zero point of this relation has been set using the strongest lines, those that define the plateau (see text for details). The solid lines correspond to the predictions of the 3D model (cf. Fig 3.15) assuming $R = 180,000$ and $V \sin i = 1.5$ km s^{-1}. Note that the x-axis scale is logarithmic. The dotted line corresponds to zero line-shift, which is calibrated using the strongest lines (see text for details).

The basic signature of granulation is evident in all cases. The strongest lines show the smallest blueshifts while weaker lines are significantly blueshifted. Furthermore, the slope in the line shift vs. equivalent width relation is larger for the skylight compared to the K-dwarf observations and probably even larger for Procyon, although the scatter for the latter is large and there is not enough line strength coverage to draw in reasonably well the actual form of the trend.

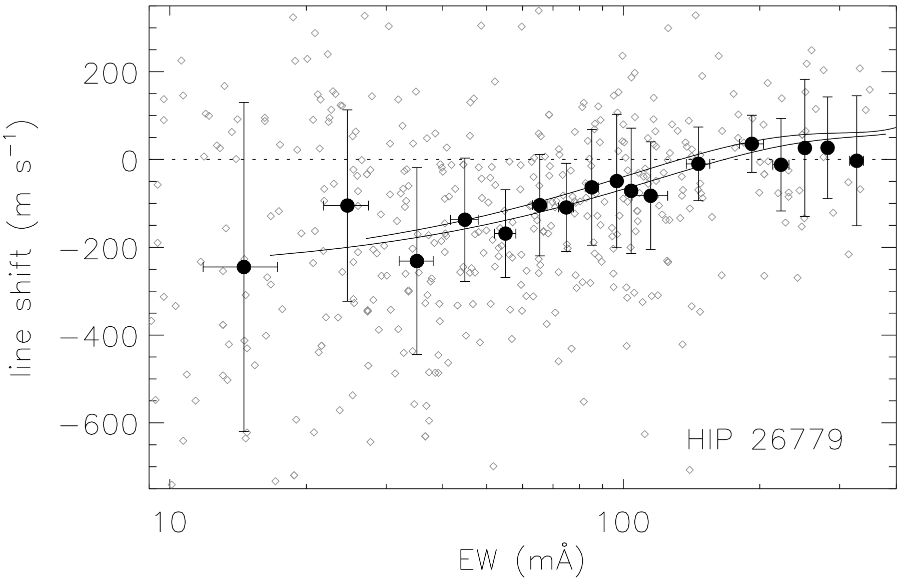

Figure 3.34: As in Fig. 3.33 for HIP 26779.

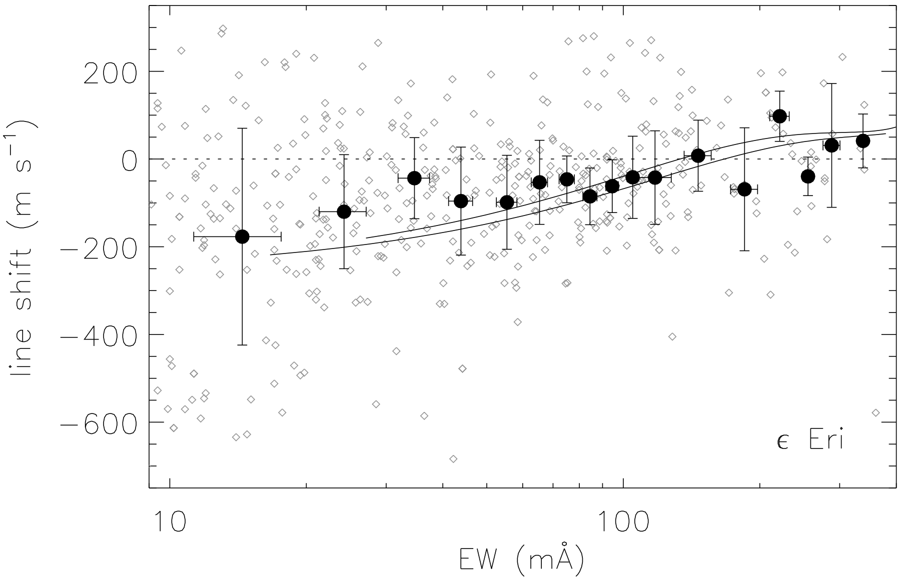

Figure 3.35: As in Fig. 3.33 for ϵ Eri.

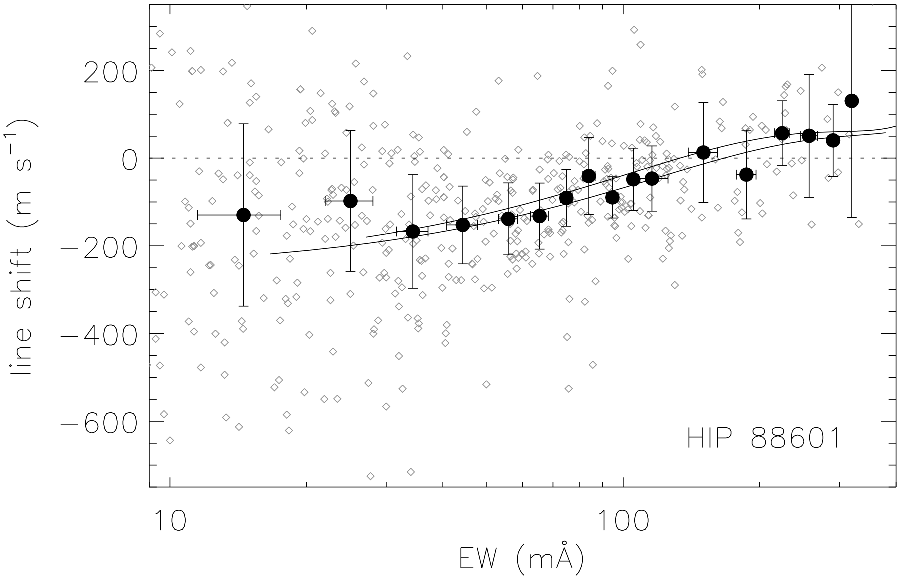

Figure 3.36: As in Fig. 3.33 for HIP 88601.

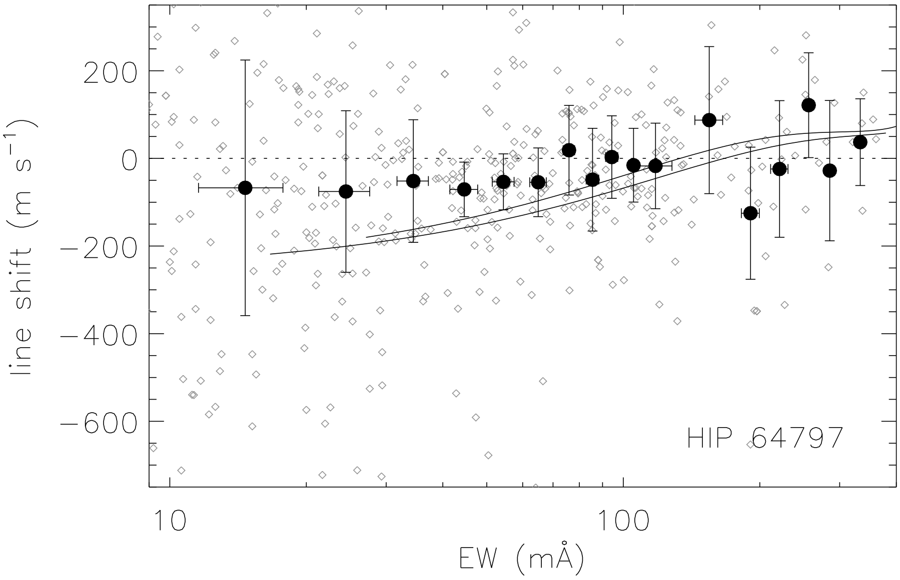

Figure 3.37: As in Fig. 3.33 for HIP 64797.

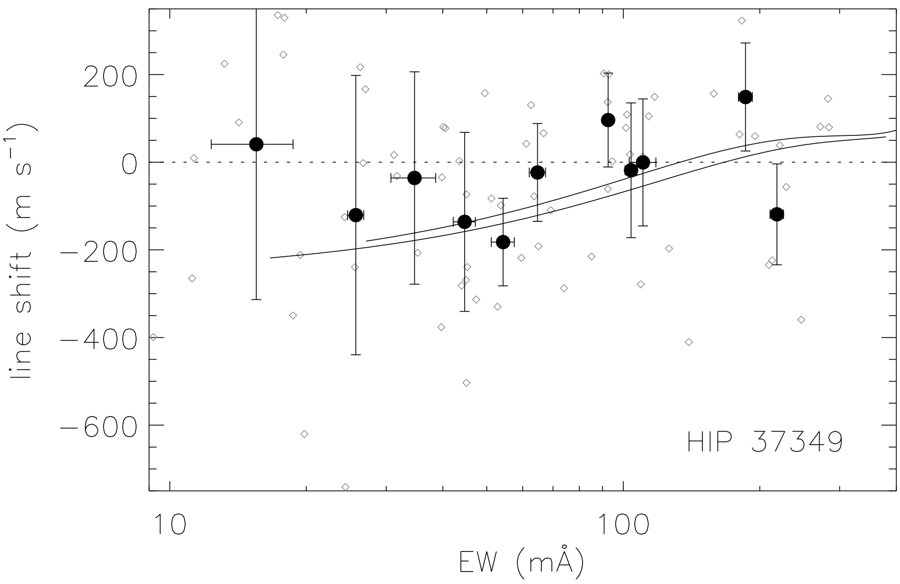

Figure 3.38: As in Fig. 3.33 for HIP 37349.

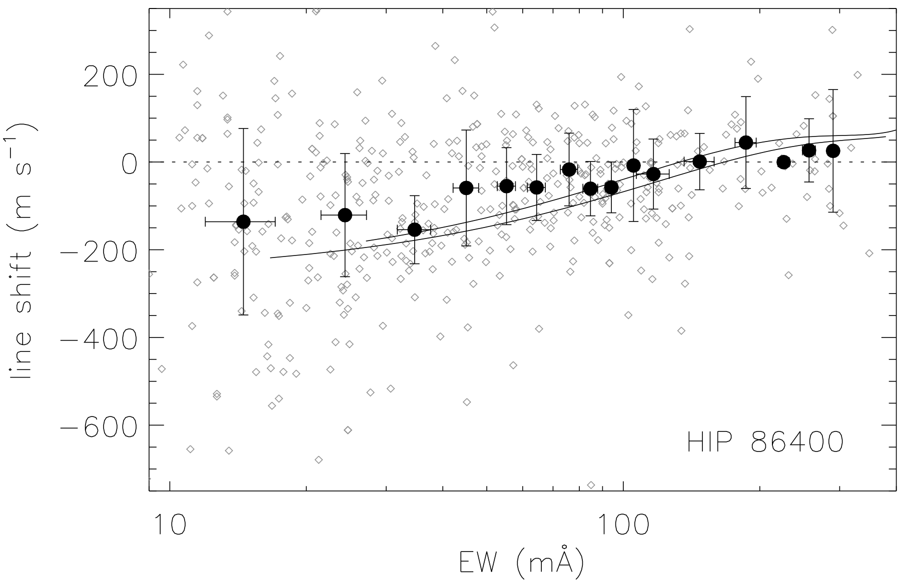

Figure 3.39: As in Fig. 3.33 for HIP 86400.

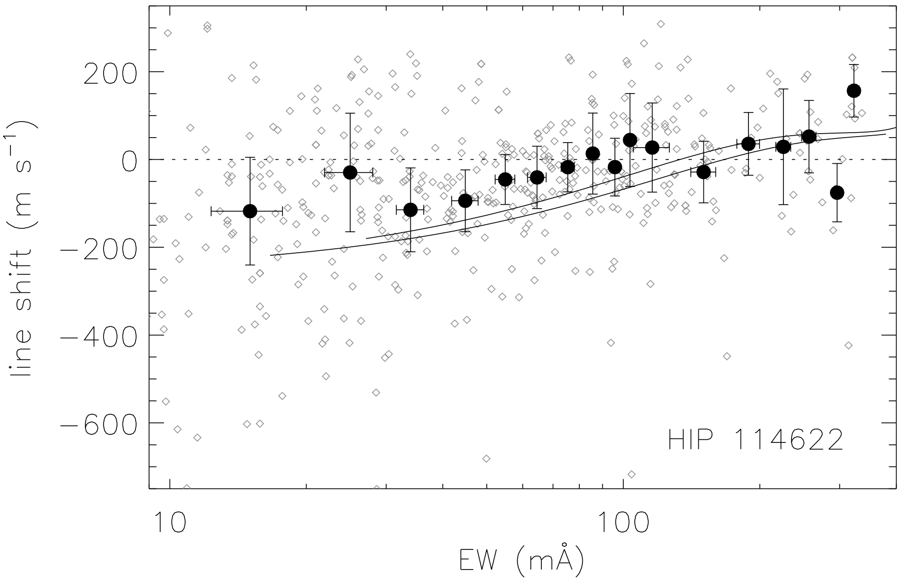

Figure 3.40: As in Fig. 3.33 for HIP 114622.

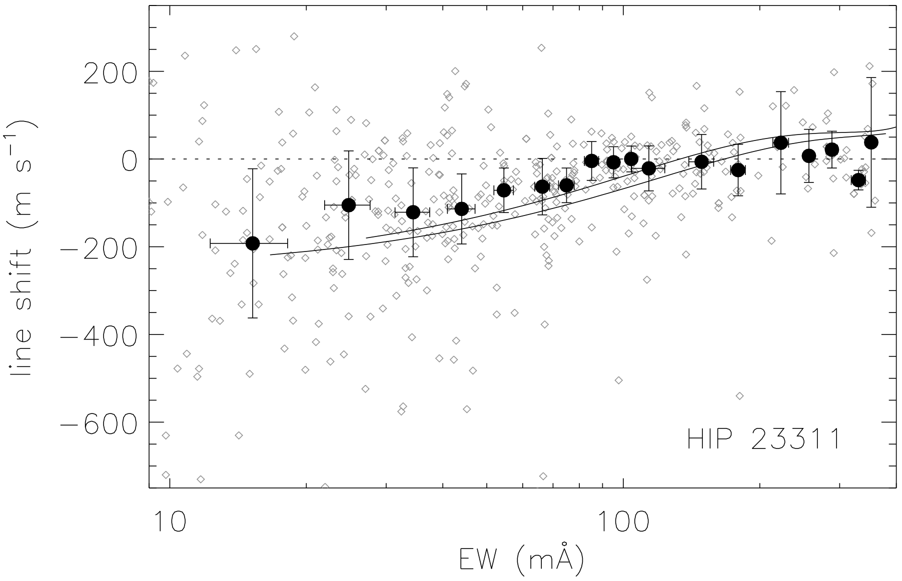

Figure 3.41: As in Fig. 3.33 for HIP 23311.

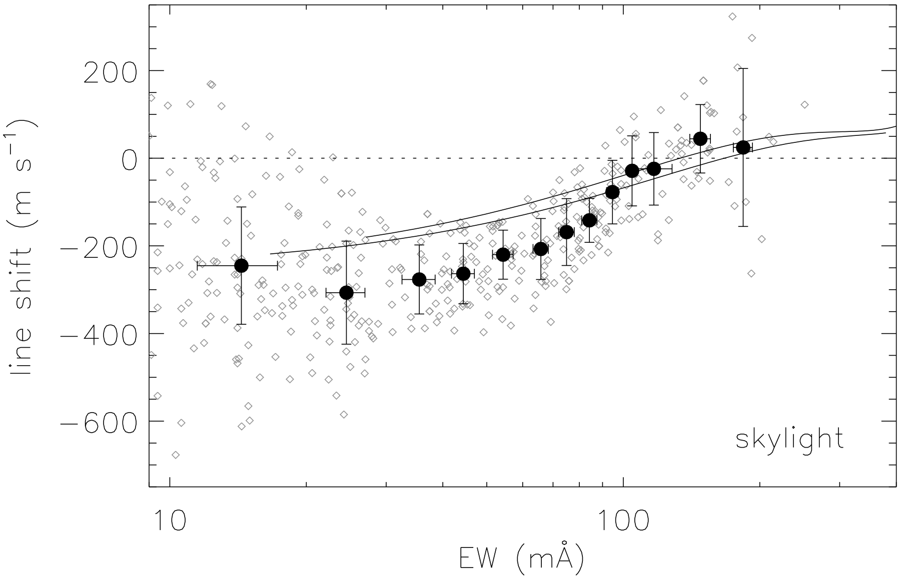

Figure 3.42: As in Fig. 3.33 for the skylight.

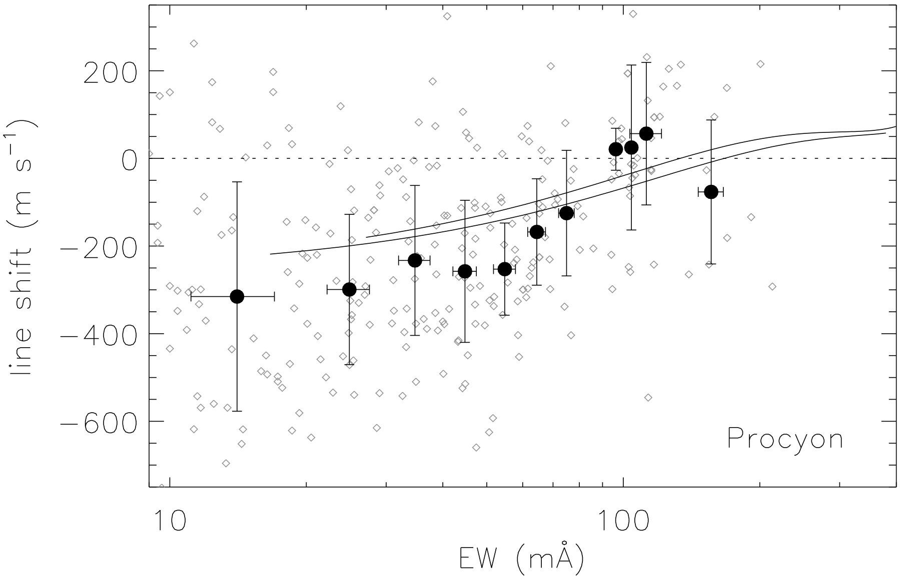

Figure 3.43: As in Fig. 3.33 for Procyon.

In several cases (e.g., HIP 96100, HIP 26779, HIP 86400, HIP 23311) it is clear that the trend is nearly linear for the weak lines but it reaches a saturation point at about $100 - 150$ mÅ, from where it becomes a *plateau*. The detection of this plateau is of utmost importance, as it will be argued later. As we mentioned above, the line shifts were displaced arbitrarily so that the strongest lines have zero shifts. We define the set of strong lines as those belonging to the plateau, where it is detectable. In other cases we assume that lines with $EW > 150$ mÅ are "strong" in this context.

To determine the quality of the model predictions when compared to the observed data shown in Figs. 3.33 to 3.43, we used χ^2 statistics, as was done in Sect. 3.2.1. We used Eqs. 3.11 and 3.12 to calculate the probability that the model predictions correspond to the observations within the uncertainties, replacing the Δv (bisector abscissa value) in Eq. 3.11 with the binned central wavelength shifts. The results of these calculations are given in Table 3.6. Three probabilities were computed for each star, one for all lines, and the other two using only lines of EW $<$ 100 mÅ, and EW $<$ 200 mÅ, to reduce the impact of the uncertain theoretical predictions at large EW values. As explained in Sect. 3.1.3, the predicted convective redshifts for very strong lines are likely to be due to model deficiencies and numerical artifacts, a conclusion based on observations of the solar line shifts, which are not compatible with the model predictions for the strongest lines but accurately match the theoretical expectations for the weaker and intermediate strength ones (Asplund et al. 2000b). The probabilities for the EW $<$ 100 mÅ lines are the most

Object	EW (mÅ)		
	< 100	< 200	> 0
HIP 96100	99.1	99.3	99.3
HIP 26779	100.0	100.0	100.0
ϵ Eri	84.0	97.2	88.2
HIP 88601	99.6	100.0	100.0
HIP 64797	53.2	75.8	91.0
HIP 37349	63.5	80.7	69.9
HIP 86400	91.2	99.3	99.8
HIP 86400	91.2	99.3	99.8
HIP 114622	31.6	57.7	37.7
HIP 23311	42.5	69.1	87.8
skylight	8.1	28.9	28.9
Procyon	51.8	74.7	74.7

Table 3.6: Probability that the 3D model predictions (assuming $R = 180,000$ and $V \sin i = 1.5$ km s^{-1}) for the central wavelength shift vs. equivalent width relation correspond to the observations. Three values are given for each star and they correspond to the probabilities calculated restricting the lines by maximum equivalent width. The boxed entry corresponds to our reference star, HIP 86400.

reliable ones and we will adopt them hereafter.

Since the error bars of the observational data shown in Figs. 3.33 to 3.43 are large, it is not surprising that the probabilities given in Table 3.6 are also large. In fact, for HIP 96100, HIP 26779, and HIP 88601 they are essentially 100%. The probability is slightly smaller for ϵ Eri (84%), which shows a shallower slope (Fig. 3.35), probably due to stellar activity related effects, which may affect the shapes of the line cores significantly (e.g., Gray et al. 1984a, Borrero 2008). The results for HIP 64797 and HIP 37349 are unreliable given the low quality of the data.

For HIP 86400, the reference star, the probability that model and observation match in Fig. 3.39 is about 91%. A closer inspection of Fig. 3.39 reveals that perhaps the model is overestimating the convective blueshifts below 80 mÅ, but the slope of the line shift vs. EW relation is remarkably similar to that given by the observational data.

The probabilities for the two coolest stars, HIP 114622 and HIP 23311 are both below about 40%. Note, however, that Figs. 3.40 and 3.41 show that the slope of the line shift vs. EW relations are in very good agreement with the model predictions and that they only need very small offset corrections to match, almost at the 100% probability level, the theoretical data. However, if this is done, there will not be a good agreement at larger EW values anymore.

3.3 Summary

A three dimensional radiative-hydrodynamical simulation has been computed for stellar parameters $T_{\text{eff}} = 4820$ K, $\log g = 4.5$, and [Fe/H] = 0, using the same prescription that has been successful at reproducing the granulation features in the Sun. This K-dwarf model also predicts a granulation pattern, i.e., a correlation between the intensity (or temperature), velocity, and density fields, which is, however, weaker than that found for hotter stars. Furthermore, the granulation intensity pattern is hidden beneath the visible surface but the velocity field still shows significant fluctuations in higher photospheric layers. Thus, granulation signatures are expected to be detected in K-dwarf spectra, even though they are very small.

Spectrum synthesis using the 3D model predicts detectable signatures of granulation in the Fe I absorption line spectrum: line asymmetries and central wavelength shifts. Additional line broadening due to stellar rotation must be taken into account when comparing the model predictions with observational data. The impact of the finite resolving power of our observations, on the other hand, is relatively small.

The 3D calculations for typical K-dwarfs of $V \sin i = 1.5$ km s^{-1}, observed with spectral resolution $R = 180,000$, show that the theoretical line bisectors have magnitudes (extent from minimum to maximum wavelength shift across the line) between 10 and 100 m s^{-1}, depending on line strength, while the maximum central wavelength shifts (convective blueshifts) are about -200 m s^{-1}.

The very high quality data that we have obtained for a small group of K-dwarfs, as well as their careful processing, have allowed us to detect the very small signatures of granulation. Although there is a possibility that other effects, such as stellar activity and chromospheric emission, make the spectral lines slightly more symmetric, the agreement between the 3D model predictions and our observations is remarkable. The line bisectors and wavelength shifts of our reference star, for example, agree with the predicted ones at a 90 to 95% confidence level. Thus, even if there are effects other than granulation affecting the line profiles, we expect their impact to be smaller compared to that of the surface inhomogeneities modeled by our 3D simulation.

Chapter 4

Effects of Granulation on Spectroscopic Analyses

Model atmospheres are one of the most important ingredients used in the derivation of chemical compositions and fundamental parameters of stars (Sect. 1.2.1). Unrealistic models lead to systematic errors in these determinations, which are then easily propagated to the theoretical interpretations, for example those concerning the chemical evolution of the Galaxy (Sect. 1.3).

In Chapter 3, we found that a 3D radiative-hydrodynamical model atmosphere for a K-dwarf reproduced the basic observational signatures of granulation remarkably well. Since the same theoretical prescription has been used to model the surface inhomogeneities in the Sun and Procyon with a similar, if not better, success in terms of the good agreement with the observed data, we may conclude that the physics of the granulation phenomenon in FGK dwarfs is now very well understood.

Validating theoretical models, i.e., verifying that their most fundamental predictions are supported by targeted observations, allows us to explore the impact of their effects on other matters, such as the inferred chemical compositions in the case of stellar atmospheres, with confidence. Theoretical models can be computed at will, but using them is meaningless if they fail at reproducing the basic physics behind the phenomenon they intend to represent. This is not the case of our 3D K-dwarf model atmosphere. Therefore, the conclusions presented in this chapter are reliable because they are based on the use of a theoretical model that has been carefully validated.

In this chapter, we use our 3D model atmosphere to explore the effects of surface inhomogeneities on the determination of chemical compositions of K-dwarfs, in particular their iron abundances and the abundance of elements determined from molecular features. We also estimate their impact on the determination of effective temperatures of K-dwarfs using two of the most popular techniques, namely the infrared flux method and the condition of excitation equilibrium of Fe I lines. We conclude with a discussion of the application of our quantitative understanding of the granulation phenomenon in FGK dwarfs to determine absolute radial velocities.

4.1 Iron abundances

Of the 119 Fe I and 13 Fe II lines calculated with our 3D model (Sect. 3.1.2), only about a half are sufficiently "clean" (i.e., unblended) to allow a very accurate measurement of their equivalent widths. For each of these clean iron lines, we determined a curve of growth (COG) using the line profiles predicted by our 3D model calculations. Three line profiles were computed for each real spectral line: one using the measured $\log gf$ and the other two using $\log gf \pm 0.5$. Profiles for lines with intermediate $\log gf$ values were then computed by linear interpolation. The equivalent widths (EW) of the theoretical line profiles were then computed by direct integration. All lines were calculated within a spectral range that was wide enough to make this EW calculation very accurate.[1]

The measured equivalent widths in the spectrum of HIP 86400 were then used to determine the iron abundance of the star from each spectral line COG. The results of these calculations are shown in Fig. 4.1. Our HIP 86400 spectrum covers the spectral range from about 5580 to 7800 Å and therefore bluer Fe I lines from the original linelist were not included in our iron abundance analysis (the majority of them are severely blended anyway). A significant fraction of the Fe II lines, however, are in the blue region. To determine their EW values, we used the HIP 86400 spectrum from the S^4N database.

The iron abundance we find for HIP 86400 using our 3D model is $A(\mathrm{Fe}) = 7.49 \pm 0.10$, using all iron lines.[2] From the neutral iron lines (Fe I) only, we find $A(\mathrm{Fe}) = 7.48 \pm 0.10$. There is a small positive trend of the iron abundance with excitation potential (0.024 ± 0.016 dex eV^{-1}) and essentially

---

[1] However, the linear interpolation referred to as above introduces a small error in the predicted equivalent widths. A test was made comparing the EWs of all lines computed with their real $\log gf$ values and those determined from their corresponding interpolated line profiles, computed as the averages of the $\log gf + 0.5$ and $\log gf - 0.5$ profiles. The mean difference between the "real" and interpolated EWs was about 1 %. Since the maximum interpolation distance in our procedure is half of that adopted for this test, we expect our actual interpolation errors for the EW calculation to be 0.5 %, which, for lines of EW $\simeq$ 50 mÅ, corresponds to an error of 0.002 dex in the inferred abundances.

[2] In this work, the error bars given for the abundances are 1-σ errors, where σ is the standard deviation of the line-by-line abundances.

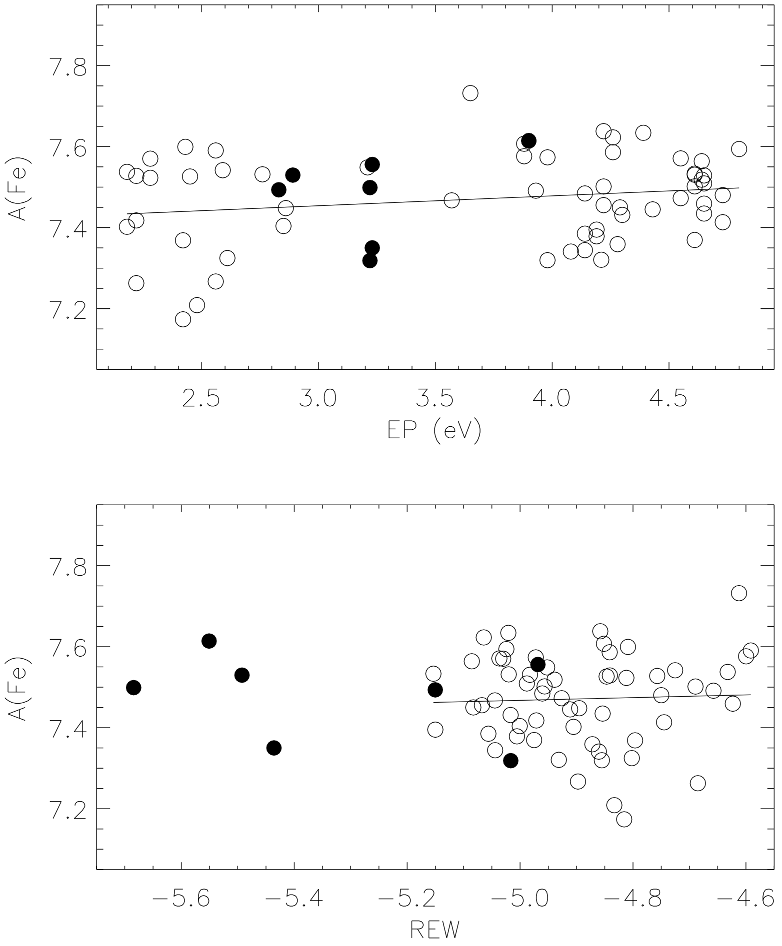

Figure 4.1: Iron abundance of HIP 86400 determined using our 3D model atmosphere as a function of excitation potential, EP, and reduced equivalent width, REW = log(EW/λ). Open circles correspond to Fe I lines and filled circles to Fe II lines. The solid lines represent linear fits to the Fe I data.

no trend with reduced equivalent width (0.034 ± 0.103 dex per REW unit). The former may suggest that the effective temperature of HIP 86400 is larger than that of the 3D model (Sect. 4.3.2) but it may be also due to non-LTE effects. The fact that there is no trend with REW implies that the velocity field desaturates the strong lines in a similar way as the microturbulent velocity does in the 1D analysis. The advantage of the 3D calculation is obviously the fact that there is no free parameter to account for the "microturbulent" broadening. We remind the reader that the 1D macroturbulent broadening is not necessary either in the 3D model fitting of spectral line profiles (cf. Sect. 3.2 and Fig. 3.19).

According to the 3D model abundance determination, the singly ionized iron lines (Fe II) result in an iron abundance $A(\mathrm{Fe}) = 7.50 \pm 0.11$. Thus, if HIP 86400 had stellar parameters identical to our 3D model ($T_{\mathrm{eff}} = 4820\,\mathrm{K}$, $\log g = 4.5$, $[\mathrm{Fe/H}] = 0$), its iron abundance determined from 3D models would be consistent with ionization equilibrium (i.e., both Fe I and Fe II lines are well fitted by a single iron abundance). However, the actual $\log g$ value of this star is slightly larger. According to Allende Prieto et al. (2004), the surface gravity of HIP 86400 is $\log g = 4.624 \pm 0.041$ while its effective temperature is about 4830 K. The parameters determined by Allende Prieto et al. are very reliable. Their adopted T_{eff} scale is tied to accurate measurements of stellar angular diameters while the error in their surface gravity determination is dominated by errors in the stellar distances or parallaxes, which are based on *Hipparcos* data. The uncertainty in the parallax of HIP 86400 is only about 1.3%.

v_t	4820 K, 4.5		4820 K, 4.6		5020 K, 4.8	
km s^{-1}	A(Fe I)	A(Fe II)	A(Fe I)	A(Fe II)	A(Fe I)	A(Fe II)
0.0	7.53	7.57	7.51	7.64	7.54	7.54
0.5	7.50	7.54	7.49	7.61	7.51	7.52
1.0	7.42	7.48	7.42	7.56	7.45	7.47
1.5	7.33	7.42	7.34	7.50	7.37	7.41
3D model (4820K, 4.5): A(Fe I) = 7.48 ± 0.10, A(Fe II) = 7.50 ± 0.11						

Table 4.1: Average iron abundance obtained using different 1D model parameters ($T_{\rm eff}$ and $\log g$ are shown in the first row). The results from Fe I and Fe II lines are given separately. The last row gives the mean iron abundance according to our 3D model calculations.

An increase in $\log g$ implies larger electron densities, which induce a decrease of the Fe II number density. Since in K-dwarfs the dominant species of iron is Fe I, the increase in $\log g$ affects mostly the strength of the Fe II features; they become weaker and, therefore, a larger iron abundance is necessary to fit the model predictions to the observed Fe II line profiles.

To quantify the effect of the $\log g$ value (and also of the effective temperature) on our determination of the iron abundance, we used 1D Kurucz models and the spectrum synthesis code MOOG, which is a very common combination in stellar abundance studies. The atomic data employed was identical to that used for the 3D calculations. We computed the iron abundance from Fe I and Fe II lines in this manner for two values of the effective temperature, 4820 K and 5020 K, and two values of $\log g$, 4.5 and 4.6. We performed these calculations for four values of the microturbulent velocity: v_t = 0.0, 0.5, 1.0, and 1.5 km s^{-1}. The results are given in Table 4.1 and are illustrated in Figs. 4.2, 4.3, and 4.4.

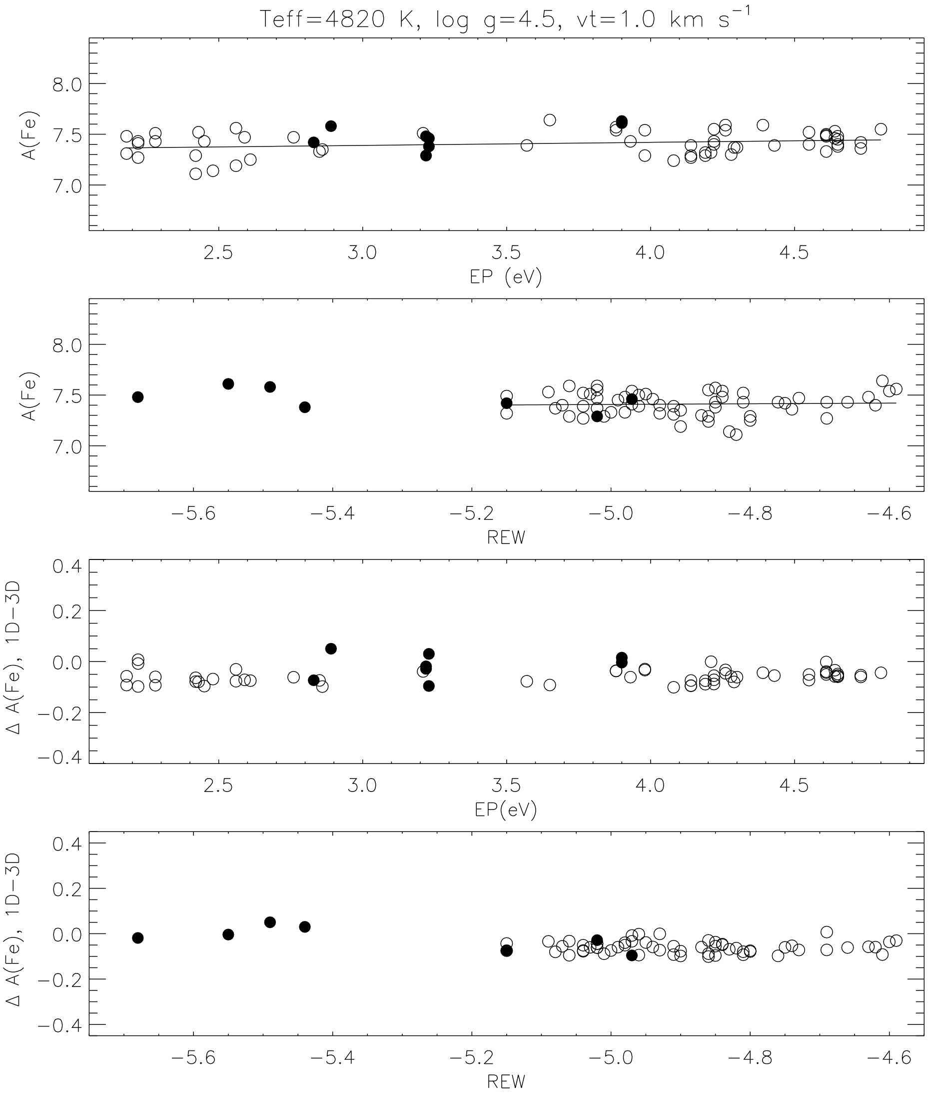

Figure 4.2: Top two panels: as in Fig. 4.1 but using a Kurucz 1D model atmosphere of $T_{\rm eff} = 4820\,{\rm K}$ and $\log g = 4.5$. Lower two panels: line-to-line difference in the iron abundances derived using the 1D and 3D models as a function of EP and REW. A microturbulent velocity of 1 km s^{-1} was adopted in the 1D case.

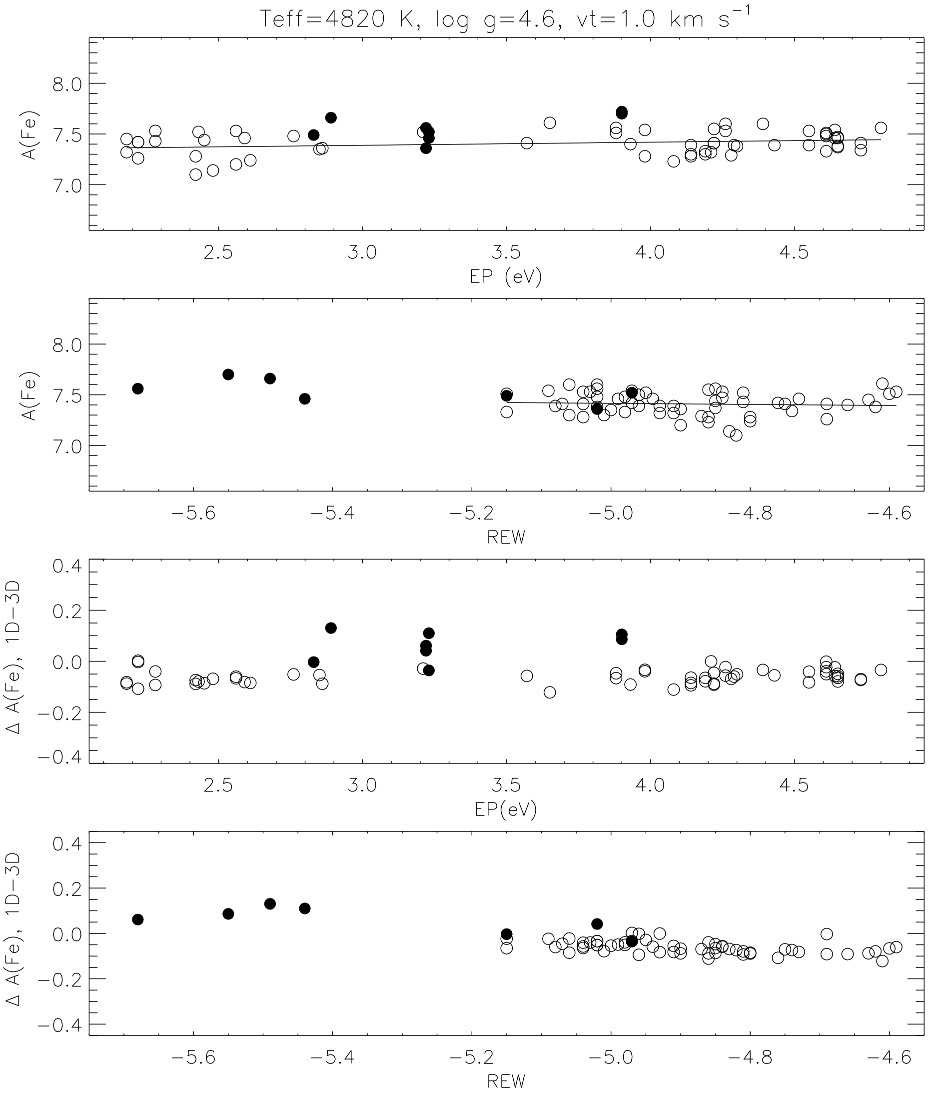

Figure 4.3: As in Fig. 4.2 but using a Kurucz 1D model atmosphere of $T_{\rm eff} = 4820\,{\rm K}$ and $\log g = 4.6$.

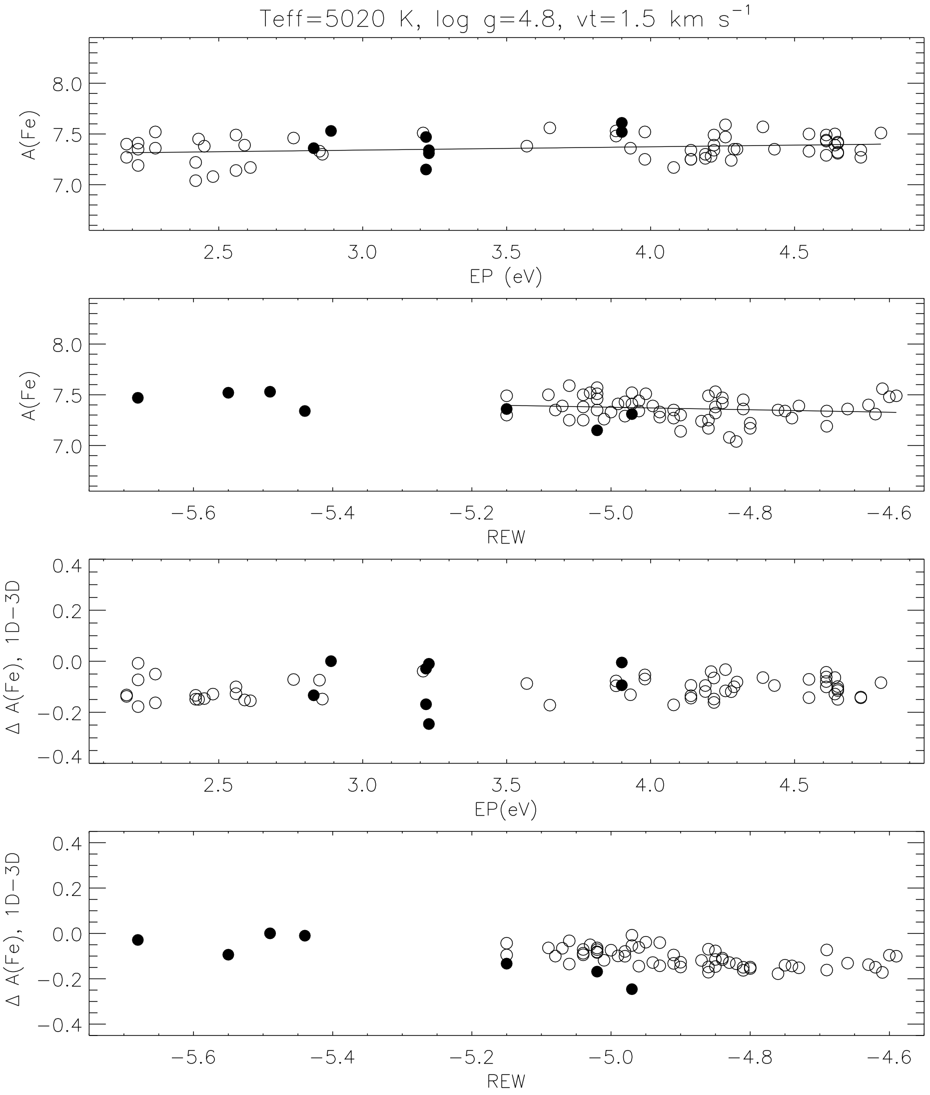

Figure 4.4: As in Fig. 4.2 but using a Kurucz 1D model atmosphere of $T_{\rm eff} = 5020\,$K and $\log g = 4.8$, and adopting a microturbulent velocity of 1.5 km s^{-1}.

According to the 1D calculations, the Fe I abundance is about 0.04 to 0.06 dex lower than the Fe II abundance for $T_{\text{eff}} = 4820\,\text{K}$, $\log g = 4.5$ (except for the largest v_t case). Given that the error bars are about 0.1 dex, one may claim this to be a satisfactory ionization equilibrium. If we use the $\log g = 4.6$ model, the Fe I abundance now results about 0.12 to 0.16 dex lower than that obtained from the Fe II lines. This is the iron ionization balance problem discussed in Sect. 1.2.2 (cf. Fig. 1.3). Although the Fe II minus Fe I abundance difference is larger (0.2–0.3 dex) for some K-dwarfs, note that they are also the more metal-rich ones (see Fig. 8 in Allende Prieto et al. 2004). In any case, it is clear that the observational errors are smaller than the difference between the average Fe I and Fe II abundances.

The 3D effect on the iron abundance determination should be estimated from a comparison of models with identical parameters ($T_{\text{eff}} = 4820\,\text{K}$, $\log g = 4.5$). The 1D model with $v_t = 1$ km s^{-1} suggests a Fe II minus Fe I abundance difference of 0.06 dex while the 3D calculation suggests 0.02 dex (below we show that the microturbulent velocity of HIP 86400 is indeed close to 1 km s^{-1}). Thus, 3D corrections reduce the Fe II minus Fe I abundance difference by a factor of 3, alleviating the ionization abundance discrepancy by 67 %.

Unfortunately, our 3D model was computed for $\log g = 4.5$ and not $\log g = 4.6$, but we suspect this effect to be small on the overall granulation intensity and velocity fields. In fact, this statement is justified by the good agreement between observed and predicted detailed line profiles for a $\log g = 4.5$ model and a $\log g = 4.6$ star (Chapter 3). Thus, it is possible that for

$\log g = 4.6$, the 3D correction to the Fe II minus Fe I abundance difference also alleviates the discrepancy by about 67 %.

Therefore, the ionization balance problem mentioned in Sect. 1.2.2 could be partially solved by including the effects of surface inhomogeneities in the K-dwarf model atmospheres, an statement that needs to be confirmed with hydrodynamic simulations of more metal-rich and cooler K-dwarf stars.

Besides apparently improving the iron ionization equilibrium, the derivation of abundances in K-dwarfs using 3D models is intrinsically more reliable. In 1D analyses, the slope of the iron abundance vs. EP and REW can be set to zero using T_{eff} and v_t as free parameters. In principle, the EP slope depends on T_{eff} and the REW one on v_t. In practice, there is a degeneracy in this procedure and usually a family of (T_{eff}, v_t) values satisfy the zero slope conditions. Even worse is the fact that, at least in K-dwarfs, the REW slope is already close to zero for $v_t = 0$ and an increase of v_t from 0 to 1 km s $^{-1}$ does not change the value of that slope (see Fig. 4.5). However, the average iron abundance does change in that v_t range by up to 0.1 dex. Note also that the EP slope changes with v_t and it is thus not only dependent on T_{eff}, as it is often assumed.

With a $T_{\text{eff}} = 4820$ K model it is not possible to satisfy all the spectroscopic equilibrium conditions, namely identical Fe I and Fe II abundances and zero EP/REW slopes. However, when we use the $T_{\text{eff}} = 5020$ K, $\log g = 4.8$ model, all these conditions are accurately satisfied if we adopt $v_t = 1$ km s^{-1}. If we were performing a standard 1D spectroscopic analysis with the HIP 86400

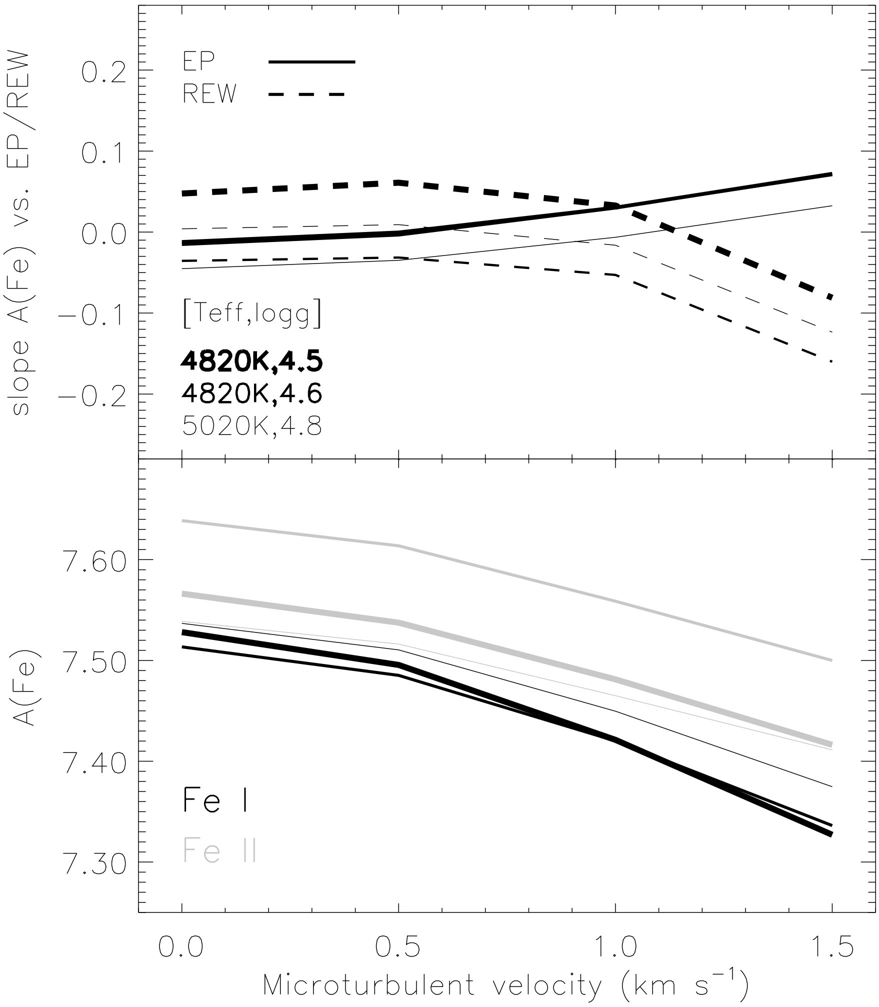

Figure 4.5: Upper panel: Slope of the A(Fe) (Fe I lines only) vs. EP (solid lines) and REW (dotted lines) relation for different 1D model parameters (see legend on bottom left). The EP slopes for the $T_{\rm eff} = 4820$ K models ($\log g = 4.5$ and 4.6 are superimposed). Lower panel: mean iron abundance determined with different 1D model parameters measured from the Fe I (black lines) and Fe II lines (gray lines).

data, we would conclude that its effective temperature is 5020 K and its $\log g = 4.8$. As we mentioned above, however, the fundamental parameters of this star have been determined accurately and do not correspond to these values, even if we consider typical observational errors.

The difference between the 1D and 3D iron abundances is shown in Fig. 4.6 as a function of the 1D model parameters. Also shown in this figure is the scatter in the line-to-line 1D vs. 3D differences. Interestingly, the line-to-line scatter of the 1D minus 3D abundance difference has a minimum at $v_t = 1$ km s^{-1} for the $T_{\rm eff} = 4820$ K models. Since the microturbulence is the 1D parameterization of the 3D granulation effects (for the line broadening alone), minimizing this scatter is equivalent to finding the 1D microturbulent velocity that would make the 1D line profiles agree with those computed with the 3D model. The v_t value of HIP 86400 could not be determined from the 1D Fe I vs. REW relation because the slope was already zero for $v_t = 0$ and remained zero up to $v_t = 1$ km s^{-1}.

Along these lines, note that the hot model ($T_{\rm eff} = 5020$ K) requires a larger v_t value ($v_t = 1.5$ km s^{-1}) to minimize the scatter of the 1D vs. 3D abundance differences. However, for this large v_t value, spectroscopic equilibrium is no longer fully satisfied. Although the average Fe I and Fe II abundances still agree reasonably well (0.04 dex difference), the EP and REW slopes are no longer zero (see Fig. 4.5). Also, note that the scatter for the Fe II lines increases with v_t and has a minimum at $v_t = 0.5$ km s^{-1}.

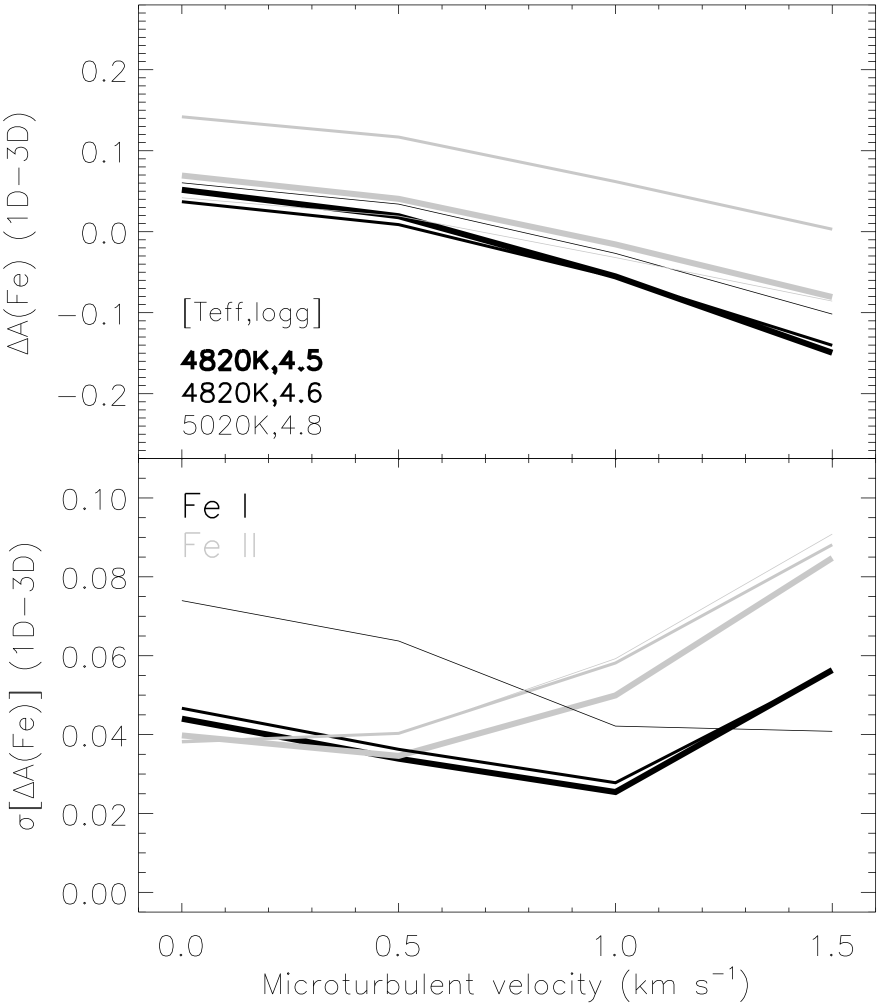

Figure 4.6: Upper panel: difference in the mean iron abundances determined with the 1D and 3D models using different 1D model parameters (see legend on bottom left). The iron abundance difference using Fe I lines are shown in black and those using Fe II lines are shown in gray. Lower panel: line-to-line scatter of the 1D minus 3D difference in the mean iron abundance as a function of 1D model parameters.

4.2 Molecular features

Spectral features due to absorption by molecules are highly sensitive to surface inhomogeneities. In metal-poor stars, these effects are extreme (Sect. 1.2.2), leading to corrections to the inferred abundances of up to one order of magnitude (Asplund & García Pérez 2001, Collet et al. 2006, 2007). There, the mean temperature of the layers where molecular bands are formed, according to the 3D model, is about one thousand degrees lower than the corresponding 1D temperature. This results in an increased rate of molecule formation and therefore stronger molecular features. In our case, the mean temperature of the regions of line formation according to the 3D simulation are only slightly cooler (on the order of 50 K) than the temperatures predicted by 1D models (Fig. 3.1). However, the inhomogeneities of the temperature field can still have a significant impact on the average rate of molecule formation at a given photospheric layer.

Due to granulation, in the photospheric regions where molecular bands are formed, patches cooler and hotter compared to the average temperature are encountered. The increase in the number density of molecules in the cool patches compared to the number density that corresponds to the average temperature is not compensated by the decrease of the number density in the hot regions because of the non-linear dependence of the molecular formation rates on temperature. Thus, even if at a given layer, 1D and 3D models predict the same mean temperature, the temperature inhomogeneities of the 3D simulation allow an effective increase of the number density of molecules and therefore predict stronger molecular features compared to the 1D case.

Fig. 4.7 shows the spectral region between about 5154 and 5164 Å, which contains a number of atomic lines (in particular Ni I, Fe I, Si I, Co I, Ti I, and Cr I) as well as MgH molecular bands (which correspond to most of the strong features not identified as being due to atomic absorption in Fig. 4.7).

In Fig. 4.7, the observed data (open circles connected by the dotted line) correspond to our reference star, HIP 86400, and were obtained from the S^4N database. Two model predictions are superimposed on the observed data, one corresponding to our 3D K-dwarf model atmosphere (red line) and a 1D Kurucz model (blue line) of parameters identical to those of the 3D model. In both cases, the synthesis was made with the same atomic and molecular input data, solar abundances, and using the same code, Assϵt (Koesterke et al. 2008), which is briefly described in Appendix B. The electron densities in the 1D and 3D calculations were also computed in a consistent manner, including the effects of molecule formation. For the 3D calculations, all snapshots were used and time-averaged. The red line in Fig. 4.7, which represents the average theoretical spectrum, has a thickness that corresponds to the RMS of the theoretical spectra from the multiple snapshots. As seen there, the difference in the predicted line strengths between snapshots is very small. Both the 1D and 3D model predictions were convolved with rotational and instrumental profiles, as for the atomic features in Sect. 3.1.3. In addition, micro and macroturbulent velocities ($v_t = 1.0$ km s^{-1}, $v_{\rm mac} = 2.5$ km s^{-1}) were included in the calculation of the 1D spectrum.

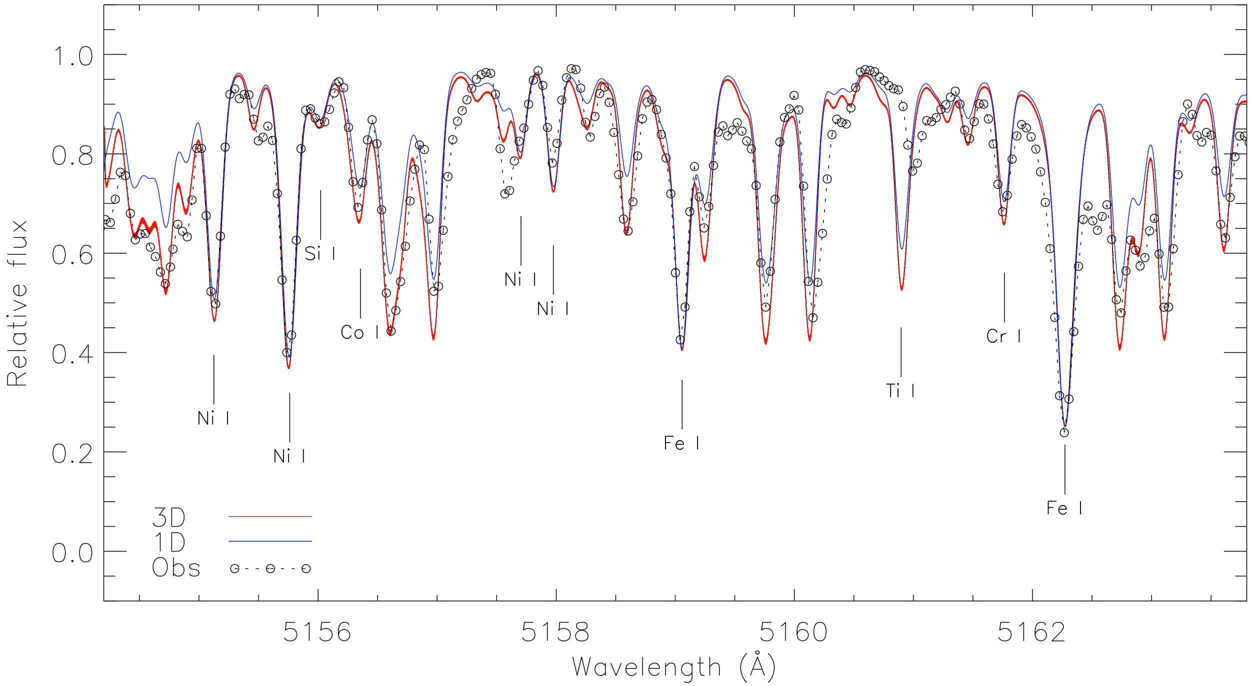

Figure 4.7: Spectral region showing several atomic lines, the strongest of them are properly identified. The rest of the strong features seen in this region are due mainly to MgH. The observed data correspond to our reference star, HIP 86400, and are shown with open circles (connected by dotted lines) while the red and blue lines correspond to the predictions of 3D and 1D model atmospheres, respectively.

As expected, the molecular bands are stronger according to the 3D calculations. More remarkable is the fact that the 3D prediction matches the observed data much better than the 1D calculation. There are no significant differences for the strengths of the atomic lines present everywhere within this region, which shows that this is not an effect of dissimilar continuum opacities or errors in the normalization of the observational data but a true 3D effect (although there appear to be 1D vs. 3D differences for some Ti I and Ni I lines, they are due to blends with MgH features, as corroborated by the synthesis of this spectral region using only atomic or only molecular features). Thus, the temperature inhomogeneities of our 3D model in the photospheric regions where MgH is abundant are fairly realistic, given that they accurately reproduce their absorption features within this band.

In order to match the observed data, the 1D calculations require a Mg abundance of $A_{\mathrm{Mg}} = 7.81$, which is about twice as large as the solar value. Thus, we conclude that the 3D correction to the abundance of Mg inferred with 1D Kurucz models using MgH molecular bands is about 0.3 dex. In addition to their large impact on abundance determinations from molecular features, these 3D corrections will have a non-negligible effect on the results obtained from synthetic photometry, given that molecular bands contribute significant absorption across wide spectral ranges. Also, the presence of surface inhomogeneities may affect somewhat the determination of Mg isotopic ratios, as noted by Lambert et al. (1971) in their study of sunspot umbrae spectra. The MgH absorption line strength increases with decreasing temperature and the lines are stronger for ^{24}MgH than ^{25,26}MgH. In stellar granulation, saturated ^{24}MgH features formed in cool regions can be diluted (i.e., their flux minima increase) by radiation from the hot areas. Thus, the flux of the minima of the ^{24}MgH features is underestimated (i.e., absorption features are stronger) by 1D models because do not take into account the temperature inhomogeneities and therefore the derived ^{24}MgH abundances are smaller. This results in overestimated ^{25,26}Mg/^{24}Mg isotopic ratios (Yong et al. 2003, 2004).

4.3 Effective temperatures

4.3.1 The infrared flux method

By definition, the effective temperature of a star is

$$T_{\rm eff} = \left(\frac{4f_{\rm bol}}{\sigma\theta^2}\right)^{1/4} , \tag{4.1}$$

where σ is the Stefan-Boltzmann constant, and $f_{\rm bol}$ and θ are the bolometric flux and angular diameter of the star, respectively. The monochromatic flux ψ_λ that emerges from the stellar surface is related to the flux received on Earth, f_λ, by the inverse square law, i.e.,

$$f_\lambda = \left(\frac{\theta^2}{4}\right)\psi_\lambda . \tag{4.2}$$

Since stellar angular diameters are very difficult to measure, Eqs. 4.1 and 4.2 can be used to determine $T_{\rm eff}$ from basic principles without invoking θ measurements, provided $f_{\rm bol}$, f_λ, and ψ_λ are known. We find that the ratio of bolometric to monochromatic fluxes is independent of θ:

$$\frac{\sigma T_{\rm eff}^4}{\psi_\lambda} = \frac{f_{\rm bol}}{f_\lambda} . \tag{4.3}$$

The right hand side of this equation is an observational quantity (both f_{bol} and f_λ can be estimated from broadband photometry) and so the ideal wavelength range for this method of T_{eff} determination would be the one for which the temperature sensitivity of $\sigma T_{\mathrm{eff}}^4/\psi_\lambda$ is the largest and ψ_λ well modeled (i.e., where different theoretical calculations agree), such as the infrared. This is the basic idea behind the infrared flux method (IRFM; Blackwell & Shallis 1977, Blackwell et al. 1980).

Alonso et al. (1996a) and later Ramírez & Meléndez (2005a) implemented the IRFM and carefully adjusted its zero point in such a way that the temperatures inferred from it for stars with accurate measurements of angular diameter were consistent with the θ measurements.[3] Their IRFM T_{eff} scale is in good agreement with the T_{eff} values determined directly from very precise measurements of angular diameters and bolometric flux estimates in both giant and main-sequence FGK stars. The mean difference between IRFM and direct temperatures is only $8 \pm 61\,\mathrm{K}$ for dwarf stars and $18 \pm 62\,\mathrm{K}$ for giants (see Figs. 13 and 16 in Ramírez & Meléndez 2005a).

The effective temperature of HIP 86400 has not been determined with the IRFM, but photometric calibrations based on IRFM temperatures allow us to determine its IRFM temperature from its measured colors. Allende Prieto et al. (2004) used Alonso et al. (1996b) calibrations for Strömgren photometry

---

[3] This adjustment involved determining an absolute flux calibration in the infrared, i.e., calculating the monochromatic fluxes corresponding to the effective wavelengths of the J, H, and K photometric bands for a zero magnitude star, which, however, are not consistent with the observations, as pointed out by Casagrande et al. (2007).

and the $B - V$ index and found $T_{\rm eff} = 4833 \pm 86\,{\rm K}$. The more recent and improved multi-color calibrations of Ramírez & Meléndez (2005b) result in $4811 \pm 43\,{\rm K}$ (average of 14 colors). Note that both Alonso et al. and Ramírez & Meléndez calibrations are valid for the parameters of HIP 86400. Taking into account the systematic error of 8 K and the random error of 61 K of the IRFM $T_{\rm eff}$ scale (from the comparison with direct temperatures), the error in the IRFM temperature of HIP 86400 is at most 75 K.

Since the IRFM depends on model atmosphere predictions for ψ_λ, it is not immune to the effects of surface inhomogeneities, although it has been shown that the corrections are not severe. Using the predictions of 1D and 3D models for the continuum flux at $2.2\,\mu$m, Asplund & García Perez (2001) found that the 3D corrections to the IRFM temperatures are about 20 K for solar temperature stars and negligible for turn-off F-type stars of metallicities between $[{\rm Fe/H}] = -3$ and solar.

As explained above (cf. Eq. 4.3), the temperature indicator of the IRFM is the theoretical value of $\sigma T_{\rm eff}^4/\psi_\lambda = \int \psi_\lambda \, d\lambda/\psi_\lambda = R_\lambda$, which is roughly proportional to $T_{\rm eff}^3$ given that $\psi_\lambda \propto T_{\rm eff}$ in the infrared. Thus, a difference between the ψ_λ values predicted by 1D and 3D models corresponds to a 3D correction to the IRFM temperatures of about one third of the relative (percentage) ψ_λ difference. In practice, the continuum fluxes at the effective wavelengths of the J, H, and K bands (1.2, 1.6, and 2.2μm, respectively) are used in the IRFM. Figs. 4.8 and 4.9 show the 1D and 3D model predictions for the continuum flux from the UV to the IR as well as their difference for the Sun and the

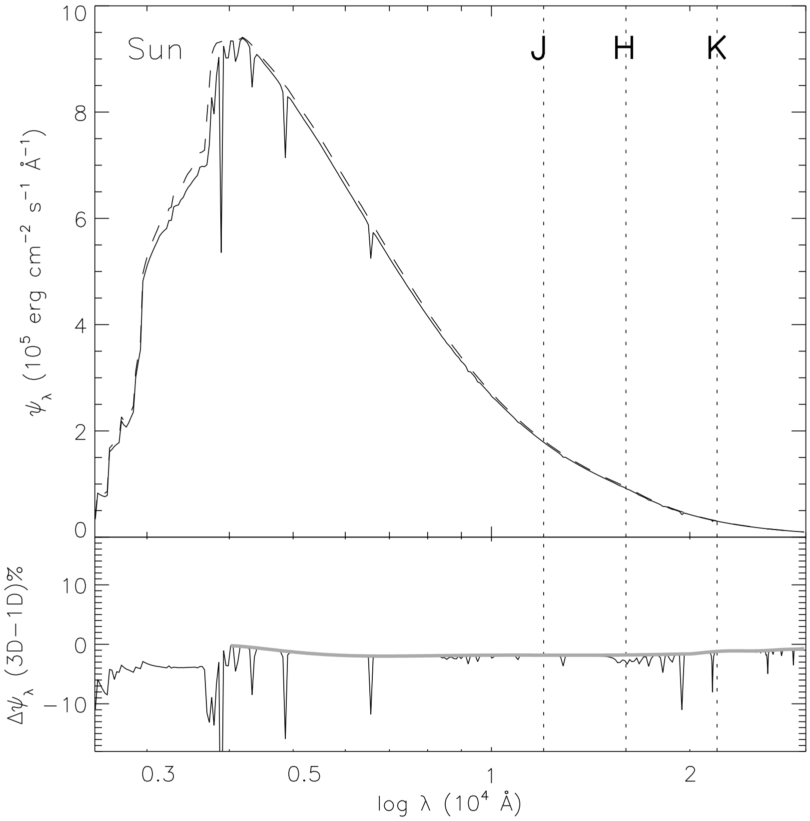

Figure 4.8: Theoretical spectral energy distribution of the Sun according to 3D (solid lines) and 1D (dashed lines) models. The lower panel shows the difference between the 3D and 1D model predictions. The dotted lines mark the effective wavelengths of the *J*, *H*, and *K* photometric bands. The gray thick line in the lower panel is the 3D minus 1D difference excluding the hydrogen lines of the 3D calculation.

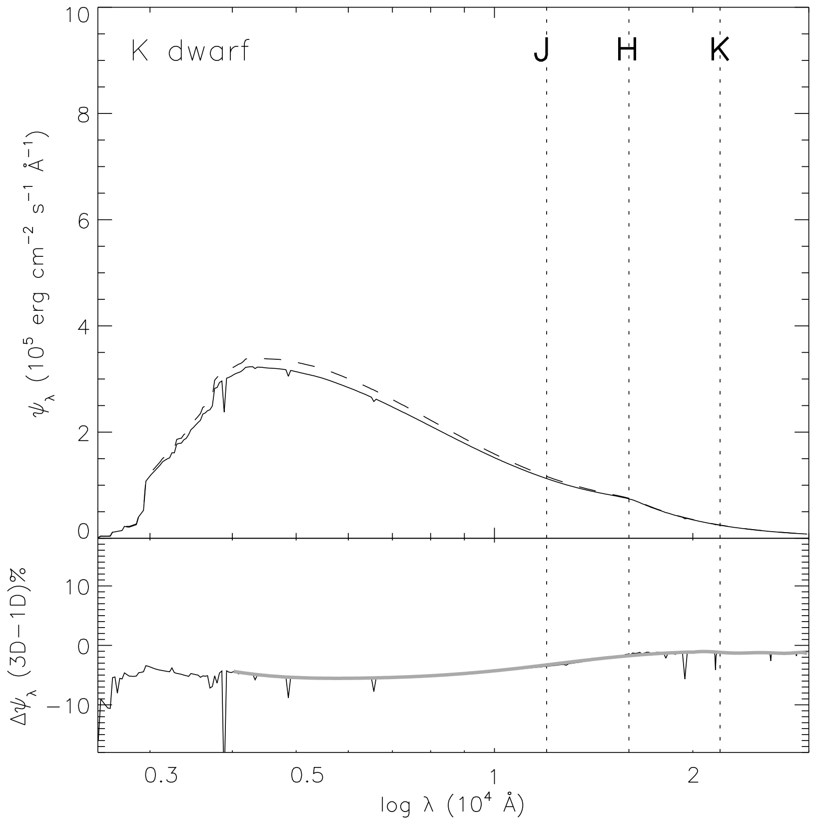

Figure 4.9: As in Fig. 4.8 for the K-dwarf case. The axis scales are the same as in Fig. 4.8.

K-dwarf. These fluxes were computed with the 3D spectrum synthesis code Assϵt (Koesterke et al. 2008; see Appendix B). All the snapshots of the 3D simulation were used to compute these fluxes. The continuum fluxes shown in Figs. 4.8 and 4.9 do not include the effects of line opacity for the continuum calculation. Only for the 3D fluxes, the atomic hydrogen lines were considered. Consequently, when comparing the 1D and 3D fluxes, we define a new continuum for the 3D fluxes excluding the hydrogen lines (see the gray lines in the flux differences shown in the bottom panels of Figs. 4.8 and 4.9).

Note that the integrated flux from these spectral energy distributions differ from the expected $\sigma T_{\rm eff}^4$ value due to the lack of line opacity. In 1D, the values of $T_{\rm eff}$ derived from integration of the fluxes shown in Figs. 4.8 and 4.9 are 5964 and 5002 K, respectively. Including line opacity (which is practical for 1D models only), these values reduce to 5776 and 4820 K, i.e., the adopted $T_{\rm eff}$ values. Using these numbers we can correct the temperatures that result from the 3D spectral energy distributions without line opacity, which are 5925 K for the solar model and 4948 K for the K-dwarf model. The corrected temperatures are $(5776/5964) \times 5925 = 5738$ K (solar model), and $(4820/5002) \times 4948 = 4768$ K (K-dwarf). These values are lower than the adopted effective temperatures due to the presence of hydrogen lines.

Considering the differences in the predicted continuum fluxes in the infrared, we find that, after correcting for 3D effects, the IRFM temperature of the Sun increases by 35, 34, and 23 K when applied in the J, H, and K bands, respectively.[4] This results from the fact that $\psi_\lambda^{\rm 3D}$ is smaller than $\psi_\lambda^{\rm 1D}$ in those bands, which leads to larger R_λ values and hence larger $T_{\rm eff}$. A similar correction is predicted for the K-dwarf case. Fig. 4.9 shows that the 3D continuum flux in the J, H, and K bands is smaller compared to the 1D case by about 4, 2, and 1%, respectively, which leads to 3D corrections to the IRFM temperature of 52 (J band), 27 (H band), and 18 K (K band).

Averaging the results for the three bands we find that the 3D correction

---

[4] Note that the latter (the K-band result) is in excellent agreement with the Asplund & García Perez (2001) result.

to the IRFM temperatures of both the Sun and K-dwarfs is about +30 K. Interestingly, Ramírez & Meléndez (2005a) find 5756 K for the Sun using Kurucz 1D models, i.e. 21 K below the measured value (5777 K). After correcting for 3D effects, this difference reduces to +9 K. For our reference star, HIP 86400, the IRFM temperature, corrected by 3D effects, is about 4840 ± 80 K.

4.3.2 Excitation equilibrium of neutral iron lines

In many standard 1D abundance analyses, the effective temperature (T_{eff}) of a star is first inferred from photometric calibrations and later modified to satisfy the condition of excitation equilibrium of Fe i lines (Sect. 4.1). In practical terms, this criterion involves fine tuning the T_{eff} value so that no trends remain in the relation between iron abundance and excitation potential of the lower level of the line transitions.

Fig. 4.10 shows how the slope of the iron abundance vs. excitation potential relation of Fe i lines in the spectrum of our reference star, HIP 86400, changes with the adopted model effective temperature. An increase of the effective temperature results in a lowering of the population of the low excitation potential levels and therefore weaker theoretical low EP lines. Thus, to match the model predictions to the data, the iron abundance for those low EP lines has to increase. The opposite happens for high EP lines; a higher T_{eff} implies stronger theoretical high EP lines and requires lower iron abundances to match the data. Thus, increasing the model T_{eff} decreases the slope of the A(Fe) vs. EP relation, as demonstrated by Fig. 4.10.

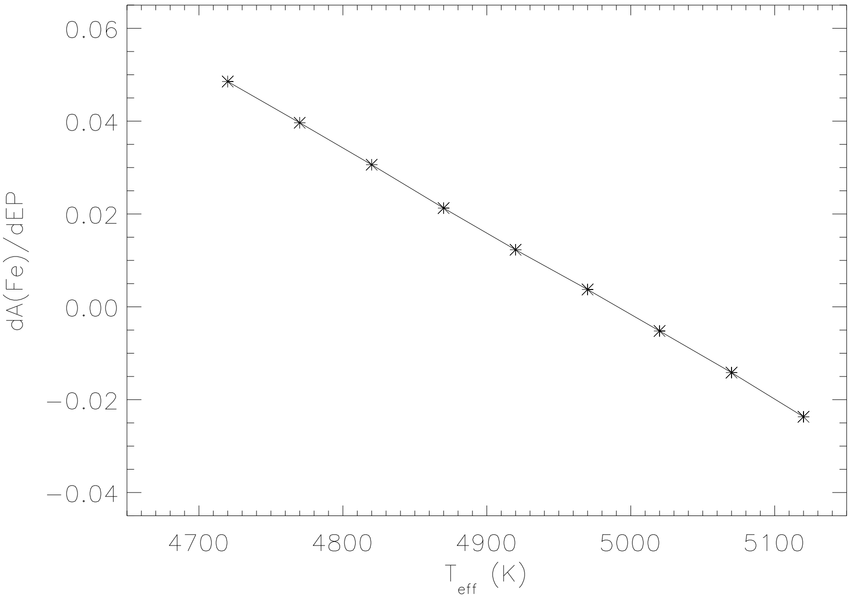

Figure 4.10: Slope of the iron abundance vs. excitation potential relation for Fe I lines in the HIP 86400 spectrum using Kurucz 1D models of $\log g = 4.6$ and adopting $v_t = 1$ km s^{-1}, as a function of the effective temperature of the model. The A(Fe) vs. EP slope is given in dex eV^{-1}.

The change of slope with temperature shown in Fig. 4.10 is ultimately linked to the Boltzmann equation for the atomic level populations. Thus, although the exact $T_{\rm eff}$ values can be model dependent, the relative change of slope with temperature must be a common feature among LTE models. The relation shown in Fig. 4.10 is almost linear; for an increase of 10 K, the A(Fe) vs. EP slope is lowered by about 0.0018 dex eV^{-1}.

According to the 1D Kurucz model calculations, the excitation equilibrium temperature of HIP 86400 should be about 5000 K, which corresponds to a zero slope in the A(Fe) vs. EP relation, as shown in Fig. 4.10. The excitation equilibrium temperature is thus about 160 K larger than our best available estimate of the effective temperature of the star. This result casts doubt upon the classical spectroscopic method of $T_{\rm eff}$ fine tuning by excitation equilibrium of Fe I lines.

Interestingly, the A(Fe) vs. EP relation that we obtain when we use our 3D model to derive the iron abundances from Fe I lines is 0.024 ± 0.016 dex eV^{-1}, i.e., non-zero. If we assume that the change of A(Fe) vs. EP slope (cf. Fig. 4.10) is independent of the model atmosphere, as long as the LTE approximation is adopted in all of them, then this positive slope of our 3D calculations suggests that the effective temperature of HIP 86400 is 130 ± 90 K larger than that of the 3D model, i.e., 4950 ± 90 K. Therefore, 3D corrections to the iron abundances from Fe I lines do not improve significantly the excitation imbalance obtained with 1D models. Furthermore, our 3D model calculations also suggest that the effective temperature of HIP 86400 is larger by about 110 K compared to the most reliable $T_{\rm eff}$ determinations.

In conclusion, regarding the excitation balance of Fe I lines, the Kurucz 1D and our 3D model atmosphere appear to suffer from the same limitation. Given the nature of the problem and the similarities between these 1D and 3D models, one may be tempted to conclude that this is due to non-LTE effects. In any case, the LTE excitation equilibrium of Fe I lines condition should not be used to fine tune the effective temperatures of K-dwarfs.

4.4 Absolute radial velocities

Accurate radial velocities of stars are useful for studies of Galactic structure (e.g., Bienaymé 1999, Nordström et al. 2004), orbits of binary stars (in particular those with long periods), and star cluster distances (e.g., Sagar & Bhatt 1988). Although ultra high precision (close to the meter per second accuracy) can be achieved for relative measurements (e.g., Marcy & Butler 1998, Endl et al. 2005), absolute radial velocities are subject to a series of systematic errors that are very difficult to remove (Lindegren et al. 1999, Lindegren & Dravins 2003). The first of these is the gravitational redshift (Sect. 1.3 and Eq. 1.7), which is on the order of 0.6 km s^{-1} in FGK stars. A secondary relativistic correction (transversal Doppler effect) is also required for high velocity stars, where it amounts to about 50 m s^{-1} (Lindegren et al. 1999). Both of these effects introduce a constant shift in the radial velocity zero point of the star. More importantly, however, is the effect of granulation.

Spectral lines formed in inhomogeneous stellar photospheres are asymmetric and blueshifted. If the cross-correlation method is used to determine the radial velocity of a star, then only when a very similar object is used as a radial velocity standard will the method be successful. This is due to the fact that the line spectra of stars with different fundamental parameters suffer from different granulation effects because of their different intensity and velocity field contrasts (Sect. 3.1.1, Nordlund & Dravins 1990). On the other hand, measuring the central wavelengths of a multitude of spectral lines and applying the Doppler formula to determine the stellar radial velocity introduces the error of the unknown convective blueshift to the measurements. However, as explained in Sect. 3.2.2, the wavelengths of the cores of very strong Fe I lines in K-dwarfs (and also G-dwarfs and K-giants; Appendix A) are not shifted by granulation because they form in very high photospheric layers, where the correlation between intensity and velocity fields is weak. Therefore, one can avoid the effects of granulation in radial velocity measurements by only using spectral lines whose convective line-shifts fall in the "plateau" region of the line-shift vs. equivalent width relation (Figs. 3.33 to 3.43), provided the plateau is reliably detected, as it is the case of some of our K-dwarfs: HIP 96100, HIP 86400, HIP 23311, HIP 88601, and HIP 26779.

The radial velocities we determined by cross-correlation of our cs21 spectra with each other and with their corresponding HET spectrum (see Chapter 2 for details) are shown in Fig. 4.11 and their average values are given in Table 4.2. Note that while our relative velocities are very accurate (the relative velocities of cs21 pairs have a mean uncertainty of 12 m s^{-1} while that of a cs21-HET pair is about 70 m s^{-1}), the HET reference spectrum has been only approximately corrected for the stellar radial velocity by using the Doppler shifts measured for a large number of strong spectral lines. The granulation effects are not yet removed from these data.

Fig. 4.11 and Table 4.2 show that almost all of our sample stars have nearly constant radial velocity, which makes them useful as radial velocity standards. HIP 88601, however, is a very long period visual binary star, while HIP 26779 is a suspected long period radial velocity variable (see details be-

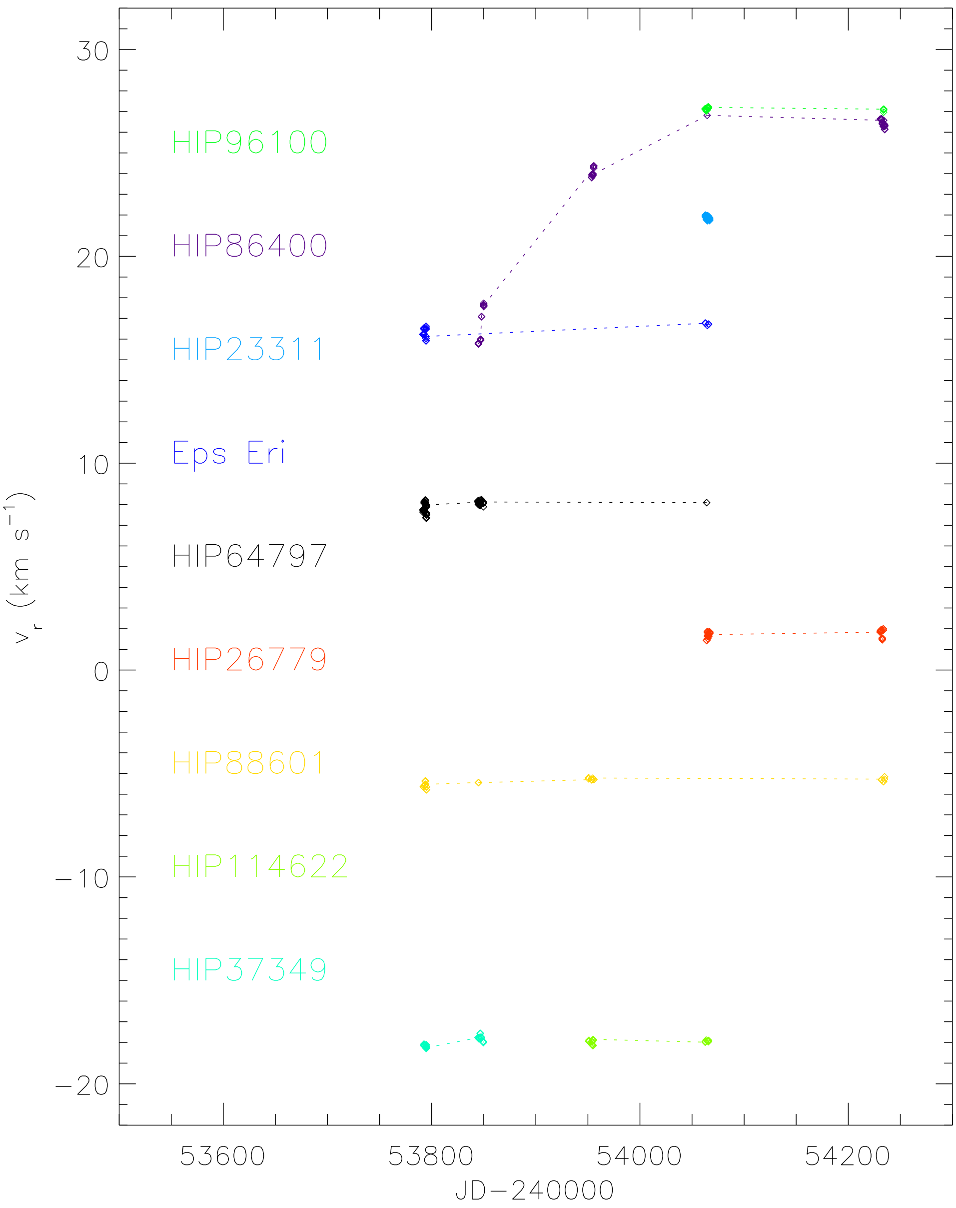

Figure 4.11: Radial velocities of our K-dwarf sample stars as a function of time of observation. The dotted lines simply connect velocities for the same object; they are not fits to the data. Five groups of data points are clearly seen, which correspond to our five observing runs (Table 2.3).

Object	v_r	$\sigma(v_r)$	n
	km s^{-1}		
HIP 96100	27.143	0.062	31
HIP 86400	23.269	4.176	72
HIP 23311	21.863	0.081	41
ϵ Eri	16.401	0.256	30
HIP 64797	7.893	0.258	106
HIP 26779	1.733	0.173	53
HIP 88601	-5.430	0.174	31
HIP 114622	-17.972	0.086	30
HIP 37349	-18.028	0.219	35

Table 4.2: Mean radial velocities and their standard deviations obtained for our sample stars using our data. The last column corresponds to the total number of observations. HIP 86400 is a confirmed single-lined spectroscopic binary; its orbital parameters are given in Table 4.3.

low). Only HIP 86400, our reference star, shows large, relatively short-term, radial velocity variations.

Combining our radial velocity data with those of Tokovinin (1991), we were able to fit a spectroscopic orbit for the primary star of the HIP 86400 system using the GaussFit package (Jefferys et al. 1988). The resulting orbital parameters are given in Table 4.3 and the model fit to the data is shown in Fig. 4.12. The mass function of the system is $0.00153 \pm 0.00008 M_\odot$, which implies a mass of about $0.42 M_\odot$ for the secondary, assuming a mass of $0.85 M_\odot$ for the primary (determined from isochrones) and $\sin i = 0.32$ (as measured astrometrically by Jancart et al. 2005). This corresponds to an M-dwarf star of effective temperature around 3500 K (Baraffe & Chabrier 1996, Basri et al. 2000) whose contribution to the flux is relatively small in the

Parameter	Value	Error	Units
Orbital period (P)	83.713	0.005	days
Time of periastron passage (T)	2447723.54	0.47	JD
Eccentricity (e)	0.288	0.012	
Longitude of periastron (ω)	135.99	1.97	degrees
Semi-amplitude of RV curve (K_1)	5.86	0.10	km s^{-1}
Velocity of the center of mass (γ_a)	22.095	0.077	km s^{-1}
Velocity of the center of mass (γ_b)	21.194	0.070	km s^{-1}
Mass function (f_m)	0.00153	0.00008	$M_\odot$

Table 4.3: Orbital parameters obtained by fitting the radial velocity data of HIP 86400. Two values for γ are given; the first one, γ_a, corresponds to our observations, while γ_b was obtained for Tokovinin (1991) data. A systematic difference of about 0.9 km s^{-1}, with our velocities being larger, is present between the two data sets. The rest of the parameters were derived using the combined data set. The radial velocity curve of HIP 86400 is shown in Fig. 4.12.

visible and near infrared (a secondary spectrum has not been detected yet) and therefore does not affect significantly our measurements of line shapes (Sects. 3.2.1 and 3.2.2) or effective temperatures from, mainly, optical colors (Sect. 4.3.1). Indeed, using the spectral energy distributions calculated from Kurucz model atmospheres, we find that the surface flux from the M-dwarf in the HIP 86400 system is about 8% of the flux emitted by the K-dwarf in the spectral region of interest for this work. Considering that the flux received on Earth is proportional to the angular diameter of the star squared (Eq. 4.2) and the radii of $0.4M_\odot$ dwarfs are about $0.4R_\odot$ (Beatty et al. 2007), the contribution to the flux from the M-dwarf to our observed spectrum of HIP 86400 is about $(0.4/0.8)^2 \times 8\% = 2\,\%$, given that the radius of the primary, the K-dwarf, is about $0.8R_\odot$.

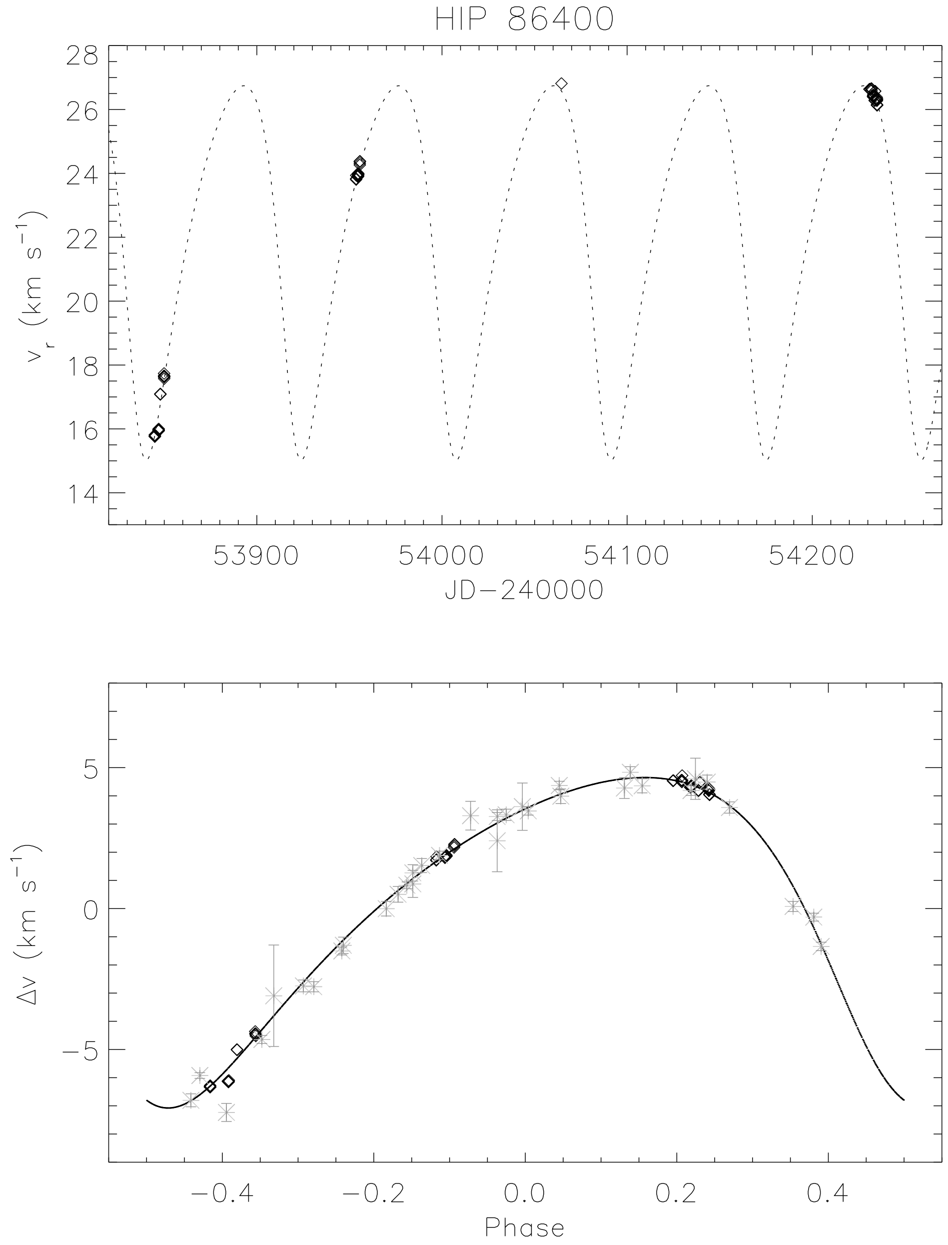

Figure 4.12: Upper panel: radial velocities of HIP 86400 obtained from our observations. The dotted line is a model fit to the data. Lower panel: fit to our radial velocity data (black diamonds) and those of Tokovinin (1991; gray asterisks with error bars). The orbital parameters are given in Table 4.3.

The absolute radial velocities of the non-variable stars HIP 96100 and HIP 23311 can be determined from measurements of the central wavelength shifts of their plateau lines. In a similar way, we can determine absolute radial velocities for HIP 26779, a suspected radial velocity variable, and HIP 88601, which is the primary star of a visual binary system that has an orbital period of 88.3 years and a velocity semi-amplitude of about 3.4 km s^{-1} (Heintz 1988). These measurements can be useful to improve the orbital solution of the systems or look for second order variations in the future.

As explained in detail in Chapter 2, one HET spectrum was used as a radial velocity template on which the cs21 pieces of the spectrum were put together. This HET spectrum was first shifted to an approximate laboratory wavelength frame by using a velocity obtained by comparing the observed central wavelengths of a large set of atomic lines with those measured in the laboratory. At that point, we were not interested in the absolute radial velocity of the star but only required to have the spectrum within about 1 km s^{-1} of its actual radial velocity for the purposes of unequivocally identifying spectral features. We will denote this first approximation to the radial velocity of the star with $\Delta v_r^{\mathrm{HET}}$ (see Table 4.4). The barycentric correction for the Earth-Moon system orbit around the Sun ($\Delta v_r^{\mathrm{bary}}$) was then determined using the method outlined by McCarthy (1995). The maximum error for this correction is expected to be about 5 m s^{-1} (M. Endl; private communication).

Our merged cs21 spectra were used to determine the line shift vs. equivalent width relations shown in Figs. 3.33 to 3.43. In these figures, the plateau

HIP	JD-2454000	$\Delta v_r^{\rm HET}$	$\Delta v_r^{\rm bary}$	$\Delta v_r^{\rm plat}$ (std. error)
96100	231.936693	25.451	1.555	$-0.073 \pm 0.039(0.006)$
23311	406.891895	7.577	14.347	$-0.008 \pm 0.027(0.005)$
88601	205.922914	-29.538	24.810	$-0.032 \pm 0.064(0.008)$
26779	350.969887	-23.794	25.186	$-0.146 \pm 0.064(0.008)$

HIP	$v_r^{\rm cl}$	$\Delta v_r^{\rm rel}$	v_r
96100	26.933 ± 0.008	-0.684 ± 0.057	26.249 ± 0.058
23311	21.916 ± 0.007	-0.709 ± 0.050	21.207 ± 0.050
88601	-4.760 ± 0.009	-0.652 ± 0.063	-5.412 ± 0.064
26779	1.246 ± 0.009	-0.709 ± 0.063	0.537 ± 0.064

Table 4.4: Radial velocities of four of our sample stars. The several corrections are explained in detail in the text. The last column in the bottom table gives our best estimate of their absolute radial velocities. All velocities are given in km s^{-1}.

lines have been put to zero velocity (on their average) by applying the $\Delta v_r^{\rm plat}$ corrections given in Table 4.4. Since, in principle, the plateau lines have zero convective blueshifts, this correction is precisely what is needed to convert $\Delta v_r^{\rm HET} + \Delta v_r^{\rm bary}$ into the absolute radial velocity of the star, but still uncorrected for relativistic effects ($v_r^{\rm cl}$). Note that the standard deviation σ from the mean estimate of $\Delta v_r^{\rm plat}$ is between 30 and 60 m s^{-1}. Assuming that the line shifts of very strong lines in K-dwarfs are not affected by any other systematic error, the standard error $\sigma/\sqrt{n}$ would be an appropriate estimate of the uncertainty of this correction (n being the number of strong lines used to determine the average value). Thus, after including the uncertainty of the barycentric correction, the error in our estimate of $v_r^{\rm cl}$ is less than 10 m s^{-1}.

To finally determine the absolute radial velocity of these two stars, the relativistic gravitational redshift must be removed. From Eq. 1.7 we find that $\Delta v_r^{\mathrm{rel}} = -c\Delta\lambda/\lambda = [-636(M/R) + 3]$ m s^{-1}, if M and R are given in solar units. The +3 term corrects for the effects of the Earth's gravitational field (e.g., Dravins et al. 1999). The negative sign is required here given that this is the correction to be applied; by definition, redshift is always positive. We estimated the masses and radii of the four stars listed in Table 4.4 from the theoretical isochrones by Bertelli et al. (1994), using the methods described in Reddy et al. (2003) and Allende Prieto et al. (2004). Using the mass-to-radius ratios inferred from these calculations, we determined the $\Delta v_r^{\mathrm{rel}}$ values, which allowed us to determine the absolute radial velocities, v_r, given in the last column of the lower section of Table 4.4.

From the calculations presented above, we conclude that only after the granulation effects have been properly taken into account, which implies reliably detecting the plateau in the line shift vs. equivalent width relation and accurately measuring the line shifts of the spectral lines that define the plateau, the uncertainty in the absolute radial velocity of a star is dominated by the error in the gravitational redshift.

Nidever et al. (2002) have determined the absolute radial velocities of a large sample of late-type stars, including HIP 96100, HIP 23311, and HIP 26779. Their approach combines the classical method of cross-correlation with standard star templates (in this case the solar spectrum and an M-dwarf synthetic spectrum for their coolest stars) with the very accurate relative radial velocity determination techniques used in spectroscopic exoplanet detection.

Excluding systematic errors (in particular granulation effects and gravitational redshift), they claim to achieve a precision of about 20 m s^{-1}, although they also provide a more conservative estimate of the error as 30 m s^{-1}, based on comparisons with previous studies.

For HIP 96100, HIP 23311, and HIP 26779, Nidever et al. derived 26.691, 21.552, and 1.207 km s^{-1}, respectively. The differences from our values correspond to 0.442, 0.345, and 0.670 km s^{-1}, with our velocities being smaller in all cases. Since their velocities were obtained by comparison with the solar spectrum, the gravitational redshift has been partially removed. However, in HIP 96100, HIP 23311, and HIP 26779, the gravitational redshifts are 48, 73, and 16 m s^{-1} larger than the solar value, respectively. If these differences are taken into account, the discrepancies between our velocities and those of Nidever et al. reduce to 0.394, 0.272, and 0.654 km s^{-1}.

A similar correction must be taken into account for a "differential" granulation effect. Nidever et al. velocities are affected by the solar convective blueshifts, which are, on average, around 300 m s^{-1} (see Fig. 2 in Allende Prieto & García López 1998), while the blueshifts that we measure in these two K-dwarfs are, on average, about 100 m s^{-1} (Figs. 3.33 and 3.41). Nidever et al. adopted a zero radial velocity for the Sun without correcting for granulation effects (i.e., their analysis assumes that the granulation effects in all stars are the same as in the solar case). When cross-correlating, the resulting radial velocities are redshifted because in reality the reference solar spectrum must be blueshifted. Assuming that the error introduced by granulation in a cross-correlation is the average value of the difference in the convective blueshifts of the two objects, the Nidever et al. velocities for K-dwarfs are further redshifted by about 200 m s^{-1} due to this differential granulation effect. Taking this into account, the differences from our radial velocities reduce to 0.194 km s^{-1} for HIP 96100, 0.072 km s^{-1} for HIP 23311, and 0.454 km s^{-1} for HIP 26779. Note that Nidever et al. already estimated their systematic error due to these effects to be about +0.3 km s^{-1} in K-dwarfs.

The large difference obtained between our radial velocities and those of Nidever et al. for HIP 26779 suggests long-period variability, but the fact that all our radial velocities are smaller than theirs also suggests a systematic difference in the zero point of the two radial velocity scales.

The high stability of the radial velocities of HIP 96100 and HIP 23311 make them good targets for radial velocity standardization, while the precise radial velocity determinations for HIP 26779, a star suspected to have variable radial velocity, and HIP 88601, a confirmed binary star, will be useful to explore their long-term variability. The fact that we detect the plateau in the line shift vs. equivalent width relation due to granulation allows us to remove the effects of surface inhomogeneities and therefore minimize their impact on the absolute radial velocities in such a way that now the error in the gravitational redshift is the dominant source of uncertainty. According to our calculations, the *absolute* radial velocities of these two K-dwarfs are known with an accuracy of about 60 m s $^{-1}$. Furthermore, for HIP 96100, Gray et al. (1992) have shown that the line bisectors are time independent, which suggests that the line shifts (and therefore the granulation correction to the absolute radial velocity) could also be constant, given that they are both observable manifestations of the same phenomenon.

Chapter 5

Summary and Conclusions

The atmospheric structures of cool stars with convective envelopes are inhomogeneous due to the interplay between the radiation field and the hydrodynamic properties of the gas. Near the surface, radiation losses and the strong temperature sensitivity of the continuum opacity induce a very steep temperature gradient, driving convection: ascending cells of gas (the granules) cool down quickly and fall, literally by their own weight, back into the stellar interior through filamentary structures (the intergranular lanes).

Surface convection manifests as the granulation phenomenon, which is directly observed in spatially resolved images of the solar disk. For distant stars, the signatures of granulation can be detected in their spectra using precise measurements of absorption line profiles. The high degree of correlation between the intensity and velocity fields in inhomogeneous stellar atmospheres produces asymmetric lines, with characteristic C-shape bisectors, although in some cases the bisectors resemble only the upper or lower parts of the letter C. In addition, the central wavelengths of spectral lines formed in stellar granulation are blueshifted, owing to the larger contribution to the emergent flux from the brighter, hotter ascending gas.

In this work, the signatures of granulation on the spectra of a small sample of K-dwarfs were detected using very high resolution ($R \simeq 180,000$), high signal-to-noise ($S/N > 300$) observations with a spectral coverage from 5580 to 7800 Å. Not only were the data of very high quality, but also the reduction and post-reduction processing was carefully designed to preserve the relatively small effects of surface inhomogeneities. Thus, we were able to determine relative radial velocity shifts with a mean accuracy of 12 m s^{-1} for pairs of spectra of the same object, without requiring the spectrograph to be placed in a vacuum chamber or superimposing iodine features on the stellar spectra. The accurate determination of relative shifts was crucial for coadding multiple exposures of the same object to increase the signal-to-noise ratio of the observations while keeping the data useful for the detection and measurement of the relatively weak granulation signatures, which in fact require very high S/N. However, we cannot guarantee that these values correspond to the real relative velocity variations of the stars because of shifts that could have been introduced by instrumental imperfections and/or environmental effects (e.g., variations of the air properties in the spectrograph room).

Using our processed spectra, we measured the bisectors of a large number of Fe I lines and averaged them out in groups of similar line-strength to minimize the impact of blends and noise. The observed mean bisectors for the strongest lines have a shape resembling the lower part of the letter C (sometimes also referred to as a backslash shape; \), which spans up to about 100 m s^{-1} (this value corresponds to the difference in velocity between the bluest and reddest points of the line bisector), even though the exact value depends on the particular K-dwarf star under consideration. We find that stellar rotation, and perhaps also activity, influence the shapes of the line bisectors, reducing their magnitudes by up to one half compared to inactive stars with low $V \sin i$ values, thus making the lines appear more symmetric. Although the effect of the projected rotational velocity is well understood, we can only speculate about the impact of stellar activity based on an apparent correlation of level of chromospheric emission with line bisector span.

Central wavelength shifts were also determined for all our K-dwarf sample stars and they were found to show the typical properties of stellar granulation; for example, the weakest lines, which are formed in deep regions of the photosphere, where the correlation between temperature and velocity fields is very strong, show the largest blueshifts. Furthermore, the blueshifts decrease (i.e., the central wavelength shift, by definition positive for redshift, increases) for stronger lines and, for some of our sample stars, they appear to reach a constant value for Fe I lines stronger than about 100 mÅ. We interpret this plateau as line formation taking place in high photospheric layers, where the correlation between intensity and velocity fields is very weak or null and therefore the convective line shifts are expected to be nearly zero. This behavior had only been identified before in the solar spectrum. The detection of the plateau allows us to determine the zero point of the convective blueshifts, which is necessary to remove the large uncertainties due to granulation in the determination of absolute stellar radial velocities (see below). In some of our

K-dwarfs, the plateau could not be reliably detected, most likely due to extrinsic effects such as observational noise, scatter due to large rotational velocities, or stellar activity.

Thanks to our quantitative understanding of the effects of granulation on the central wavelengths of Fe I lines in the spectra of K-dwarfs, we have been able to determine the absolute radial velocities of two stars that have non-variable radial velocities and a very well defined plateau in the convective blueshift vs. line strength relation. For these stars we find:

$$v_r = +26.246 \pm 0.058 \text{ km s}^{-1} \text{ (HIP 96100)}$$

$$v_r = +21.204 \pm 0.050 \text{ km s}^{-1} \text{ (HIP 23311)}$$

where the uncertainties are dominated by errors in the determination of the gravitational redshifts that affect the radial velocities. These extremely accurate measurements make these stars, together with the Sun and asteroids with known orbits, the best radial velocity standards available. In addition, we have measured radial velocities with similar precision for two stars that show long-term variability:

$$v_r = -5.412 \pm 0.064 \text{ km s}^{-1} \text{ (HIP 88601, RJD} = 205.922914)$$

$$v_r = +0.537 \pm 0.064 \text{ km s}^{-1} \text{ (HIP 26779, RJD} = 350.969887)$$

where RJD=JD–2454000. HIP 88601 is the primary star of a visual binary system while HIP 26779 is a suspected radial velocity variable.

As explained above, the apparent non-detection of the plateau in other sample stars does not imply that granulation on their surfaces behaves differently, given that they suffer from other phenomena that preclude detection. Therefore, we expect the effects of surface inhomogeneities on central wavelength shifts to be similar among all K-type dwarfs, which implies that, in principle, the uncertainties in their radial velocity determinations can be significantly reduced by removing the effects of granulation using our findings. In particular, the absolute radial velocity of any K-dwarf star could be determined from the wavelength shifts of their Fe I lines stronger than about 100 mÅ because we have shown that the convective blueshifts vanish for such strong lines. This could be extremely useful for future massive spectroscopic surveys (e.g, GAIA), where millions of K-type dwarfs (and also G-type dwarfs and K-giants, see below) can be used to establish an accurate zero point for the stellar radial velocities.

A state-of-the-art radiative-hydrodynamic three-dimensional simulation of a K-dwarf stellar atmosphere with fundamental parameters: $T_{\rm eff} = 4820\,{\rm K}$, $\log g = 4.5$, and $[{\rm Fe/H}] = 0$, was computed using a theoretical prescription that has proven successful at reproducing the observed properties of solar granulation. We used this model to calculate theoretical Fe I line profiles affected by granulation. After carefully taking into account the effects of stellar rotation and finite spectral resolution, the line bisectors and wavelength shifts obtained from these theoretical calculations were shown to agree with the observed ones at a level of about 90–95 %. This good agreement demonstrates that the 3D model for K-dwarf granulation accounts for most of the factors that determine the detailed shapes of Fe I line profiles. This, in turn, means that the physics invoked in these parameter-free simulations is very realistic and only minor details may need to be revised. We have therefore validated the 3D K-dwarf model atmosphere for use in other types of studies. It should be emphasized that, although the 3D model represents a significant improvement relative to the 1D scenario, there is still room for improvement; for example, the simulation predicts convective redshifts of about 70 m s^{-1} for the strongest Fe I lines, even though we expect them to be nearly zero.

Spectrum synthesis using the K-dwarf hydrodynamic model atmosphere allowed us to quantify 3D effects on the classical spectroscopic determination of chemical compositions and fundamental parameters of K-dwarfs. Using data for one of our sample stars with parameters very similar to those of the 3D model, we find that the classical spectroscopic abundance analysis using 1D model atmospheres results in an abundance difference of about 0.15 dex for the iron abundance when determined from Fe I and Fe II lines separately (the former giving smaller abundances). Calculations using the 3D model show that this difference could be reduced by up to two thirds, i.e., the Fe I vs. Fe II discrepancy could be 0.05 dex if 3D effects are taken into account. This improvement factor of 2/3 was determined using models with a surface gravity of $\log g = 4.5$, where the Fe II minus Fe I abundance difference in 1D is 0.06 dex and 0.02 dex in 3D, while K-type dwarfs, however, have $\log g \simeq 4.6$. This statement therefore needs to be confirmed with 3D models of $\log g = 4.6$

and also for more metal rich and cooler dwarf stars, where the iron ionization imbalance obtained with 1D models is more severe.

Moreover, we find that the observed line broadening of Fe I lines is accurately reproduced by the 3D model calculations without introducing the fudge factors of micro and macroturbulence; i.e., the granulation velocity fields predicted by the model replace those 1D free parameters. This has important consequences for the determination of abundances and stellar rotation rates. The microturbulence (v_t) affects the strengths of the lines, and, if it is not accurately determined, it could introduce a spurious shift to the abundances derived in classical spectroscopic analyses. For example, we find that, in one of our sample stars, v_t could be anywhere between 0 and 1 km s^{-1}, which corresponds to an uncertainty in the iron abundance of about 0.1 dex. This error is eliminated completely by the 3D model calculations, because the v_t parameter is no longer required. On the other hand, in classical spectroscopic analyses, the predicted lines are convolved with rotational and macroturbulence profiles to match the observed data. Two free parameters enter in this procedure, namely the projected rotational velocity of the star, $V \sin i$, and the macroturbulence v_{mac}. Our 3D model calculations show that the predicted line profiles are in excellent agreement with the observed ones for lines convolved with rotational profiles alone, thus excluding the need for the uncertain v_{mac} parameter.

The synthesis of a spectral region containing both atomic and molecular (MgH) features shows that while 1D and 3D model predictions agree on the strengths of atomic lines, the molecular features are significantly stronger in the 3D calculations. When compared with the observations, it is shown that the 3D case provides a much better fit to the data. In order for 1D models to produce similar good agreement, the abundance of Mg must be increased by a factor of 2 (or 0.3 dex in [Mg/H]). While this finding is encouraging, similar analyses must be done for more spectral regions affected by molecular bands, especially due molecules other than MgH, to corroborate that 3D corrections to abundances derived from molecular features have indeed those large magnitudes and successfully model the observed data. If these 3D corrections are proven robust, they can be crucial not only for spectroscopic analyses of molecular features but also for the interpretation of broad and medium band photometry, which is significantly affected by the presence of strong molecular bands in cool stars (for example, the G-band, due to CH, affects photometric measurements in the UV and blue spectral regions).

Due to the different values of the continuum infrared fluxes predicted by 1D and 3D models, 3D corrections are necessary for the effective temperature determination via the so-called infrared flux method (IRFM), which we believe remains the most accurate method of T_{eff} determination for nearby stars. Nonetheless, the 3D corrections to the IRFM temperatures are modest, amounting to about +30 K for both solar-type stars and K-dwarfs. For the Sun, this correction improves the agreement with the value measured directly; the difference between IRFM and direct solar temperatures is changed from about −30 K to +10 K.

The 3D iron abundances from Fe I lines determined for the K-dwarf star in our sample with parameters identical to those of the 3D model show a dependence with the excitation potential of the transitions, thus implying a larger excitation temperature. The trend is almost identical to that obtained with 1D Kurucz models, which suggests that other factors, perhaps departures from LTE, are responsible for the discrepancy.

Very high resolution, high signal-to-noise observations, similar to those obtained for our K-dwarfs but with a different spectral coverage (4400–7500 Å), were obtained for five stars covering most of the regions of the HR diagram where granulation is expected to be present, namely FGK dwarfs and K-giants. The analysis of these data is presented in Appendix A. As expected, surface inhomogeneities explain the line bisectors and wavelength shifts observed in the spectra of these stars. Moreover, the span of the line bisectors, and the magnitude of the maximum blueshifts increase for higher effective temperatures and lower surface gravities, as predicted by models of stellar granulation. In particular, we confirm bisector spans of several hundreds of meters per second for F-dwarfs and K-giants. Besides showing different spans, the detailed shapes of the line bisectors of K-type dwarf and giants also differ significantly. The bisectors of the strongest lines in the spectra of K-dwarf resemble the lower part of the letter C while those observed in the K-giants resemble more the upper part of the letter C. We also find a plateau in the convective blueshift vs. equivalent width relations of G and K dwarfs, as well as K-giants, implying that very accurate absolute radial velocities can be determined for these types of objects. Furthermore, the lowest EW value of the plateau in these relations is found to increase with effective temperature. The plateau is not detected in Procyon (an F5 subgiant) and it is not clear whether lines stronger than around 250 mÅ need to be analyzed or if the plateau does not exist.

Our work demonstrates that the relatively small impact of surface inhomogeneities on stellar spectra can not only be detected but also accurately quantified with well planned observing and data processing strategies. The results can be used to constrain state-of-the-art hydrodynamic simulations of stellar atmospheres, which is important not only because they help understanding the physics behind stellar granulation but also because they will eventually become the standard in spectroscopic studies of stellar abundances.

Appendix A

Granulation across the HR diagram

Very high resolution spectra of five bright stars scattered through the HR diagram were acquired by C. Allende Prieto and D. L. Lambert using the 2dcoudé spectrograph (cs21 mode) on the 2.7-m Telescope at McDonald Observatory during three observing runs in June 2000, November 2000, and March 2001. Day skylight observations were also acquired in this period. The five stars observed are listed in Table A.1. These cs21 observations fully cover the spectral range from about 4400 to 7500 Å, except those for β Vir, for which the lower limit is 5320 Å, and have very high signal-to-noise ratios ($S/N > 600$, otherwise limited by the S/N ratios of the flat fields, which are around 1,000). The spectral resolution of the data ($R \sim 200,000$) is ideal for granulation studies. Similarly to the K-dwarf observations made for this thesis, these data are of unprecedented quality, but note that the wavelength coverages are different (the K-dwarf data covers from about 5580 to 7800 Å).

We reduced and processed these spectra using the methods described in Chapter 2. In particular, between 2007 and 2008, we acquired HET spectra of these objects to use them as radial velocity templates and applied the normalization of the S^4N spectra to the data, as explained in detail in Sect. 2.4. For τ Cet, however, we used the HET spectrum of HIP 96100 as the radial velocity

Object	Spectral Type	V mag	$T_{\rm eff}, \log g$, [Fe/H] K,[cm s^{-2}],dex	Observed
Procyon	F5IV-V	0.3	$6591, 4.04, -0.01$	Nov-00, Mar-01
β Vir	F9V	3.6	$6075, 4.16, +0.13$	Jun-00, Nov-00
τ Cet	G8.5V	3.5	$5372, 4.36, -0.54$	Nov-00
Arcturus	K1.5III	0.0	$4231, 1.67, -0.55$	Jun-00, Mar-01
Pollux	K0IIIb	1.2	$4833, 2.70, -0.02$	Nov-00

Table A.1: Sample of stars observed with the 2dcoudé spectrograph. The spectral types are those given by SIMBAD and the fundamental parameters are those determined by Ramírez & Meléndez (2005a).

template because of its low declination ($\delta \sim -15°$), which is unreachable by the HET. Note that this does not change the line bisector shapes of τ Cet but it can introduce noise to the line shift vs. equivalent width trend (although it will not alter its shape) due to errors in the merging procedure (Sect. 2.4).

Using the techniques described in Sects. 3.2.1 and 3.2.2, we measured the bisectors and central wavelength shifts of a large number of Fe I lines listed in the catalog of Nave et al. (1994). For the wavelength shifts, we only used those lines that have measured wavelengths with an uncertainty of about 75 m s^{-1} or less. As we did for the K-dwarfs, the line shifts measured in the skylight spectrum were used to further clean the line list (cf. Sect. 3.2.2).

For each star, the individual line bisectors were averaged for four groups of lines of similar strength. The mean line bisectors are shown in Figs. A.1 to A.7. For comparison, we also include the skylight (Fig. A.3) and HIP 96100 (Fig. A.5) results. The latter come from the observations made recently for this thesis. Note that these figures are similar to Figs. 3.21 to 3.31 but the axes scales are different (they are larger here to account for the larger granulation effects of some of these stars).

Similarly, Figs. A.8 to A.14 show the central wavelength shifts measured in the spectra of these bright stars, as well as those obtained from the skylight spectrum and that of HIP 96100, the latter from our recent observations, for comparison. These figures are also similar to those shown in Figs. 3.33 to 3.43 for our K-dwarfs but the y-axis scale has been expanded.

Procyon, β Vir, τ Cet, and HIP 96100 cover the main-sequence from mid-F to early-K spectral types, although Procyon is a subgiant. The magnitude of the line bisectors, as well as the maximum convective blueshifts (in absolute value), clearly increase with effective temperature. In Procyon, the line bisectors of the strongest lines span up to 500 m s^{-1}, while bisectors of lines of depth around 0.75 have a magnitude of about 300 m s^{-1}. In K-dwarfs, these numbers reduce to about 100 m s^{-1} for the strong lines and almost 0 for the weak lines. The maximum convective blueshift in Procyon is probably larger than about 500 m s^{-1} (the plateau could not be detected in Fig. A.8 and therefore the zero point of the y-axis in that figure is not well defined), while that for the K-dwarf is about 200 m s^{-1}. The line bisectors show the characteristic C-shape for the late-F and early-G type stars. In Procyon, the line bisectors have a shape that resemble only the upper part of the letter C, while those in the late-G and K-dwarf stars have a backslash (\) shape (or the shape of the lower part of the letter C). The point of inflection of the line bisectors is therefore sensitive to the effective temperature.

A comparison of our measurements of line bisectors and wavelength shifts in the spectrum of Procyon with those determined by Allende Prieto et al. (2002) reveal an excellent agreement. Our data, however, has a wavelength coverage about 3 times larger than that used by Allende Prieto et al., which goes from about 4560 to 5780 Å.

The line shift vs. equivalent width relations in the F dwarfs show a linear trend with no clear signature of a plateau at large EW values for Procyon. Although it is difficult to confirm because of the large scatter, the plateau is also probably present in β Vir (Fig. A.9). On the other hand, the plateau is clearly detected in the G and K dwarfs. Furthermore, the minimum EW of the plateau seems to depends on $T_{\rm eff}$; it is roughly at 170 mÅ in the Sun, at 120 mÅ in τ Cet, and slightly below 100 mÅ in HIP 96100; for the late F-type star β Vir, it is probably at about 200 mÅ. Extrapolating to its effective temperature, the plateau in Procyon should be located at EW $>$ 250 mÅ, which would explain why it is not detected; only three points in Fig. A.8 have $EW > 250$ mÅ. Observations in the near UV, where many very strong Fe I lines are present, could help determining whether such plateau exists, although the accurate measurement of equivalent widths is extremely difficult there due to line-blending. As explained in Sect. 4.4, detecting the plateau is necessary for accurate absolute radial velocity measurements.

For the cool K-giants, the line bisectors resemble those of the warm F-dwarfs more than those of the K-dwarfs. Their magnitudes are also as large as the F-dwarf case. However, it seems that the bluest point of the bisector corresponds to a larger line-depth in the K-giants compared to the F-dwarfs. The effect is even more clear when comparing the bisectors of K-dwarfs with K-giants; the relative flux value of the bluemost point of the line bisector is larger for the dwarfs and smaller for the giants. This effect has been studied in detail by Gray (2005) using a single spectral feature. Our results confirm his finding that the flux values of the bluemost points of the line bisectors are sensitive to the luminosity type of the star.

Contrary to the F-dwarf case, even though the convective blueshifts observed in the spectra of K-giants are large (the maximum blueshift is about 700 m s^{-1}), a plateau is clearly detected for lines stronger than about 270 mÅ. In addition to allowing us to determine the zero point of the line-shift vs. equivalent width relation, the detection of the plateau opens the possibility of determining accurate absolute radial velocities of K-giants, which may be very important given the large magnitude of the granulation effects.

From the analysis of the detailed line profiles of these 5 bright stars, a very obvious qualitative conclusion can be made; the effects of granulation increase with higher effective temperature and lower surface gravity. Older hydrodynamic models (Nordlund & Dravins 1990) have been successful at reproducing these trends, but a detailed comparison of these observations with the predictions of more recent and improved simulations (e.g., Trampedach 2007) can help us to better understand the physics of the granulation phenomenon, as well as serve as fundamental tests of the accuracy and realism of the 3D simulations.

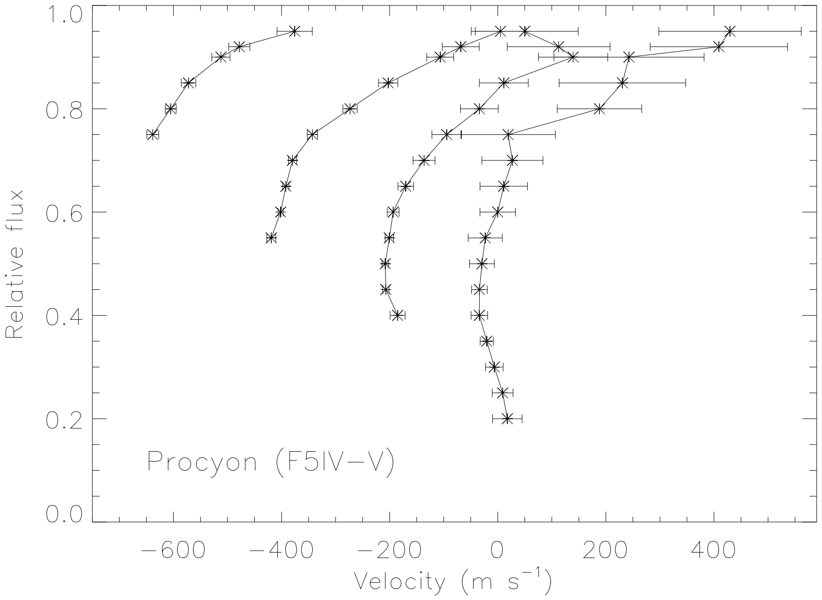

Figure A.1: Mean line bisectors of four groups of spectral lines of similar strength in the spectrum of Procyon. All line bisectors were measured with respect to their central wavelengths; shifts of -200, -400, and -600 m s^{-1} have been applied here to the weaker lines for clarity. The error bars correspond to the standard error of the line-to-line scatter; i.e., $\sigma/\sqrt{n}$, where σ is the standard deviation and n the number of lines.

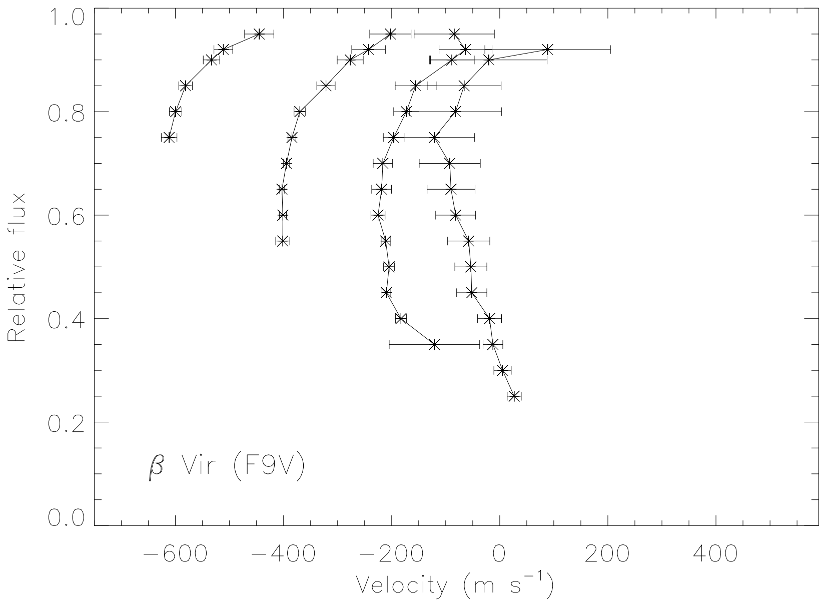

Figure A.2: As in Fig. A.1 for β Vir.

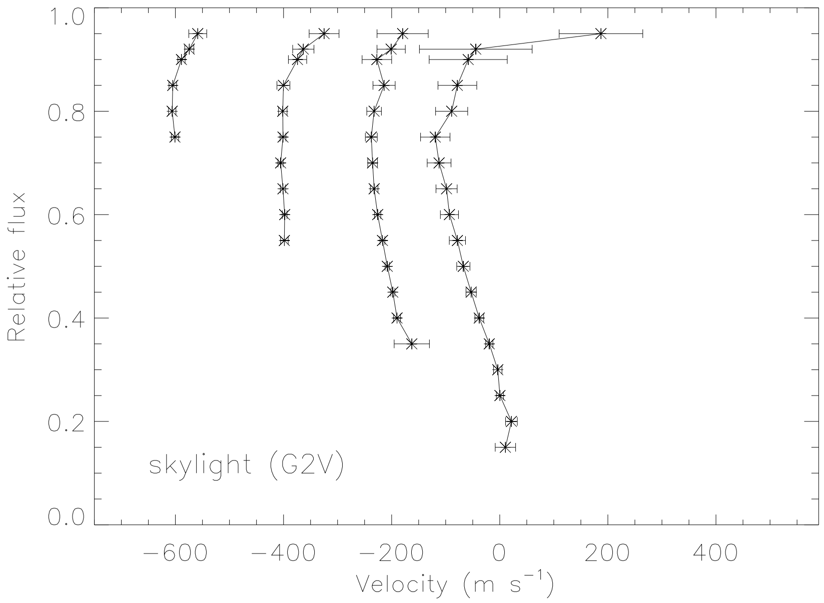

Figure A.3: As in Fig. A.1 for the skylight observations.

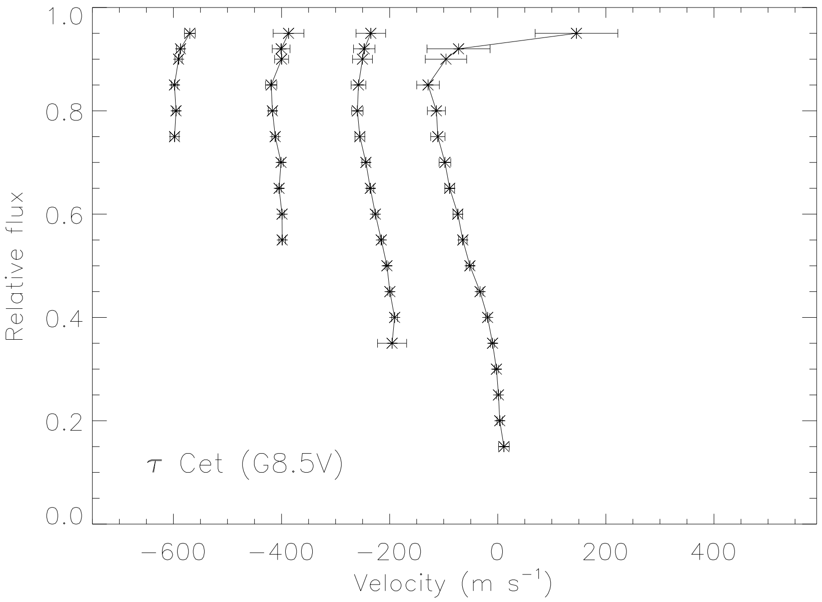

Figure A.4: As in Fig. A.1 for τ Cet.

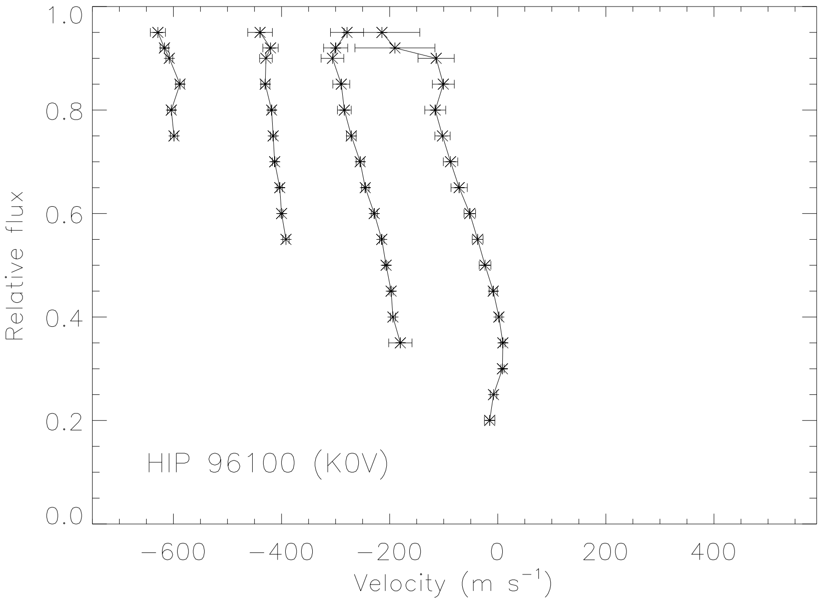

Figure A.5: As in Fig. A.1 for HIP 96100 (compare with Fig. 3.21).

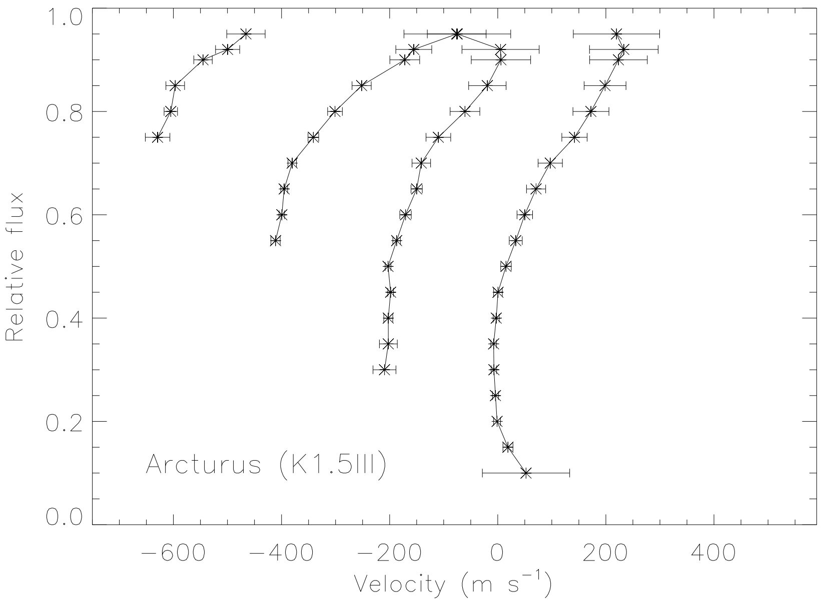

Figure A.6: As in Fig. A.1 for Arcturus.

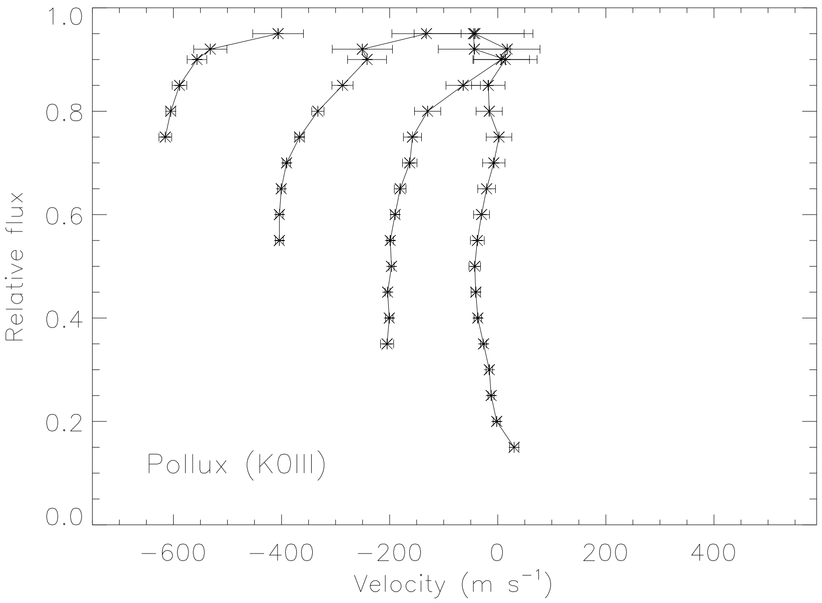

Figure A.7: As in Fig. A.1 for Pollux.

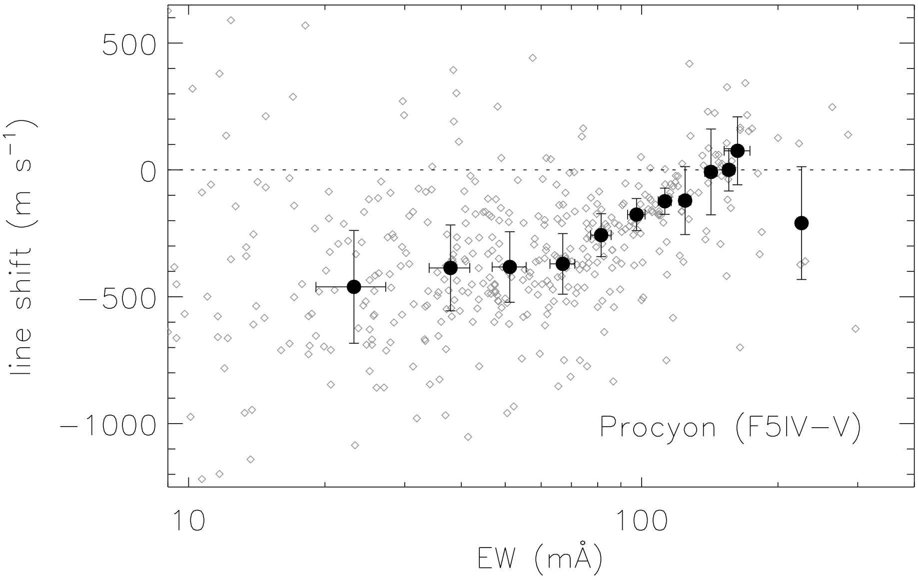

Figure A.8: Central wavelength shifts measured in the spectrum of Procyon as a function of line equivalent width (small diamonds). The filled circles with error bars represent average values in bins of equivalent width. The zero point of this relation has been set using the strongest lines, those that define the plateau (see text for details). Note that the x-axis scale is logarithmic.

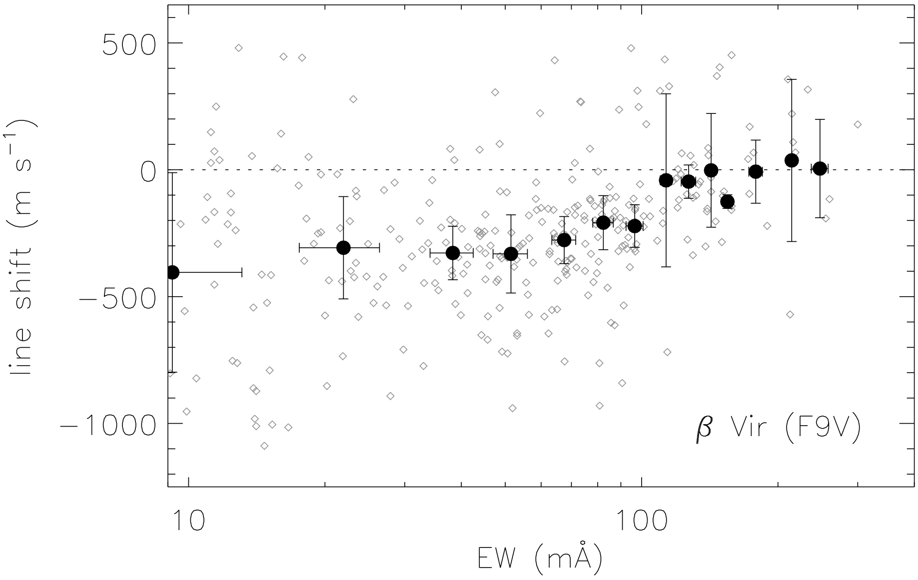

Figure A.9: As in Fig. A.8 for β Vir.

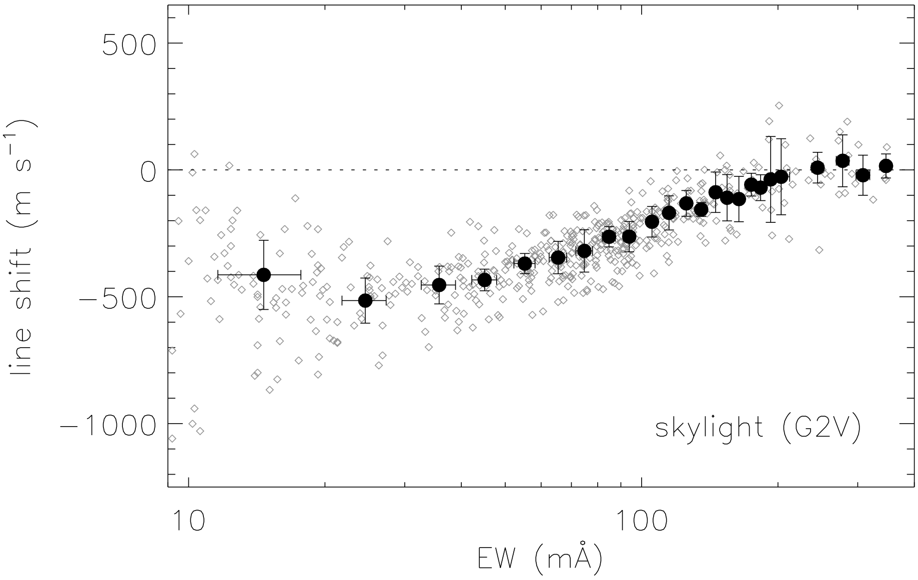

Figure A.10: As in Fig. A.8 for the skylight observations.

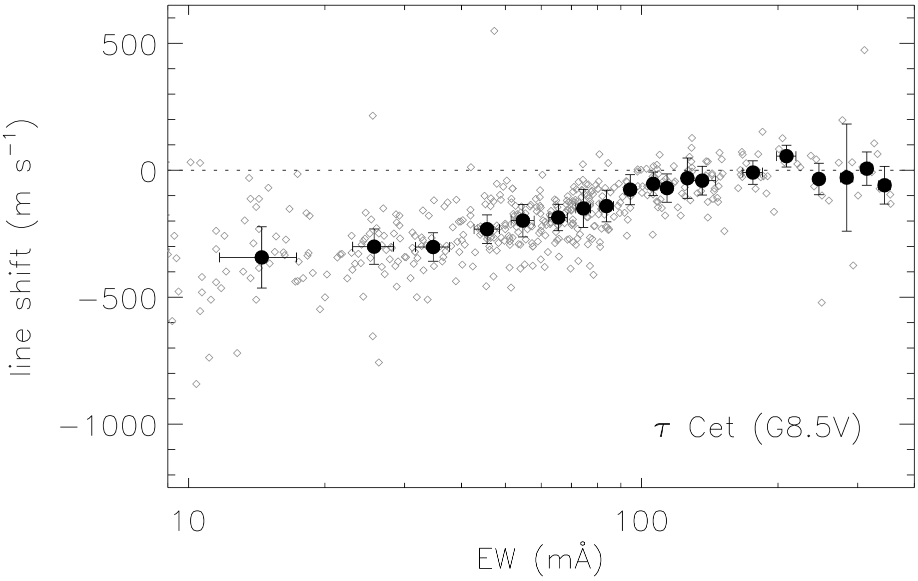

Figure A.11: As in Fig. A.8 for τ Cet.

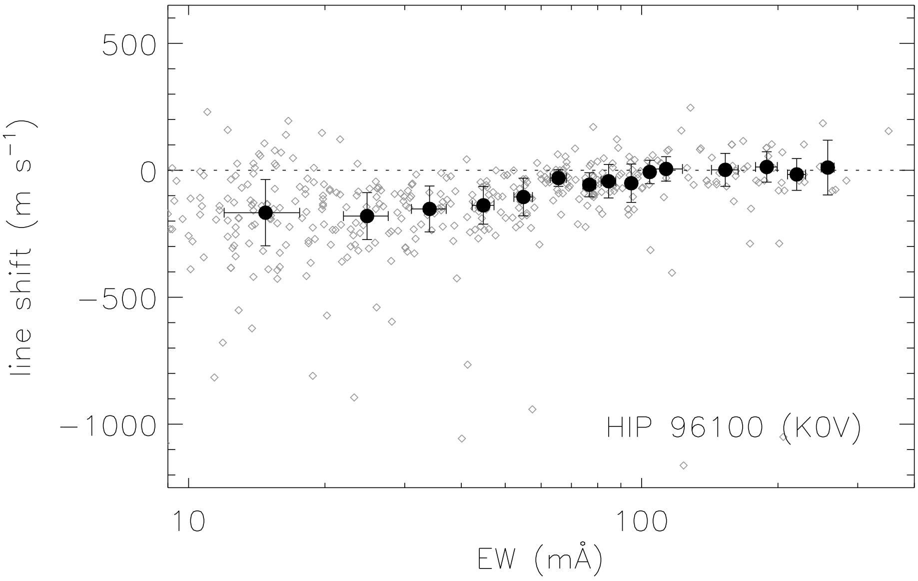

Figure A.12: As in Fig. A.8 for HIP 96100 (compare with Fig. 3.33).

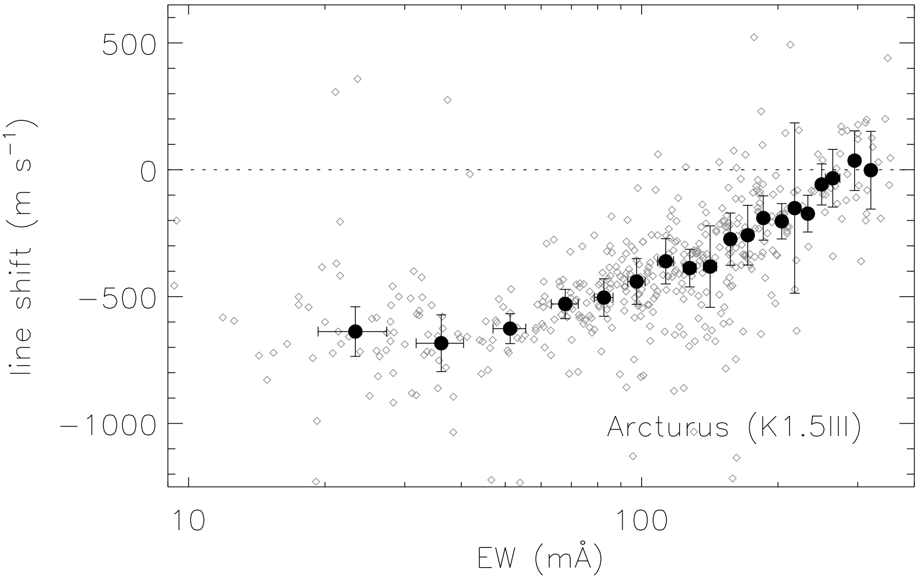

Figure A.13: As in Fig. A.8 for Arcturus.

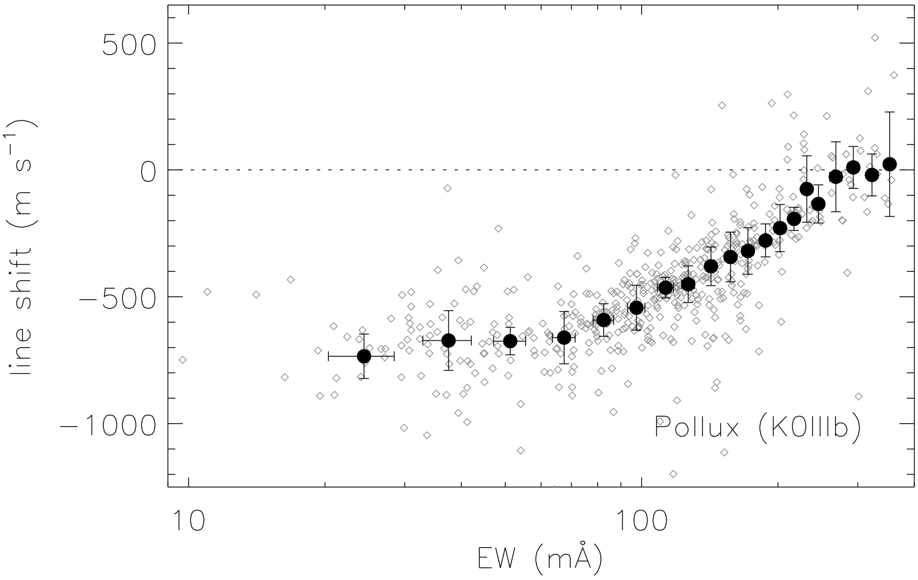

Figure A.14: As in Fig. A.8 for Pollux.

Appendix B

The Advanced Spectrum Synthesis 3D Tool

A computer code for solving the radiative transfer problem in 3D model atmospheres has been recently developed by L. Koesterke, in collaboration with C. Allende Prieto and D. L. Lambert, and was kindly made available for this thesis. A brief description of the code is given by Koesterke et al. (2008), who used it to study the center-to-limb variation of the solar continuum and a few spectral lines.

Koesterke et al. (2008) "Advanced Spectrum Synthesis 3D Tool" (Assϵt) represents an improvement over previous 3D codes because it is not limited to the calculation of single lines, simple blends, or constant background opacities. Also, it properly includes electron and Rayleigh scattering due to atomic hydrogen, and it uses improved (higher-order) interpolation schemes within the simulation grid points for the calculation of opacities and intensities. In addition, Assϵt is capable of working with 1D models, which allows 1D vs. 3D comparisons to be made in a consistent manner. Furthermore, the opacity calculation is based on a modified version of the thoroughly tested 1D code `SYNSPEC` (Hubeny 1998, Hubeny & Lanz 1995).

In this work, we used Assϵt to calculate molecular features (Sect. 4.2) as well as stellar continua to explore 3D effects on the determination of effective temperatures with the infrared flux method (Sect. 4.3.1). For the synthesis of atomic lines, however, we used the 3D code “`lte-H`” (e.g., Asplund et al. 2000), as described in Sect. 3.1.2. Figs. B.1 and B.2 show a comparison of atomic line profiles (as well as their bisectors and central wavelength shifts) computed with both 3D codes for a few snapshots of our K-dwarf hydrodynamic simulation. The same input parameters (in particular the atomic data) were adopted in both calculations to ensure a fair comparison.

The maximum difference in the fluxes predicted for the 6151 Å Fe I line occurs near the line center. While Assεt predicts larger absorption there, the maximum difference is only about 1.2 %. The RMS difference, on the other hand, is slightly less than 0.5 %. The shapes of the line bisectors calculated with the two codes agree within about 6 $\mathrm{m\ s^{-1}}$, except near the core of the line and in the vicinity of the continuum. However, the largest differences seen there are only about 20 $\mathrm{m\ s^{-1}}$. The agreement between the two codes from the comparison of the 5197.6 Å Fe II line is only slightly degraded; the fluxes differ by about 0.6 % with a maximum difference of about 1.8 % near the line center, while the line bisectors agree within about 9 $\mathrm{m\ s^{-1}}$ and the maximum difference occurs near the continuum, where it amounts to about 20 $\mathrm{m\ s^{-1}}$. In both Figs. B.1 and B.2 it is also seen that the bisectors of the lines computed with Assεt are smoother than those from `lte-H`, which could be due to the improvement of the interpolation schemes in the former or rounding errors for the latter. This speculative statement must be confirmed with further tests.

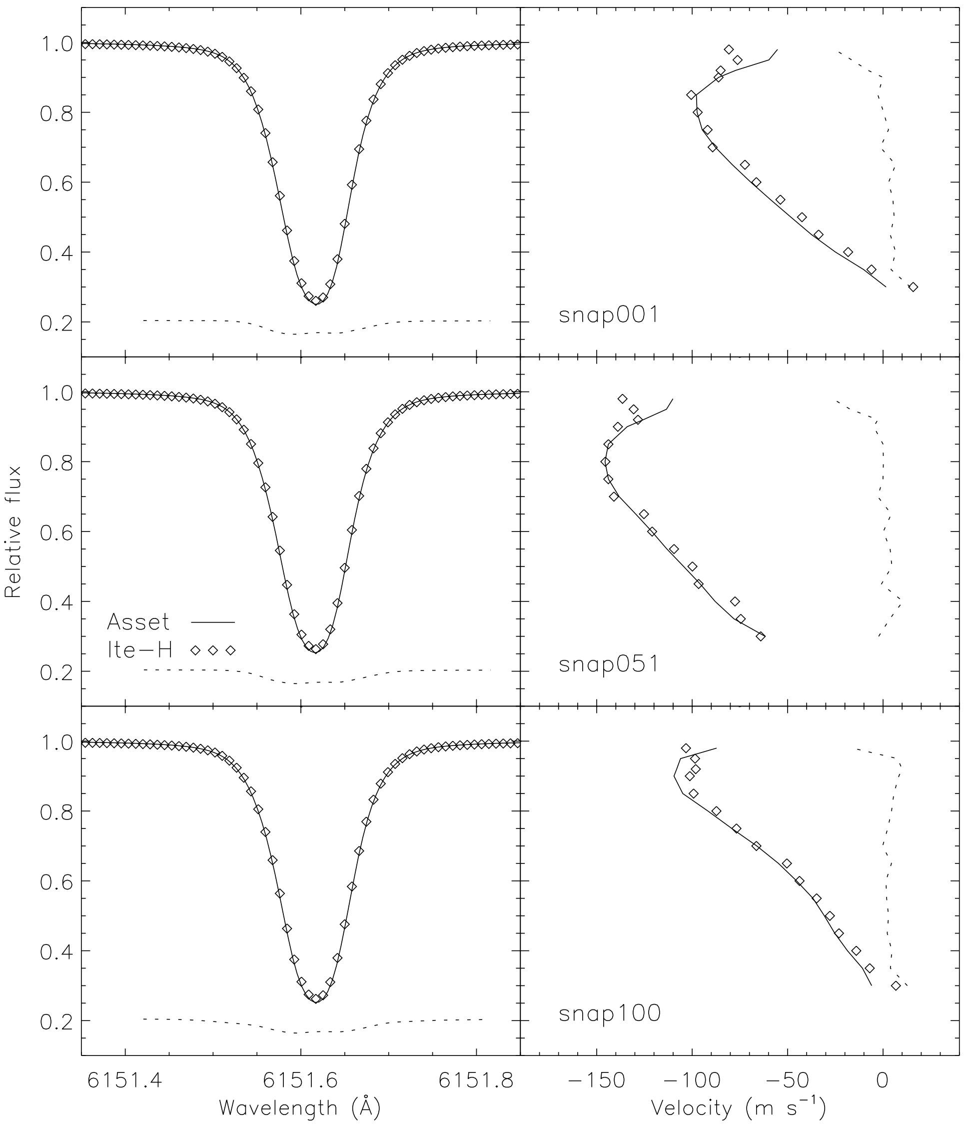

Figure B.1: Line profiles for the 6151.6 Å Fe I line calculated using 2 different spectrum synthesis codes (Asset and `lte-H`; see legend in middle left panel) but the same hydrodynamic simulation (our 3D K-dwarf model). The right panels show the bisectors, including the net convective blueshift, associated with the line profiles. Calculations for three snapshots of the simulation, the first (snap001), last (snap100), and an intermediate one (snap051), are shown. The dotted lines represent the difference between the two model predictions in flux (multiplied by a factor of 3 and shifted to a flux value of 0.2, left panels) and line asymmetry (right panels).

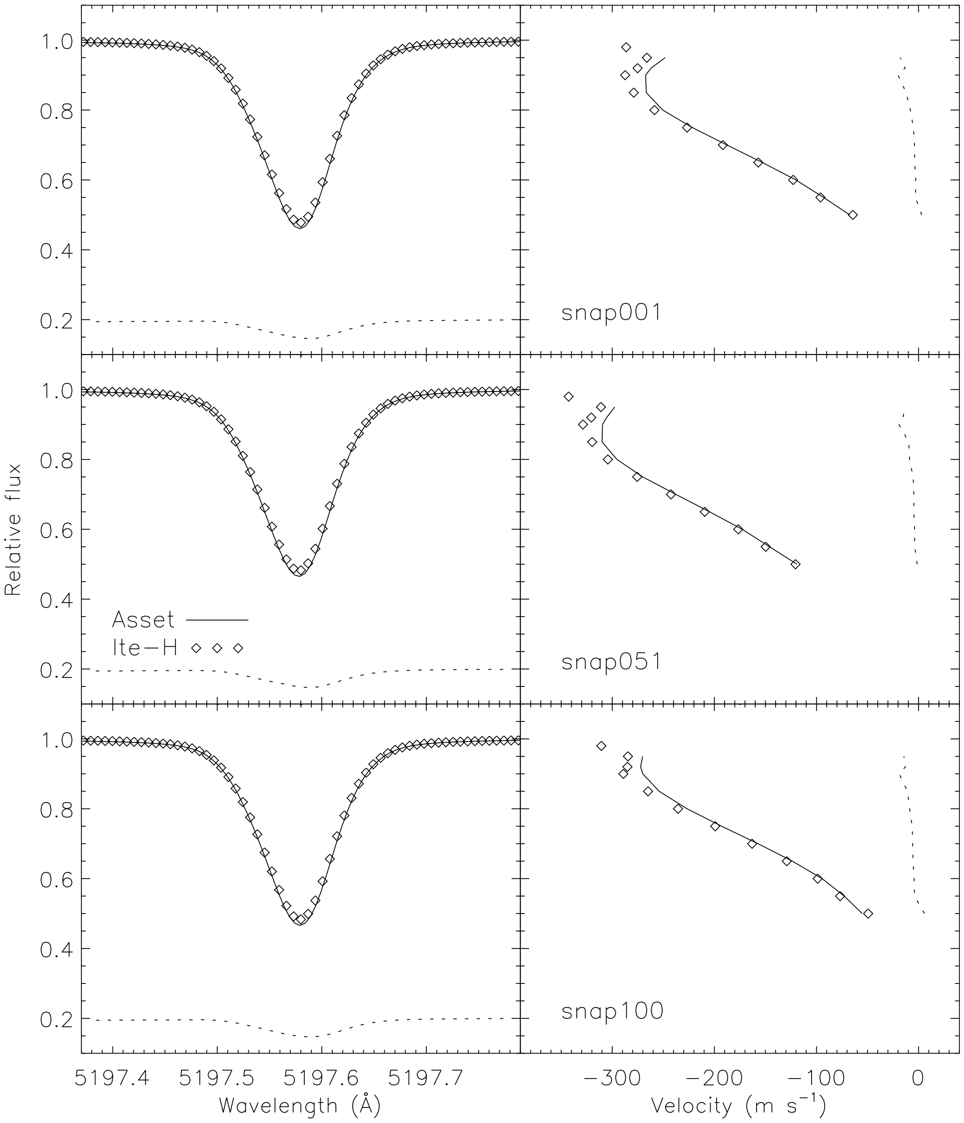

Figure B.2: As in Fig. B.1 for the 5197.6 Å Fe II line. Note that the scale of the x-axis on the right panels is larger than in Fig. B.1.

References

Abramowitz, M., & Stegun, I. A. 1972, *Handbook of Mathematical Functions*, New York: Dover

Achmad, L., de Jager, C., & Nieuwenhuijzen, H. 1991, A&A, 250, 445

Allende Prieto, C. 2007, in *Proceedings of the 14th Cambridge Workshop on Cool Stars, Stellar Systems, and the Sun*, ed. G. van Belle, in press (astro-ph/0702429)

Allende Prieto, C., & García López, R. J. 1998, A&AS, 129, 41

Allende Prieto, C., García López, R. J., & Trujillo Bueno, J. 1997, ApJ, 483, 941

Allende Prieto, C., García López, R. J., Lambert, D. L., & Gustafsson, B. 1999, ApJ, 526, 991

Allende Prieto, C., Asplund, M., García López, R. J. 2002, ApJ, 567, 544

Allende Prieto, C., Barklem, P. S., Lambert, D. L., & Cunha, K. 2004, A&A, 420, 183

Alonso, A., Arribas, S., & Martinez-Roger, C. 1996a, A&A, 117, 227

Alonso, A., Arribas, S., & Martinez-Roger, C. 1996b, A&A, 313, 873

Anders, E. & Grevesse, N. 1989, Geochimica et Cosmochimica Acta, 53, 197

Asplund, M. 2005, ARA&A, 43, 481

Asplund, M., & García Pérez, A. E. 2001, A&A, 372, 601

Asplund, M., Nordlund, Å., Trampedach, R., & Stein, R. F. 1999, A&A, 346, L17

Asplund, M., Ludwig, H.-G., Nordlund, Å., & Stein, R. F. 2000a, A&A, 359, 669

Asplund, M., Nordlund, Å., Trampedach, R., et al. 2000b, A&A, 359, 729

Asplund, M., Grevesse, N., Sauval, A. J., et al. 2004, A&A, 417, 751

Asplund, M., Grevesse, N., Sauval, A. J., et al. 2005a, A&A, 431, 693

Asplund, M., Grevesse, N., & Sauval, A. J. 2005b, in *Cosmic Abundances as Records of Stellar Evolution and Nucleosynthesis*, Astronomical Society of the Pacific Conference Series 336, eds. T. G. Barnes and F. N. Bash, F. N., p. 25

Bahcall, J. N., Serenelli, A. M., & Pinsonneault, M. 2004, ApJ, 614, 464

Bahcall, J. N., Basu, S., Pinsonneault, M., & Serenelli, A. M. 2005, ApJ, 618, 1049

Baraffe, I., & Chabrier G. 1996, ApJ, 461, L51

Barklem, P. S., Piskunov, N., & O'Mara, B. J. 2000, A&AS, 142, 467

Barklem, P. S., Stempels, H. C., Allende Prieto, C., et al. 2002, A&A, 385, 951

Basri, G., Mohanty, S., Allard, F., et al. 2000, ApJ, 538, 363

Basu, S., & Antia, H. M. 1997, MNRAS, 287, 189

Basu, S., & Antia, H. M. 2008, Physics Reports, 457, 217

Bean, J. L., Sneden, C., Hauschildt, P. H., et al. 2006, ApJ, 652, 1604

Beatty, T. G., Fernández, J. M., Latham, D., et al. 2007, ApJ, 663, 573

Beers, T. C., & Christlieb, N. 2005, ARA&A, 43, 531

Bensby, T., Feltzing, S., Lundström, I., & Ilyin, I. 2005, A&A, 433, 185

Benz, W., & Mayor, M. 1984, A&A, 138, 183

Bertelli, G., Bressan, A., Chiosi, C., et al. 1994, A&AS, 106, 275

Bienaymé, O. 1999, A&A, 341, 86

Blackwell, D. E., & Shallis, M. J. 1977, MNRAS, 180, 177

Blackwell, D. E., Ibbetson, P. A., Petford, A. D., & Willis, R. B. 1976, MNRAS, 177, 219

Blackwell, D. E., Petford, A. D., & Shallis, M. J. 1980, A&A, 82, 249

Borrero, J. M. 2008, ApJ, 673, 470

Bray, R. J., Loughhead, R. E., & Durrant, C. J. 1984, *The solar granulation*, 2nd ed., Cambridge University Press

Burrows, A., Sudarsky, D., & Hubeny, I. 2006, ApJ, 640, 1063

Carbon, D. F., 1979, ARA&A, 17, 513

Casagrande, L., Portinari, L., & Flynn, C. 2006, MNRAS, 373, 13

Casuso, E., & Beckman, J. E. 2004, A&A, 419, 181

Cayrel, R., & Strobel, G. C. 1966, ARA&A, 4, 1

Chiappini, C., Matteucci, F., & Gratton, R. 1997, ApJ, 477, 765

Cohen, J., Shectman, S., Thomson, I., et al. 2005, ApJ, 633, L109

Claret, A. 1998, A&A, 335, 647

Claret, A. & Giménez, A. 1990, A&A, 230, 412

Colavitti, E., Matteucci, F., & Murante, G. 2008, A&A, in press (astro-ph/0802.1847)

Collet, R., Asplund, M., & Trampedach, R. 2006, ApJ, 644, L121

Collet, R., Asplund, M., & Trampedach, R. 2007, A&A, 469, 687

Dawes, W. R. 1864, MNRAS, 24, 161

Delahaye, F., & Pinsonneault, M. H. 2006, ApJ, 649, 529

Dialetis, D., Macris, C., Muller, R., & Prokakis, T. 1988, A&A, 204, 275

Dravins, D. 1987a, A&A, 172, 200

Dravins, D. 1987b, A&A, 172, 211

Dravins, D., & Nordlund, Å. 1990a, A&A, 228, 184

Dravins, D., & Nordlund, Å. 1990b, A&A, 228, 203

Dravins, D., Lindegren, L., & Nordlund, Å. 1981, A&A, 96, 345

Dravins, D., Gullberg, D., Lindegren, L., & Madsen, S. 1999, in *Precise Stellar Radial Velocities*, ASP Conf. Series 185, eds. J. B. Hearnshaw & C. D. Scarfe, p. 41

Edvardsson, B. Andersen, J., Gustafsson, B., et al. 1993, A&A, 275, 101

Endl, M., Cochran, W. D., Hatzes, A. P., & Wittenmyer, R. A. 2005, in *The Ninth Texas-Mexico Conference on Astrophysics*, RMxAA Ser. Conf. 23, eds. S. Torres-Peimbert and G. MacAlpine, p. 64

Fekel, F. C. 1997, PASP, 109, 514

Flynn, C., & Morell, O. 1997, MNRAS, 286, 617

Fulbright, J. P. 2000, AJ, 120, 1841

Gaidos, E. J., Henry, G. W., & Henry, S. M. 2000, AJ, 120, 1006

Getling, A. V., & Brandt, P. N. 2002, A&A, 382, L5

Glebocki R., Gnacinski P., & Stawikowski A. 2000, Acta Astron., 50, 509

Gray, D. F. 1975, ApJ, 202, 148

Gray, D. F. 1978, Solar Physics, 59, 193

Gray, D. F. 1982, ApJ, 255, 200

Gray, D. F. 1984a, ApJ, 277, 640

Gray, D. F. 1984b, ApJ, 281, 719

Gray, D. F. 1986, PASP, 98, 319

Gray, D. F. 1992, *The Observation and Analysis of Stellar Photospheres*, 2nd ed., Cambridge University Press

Gray, D. F. 2005, PASP, 117, 711

Gray, D. F., & Toner, C. G. 1985, PASP, 97, 543

Gray, D. F., & Nagel, T. 1989, ApJ, 341, 421

Gray, D. F., Baliunas, S. L., Lockwood, G. W., & Skiff, B. A. 1992, ApJ, 400, 681

Gray, D. F., Tycner, C., & Brown, K. 2000, PASP, 112, 328

Gray, R. O., & Corbally, C. J. 1994, AJ, 107, 742

Grevesse, N., & Sauval, A. J. 1998, Space Science Reviews, 85, 161

Grevesse, N., Asplund, M., & Sauval, A. J. 2007, Space Science Reviews, 130, 105

Griffin, R. E., & Griffin, R. 1996, VizieR On-line Data Catalog: III/169A. Originally published as *A photometric atlas of the spectrum of Procyon* $\lambda\lambda = 3140 - 7470\,\text{Å}$; Cambridge: Institute of Astronomy, Observatories, 1979

Gustafsson, B., Bell, R. A., Eriksson, K., & Nordlund, Å. 1975, A&A, 42, 407

Gustafsson B., Edvardsson B., Eriksson K., et al. 2003, ASP Conf. Series 288, eds. I. Hubeny, D. Mihalas, and K.Werner, p. 331

Hale, A. 1994, AJ, 107, 306

Hathaway, D. H., Beck, J. G., Bogart, R. S., et al. 2000, Solar Physics, 193, 299

Hauschildt, P. H., Allard, F., & Baron, E. 1999, ApJ, 512, 377

Haywood, M. 2006, MNRAS, 371, 1760

Heintz, W. D. 1988, JRASC, 82, 140

Herschel, W. 1801a, Philosophical Transactions Series I, 91, 265

Herschel, W. 1801b, Philosophical Transactions Series I, 91, 354

Hill, G. J., MacQueen, P. J., Palunas, P., et al. 2006, in *Ground Based and Airborne Instrumentation for Astronomy*, Proceedings of the SPIE 6269, ed. I. C. McLean and M. Iye, p. 5

Hinshaw, G., Weiland, J. L., Hill, R. S., et al. 2008, ApJS, submitted (astro-ph/0803.0732)

Hirzberger, J., Vásquez, M., Bonet, J. A., et al. 1997, ApJ, 480, 406

Holweger, H. & Mueller, E. A. 1974, Solar Physics, 39, 19

Hubeny, I. 1988, Computer Phys. Comm., 52, 103

Hubeny, I., & Lanz, T. 1995, ApJ, 439, 875

Jancart, S., Jorissen, A., Babusiaux, C., & Pourbaix, D. 2005, A&A, 442, 365

Janssen, J. 1896, Ann. Obs. Astrophys. Paris Meudon, 1, 91

Jefferys, W. H., Fitzpatrick, M. J., & McArthur, B. E. 1988, Celestial Mechanics, 41, 39

King, J. R., Villareal, A. R., Soderblom, D., et al. 2003, AJ, 125, 1980

Kobayashi, C., Umeda, H., Nomoto, K., et al. 2006, ApJ, 653, 1145

Koesterke, L., Allende Prieto, C., & Lambert, D. L. 2008, ApJ, in press (astro-ph/0802.2177)

Korn, A. J., Shi, J., & Gehren, T. 2003, A&A, 407, 691

Korn, A. J., Grundahl, F., Richard O., et al. 2006, Nature, 442, 657

Kotoneva, E., Flynn, C., Chiappini, C., & Matteucci, F. 2002, MNRAS, 336, 879

Kurucz, R. L. 1979, ApJS, 40, 1

Kurucz, R. L. 1993a, *ATLAS9 Stellar Atmosphere Programs and 2 km/s grid.* Kurucz CD-ROM No. 13. Cambridge, Mass.: Smithsonian Astrophysical Observatory

Kurucz, R. L. 1993b, *SYNTHE Spectrum Synthesis Programs and Line Data.* Kurucz CD-ROM No. 18. Cambridge, Mass.: Smithsonian Astrophysical Observatory

Kurucz, R. L., Furenlid, I., Brault, J., & Testerman, L. 1984, *Solar flux atlas from 296 to 1300 nm*, National Solar Observatory Atlas, Sunspot, New Mexico: National Solar Observatory, 1984

Lambert, D. L. 2004, in *The New Cosmology: Conference on Strings and Cosmology*, American Institute of Physics Conference Series, 743; eds. Allen, R. E., Nanopoulos, D. V., & Pope, C. N., p. 206

Lambert, D. L., Mallia, E. A., & Petford, A. D. 1971, MNRAS, 154, 265

Landau, L. D., & Lifshitz, E. M. 1987, *Fluid Mechanics*, 2nd edition, Butterworth-Heinemann, Oxford

Lanz, T., & Hubeny, I. 1995, ApJ, 439, 905

Lawrence, J. K., Cadavid. A. C., & Ruzmaikin, A. A. 1999, ApJ, 513, 506

Lindegren, L., & Dravins, D. 2003, A&A, 401, 1185

Lindegren, L., Dravins, D., & Madsen, S. 1999, in *Precise Stellar Radial Velocities*, ASP Conf. Ser. 185, eds. J. B. Hearnshaw and C. D. Scarfe, p. 73

Lucatello, S., Tsangarides, S., Beers, T., et al. 2005, ApJ, 625, 825

Magain, P. 1986, A&A, 163, 135

Majewski, S. R., Skrutskie, M. F., Schiavon, R. P., et al. 2008, American Astronomical Society Meeting #211, #132.08

Marcy, G. W., & Butler, R. P. 1998, ARA&A, 36, 56

Mashonkina, L., Korn, A. J., & Przybilla, N. 2007, A&A, 461, 261

Matteucci, F., & François, P. 1989, MNRAS, 239, 885

McCarthy, C. 1995, Master's Thesis, San Francisco State University

McWilliam, A. 1997, ARA&A, 35, 503

Meléndez, J., & Ramírez, I. 2004, ApJ, 615, L33

Meléndez, J., & Ramírez, I. 2007, ApJ, 669, L89

Meléndez, J., Shchukina, N. G., Vasiljeva, I. E., & Ramírez, I. 2006, ApJ, 642, 1082

Mihalas, D., Däppen, W., & Hummer, D. G. 1988, ApJ, 331, 815

Muller, R. 1999, in *Motions in the Solar Atmosphere*, Astrophysics and Space Science Library 239, eds. A. Hanslmeier, A. and M. Messerotti, p. 35

Murphy, M. T., Tzanavaris, P., Webb, J. K., & Lovis, C. 2007, MNRAS, 378, 221

Nave, G., Johansson, S., Learner, R. C. M., et al. 1994, ApJS, 94, 221

Nasmyth, J. 1865, Astronomical Register, 3, 223

Nesis, A., Hanslmeier, A., Hammer, R., et al. 1992, A&A, 253, 561

Nidever, D. L., Marcy, G. W., Buttler, R. P., et al. 2002, ApJS, 141, 503

Nissen, P. E., & Schuster, W. J. 1997, A&A, 326, 751

Nordlund, Å. 1982, A&A, 107, 1

Nordlund, Å. & Dravins, D. 1990, A&A, 228, 155

Nordström, B., Mayor, M., Andersen, J., et al. 2004, A&A, 418, 989

Pagel, B. E. J., & Patchett, B. E. 1975, MNRAS, 172, 13

Palme, H. & Jones, A. 2005, in *Meteorites, Comets and Planets: Treatise on Geochemistry*, 1; Published by Elsevier B. V., Amsterdam; ed. A. M. Davis, p. 41

Perryman, M. A. C. 2005, in *The Three-Dimensional Universe with Gaia*, ESA Special Publication 576, eds. C. Turon, C., K. S. O'Flaherty, K. S., & M. A. C. Perryman, p. 15

Rana, N. C., 1991, ARA&A, 29, 129

Ramírez, I., & Meléndez, J. 2005a, ApJ, 626, 446

Ramírez, I., & Meléndez, J. 2005b, ApJ, 626, 465

Ramírez, I., Allende Prieto, C., & Lambert, D. L. 2007, A&A, 465, 271

Re Fiorentin, P., Bailer-Jones, C. A. L., Lee, Y. S., et al. 2007, A&A, 467, 1373

Reddy, B. E., Tomkin, J., Lambert, D. L., & Allende Prieto, C. 2003, MNRAS, 340, 304

Reddy, B. E., Lambert, D. L., & Allende Prieto, C. 2006, MNRAS, 367, 1329

Robinson, F. J., Demarque, P., Li, L. H., et al. 2003, MNRAS, 340, 923

Rocha Pinto, H. J., & Maciel, W. J. 1998a, MNRAS, 298, 332

Rocha Pinto, H. J., & Maciel, W. J. 1998b, A&A, 339, 791

Roudier, T., & Muller, R. 1987, Solar Physics, 107, 11

Roudier, T., Mein, P., Muller, R., et al. 1991, A&A, 248, 237

Rutten, R. J., Hammerschlag, R. H., Bettonvil, F. C. M., et al. 2004, A&A, 413, 1183

Saar, S. H., & Brandenburg, A. 1999, ApJ, 524, 295

Saar, S. H., & Donahue, R. A. 1997, ApJ, 485, 319

Saar, S. H., & Osten, R. A. 1997, MNRAS, 284, 803

Sagar, R., & Bhatt, H. C. 1988, Journal of Astrophysics and Astronomy, 9, 117

Sánchez Almeida, J., Ruiz Cobo, B., del Toro Iniesta, J. C. 1996, A&A, 314, 295

Scharmer, G. B., Bjelksjo, K., Korhonen, T. K., et al. 2003, in *Innovative Telescopes and Instrumentation for Solar Astrophysics*, Proceedings of the SPIE 4853, eds. S. L. Keil and S. V. Avakyan, p. 341

Scharmer, G. B., Brown, D. S., Petterson, L., & Rehn, J. 1985, Applied Optics, 24, 2558

Schuler, S. C., King, J. R., Terndrup, D. M., et al. 2006a, ApJ, 636, 432

Schuler, S. C., Hatzes, A. P., King, J. R., et al. 2006b, AJ, 131, 1057

Schuster, W. J., & Nissen, P. E. 1989, A&A, 221, 65

Shchukina, N., & Trujillo Bueno, J. 2001, ApJ, 550, 970

Smith, M. A. 1978, ApJ, 224, 584

Smith, M. A. 1983, PASP, 95, 268

Sneden, C. 1973, PhD Thesis, The University of Texas at Austin

Sobeck, J. S., Lawler, J. E., & Sneden, C. 2007, ApJ, 667, 1267

Spite, F., & Spite, M. 1982, A&A, 115, 357

Stefanik, R. P., Latham, D. W., & Torres, G. 1999, in *Precise Stellar Radial Velocities*, ASP Conf. Series 185, eds. J. B. Hearnshaw & C. D. Scarfe, p. 354

Steigman, G. 2006, International Journal of Modern Physics E, 15, 1

Stein, R. F., & Nordlund, Å. 1998, ApJ, 499, 914

Steffen, M., & Freytag, B. 1991, Reviews in Modern Astronomy, 4, 43

Steinmetz, M., Zwitter, T., Siebert, A., et al. 2006, AJ, 132, 1645

Struve, O., & Elvey, C. T. 1934, ApJ, 79, 409

Sudarsky, D., Burrows, A., & Hubeny, I. 2003, ApJ, 588, 1121

Timmes, F. X., Woosley, S. E., & Weaver, T. A. 1995, ApJS, 98, 617

Tinsley, B. M. 1980, Fund. Cosmic Phys., 5, 287

Tokovinin, A. A. 1991, A&AS, 91, 497

Tokovinin, A. A. 1992, A&A, 256, 121

Tonry, J., & Davis, M. 1979, AJ, 84, 1511

Trampedach, R. 2007, in *Unsolved Problems in Stellar Physics*, AIP Conf. Proc. 948, eds. R. J. Stancliffe et al., p. 141

Tull, R. G. 1998, in *Optical Astronomical Instrumentation*, Proceedings of the SPIE 3355, ed. S. D'Odorico, p. 387

Tull, R. G., MacQueen, P. J., Sneden, C., & Lambert, D. L. 1995, PASP, 107, 251

Vögler, A. 2004, A&A, 421, 755

Woolf, V., & Wallerstein, G. 2005, MNRAS, 356, 963

Wheeler, J. C., Sneden, C., & Truran, J. W. 1989, ARA&A, 27, 279

Yong, D., Lambert, D. L., & Ivans, I. I. 2003, ApJ, 599, 1357

Yong, D., Lambert, D. L., Allende Prieto, C., & Paulson, D. B. 2004, ApJ, 603, 697

Vita

Iván Ramírez was born in Lima, Peru on January 15, 1979, the son of Rufino Ramírez and Catalina Carrascal. As an undergraduate, he participated in astronomical research funded by the Consejo Nacional de Ciencia y Tecnología of Peru. After obtaining a degree in Physics from Universidad Nacional Mayor de San Marcos, Lima in December 2002, he worked at the Space Telescope Science Institute in the summer of 2003. In August 2003, he started graduate studies at the University of Texas, where he obtained a Master's degree from the Department of Astronomy in 2005.

Permanent address: Jr. Casma 224, Los Olivos
Lima, Peru

This dissertation was typeset with LaTeX[†] by the author.

[†] LaTeX is a document preparation system developed by Leslie Lamport as a special version of Donald Knuth's TeX Program.